AD NUMBER

AD901465

NEW LIMITATION CHANGE

TO

Approved for public release, distribution unlimited

FROM

Distribution authorized to U.S. Gov't. agencies only; Test and Evaluation; Apr 1972. Other requests shall be referred to ASD[SDQR], Wright-Patterson AFB, OH, 45433.

AUTHORITY

AFFDL ltr, 12 Nov 1973

FTC-TD-71-8

FTC-TD-71-8

VOLUME I OF II

FLIGHT TEST AND WIND TUNNEL PERFORMANCE CHARACTERISTICS OF THE X-24A LIFTING BODY

LAWRENCE G. ASH
Captain, USAF
Aerospace Research Engineer

TECHNOLOGY DOCUMENT NO. 71-8

JUNE 1972

AFTC

AIR FORCE FLIGHT TEST CENTER
EDWARDS AIR FORCE BASE, CALIFORNIA
AIR FORCE SYSTEMS COMMAND
UNITED STATES AIR FORCE

AFSC-EDWARDS AFB, MUROC CAL

FTC-TD-71-8

VOLUME I OF II

FLIGHT TEST AND WIND TUNNEL PERFORMANCE CHARACTERISTICS OF THE X-24A LIFTING BODY

LAWRENCE G. ASH
Captain, USAF
Aerospace Research Engineer

FOREWORD

This technology document presents the performance characteristics of the X-24A lifting body obtained from flight data and compares them with wind tunnel predictions. The X-24A flight test program began 17 April 1969 and was completed on 4 June 1971. References 1 through 8 are related documents reporting the flight test results from the X-24A program.

The author wishes to acknowledge the efforts of Mr. David F. Richardson for developing the computer program used to calculate performance parameters from flight data (appendix IV) and Mr. Christopher J. Nagy who developed the X-24A position error correction (appendix III). The author also wishes to acknowledge Mr. Robert G. Hoey for his study on tip fin flow separation (appendix V) and for his advice and assistance in writing this report.

The participation of AFFTC personnel in this program was authorized by Project Directive 69-38. The assigned Program Structure was 680A.

Foreign announcement and dissemination by the Defense Documentation Center are not authorized because of technology restrictions of the U.S. Export Control Acts as implemented by AFR 400-10.

Prepared by:

Lawrence G. Ash

LAWRENCE G. ASH
Captain, USAF
Aerospace Research Engineer

Reviewed and approved by:

1 JUNE 1972

James W. Wood

JAMES W. WOOD
Colonel, USAF
Commander, 6510th Test Wing

Robert M. White

ROBERT M. WHITE
Brigadier General, USAF
Commander

ABSTRACT

The objectives of determining the performance characteristics of the X-24A lifting body from flight test data and correlating these results with wind tunnel predictions were successfully accomplished. Lift and drag characteristics were computed from onboard measured accelerations and flight conditions while the vehicle was in gliding flight. Performance data were obtained over Mach number and angle of attack ranges of 0.26 to 1.5 and 1.5 to 19.6 degrees, respectively. Discrepancies were apparent between different wind tunnel predictions. However, flight test data generally exhibited lower lift and slightly lower drag than wind tunnel predictions with the result that flight test and wind tunnel L/D values were in reasonably good agreement. Effects of Mach number, vehicle control surface configuration, and landing gear deployment on performance parameters were determined. Degradation of flight performance at low subsonic Mach numbers was attributed to tip fin flow separation. In Volume II of this report, supersonic performance comparisons are made between the PRIME and X-24A vehicles, both of which were of the same aerodynamic configuration (SV-5). A significant degradation in subsonic performance due to simulated ablative surface roughness was obtained in full scale wind tunnel tests. Flight testing of simulated ablatives on the X-24A was not pursued; however, the estimated effects of the ablatives are discussed in Volume II.

table of contents

[1]These CONFIDENTIAL appendicies will be published separately as Volume II to this report.

list of illustrations

list of tables

list of abbreviations and symbols

Item	Definition	Units
a_{x_b}	acceleration along body x-axis (longitudinal)	g's
a_{z_b}	acceleration along body z-axis (normal)	g's
b	reference span (10 ft)	ft
$\bar{c}$	reference length (23 ft)	ft
C_c	chord force coefficient	dimensionless
$C_{c_{\delta e}}$	$\partial C_c/\partial \delta e$	per rad, per deg
C_D	vehicle total drag coefficient	dimensionless
C_{D_0}	zero lift drag coefficient (trimmed drag at zero lift)	dimensionless
C_L	vehicle lift coefficient	dimensionless
$C_{L_{ic}}$	vehicle lift coefficient based on indicated airspeed (corrected for instrument error)	dimensionless
C_{L_α}	$\partial C_L/\partial \alpha$	per deg
C_ℓ	rolling moment coefficient	dimensionless
C_{ℓ_β}	$\partial C_\ell/\partial \beta$	per deg
$C_{\ell_{\delta a_U}}$	$\partial C_\ell/\partial \delta a_U$	per deg
C_m	pitching moment coefficient	dimensionless
C_{m_q}	$\partial C_m/\partial \left(\frac{q\bar{c}}{2V_t}\right)$	per rad
$C_{m_{\delta e}}$	$\partial C_m/\partial \delta_e$	per rad, per deg
C_N	normal force coefficient	dimensionless
C_{N_α}	$\partial C_N/\partial \alpha$	per deg
$C_{N_{\delta e}}$	$\partial C_N/\partial \delta e$	per rad, per deg
C_n	yawing moment coefficient	dimensionless
C_{n_β}	$\partial C_n/\partial \beta$	per deg
$C_{n_{\delta a_U}}$	$\partial C_n/\partial \delta a_U$	per deg
cg	center of gravity	pct $\bar{c}$
H	pressure altitude	ft
HM	hinge moment	in.-lb
ΔH_{pc}	altitude position error correction	ft
L/D	ratio of lift to drag	dimensionless
L/D_{max}	maximum ratio of lift to drag	dimensionless
M	flight or free stream Mach number	dimensionless

Item	Definition	Units
M_{ic}	indicated Mach number corrected for instrument error (not corrected for position error)	dimensionless
ΔM_{pc}	Mach correction for position error	dimensionless
NASA	National Aeronautics and Space Administration	- - -
OD	outer diameter	in.
p	roll rate	deg per sec
$\dot{p}$	roll acceleration	deg per sec^2
P_a	atmospheric or ambient pressure	psf
PCM	pulse code modulation	- - -
ΔP_p	static pressure source position error	psf
$\Delta P_p/q_{c_{ic}}$	position error pressure coefficient	dimensionless
P_s	measured static pressure	psf
q	pitch rate	deg per sec
$\dot{q}$	pitch acceleration	deg per sec^2
q_c	differential pressure	psf
$q_{c_{ic}}$	indicated differential pressure corrected for instrument error	psf
r	yaw rate	deg per sec
$\dot{r}$	yaw acceleration	deg per sec^2
R_e	Reynolds number	dimensionless
S	reference area (962 ft^2)	ft^2
SAS	stability augmentation system	- - -
T	thrust	lb
V_e	equivalent airspeed ($\approx V_t\sqrt{\sigma}$)	kt
ΔV_{pc}	airspeed position error correction	kt
V_t	true airspeed	kt
W	airplane gross weight	lb
α	true angle of attack	deg
α_{boom}	vane angle of attack with respect to the nose boom	deg
$\Delta\alpha_{bb}$	correction to angle of attack for boom bending	deg
α_i	indicated angle of attack	deg
$\Delta\alpha_q$	correction to angle of attack for pitch rate	deg

Item	Definition	Units
α_T	true angle of attack as established by the wind tunnel	deg
$\Delta\alpha_c$	correction to angle of attack for upwash	deg
β	sideslip angle	deg, rad
δa_U	upper flap aileron deflection	deg, rad
δe	elevator deflection	deg
δe_L	lower flap deflection in pitch	deg
δe_U	upper flap deflection in pitch	deg
δL_B	lower flap bias position	deg
δR_B	rudder bias position	deg
δU_B	upper flap bias position	deg
δw	wedge angle ($\delta w = \delta L_B - \delta e_U$ or $\delta e_L - \delta U_B$)	deg
σ	relative air density or air density ratio ($\sigma = \rho/\rho_{SL}$)	dimensionless

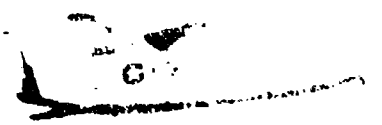

INTRODUCTION

The X-24A lifting body flight test program was conducted at the Air Force Flight Test Center between April 1969 and June 1971. In addition to proving the unpowered landing capability of this class of medium lift-to-drag ratio (L/D) reentry vehicle, extensive flight data were obtained to define the handling qualities, stability, control, and performance characteristics of the X-24A configuration through the subsonic, transonic, and supersonic Mach number (M) regions up to M = 1.60.

Design predictions of the flight characteristics of the X-24A lifting body were based on theoretical calculations and wind tunnel data obtained from small scale models. Verifying the accuracy of these data and investigating the effect of any inaccuracies on vehicle performance were major objectives of the flight test program. To accomplish these objectives, performance data were obtained from maneuvers on a flight-by-flight basis for the entire test program. This report presents the performance characteristics obtained from the 28 X-24A flights. Data were obtained for 7 fixed upper flap bias configurations and 3 rudder bias configurations, over a Mach number range of M = 0.26 to 1.50 and at angles of attack (α) from 1.5 degrees to 19.6 degrees. Flight Reynolds numbers (R_e) ranged from 12 x 10^6 to 65 x 10^6, based on the vehicle reference length of 23.0 feet. Some data were also obtained with the lower flaps at zero degrees while controlling with the upper flaps in both the landing gear up and landing gear down configurations. Flight results were compared with full scale and small scale wind tunnel predictions. Effects of Mach number, wedge angle, rudder bias, tip fin flow separation, and landing gear deployment on flight performance parameters are analyzed and discussed.

In appendices VI and VII to this report (published separately), hypersonic flight data from the subscale PRIME[2] test program were compared to the supersonic X-24A flight performance data. Also included is a study which summarized the results of several tests (including a full scale X-24A wind tunnel test) dealing with the effects of ablatives on the low speed performance characteristics of medium L/D vehicles. These effects were applied to X-24A flight test performance data in an attempt to predict the subsonic performance characteristics of an ablated X-24A.

DESCRIPTION OF THE VEHICLE

The overall shape and dimensions of the X-24A are shown in figure 1. The vehicle was wedge-shaped in planform with a flat bottom and the top a curved airfoil surface with three vertical fins. All control surfaces were located at the aft end of the vehicle and consisted of two upper and two lower flaps and two upper and two lower rudders on the outboard fins. Pilot and stability augmentation system (SAS) inputs in pitch and roll were transmitted mechanically to the lower flap actuators. When either lower flap reached the fully closed position (zero degrees), pitch and roll inputs were transferred through a clapper mechanism to the corresponding upper flap. Pilot rudder pedal and yaw SAS inputs caused motion of the upper rudders only as yaw control surfaces. Both pairs of upper and lower rudder surfaces could be deflected symmetrically (biased). Also, both pairs of upper and lower flaps could be

[2]PRIME (Precision Recovery Including Maneuvering Entry), an unmanned subscale vehicle of the same configuration as the X-24A (SV-5) which was boosted to orbital speeds on an Atlas booster.

biased within a range of positions. The flaps and rudder surfaces could be biased outward from their closed positions to increase the stability at transonic and supersonic speeds. The flap and rudder bias features were driven by slowly moving trim motors which were controlled by switches in the cockpit. Control surface bias designations and sign conventions are shown in figure 6. A complete description of the X-24A flight control system is presented in reference 1.

Most flying was accomplished with the upper flaps fixed while controlling with the lower flaps. However, two landing approaches were accomplished with the lower flaps at zero degrees, with pitch and roll control on the upper flaps. Upper flap control was also used for most of the landings after landing gear deployment. The vehicle configuration that evolved for flight at Mach numbers greater than 0.50 is shown in figure 2. The standard approach and landing configuration is shown in figure 3. A complete description of the X-24A vehicle is presented in reference 2.

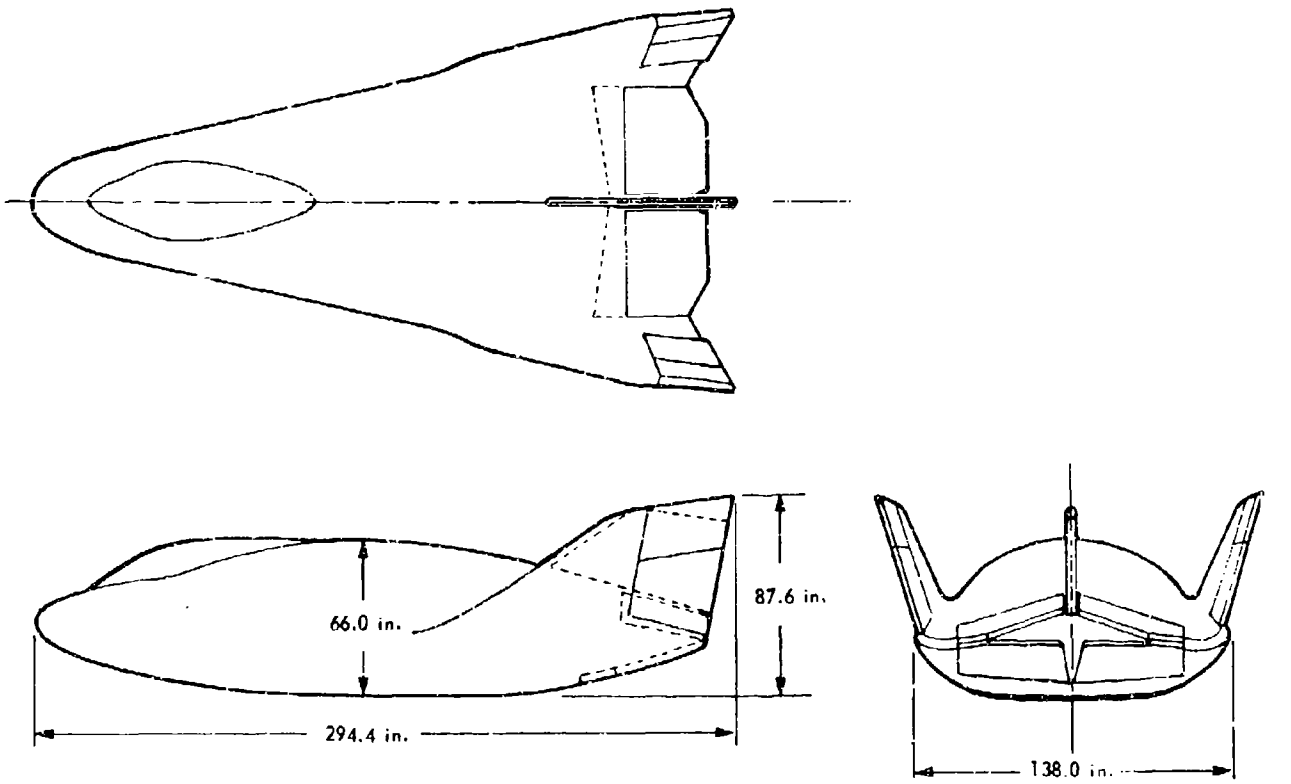

Figure 1 Three-View Drawing of the X-24A

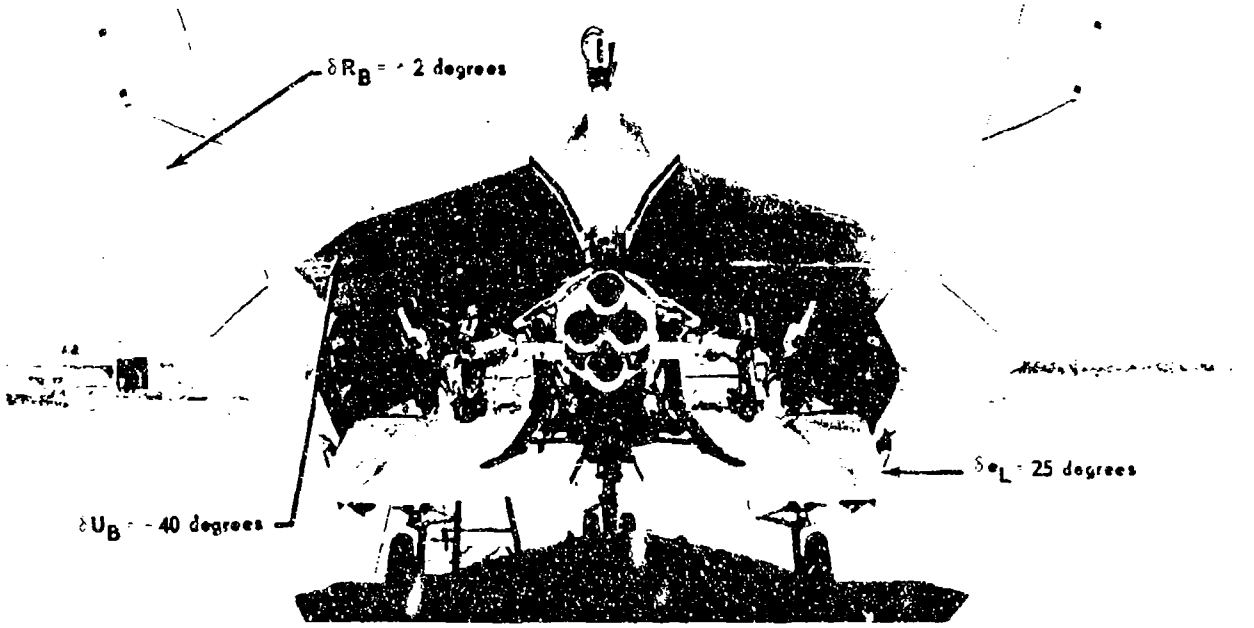

Figure 2 Transonic and Supersonic Configuration

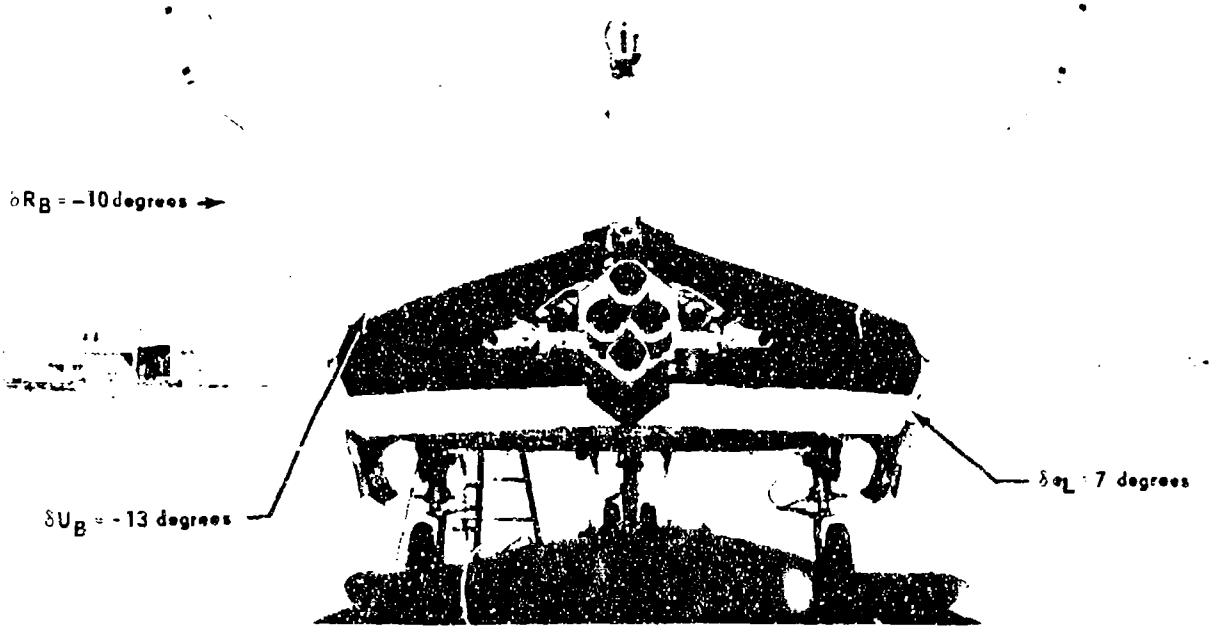

Figure 3 Subsonic Configuration

TEST METHOD

The X-24A flight program consisted of 10 glide flights and 18 powered flights using an XLR-11 rocket engine. In powered flight, the vehicle was flown to a predetermined Mach number and altitude at which time the rocket engine was shut down and the vehicle glided to an unpowered landing. A complete description of flight profiles, procedures, and objectives is presented in reference 2.

All performance data maneuvers were performed with the vehicle in gliding flight. No attempt was made to obtain lift and drag data while the rocket engine was running or during propellant jettison.

Test Performance Maneuvers

A pushover-pullup maneuver was used to obtain most of the performance flight data. A typical flight maneuver is shown in figure 4. The pilot steadily decreased angle of attack to about 3 degrees, pulled up to 14 degrees, and then returned to the original angle of attack. The pilot tried to perform the task slowly enough to avoid large pitch accelerations, but fast enough to keep Mach number somewhat constant during the maneuver. Trading off these two parameters resulted in an average Mach number change of 0.055 during subsonic performance maneuvers and 0.1 to 0.27 during supersonic maneuvers. Besides the planned performance maneuvers, additional data were obtained from any substantial α excursion where the pitch rate was fairly constant.

Instrumentation

Accelerations were measured by sensitive accelerometers placed close to the vehicle's center of gravity. Angle of attack, angle of sideslip, static pressure (P_s), and total pressure were measured by a standard NASA pitot static tube on a 6.2-foot nose boom. All parameters were telemetered to ground stations by means of a pulse code modulation (PCM) data system and recorded on magnetic tape at the ground station.

Data Analysis

The raw data were processed through a NASA data reduction follow-on computer program. This program made all the necessary corrections to the data including an upwash correction to angle of attack and a position error correction to measured static pressure. A detailed discussion of how these two corrections were developed is in appendices II and III.

For each maneuver, data were selected at points where pitch acceleration (q̇) was approximately zero. This was done in an attempt to obtain more consistent data at trimmed flight conditions. Figure 5 compares data selected at half second intervals of a maneuver, to data of the same maneuver selected at points of zero pitch acceleration. The data selected at zero pitch acceleration was more consistent and showed a smaller scatter band.

An IBM 1620 digital computer program was used to make additional corrections to the flight data and compute performance characteristics. Corrections were made to the accelerometers for misalignment and displacement from the test cg. Other corrections were made to the trim elevator

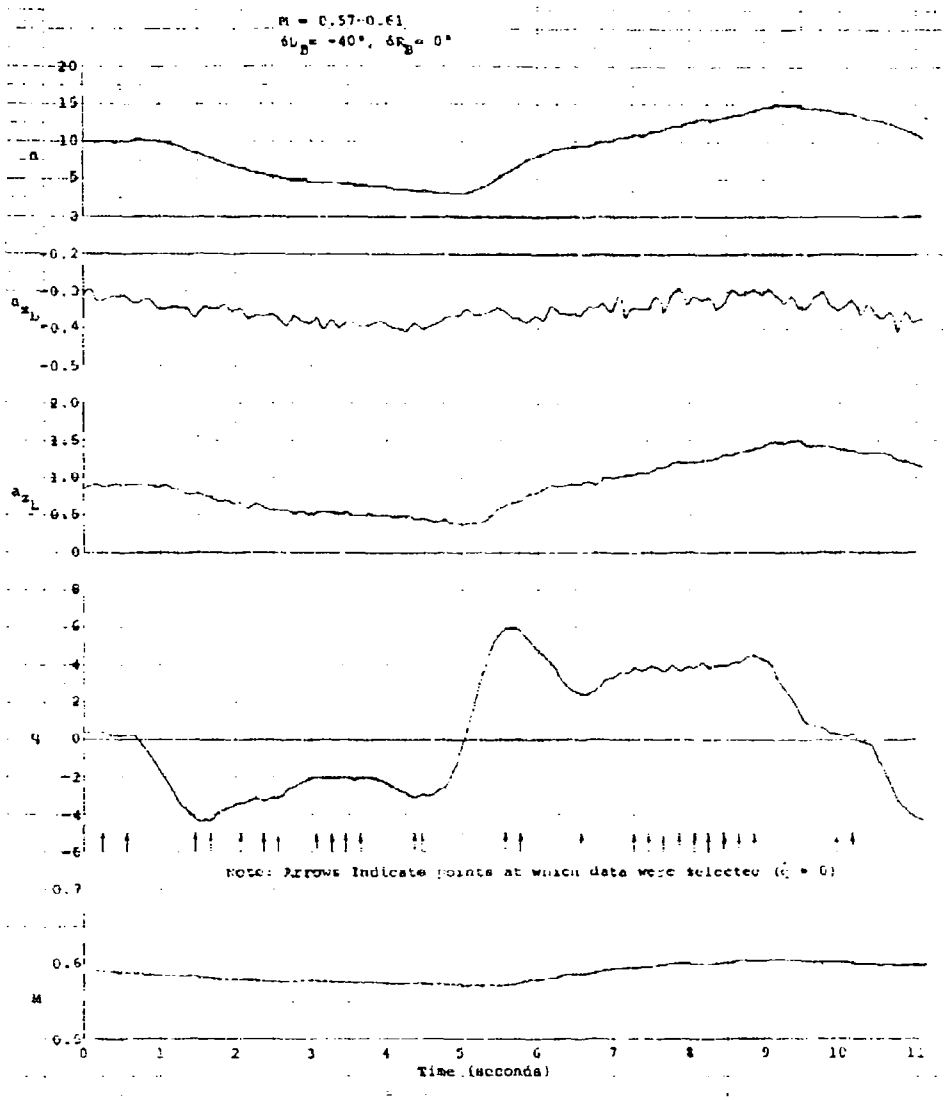

Figure 4 Time History of a Pushover-Pullup Maneuver

position for pitch rate and cg variation from a reference wind tunnel cg of 57 percent. The body axis force coefficients were computed from the corrected accelerations, calculated gross weight (reference 3), and dynamic pressure. Lift coefficient (C_L), drag coefficient (C_D) and L/D were then computed by rotating the body axis coefficients to the stability axis using true angle of attack. The body and stability axis coordinate systems showing the positive direction of forces, moments, and angles are presented in figure 6. A detailed description of the computer program along with a list of equations, a program listout, and a sample output are in appendix IV.

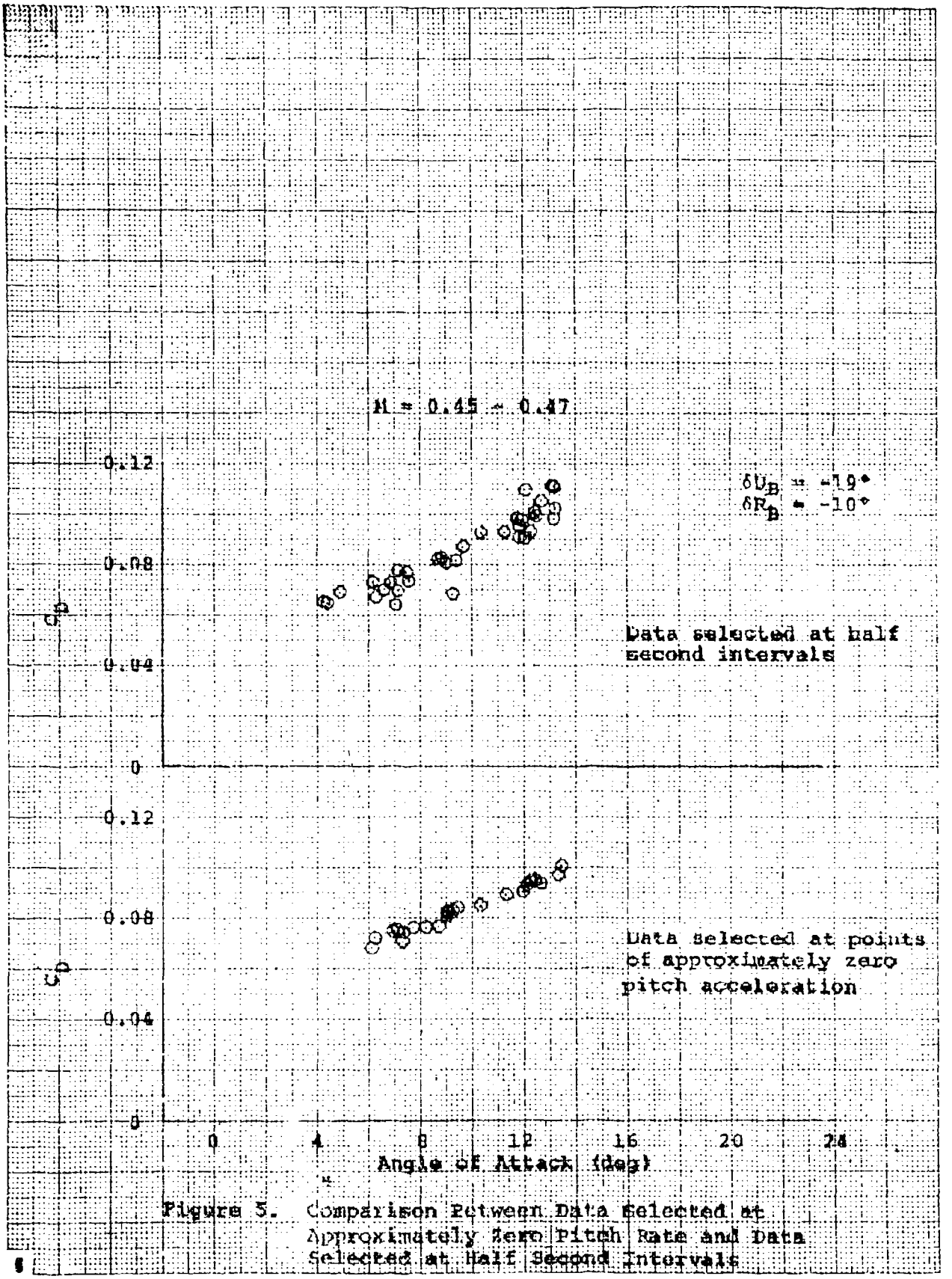

Figure 5. Comparison Between Data Selected at Approximately Zero Pitch Rate and Data Selected at Half Second Intervals

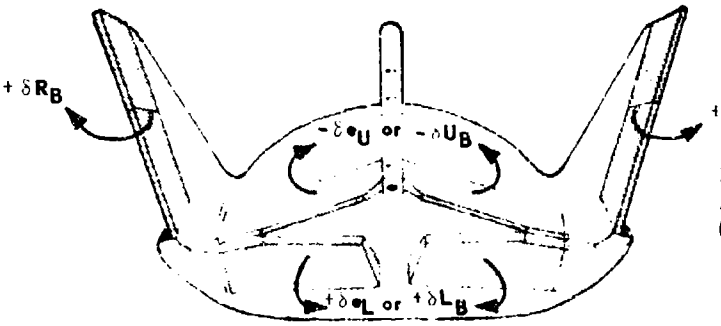

X-24A VIEW LOOKING FORWARD
ALL CONTROLS IN NEUTRAL
(δ = 0 deg) POSITION

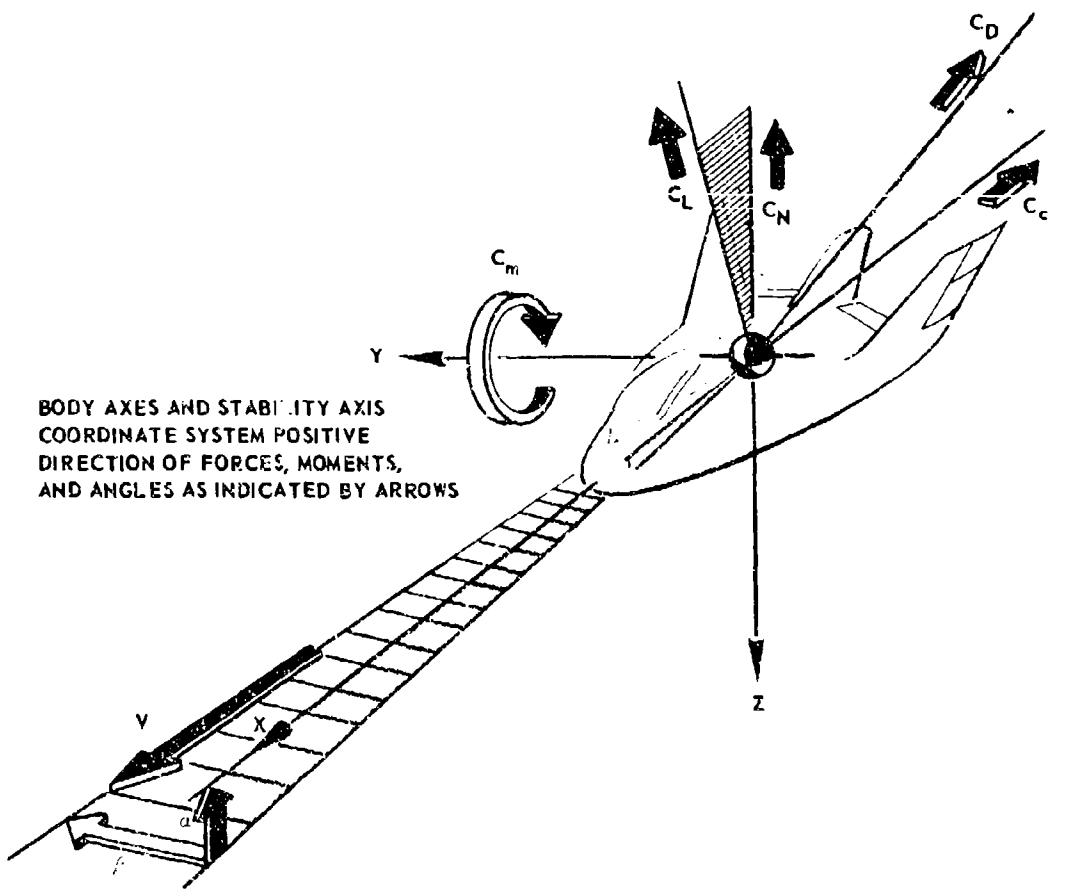

BODY AXES AND STABILITY AXIS
COORDINATE SYSTEM POSITIVE
DIRECTION OF FORCES, MOMENTS,
AND ANGLES AS INDICATED BY ARROWS

Figure 6 Control Surface Bias Designations, Axis Systems, and Sign Conventions

WIND TUNNEL TESTS

Extensive wind tunnel tests were performed on the full scale X-24A (at M = 0.2) and an 8 percent steel model of the aircraft prior to the flight test program. A wide range of vehicle control surface configurations were tested for a Mach number and angle of attack range which encompassed the X-24A flight test envelope. Table I presents a summary of the wind tunnel tests that were used for comparison with flight data in this report. Since the performance data were greatly affected by control surface configuration and Mach number, only wind tunnel data which corresponded to the configuration and flight conditions of a particular test maneuver were used for comparison. There was an exception in the case of the full scale tunnel data which were limited to 0.2 Mach number. These data were only compared to flight data below M = 0.5 in the approach and gear down landing configurations. All other flight data were compared to tunnel tests performed on eight percent models.

Most wind tunnel data taken with the vehicle in the transonic configuration, (upper flap bias position, δU_B = -30 to -40 degrees with rudder bias position, δR_B = 0 degrees), were obtained from the Langley 8-foot wind tunnel. Most tunnel data taken at the low subsonic and approach configuration (δU_B = -10 to -30 degrees, δR_B = -10 degrees), were obtained from the Langley 7- x 10-foot wind tunnel.

Additional wind tunnel tests were performed later in the flight test program at the Cornell Aeronautical Laboratories using an eight percent fiberglass model. The main purpose of these tests was to obtain additional stability and control information, and only a small amount of performance data was obtained.

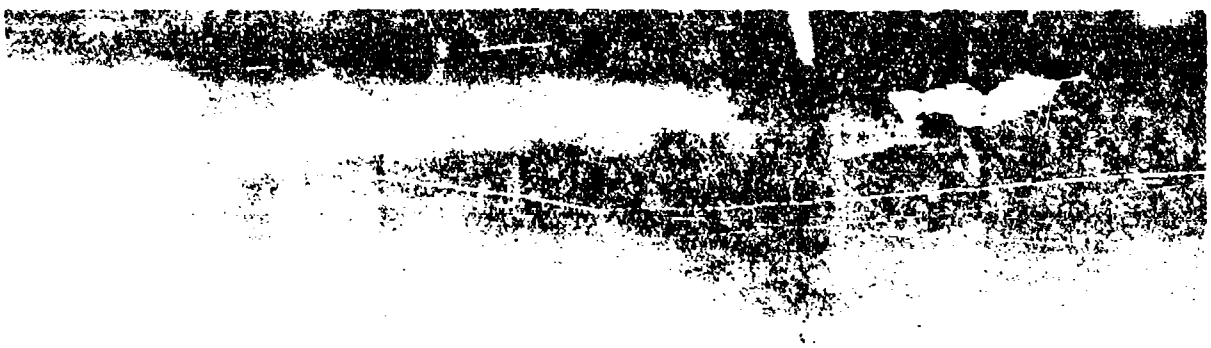

Table I

SUMMARY OF WIND TUNNEL TESTS

Wind Tunnel Size (ftxft)	Date	Mach No.	α Range (deg)	Upper Flap Setting (deg)	Lower Flap Setting (deg)	Rudder Bias Setting (deg)	$R_e \times 10^{-6}$
NASA - Langley (8 pct X-24A model)							
8x8	Apr 1965	0.60	0 to 20	-40	20	0	5.86
	Oct 1965	0.80	0 to 24		20,30		6.96
		0.90	0 to 24		20,25,30, 40		7.2
		0.95	0 to 18		20,30		7.47
		1.00			10,20,30		5.68
		1.20			20,30		5.81
		0.80	0 to 24	-35	20		6.96
		0.90	0 to 24		20,25		7.32
		0.95	0 to 18		20,25		7.47
		0.40	0 to 24	-30	0,10,20		4.25
		0.60			10,15,20		5.83
		0.80			10,15,20		6.96
7x10	Jun 1968	0.50	-4 to 20	-10,-15, -20,-25	0	-10	5.41
	Jul 1968	0.50	-4 to 22	-30	20		5.41
		0.60		-30	20		6.42
		0.60		-25	10,15,20		6.42
		0.70		-25	10,15,20		7.18
		0.50		-20	5,10,15,20		5.41
		0.60					6.42
		0.70					7.18
		0.50		-15	5,10,15		5.41
North American Aviation (8 pct X-24A model)							
7x7	Feb 1966	1.40	0 to 24	-40	10,20,30	0	---
NASA - Ames (Full scale X-24A vehicle)							
40x80	Ma. 1968	0.20	-4 to 28	-15	0,5,15	-9	29.4
		0.20		-5,-10, -15,-20	0		
		0.20		-20*	0,10,20		
		0.20		-5*-10* -20*	0		
		0.20		-20	0,5,10, 15,20,25		
		0.20		-20**	10,20		
		0.20		-60**	0,20,38	8	
Cornell Aero Laboratory (8 pct X-24A fiberglass model)							
8x8	Mar 1971	0.50	0 to 8	-13	5,10,15	-10	7.5
		0.50, 0.80, 0.95, 1.10, 1.30	4 to 28	-40	25	0	7.5 to 3.25

*Gear down

**With simulated ablatives

COMPARISON OF FLIGHT DATA TO WIND TUNNEL RESULTS

Performance flight test data are presented in figures 1 through 30, appendix I. Plots of C_L and C_D versus angle of attack, and L/D and C_D versus C_L are shown for all performance maneuvers flown and analyzed. All flight test data points were trimmed data corrected to a 57 percent reference cg for comparison with tunnel data. Curves were faired through the flight data points and are presented as dashed lines in the figures. The plots are sequenced in order of decreasing upper flap bias configuration, ending with data from the closed up approach configurations and gear down data. For each upper flap configuration, a set of performance data is presented at each individual Mach number for which flight test data were obtained and placed in order of increasing Mach number. A complete log of all flight test performance maneuvers is presented in table I, appendix I. For each maneuver, flight data were compared to all available wind tunnel trim points (zero pitching moment coefficient, for that flap setting) obtained at the corresponding Mach number and vehicle configuration. Where two or more trim wind tunnel points were available at one upper flap setting, a curve was faired through them to represent a trimmed wind tunnel curve at that upper flap configuration.

The Cornell wind tunnel trim points for the configuration in which δU_B = -40 degrees and δe_L = 25 degrees generally exhibited much higher trim angles of attack than both the Langley 8-foot tunnel and the flight data. This is suspected to be the result of a small error in the tip fin dihedral for the fiberglass model. It has been assumed that this discrepancy affected only the pitching moment data. The Cornell data points used for comparison with trimmed flight data were therefore selected at the flight determined trim angle of attack for that flap configuration.

During the flight test program there were no planned attempts to gather data at different Reynolds numbers. In some cases, however, two or more performance maneuvers were accomplished at the same flight conditions and vehicle configuration, but with different Reynolds numbers. In the flight data presented in figures 3, 5, 9, 11, 17, 27, and 28, appendix I, half solid symbols separate the maneuver which differs most in Reynolds number from the other maneuvers at each flight condition. Five different vehicle configurations and Mach numbers ranging from 0.5 to 0.9 are represented in these maneuvers. Reynolds numbers are referenced to the 23-foot reference length of the X-24A. Table II presents wind tunnel and flight Reynolds numbers for the entire flight Mach number range.

There were no variations in the flight test performance parameters which could be attributed to Reynolds number effects within the range of Reynolds numbers flown. Since the flight values of Reynolds number were always significantly larger than corresponding wind tunnel values, no conclusions could be reached as to the influence of Reynolds number on the performance discrepancies observed between flight test and wind tunnel results.

Table II

FLIGHT TEST AND WIND TUNNEL REYNOLDS NUMBER COMPARISON

Mach No.	Reynolds Number x 10^{-6}					
	Wind Tunnel Tests				Flight Test	
	Langley 8x8 ft	Langley 7x10 ft	Cornell Aero Lab	Ames Full Scale	Transonic Configuration	Subsonic Configuration
0.20				29.4		
0.35		4.32				44.6 to 54.2
0.40	4.25					
0.50		5.41	7.50		29.9 to 40.5	34.3 to 64.9
0.55					36.9, 39.6	27.5
0.60	5.83	6.42			27.2 to 34.9	35.1
0.70		7.18			18.2 to 42.1	32.3, 38.1
0.80	6.96	7.62	4.50		15.1 to 38.7	
0.90	7.32				18.6 to 30.5	
0.95	7.47		4.00			
0.97					17.3, 19.4	
1.00	5.68				14.9, 20.1	
1.10			3.75		12.5, 14.9	
1.20	5.81				12.5 to 15.6	
1.30			3.25		12.5 to 16.6	
1.40					16.6, 17.5	
1.50					17.5	

All supersonic performance flight data should be viewed with respect to the highly transient conditions under which they were obtained. A very limited amount of data was extracted from five different maneuvers during four different flights. All maneuvers were performed during periods of rapid deceleration with the aircraft undergoing ΔM changes of 0.10 to 0.27. In addition, this rapid deceleration was in excess of the measuring range of the sensitive longitudinal accelerometer ($\pm$0.5 g's). A less sensitive ($\pm$2.0 g's) accelerometer had to be used to compute axial chord force. Therefore, general trends of supersonic data should be well represented, but definite distinctions between data at different supersonic Mach numbers could not be determined as accurately as in the subsonic and transonic Mach number regions.

LIFT COEFFICIENT

Lift coefficient data shown in figures 1 through 30, appendix I, were in general agreement with wind tunnel predictions at low angles of attack (two to six degrees), but dropped below predictions at higher angles of attack. Figure 7, which presents data at δU_B = -40 degrees and δR_B = 0 degrees at 0.8 Mach number, is a good example of this effect. Flight values of trimmed lift curve slope (C_{L_α}) ranged from 12 percent above to 20 percent below trimmed wind tunnel values obtained from the Langley 8-foot and 7- x 10-foot wind tunnels for all Mach numbers and vehicle configurations. Cornell wind tunnel values of lift coefficient showed excellent agreement with flight data when compared at flight trim angles of attack. The one trim lift curve obtained from the Cornell tests in the δU_B = -13 degrees approach configuration was in excellent agreement with flight data (figure 27, appendix I).

Supersonic flight lift data are presented in figures 7 and 8, appendix I, for -40 degrees upper flap bias with 0 degrees and +2 degrees rudder bias, respectively. Supersonic flight was not performed with upper flap bias settings other than -40 degrees. Data at zero degrees δR_B from M = 1.1 to 1.2 compared well with the Langley 8-foot wind tunnel curve at M = 1.2. Flight data at +2 degrees δR_B from M = 1.4 to 1.5 showed good agreement with the North American Aviation 7- x 7-foot wind tunnel curve at M = 1.4 and +10 degrees rudder bias (figure 8, appendix I).

Full scale wind tunnel C_{L_α}'s were in good agreement with flight slopes in the two approach configurations. However, wind tunnel values of C_L for any particular angle of attack were generally higher throughout the α range (figures 27 and 28, appendix I).

Gear down flight data were obtained at two different control surface configurations and two nose gear door configurations.[3] Flight data are presented in figures 29 and 30, appendix I, along with full scale wind tunnel gear down curves. The flight data were scattered due to the different configurations, probable ground effects, and large control motions associated with the actual landings. Both sets of flight data have the same lift curve slope which is greater than the full scale wind tunnel C_{L_α}.

[3]The nose gear door was originally perpendicular to the body X-reference axis and was replaced prior to flight 9 by one canted at a 45-degree angle. Full scale wind tunnel tests were performed with the perpendicular nose gear door.

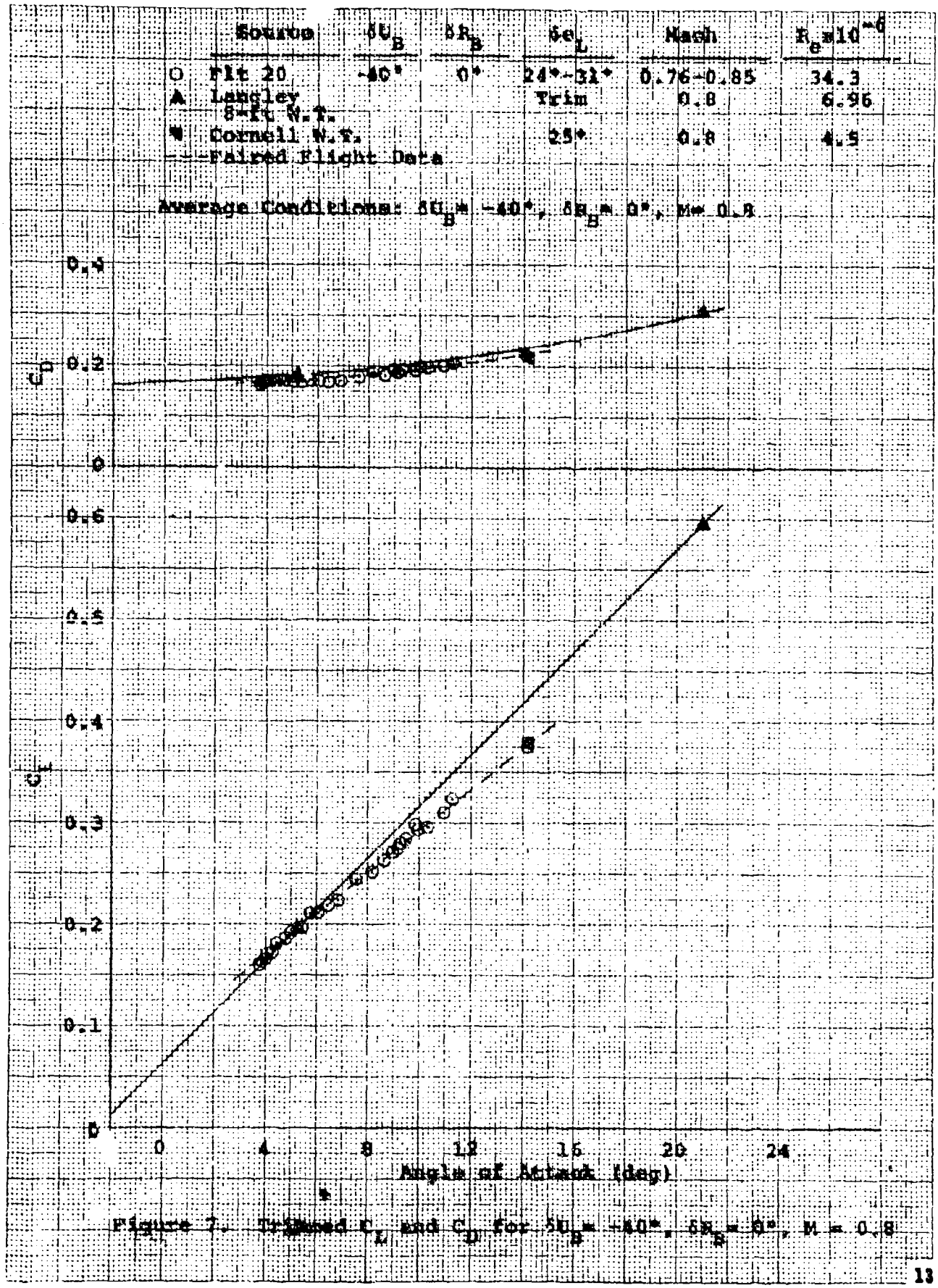

Figure 7. Trimmed C_L and C_D for δU_B = -40°, δR_B = 0°, M = 0.8

DRAG COEFFICIENT

Drag coefficient data are plotted versus angle of attack and also as drag polars (C_D vs C_L) in figures 1 through 30, appendix I. Flight data showed slightly lower drag than the Langley eight-foot wind tunnel curves for the transonic vehicle configurations (δU_B = -40, -35, and -30 degrees with δR_B = 0 degrees) at all Mach numbers. Figure 7, which presents data in the δU_B = -40 degrees and δR_B = 0 degrees configuration at 0.8 Mach number, is a good example of this trend.

Supersonic flight test drag data at 0 degrees rudder bias and -40 degrees upper flap bias (figure 7, appendix I) were lower than Langley 8-foot wind tunnel data taken at M = 1.2. Flight drag data versus angle of attack data at +2 degrees δR_B (figure 8, appendix I) within a Mach number range of 1.3 to 1.5 showed good agreement with the North American Aviation 7- x 7-foot wind tunnel curve at M = 1.4 and +10 degrees rudder bias. Drag polar data, however, were not as consistent with the wind tunnel curve and exhibited a much different drag polar curvature (drag due to lift). The +2 degrees δR_B data were less scattered than the zero degree δR_B flight data. However, there was insufficent data to draw any conclusions as to the performance effects of positive rudder deflection.

The flight drag data obtained at the smaller upper flap configurations (δU_B = -8 to -23 degrees) were compared to Langley 7- x 10-foot wind tunnel curves and showed excellent agreement (figures 21 through 28, appendix I).

Cornell wind tunnel drag values obtained with the $\delta U_B/\delta e_L$ = -40/25 degrees configuration and selected at flight trim angles of attack were in good agreement with flight data (figures 1 to 6, appendix I). The trimmed Cornell drag and drag polar curves obtained with the δU_B = -13 degrees and δR_B = -10 degrees configuration also agreed well with flight data at low C_L's, but exhibited higher values of C_D than did the flight data at C_L's above 0.3 (figure 27, appendix I).

Full scale wind tunnel drag versus angle of attack data were in excellent agreement with flight test data in the two approach configurations. Drag polars from the full scale tunnel form a lower boundary of the flight data scatter with the Langley 7- x 10-foot wind tunnel data forming the upper boundary. All of the flight gear down drag data were below full scale wind tunnel predictions.

LIFT-TO-DRAG RATIO

Lift-to-drag ratio flight data plotted versus lift coefficient are compared to wind tunnel data in figures 1 through 30, appendix I. Flight data were generally in good agreement or slightly above the Langley 8-foot and 7- x 10-foot wind tunnel data. Due to stability boundaries, many of the flight maneuvers in the transonic configurations and at high Mach numbers were not taken to an angle of attack high enough to reach maximum L/D. In most cases where flight maneuvers were taken to the maximum L/D, the values of maximum L/D and corresponding lift coefficient compared well with available trim wind tunnel curves.

Supersonic L/D flight data at 0 degrees rudder bias (figure 7, appendix I) in the M = 1.1 to 1.3 Mach number range were in good agreement with the Langley 8-foot wind tunnel curve at M = 1.2. Flight L/D data

at +2 degrees δR_B in the M = 1.3 to 1.5 range show good agreement with the North American Aviation 7- x 7-foot wind tunnel curve at M = 1.4 and δR_B = +10 degrees (figure 8, appendix I).

Flight L/D data did disagree with the Langley 7- x 10-foot wind tunnel L/D curves in several cases. In the δU_B = -21 degrees, δR_B = -10 degrees configuration at 0.5 and 0.6 Mach numbers (figures 23 and 24, appendix I), flight data appear to reach maximum L/D at a much lower C_L than the wind tunnel and drop well below wind tunnel L/D's at the higher C_L's. This data was obtained across the boundary of tip fin flow separation which is discussed in detail in the Tip Fin Flow Separation section.

Flight L/D data also differs from the Langley 7- x 10-foot wind tunnel data in the approach configurations (figures 27 and 28, appendix I). Flight data is generally higher in L/D than the tunnel curve which is at the low boundary of the scatter. The full scale wind tunnel curve forms an upper boundary of the scatter so that the two wind tunnel curves form an envelope enclosing the flight data.

Cornell wind tunnel L/D points at the $\delta U_B/\delta e_L$ = -40/25 degrees configuration, which were selected at flight trim angles of attack, were generally in good agreement with flight test data (figures 1 to 6, appendix I). The Cornell trim L/D curve at the δU_B = -13 degrees, δR_B = -10 degrees configuration was also in reasonably good agreement with flight data (figure 27, appendix I).

Flight gear down L/D data are compared to full scale wind tunnel gear down curves in figures 29 and 30, appendix I. The flight data generally exhibited higher L/D's than the wind tunnel curves. Flight data obtained with the canted gear door were generally slightly higher in L/D than those obtained with the perpendicular gear door.

FAIRED FLIGHT TEST COMPARISONS

Faired flight data are presented in terms of C_L and C_D versus α, and L/D and C_D versus C_L. Faired flight values of C_L^2 versus C_D are also presented. Comparisons are made to illustrate Mach number, wedge angle, and rudder bias effects on performance characteristics. In addition, the effects of tip fin flow separation and landing gear deployment are analyzed.

MACH NUMBER EFFECTS

For two transonic control surface configurations (δU_B = -40 degrees and -30 degrees with δR_B = 0 degrees) faired flight curves are compared for the entire Mach number range in which data was obtained, in order to show Mach number effects (figures 8 and 9).

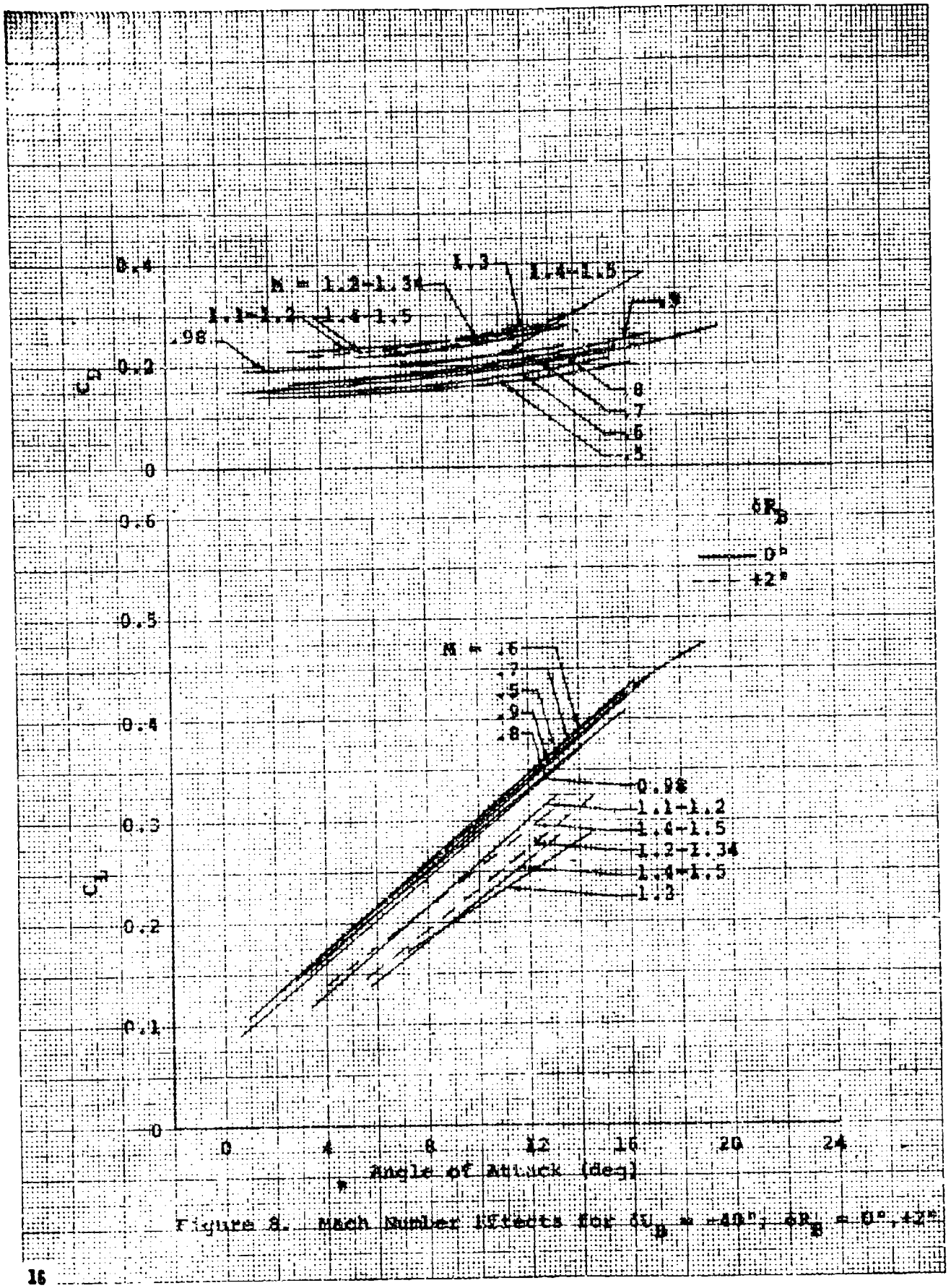

Figure 8. Mach Number Effects for $\delta T_D = -40°$, $\delta R_D = 0°, \pm 2°$

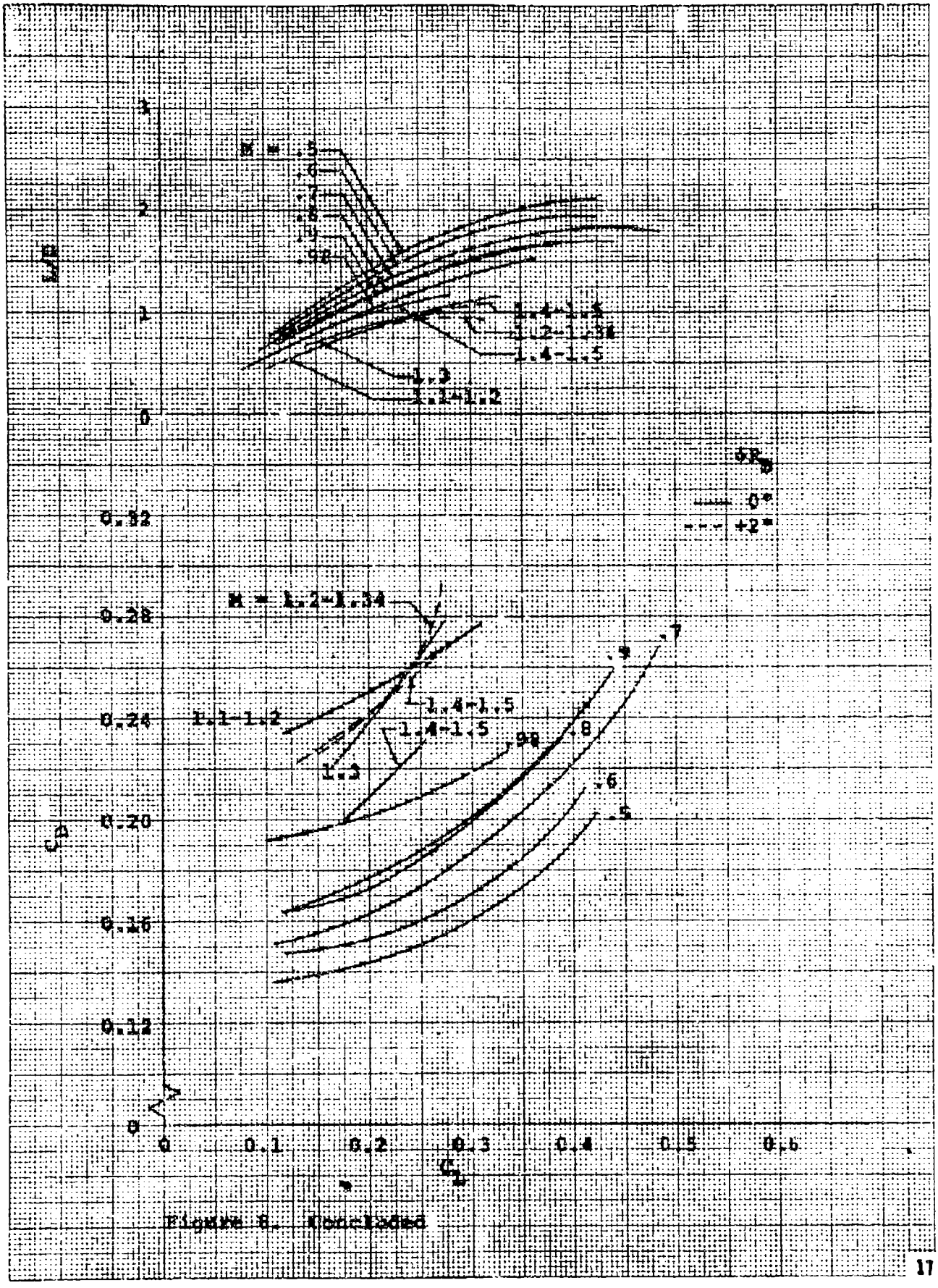

Figure 8. Concluded

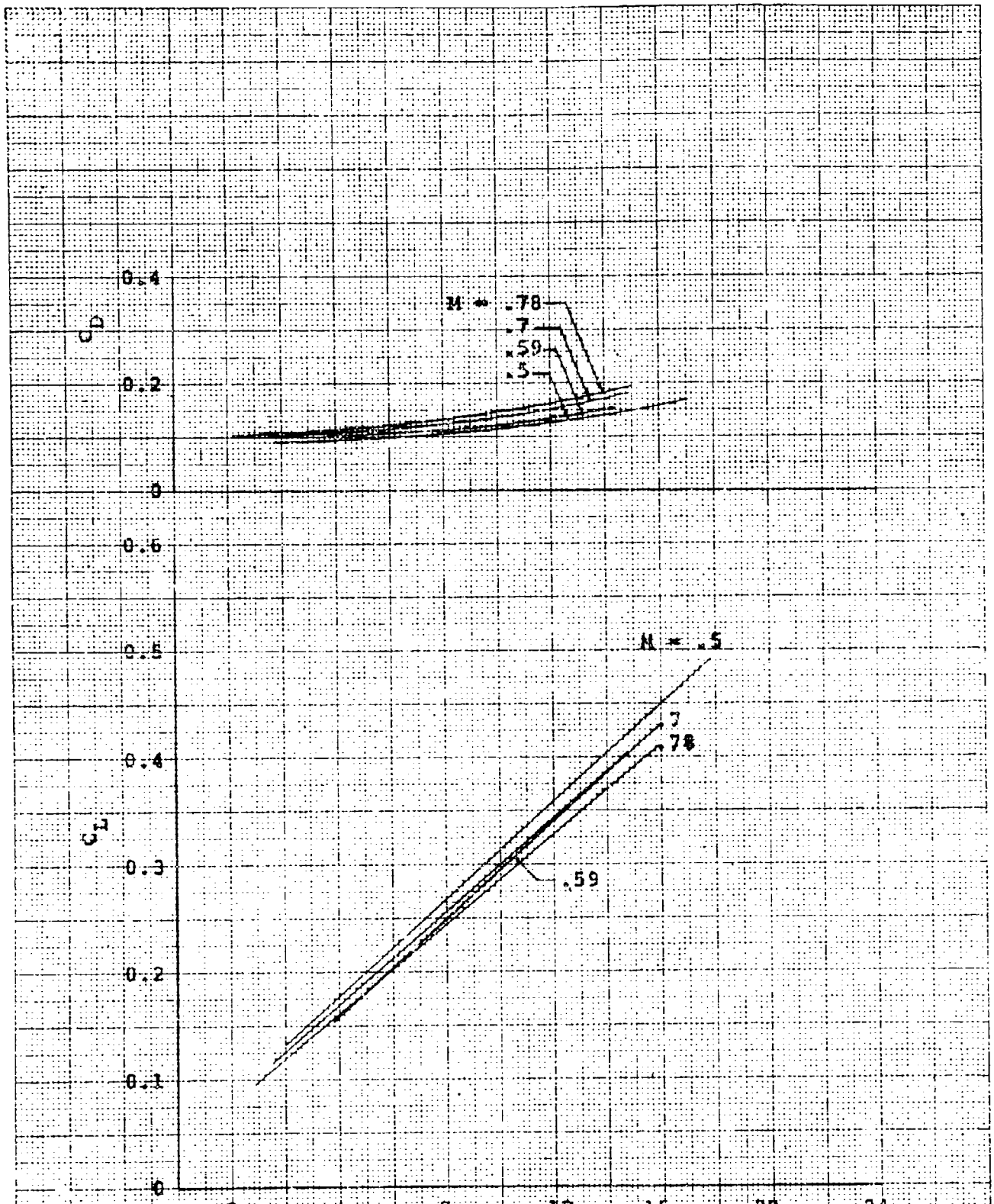

Figure 9. Mach Number Effects for $\delta i_B = -30°$; $\delta_{SB} = 0°$

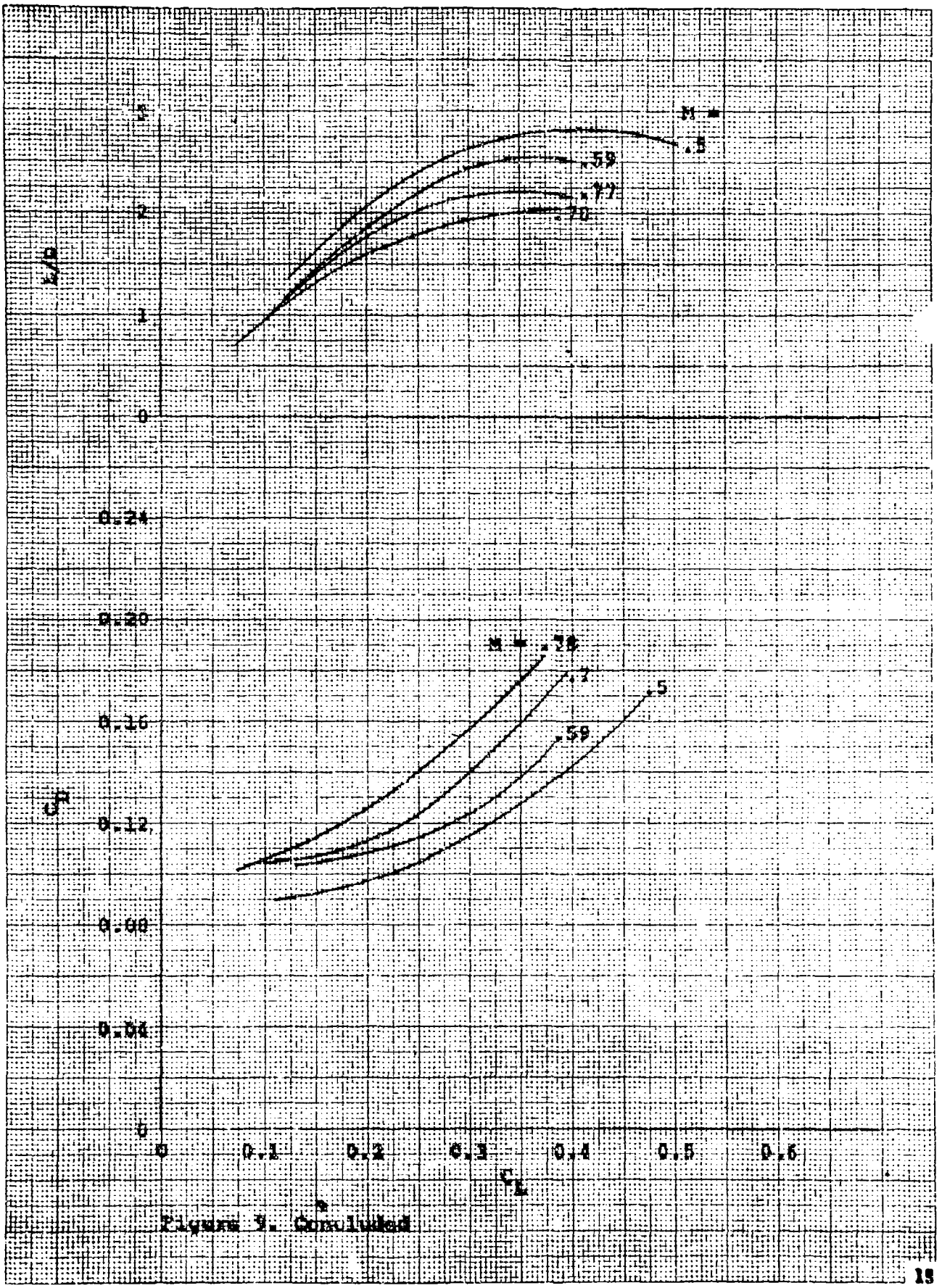

Figure 9. Concluded

Lift Coefficient

Data were obtained with -40 degrees upper flap bias for the entire Mach range of the program from M = 0.5 to 1.5 (figure 8). In the subsonic region from M = 0.5 to 0.9, there was little change in the C_L versus α curve as a function of Mach number. The actual data points fell within the same scatter band. The C_L values for a particular trim angle of attack began to decrease slightly as transonic speeds were reached, and decreased greatly at Mach 1.0. Values of C_L reached a minimum at about M = 1.3 and increased slightly at M = 1.4 to 1.5. The C_{L_α} slopes did not change significantly with Mach number.

The same general trends are apparent but not as well defined in the C_L versus α data for the -30 degrees upper flap bias configuration (figure 9).

Drag Coefficient

Paired drag coefficient versus angle of attack curves and drag polars are presented in figures 8 and 9. Figure 10 summarizes the zero lift drag (C_{D_0}) variation with Mach number for the two transonic vehicle configurations (δU_B = -40 degrees and -30 degrees with δR_B = 0 degrees). Zero lift C_D's were obtained by extrapolating the nearly linear C_L^2 versus C_D curves to C_L = 0. In addition, curves representing C_D at 10 degrees angle of attack ($C_{D_{\alpha=10}}$) are presented to illustrate the effect of drag due to lift throughout the Mach range and to show how total drag coefficient varied for a realistic flight angle of attack. Subsonically, zero lift drag increased slightly with increased Mach number. A drag divergence appeared at a Mach number of about 0.9. Maximum drag occurred at 1.15 Mach number and then slowly decreased with increasing Mach number. A comparison of the two drag curves with δU_B = -40 degrees shows that drag due to lift for this configuration was practically constant throughout the Mach range. Values of $C_{D_{\alpha=10}}$ were greater than values of C_{D_0} by a constant ΔC_D of about 0.04. For the other transonic configuration (δU_B = -30 degrees; δR_B = 0 degrees), drag due to lift appeared to increase with Mach number subsonically. The supersonic values of C_{D_0} and $C_{D_{\alpha=10}}$ were based on a very limited amount of data and were probably less accurate than subsonic values. However, there was enough information to indicate the expected relationship between drag and Mach number.

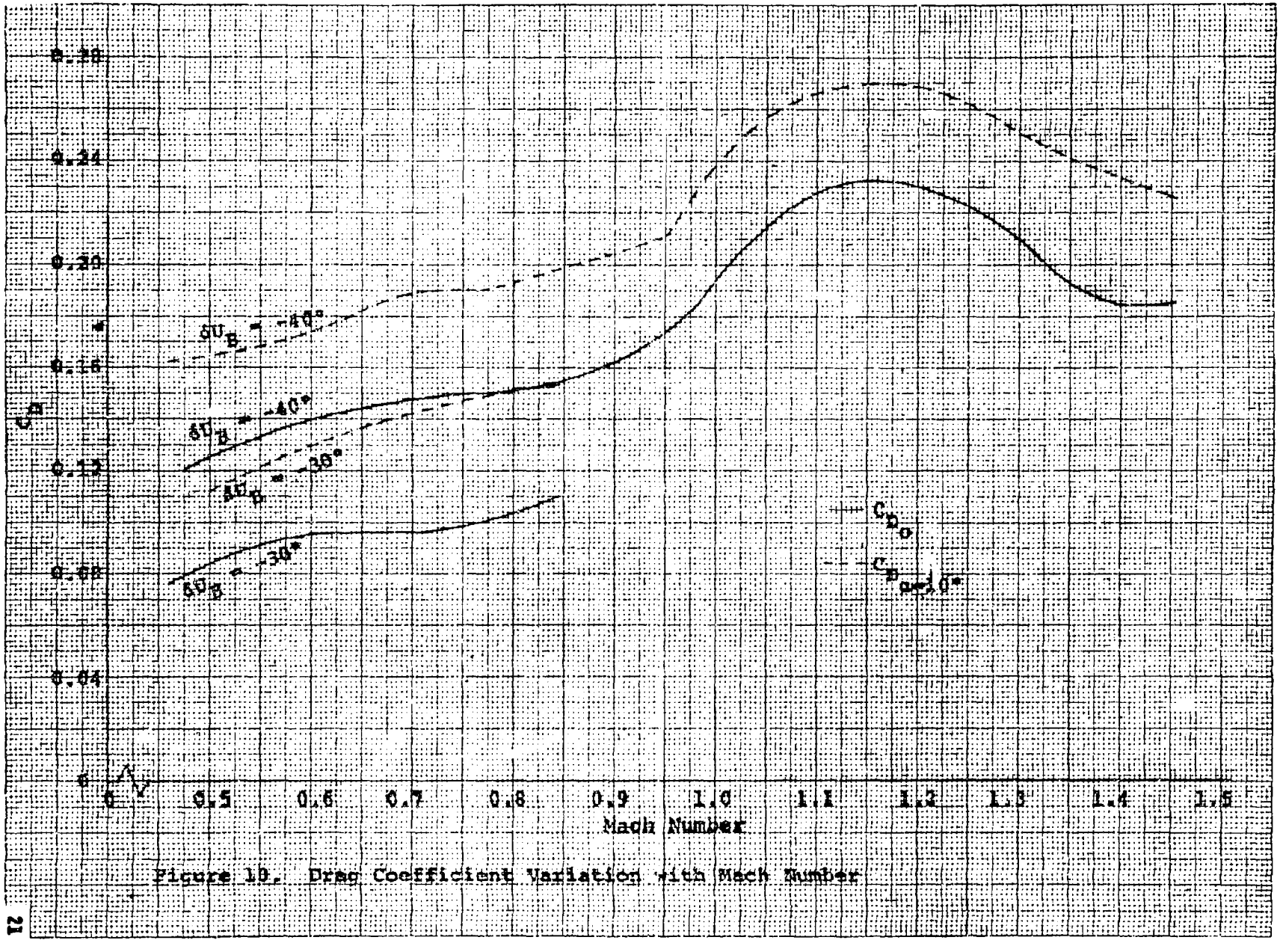

Figure 10. Drag Coefficient Variation with Mach Number

Lift-to-Drag Ratio

Faired L/D curves are plotted against C_L in figures 8 and 9. The L/D decreased with increased Mach number for both configurations. In figure 11, maximum L/D is plotted against Mach number for all fixed upper flap bias configurations for which performance data were obtained. Values of maximum L/D were obtained directly from the flight data in appendix I for those cases in which the flight maneuvers were taken to L/D_{max}. For those maneuvers in which L/D_{max} was not attained, flight lift and drag data were extrapolated to higher angles of attack to obtain the most plausible values of L/D_{max}. The curves show that maximum L/D decreased sharply with increased Mach number in the low subsonic region and leveled off in the transonic and supersonic regions. Figure 11 also indicates that this subsonic decrease in L/D_{max} was generally smaller at the higher upper flap bias configurations. The degradation in L/D_{max} with increased Mach number at low subsonic speeds was attributed to tip fin flow separation and is discussed in the section of the report with that title.

C_L^2 Versus C_D

Faired plots of C_L^2 versus C_D are presented in figure 12 for the δU_B = -40 and -30 degrees configurations. In the δU_B = -40 degrees configuration, the slopes of the resulting straight lines $\left(\frac{d(C_L^2)}{dC_D}\right)$ are 2.6 in the subsonic region (M = 0.5, 0.6), decreasing to 1.9 in the transonic region (M = 0.70 to 0.98) and ranging from 1.89 to 1.40 at supersonic Mach numbers and zero rudder bias. Supersonic data at +2 degrees rudder bias were so limited that faired $\frac{d(C_L^2)}{dC_D}$ slopes were not of sufficient accuracy to show trends. At the smaller upper flap setting (δU_B = -30 degrees), the C_L^2 versus C_D slopes had a value of about 2.7 at M = 0.5 and 0.59 and showed a steady decrease with increased Mach number.

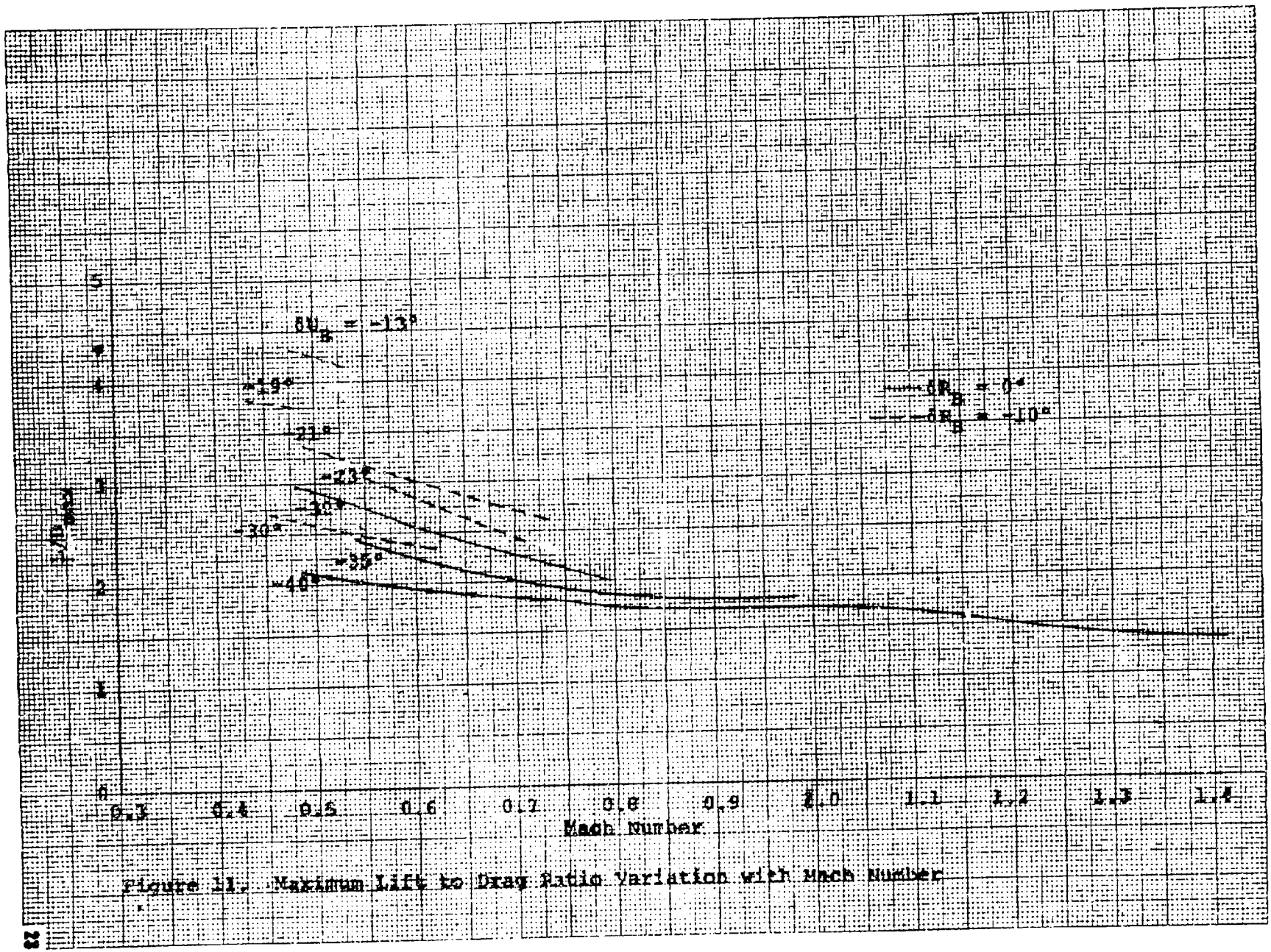

Figure 11. Maximum Lift to Drag Ratio Variation with Mach Number

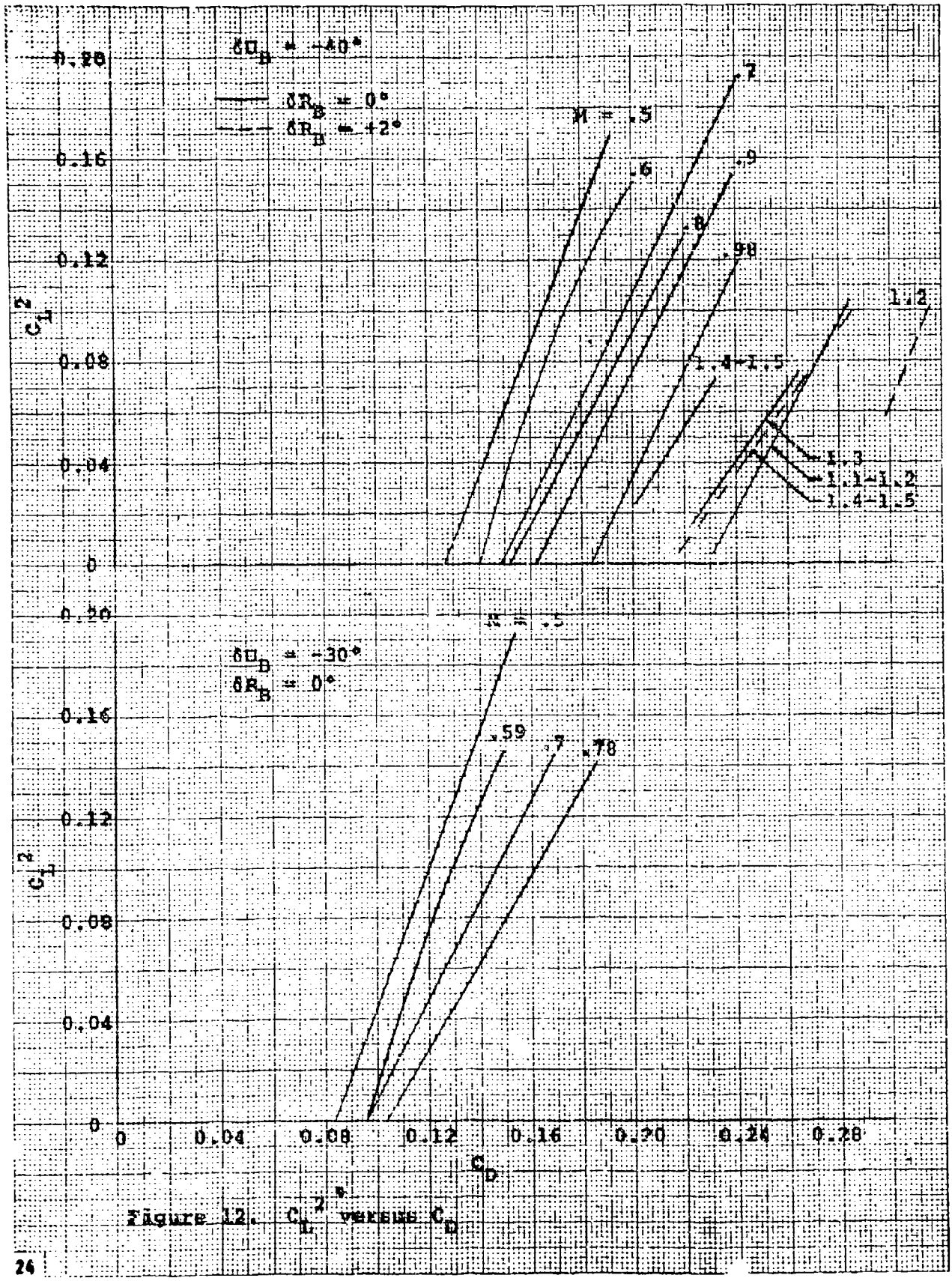

Figure 12. C_L^2 versus C_D

WEDGE ANGLE and RUDDER BIAS EFFECTS

The variable features of the X-24A flight control system allowed performance data to be collected over a reasonably wide range of upper flap, lower flap and rudder bias positions. Representative faired data at 0.5 and 0.8 Mach number are shown in figures 13 and 14. At 0.5 Mach number, trim test data were obtained at upper flap bias settings of -40 and -30 degrees with 0 degrees rudder bias; and at upper flap bias settings of -30, -21, -19 and -13 with -10 degrees rudder bias. Data were also obtained while controlling on the upper flap ($\delta L_B = 0$) at -10 degrees rudder bias. Because of the predicted poor stability levels at high Mach numbers and small upper flap settings, performance data were limited to -30, -35 and -40 degrees upper flap bias at 0.8 Mach number. These variable control settings were extremely effective in altering the performance of the X-24A especially at 0.5 Mach number where maximum L/D was doubled by closing the upper flaps from -40 to -13 degrees.

The primary effect of the flap bias feature was to alter the base area and thus, the base drag of the vehicle. When the upper flap was extended a pitch-up moment was produced which was counteracted (either by the pilot or the control system) by extending the lower flap the proper amount to remain in trimmed flight. When the upper flap was retracted the lower flap was also retracted to remain in trim. The change in base area associated with upper and lower flap changes was therefore additive and related to the change in the total angle between the upper and lower flaps, or wedge angle (δw). Movement of the rudder bias surfaces on the tip fins did not directly alter the base area or base drag of the vehicle. It did result in a strong indirect effect since the rudder position influenced the pressure in the area of the upper flaps. When the rudders were biased inboard a large pitchup moment was produced (similar to extending the upper flap). This moment was counteracted by either opening the lower flap or by closing the upper flap, thereby altering the base area and thus the base drag.

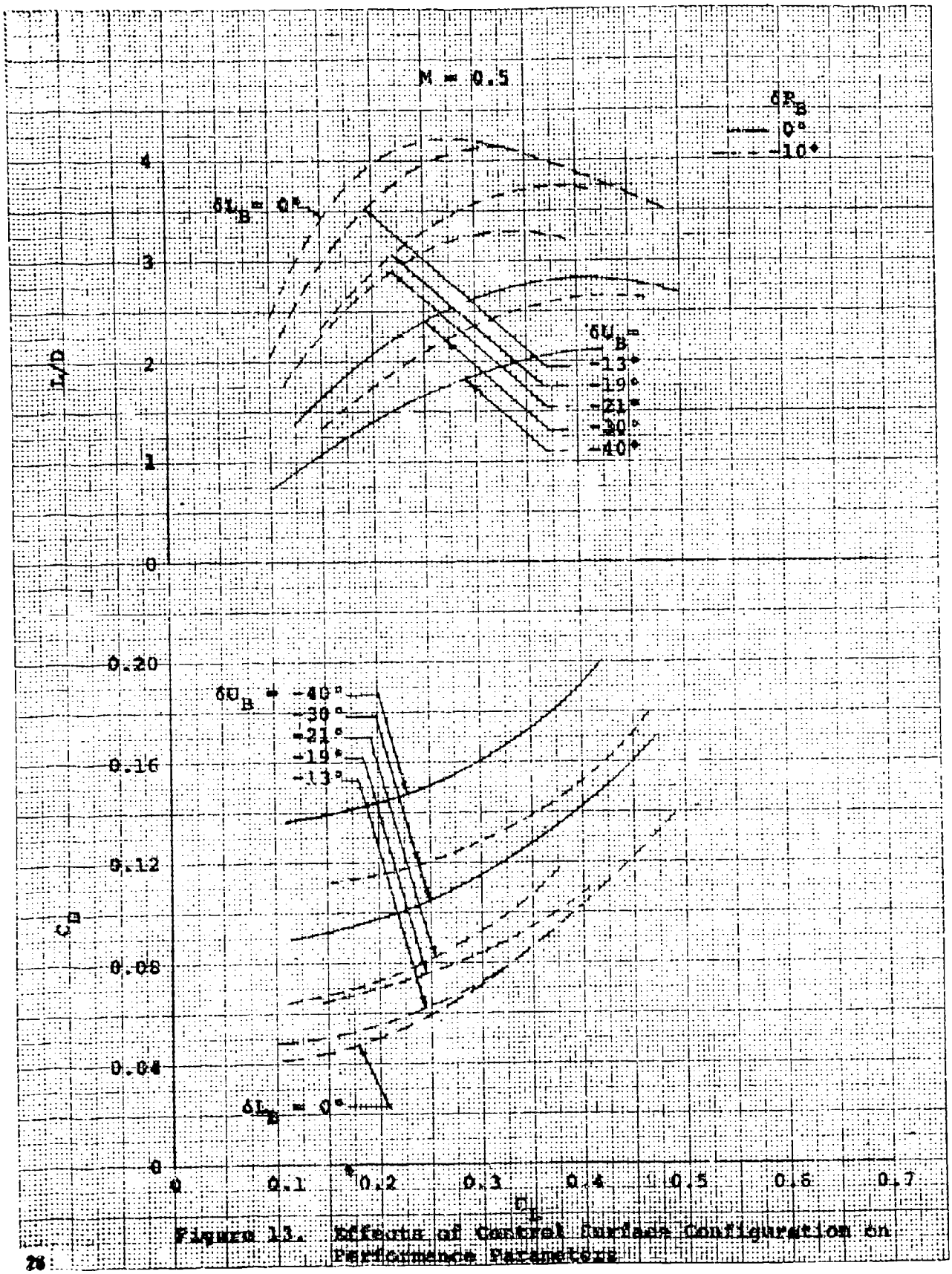

Figure 13. Effects of Control Surface Configuration on Performance Parameters

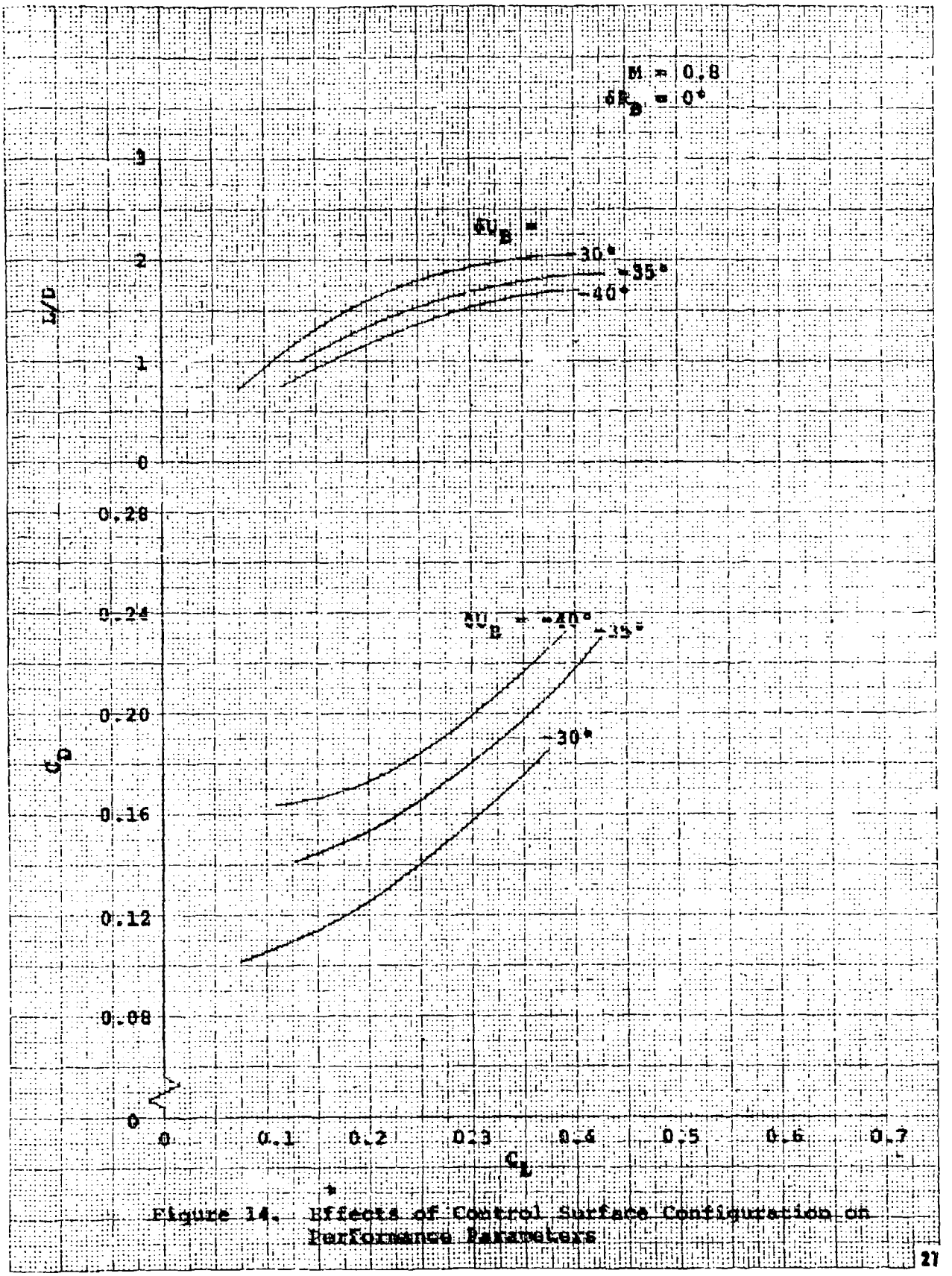

Figure 14. Effects of Control Surface Configuration on Performance Parameters

Wedge Angle Effects on Trim Normal Force Coefficient

Since the centers of pressure of the upper flap, lower flap and rudders were essentially the same distance from the center of gravity it follows that for trimmed flight, the trimmed normal force coefficient (C_N) would be independent of the flap or rudder bias configuration (figure 15). This effect was apparent in the analysis of all wind tunnel data and is confirmed by the flight data shown in figures 16 through 18. Within the scatter of the test data the trimmed C_N curve is unaffected by changes in the upper flap bias setting or rudder bias setting. The lines represent the data from the Langley 7- x 10-foot wind tunnel for all flap configurations. The slopes of C_N versus angle of attack were less for flight test data than for wind tunnel data.

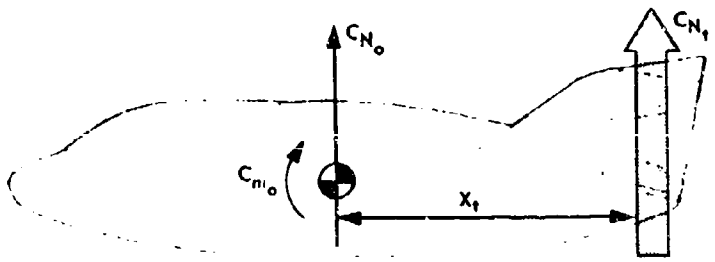

$$C_{m_o} - X_t C_{N_t} = 0 \quad \text{FOR TRIMMED FLIGHT}$$

$$C_{N_{TRIM}} \quad C_{N_o} + C_{N_t}$$

WHERE C_{m_o} = C_m FOR ZERO CONTROL SURFACE DEFLECTIONS

C_{N_o} = C_N FOR ZERO CONTROL SURFACE DEFLECTIONS

X_t = TAIL LENGTH (approximately the same for upper flap, lower flap and rudder bias)

C_{N_t} = C_N AT THE TAIL REQUIRED FOR TRIM

NOTE:

The magnitude of C_{N_t} required to produce trimmed flight is the same regardless of which control surface is used.

Figure 15 Induced Normal Forces for Trimmed Flight

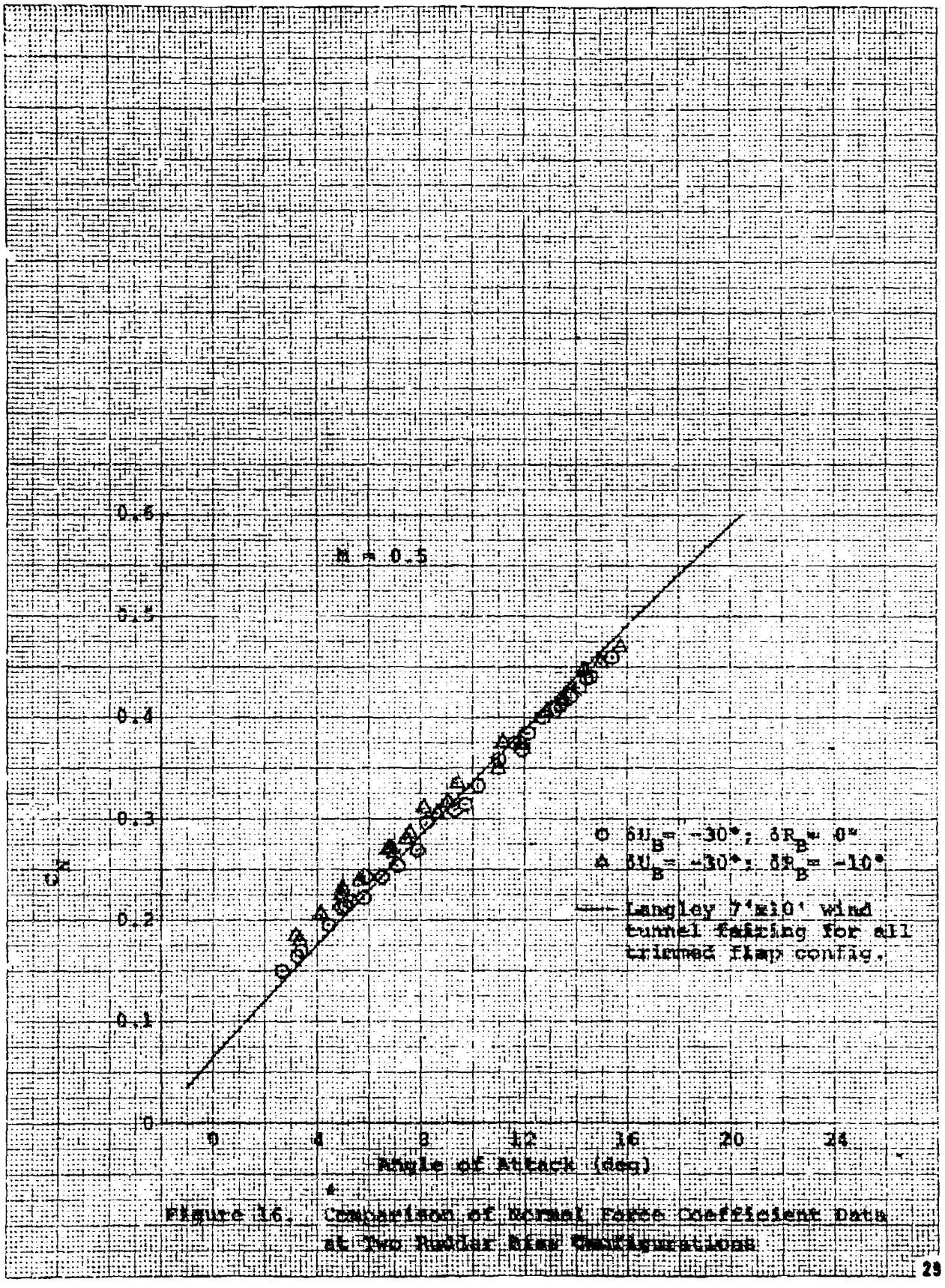

Figure 16. Comparison of Normal Force Coefficient Data at Two Rudder Bias Configurations

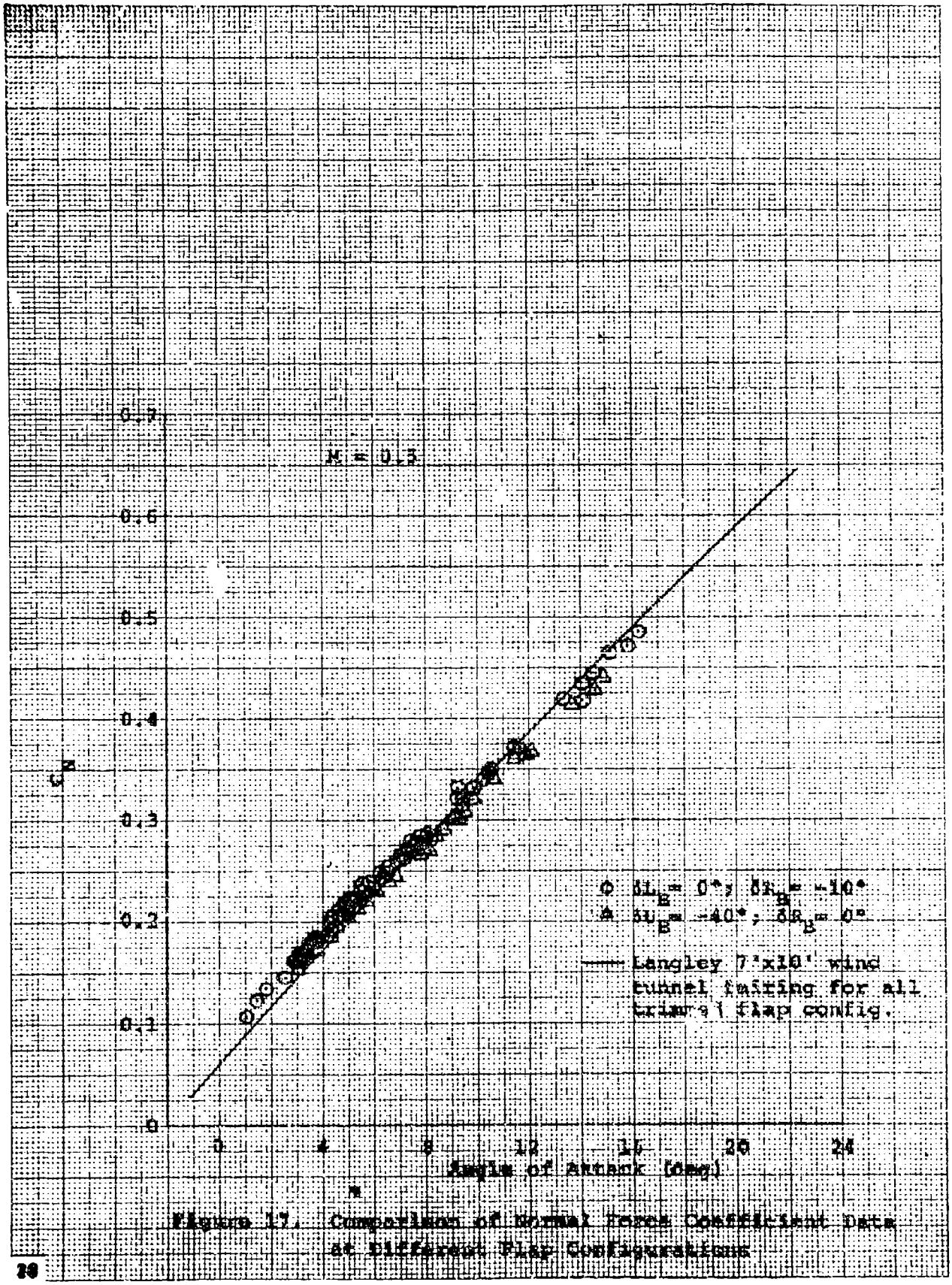

Figure 17. Comparison of Normal Force Coefficient Data at Different Flap Configurations

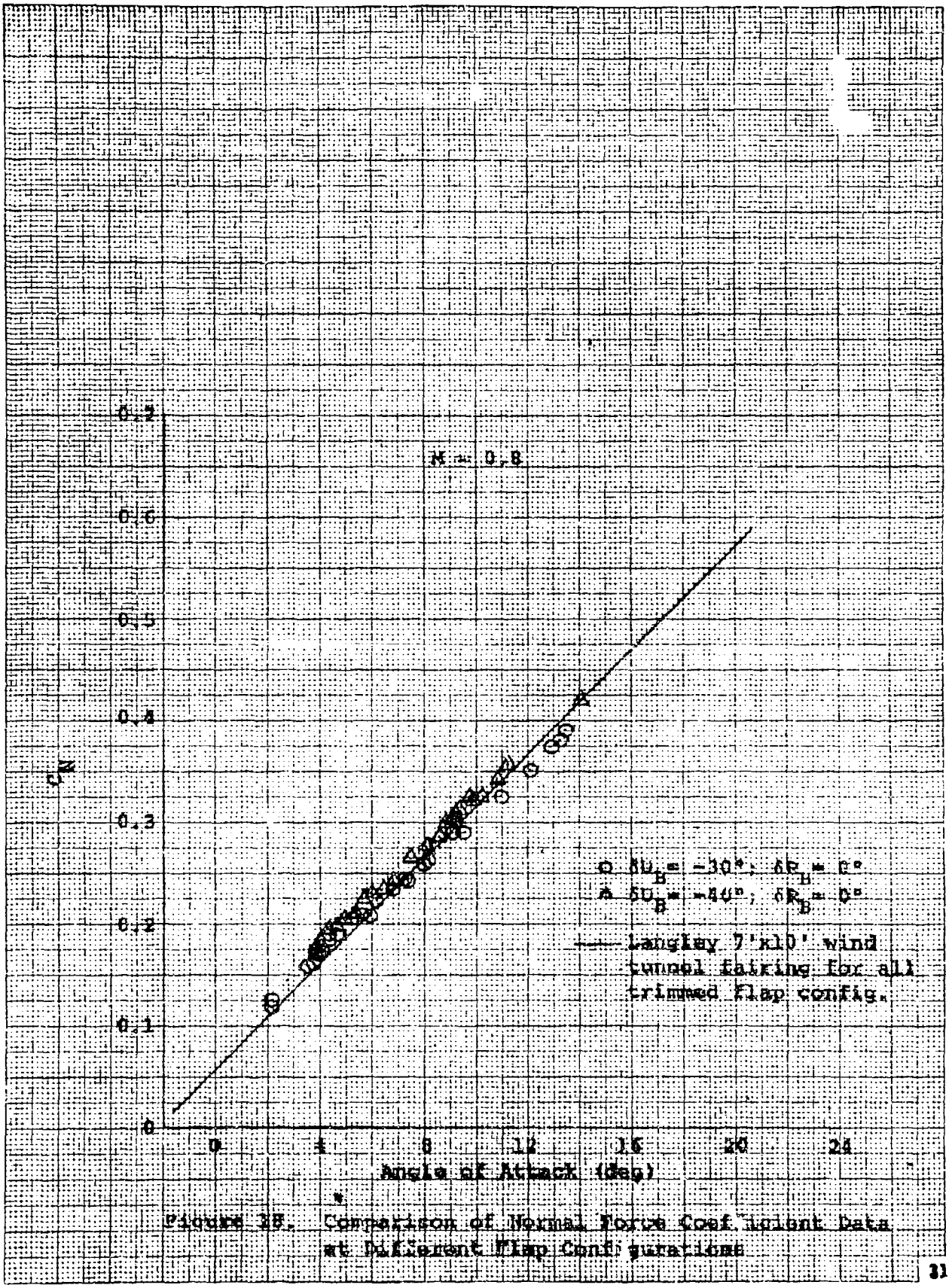

Figure 38. Comparison of Normal Force Coefficient Data at Different Flap Configurations

Wedge Angle Effects on Chord Force Coefficient

Early analysis of wind tunnel data indicated that chord force coefficient (C_C) for a particular Mach number and trimmed C_N could be related directly to total wedge angle, regardless of the positions of the individual upper or lower flaps. Furthermore, this relationship appeared to be parabolic [$C_C = f(\delta w^2)$].

The faired lines of figures 19 and 20 at 0.5 and 0.8 Mach number are cross plotted as C_C vs δw for constant trimmed C_N in figures 21 and 22. These curves are essentially parallel and do exhibit a parabolic shape at 0.5 Mach number and wedge angles below 50 degrees.

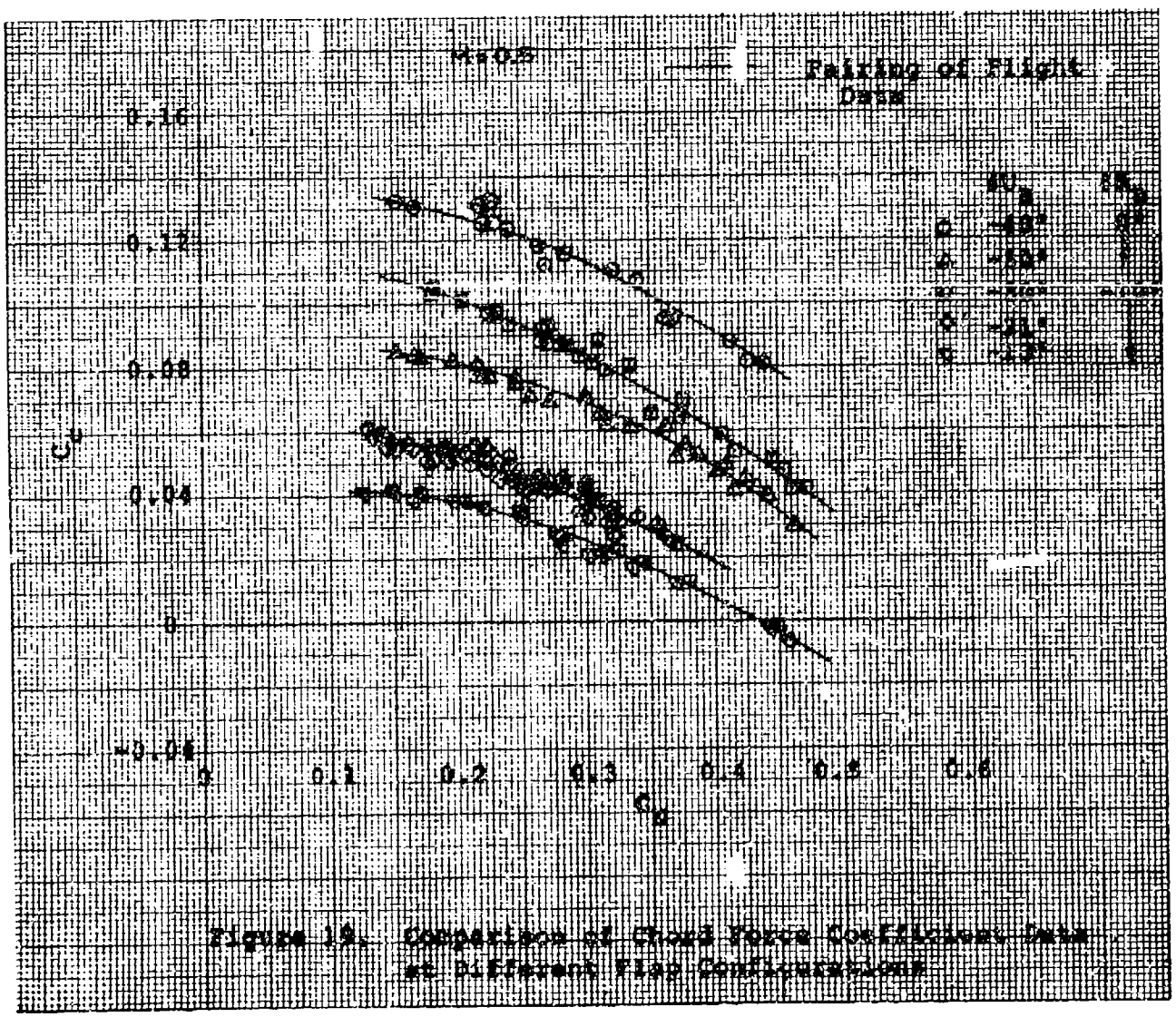

Figure 19. Comparison of Chord Force Coefficient Data at Different Flap Configurations

The flight data points were normalized with respect to δ using wind tunnel values of C_c for the -30 degrees δU_B, +20 degrees δe_L configuration. These points are shown plotted versus δw^2 in figures 23 and 24 and confirm the parabolic variation of C_c with δw. The straight line shown on each of these figures is the slope established from prior analysis of wind tunnel data and was used in the X-24A simulator.

Flight data points of trimmed C_c at 0.5 Mach number are compared with simulator values of total trimmed C_c for the same flight conditions in figure 25. The simulator values compare well with flight data except at the high wedge angles where simulator values were somewhat higher than the flight data.

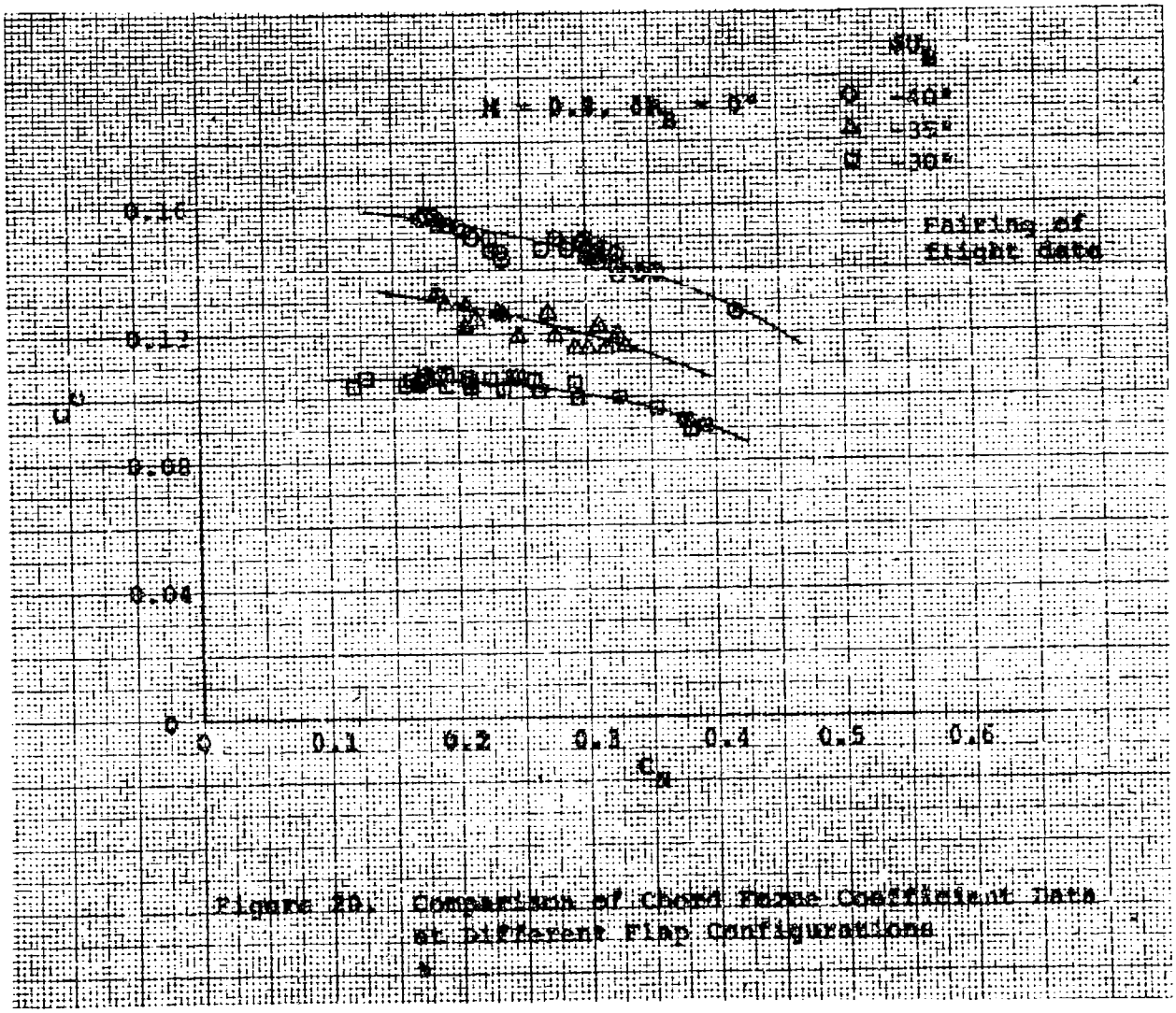

Figure 24. Comparison of Chord Force Coefficient Data at Different Flap Configurations

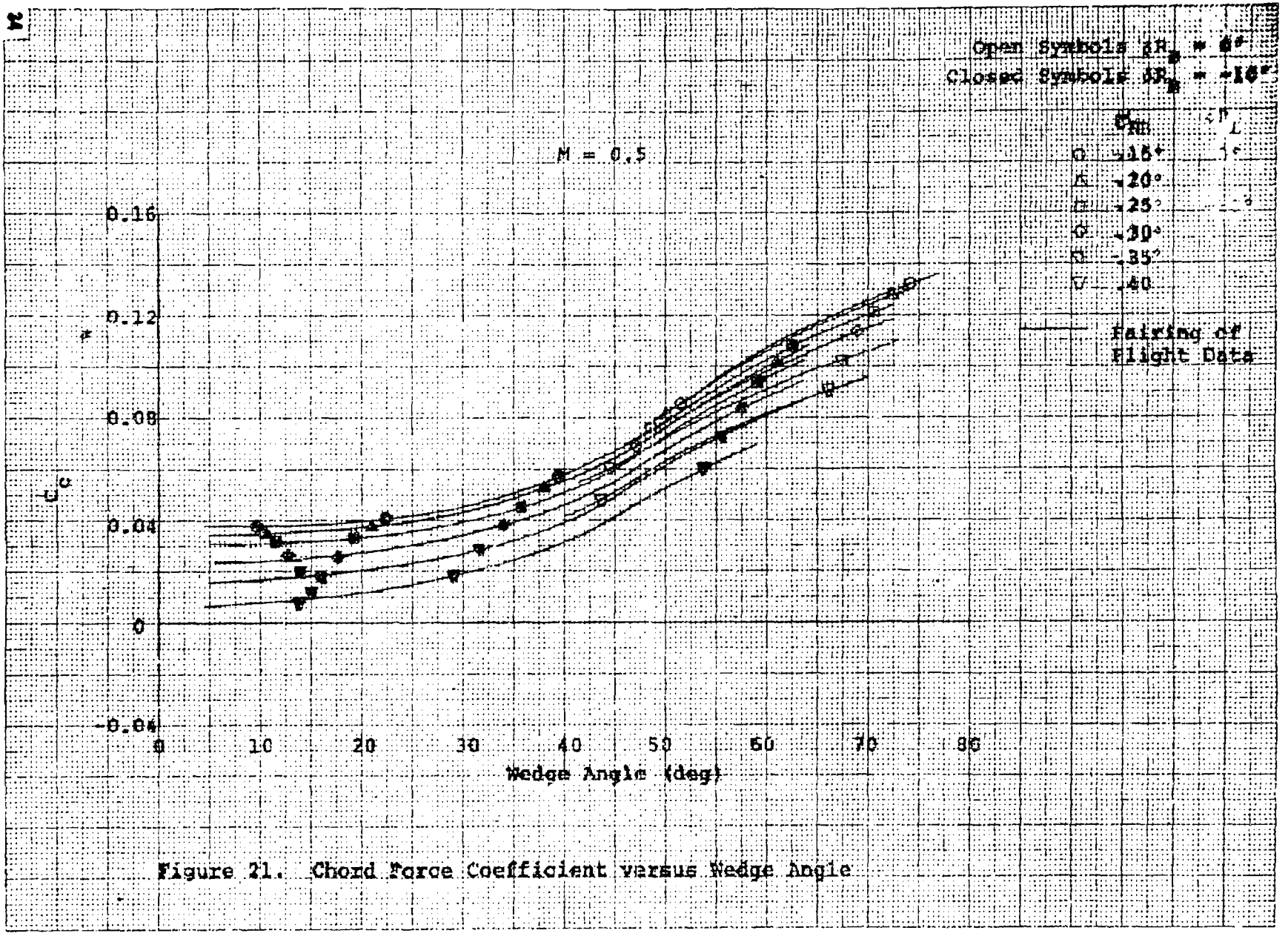

Figure 21. Chord Force Coefficient versus Wedge Angle

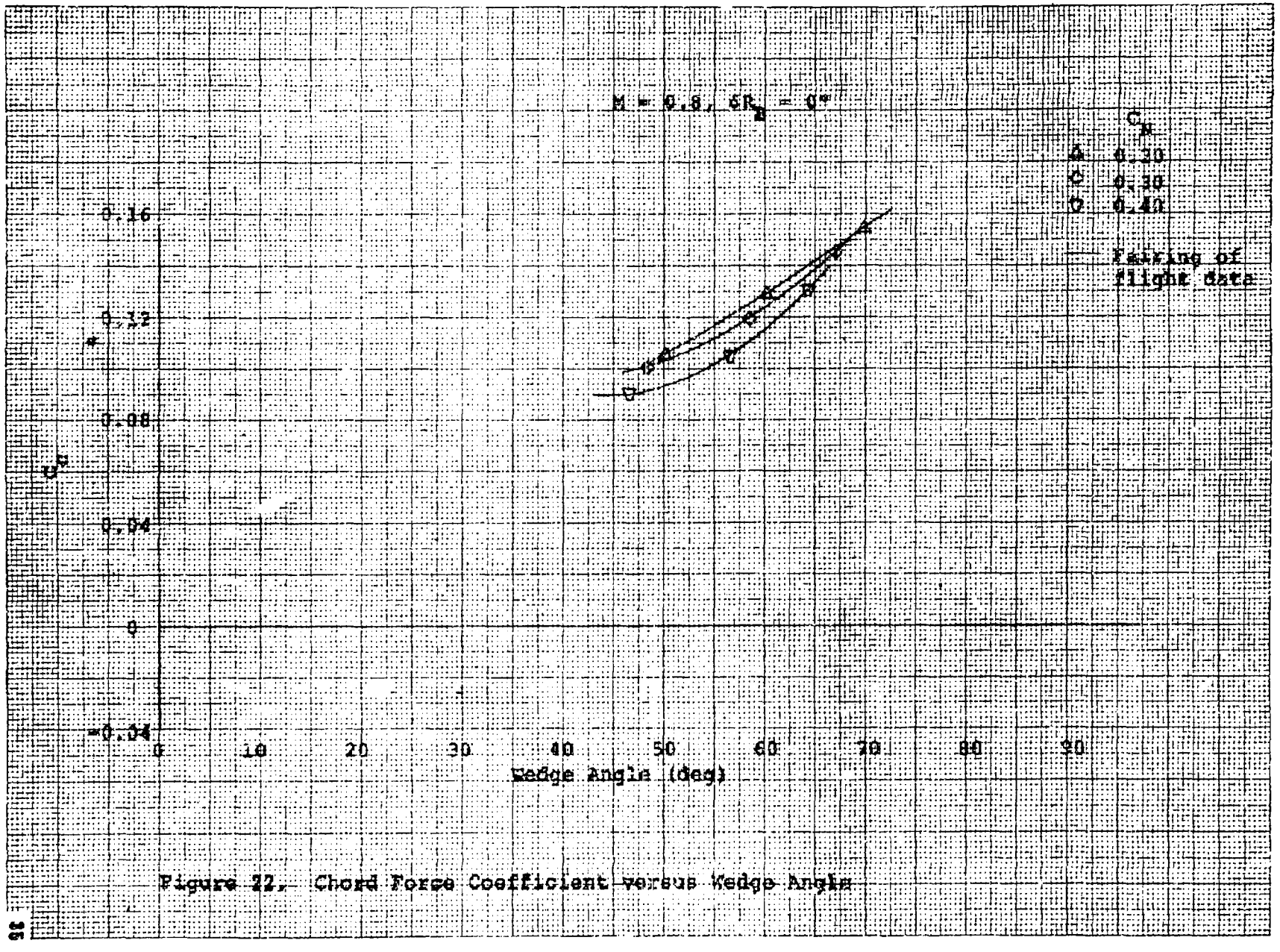

Figure 22. Chord Force Coefficient versus Wedge Angle

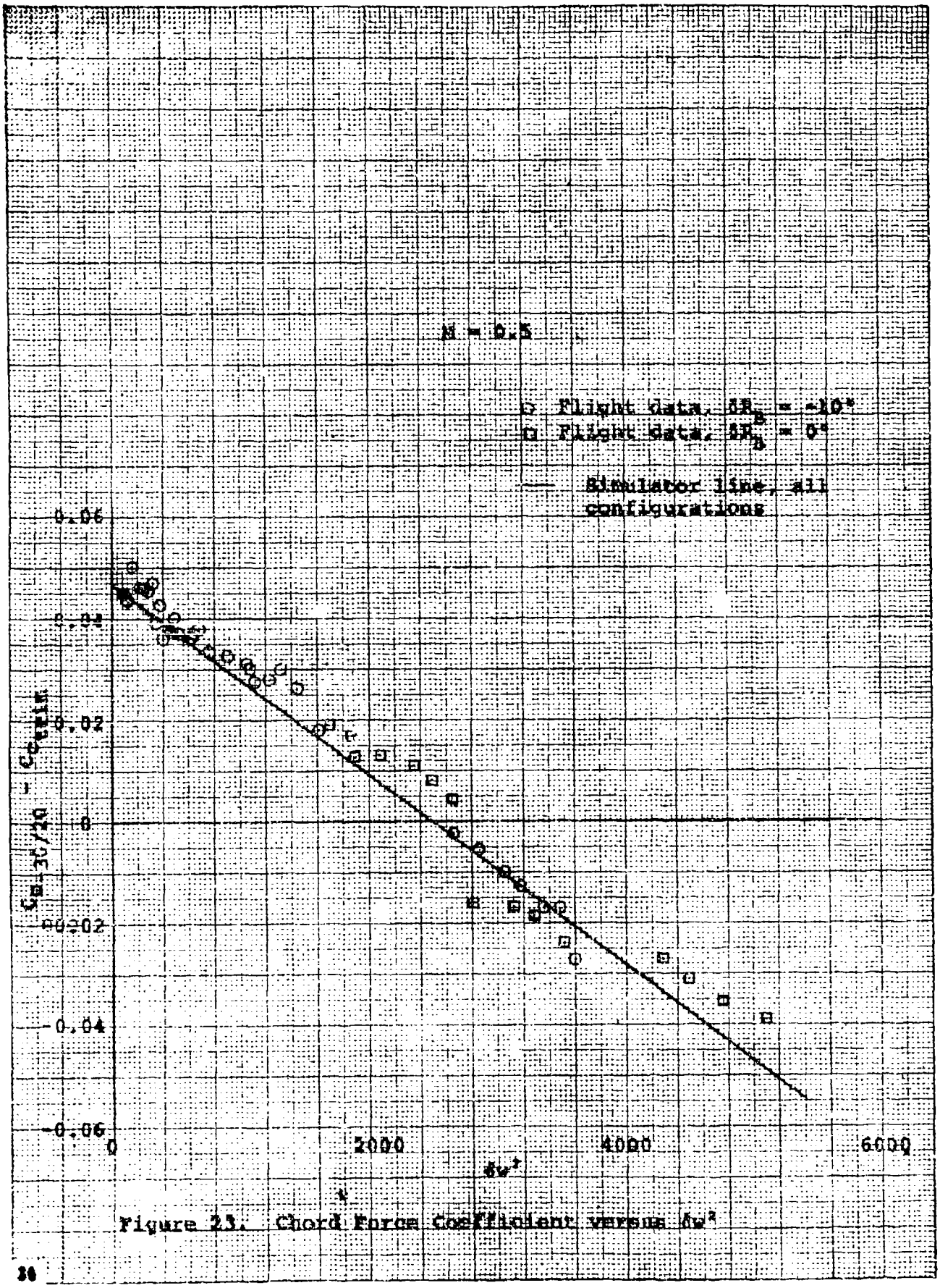

Figure 23. Chord Force Coefficient versus δw^2

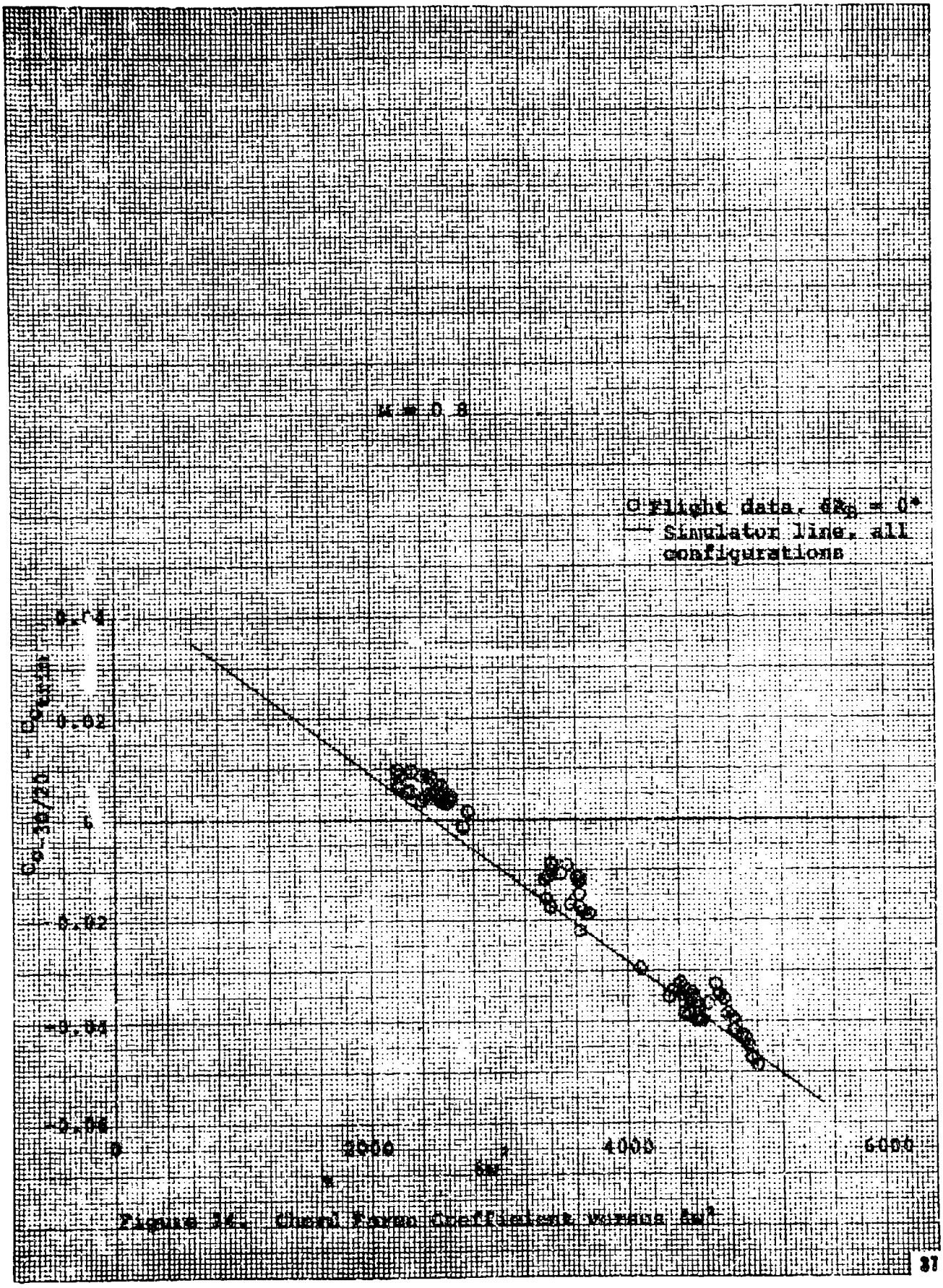

Figure 34. Chord Force Coefficient versus δR^2

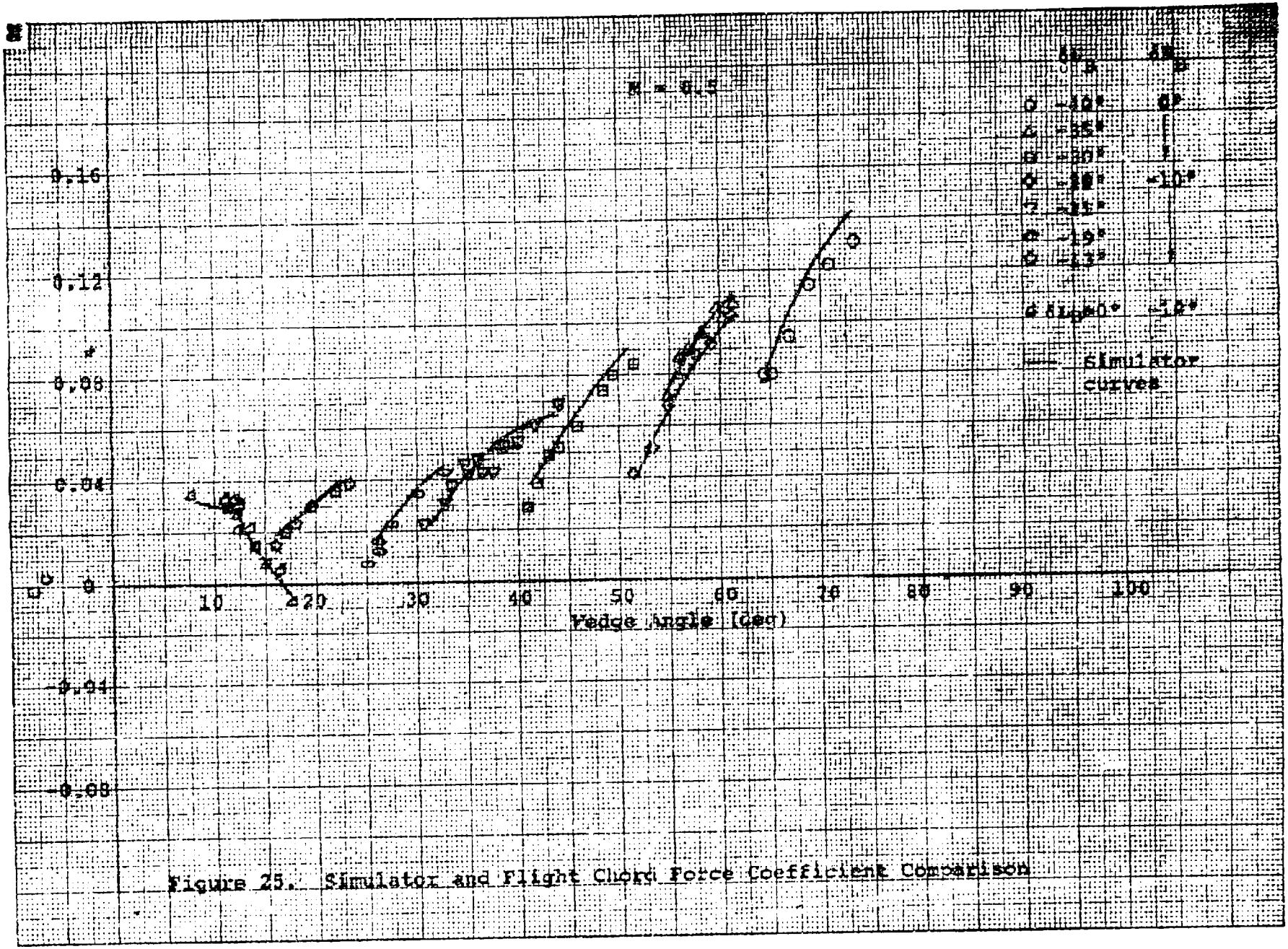

Figure 25. Simulator and Flight Chord Force Coefficient Comparison

Wedge Angle and Rudder Bias Effects on Lift-to-Drag Ratio

The combined effects of δw and δR_B on the lift-to-drag ratio at 0.5 Mach number are shown in figure 26. The indirect effect of rudder bias on the performance characteristics is evident by comparing the zero degree and -10 degrees δR_B lines in this figure. The vertical separation of these lines indicates a small apparent improvement in performance (approximately 0.1 L/D) associated with biasing the rudders inboard at constant wedge angle (direct effect of the rudders). A comparison of the two -30 degrees δU_B points, however, shows that this small positive increment is more than counteracted by the increase in wedge angle associated with extension of the lower flap to return to trim. The net result is a decrease in L/D of approximately 0.3. Note that the vehicle could also be retrimmed by retracting the upper flap and thereby decreasing the wedge angle and increasing the L/D. This is indicated by the solid point in figure 26 which is an interpolated point showing L/D at 0.3 C_N resulting from a configuration change from 0 to -10 degrees δR_B, while holding the lower flaps fixed at 17 degrees and trimming with the upper flaps (decreasing from -30 to -22 degrees).

Speed Brakes

Prior to flight nine, the automatic rudder bias feature was reprogrammed to follow the upper flap bias so that the rudder bias and upper and lower flap bias trim changes would tend to cancel (reference 1). Thus the flaps and rudders were electrically linked together and could be extended or retracted with a minimum trim change apparent to the pilot. This "speed brake" feature was used by the pilots thereafter during the landing approach. Flight data points obtained during the extend or retract cycle for two values of trimmed C_N (two α's) are shown in figure 27 and compared with previous data obtained from pushover-pullups at constant rudder bias settings. The total variation in L/D available through the use of the upper flap bias "speed brake" is shown versus C_L S/W and V_e in figure 28. The shaded portion of figure 28 presents the actual amount of speed brake used in the program.

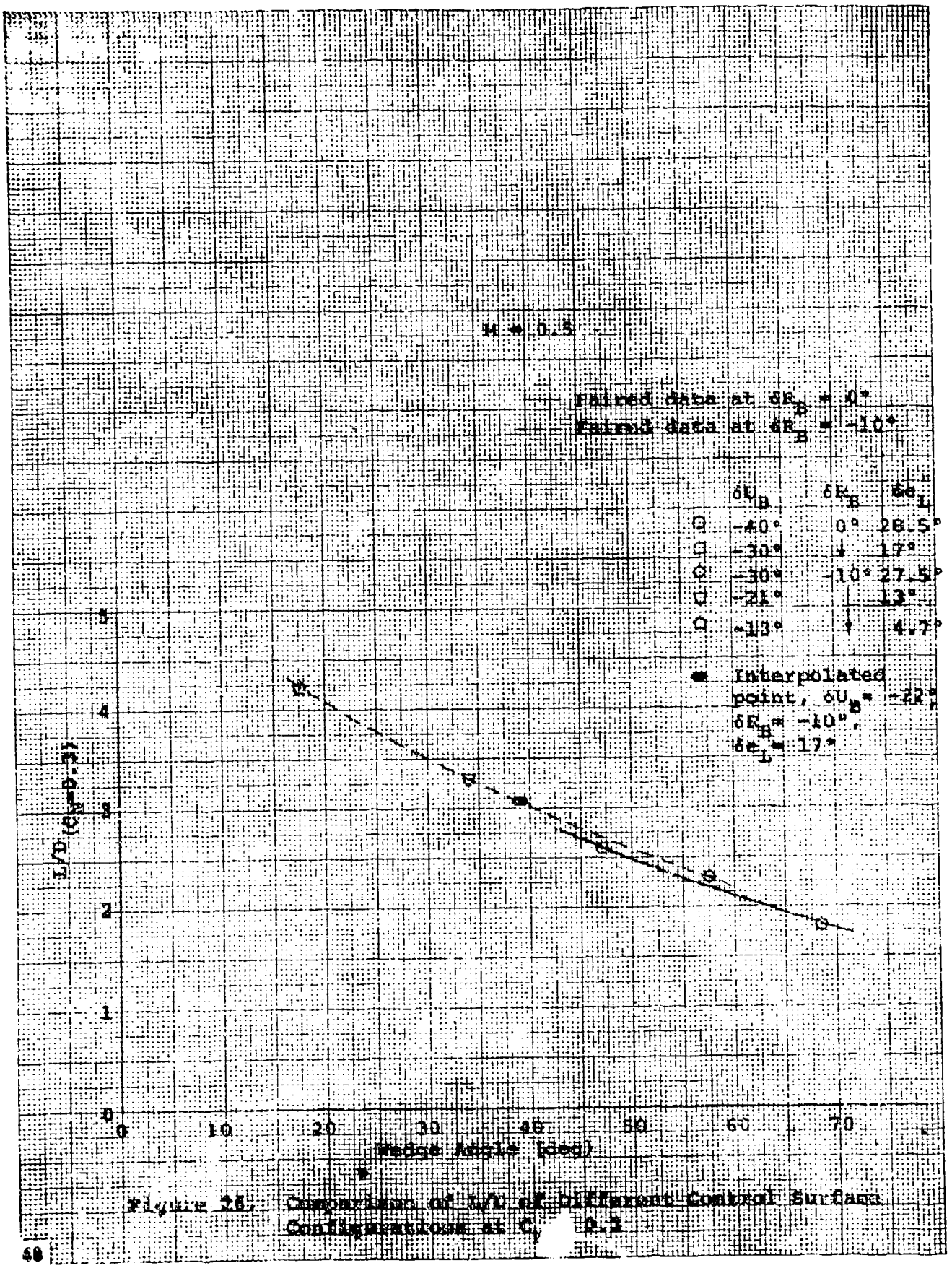

Figure 25. Comparison of L/D of Different Control Surfaces Configurations at C_y = 0.2

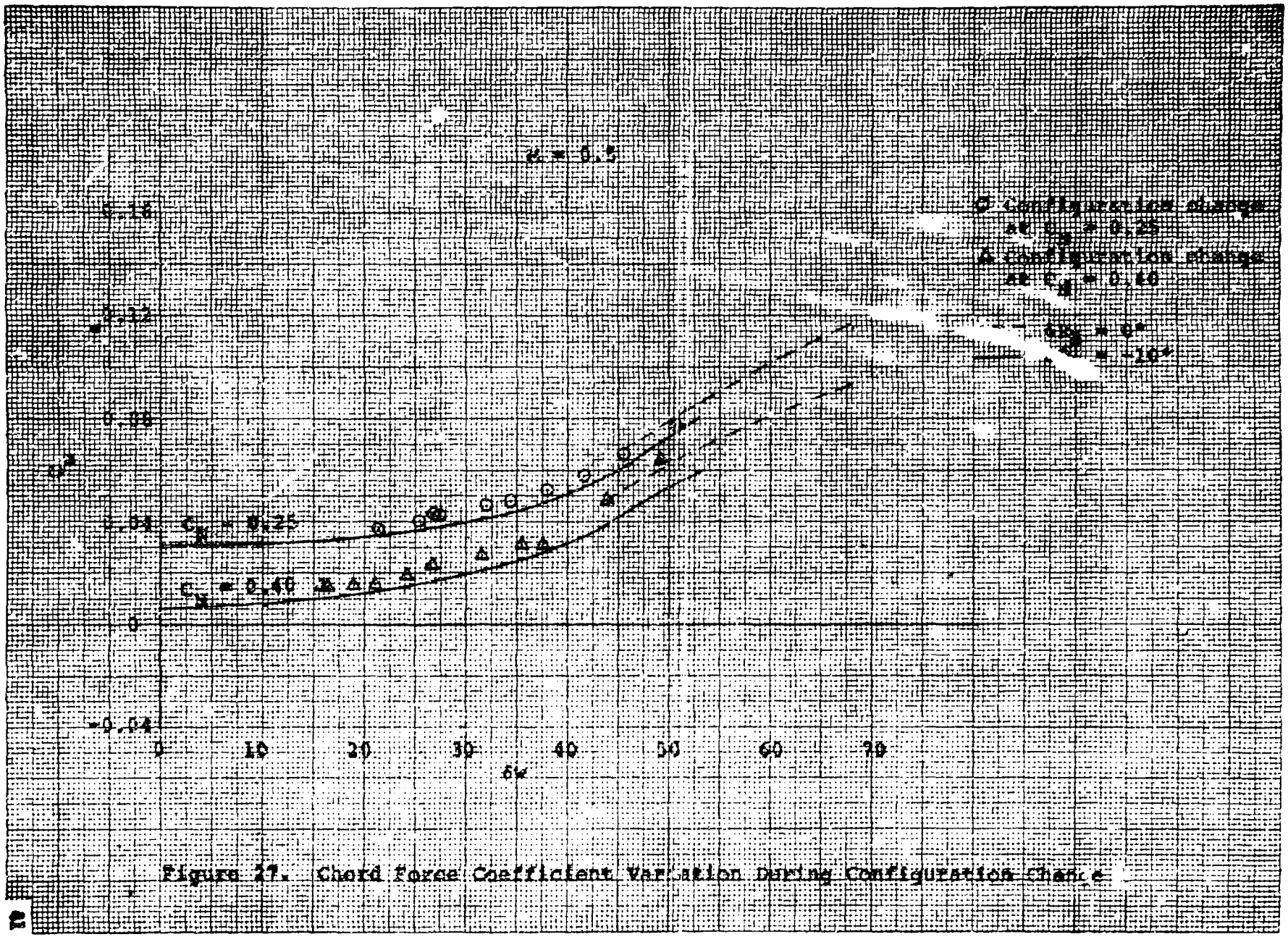

Figure 27. Chord Force Coefficient Variation During Configuration Change

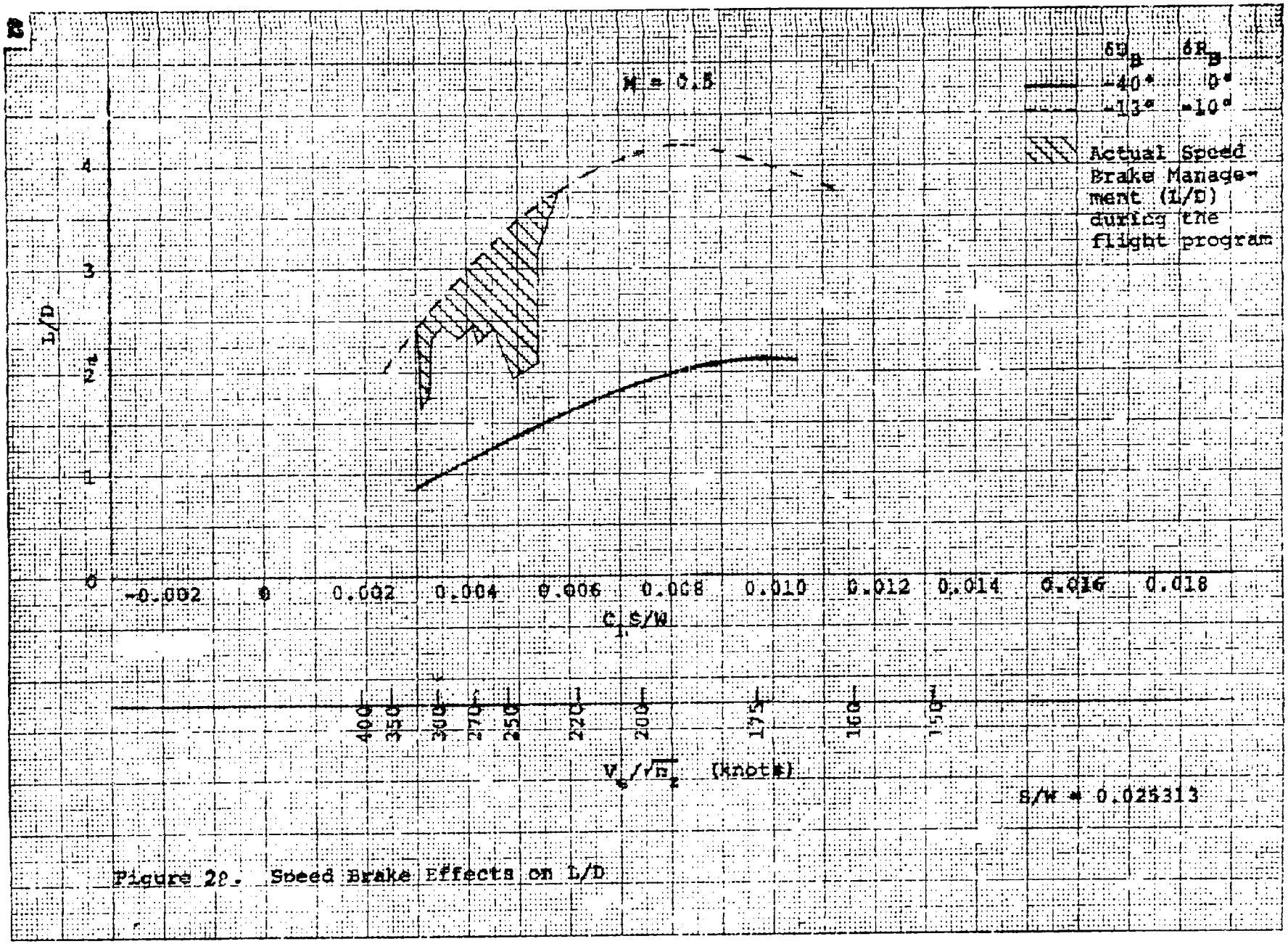

Figure 29. Speed Brake Effects on L/D

LANDING GEAR EFFECTS

Figures 29 and 31 compare gear up and gear down faired performance test data in the δL_B = 0 degrees, δR_B = -10 degrees control surface configuration. Gear down curves exhibit a greater lift curve slope, increased total drag and significantly lower L/D's when compared to corresponding gear up curves. The differences that were apparent between the gear up and gear down data were not due solely to the landing gear. Since deployment of the landing gear produced a nosedown trim change, an increase of approximately five degrees of upper flap was required to remain at the same trim lift coefficient.

The gear down lift coefficient versus α curve (figure 29) is below the gear up curve and has a steeper slope by 21 percent. The reduced gear down lift coefficient at the same angle of attack was a result of the down load at the tail (increased upper flap setting) required to compensate for the trim change. (This increment as applied to the gear up curve is shown as the dashed line in figure 29 and is based on flight measured values of $C_{N_{\delta_e}}$, reference 5.) The apparent increase in lift curve slope is probably due to ground effect since gear down data were obtained during actual landings in which the gear was extended between 40 and 120 feet above the ground. The data at the higher angles of attack and slower speeds were obtained closer to the ground and were therefore more strongly influenced by ground effect.

The total drag increment observed was the sum of the landing gear drag and the increased base drag resulting from the longitudinal trim change. To obtain the drag increment due to the landing gear alone the difference between the gear up and gear down curves in figure 29 was obtained and a correction applied for the five-degree difference in wedge angle using data in figure 21. (Notice that this correction was quite small in the wedge angle range of 15 to 20 degrees associated with landings.) The resulting drag coefficient increment due to landing gear alone was between 0.030 and 0.035 (figure 30).

Gear up and gear down L/D data are compared in figure 31. The deployment of the landing gear caused a 37 percent reduction in the maximum L/D.

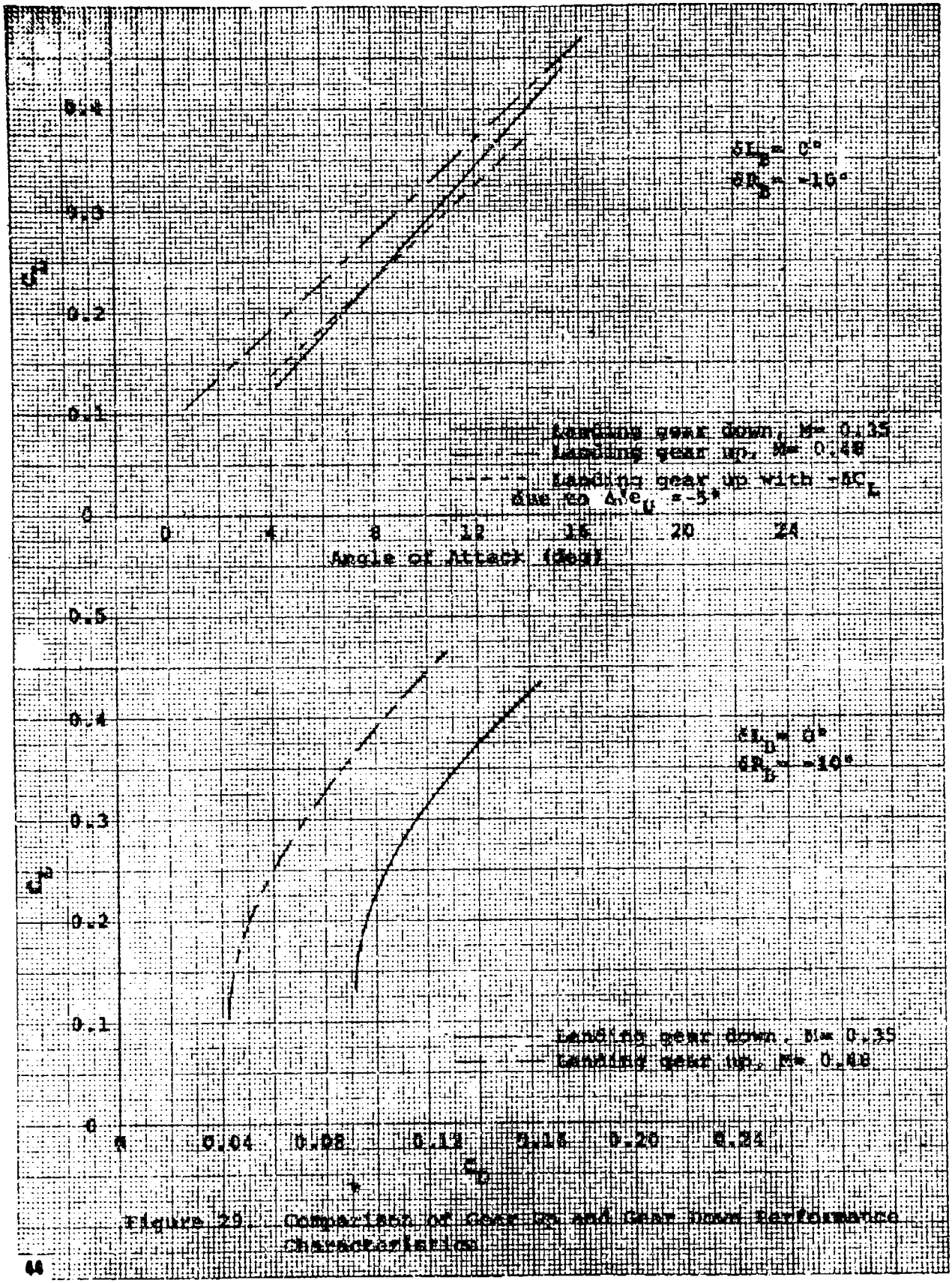

Figure 29. Comparison of Gear Up and Gear Down Performance Characteristics

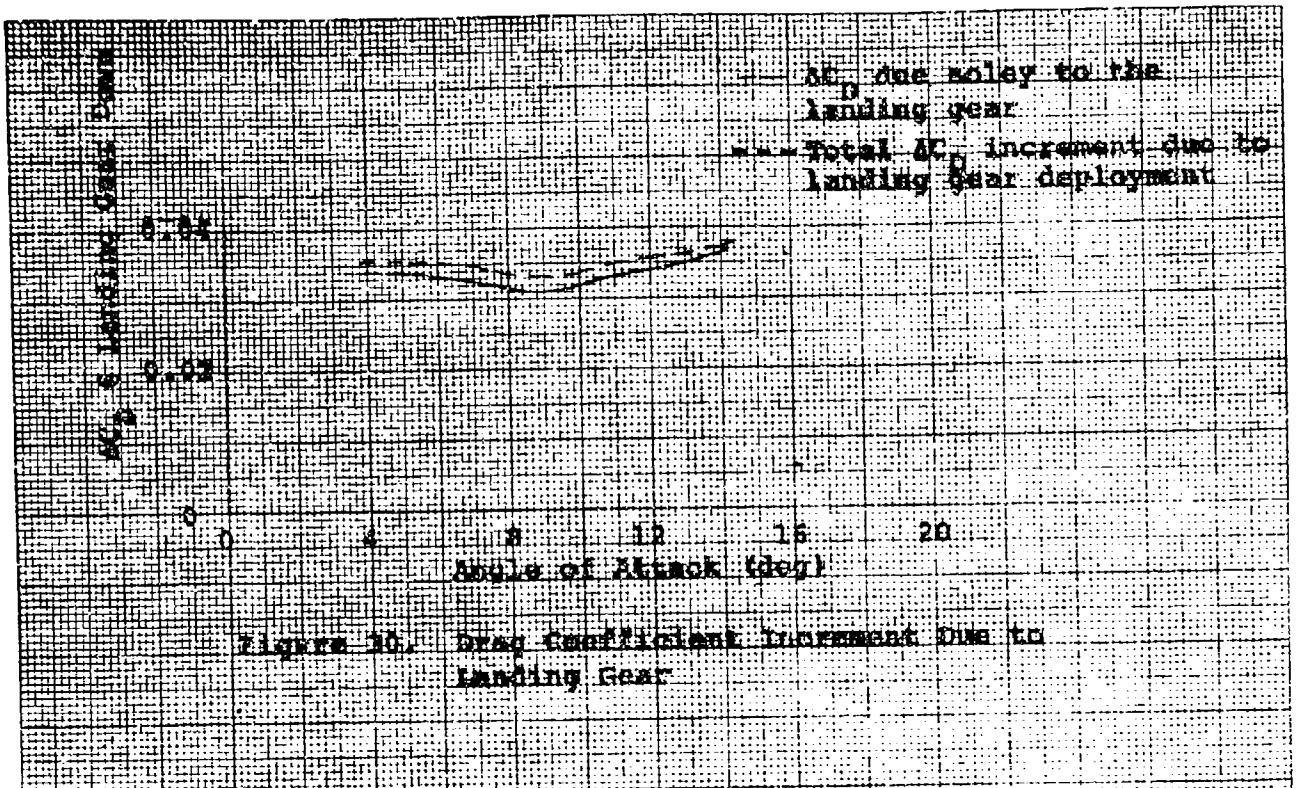

Figure 30. Drag Coefficient Increment Due to Landing Gear

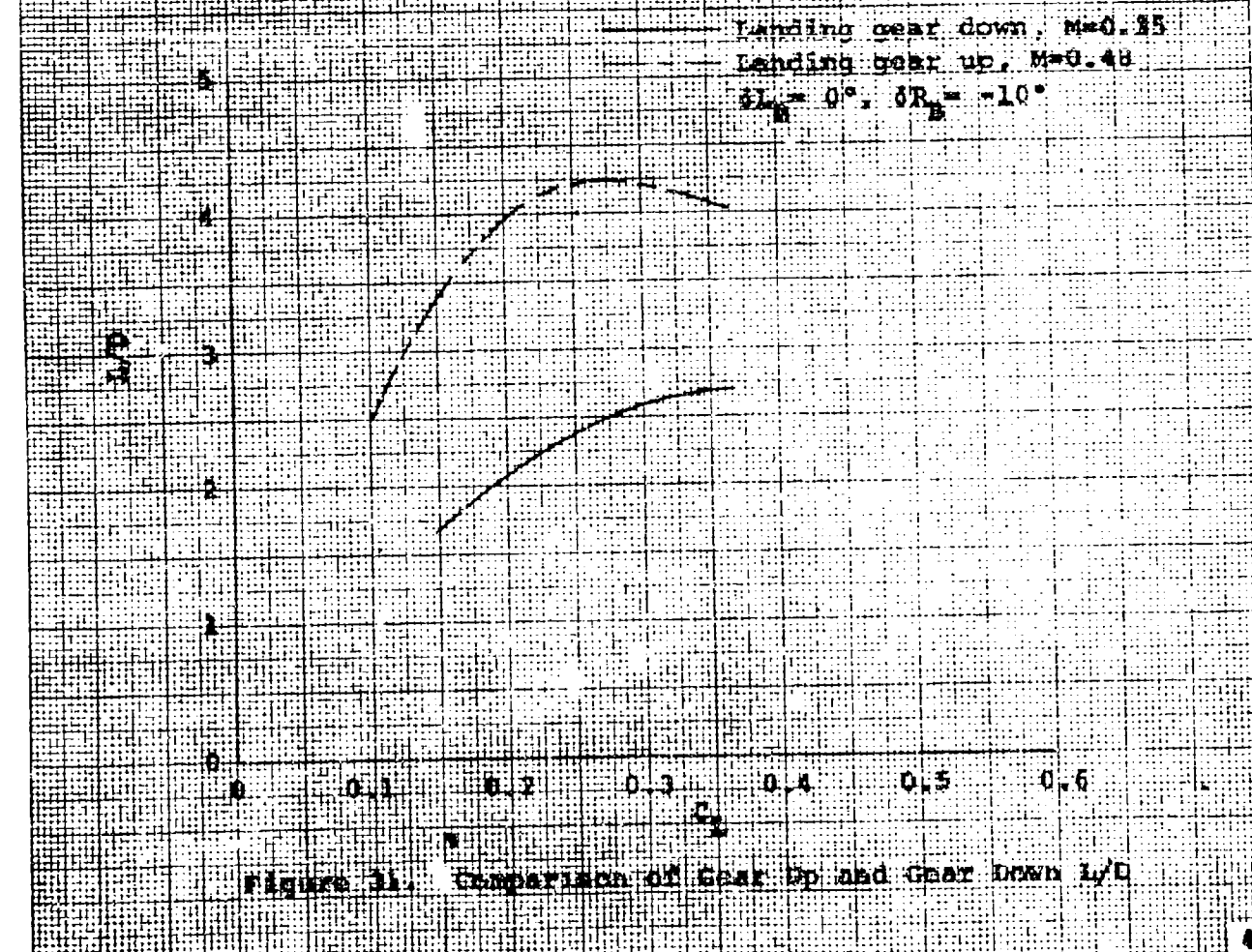

Figure 31. Comparison of Gear Up and Gear Down L/D

TIP FIN FLOW SEPARATION EFFECTS

Tip fin flow separation was noticed on early X-24A flights. A study was made to determine at what conditions separation occurred. The results of this study are reproduced in full in appendix V.

As a result of this study, a tip fin flow separation boundary was generated and presented in terms of apparent angle of attack for local tip fin stall versus Mach number. Analysis of wind tunnel data indicated that as upper flap setting was increased, static stability also increased thus apparently reducing the severity of the separation effects. However, the angle of attack at which separation occurred remained the same for all upper flap settings.

Figure 32 presents a comparison of this boundary with the full range of flight performance subsonic and transonic data obtained during the program. If the boundary is correct, a comparison of data in the unseparated and the separated regions, should show decreased performance in the latter. Also, the effects should become greater as upper flap setting is decreased. Performance flight data appear to substantiate this.

Figures 33 through 35 show faired flight data in terms of L/D versus angle of attack for three upper flap settings for a range of Mach numbers. The solid part of each curve represents data obtained in the unseparated region. The dashed part of each curve represents data obtained at angles of attack above the separation boundary (separated flow on the tip fins). With the upper flaps set at -40 degrees (figure 33), there was a gradual decrease in L/D_{max} with increased Mach number, probably due mostly to Mach number effects. Data obtained with the vehicle in the other two transonic configurations (δU_B = -35 and -30 degrees) exhibited similar trends and were not shown. However, with the upper flaps set at -23 and -21 degrees, drastic differences, both in maximum L/D and in the total shape of the L/D curve, are apparent between data obtained in the separated and unseparated regions (figures 34 and 35). The maximum L/D is drastically reduced and a significant flattening of the curve occurs in the separated region. The dramatic differences between the 0.5 and 0.7 Mach number curves at δU_B =-21 degrees, and the M = 0.56 and 0.68 curves with δU_B =-23 degrees, are very similar. At 0.6 Mach number with a -21 degrees upper flap setting, the separation boundary was crossed about midway through the maneuver. The data show a definite break at the boundary angle of attack and approaches the totally separated curve at 0.7 Mach number. Therefore, the flight performance data appear to correlate very well with the separation boundary.

Figure 36 presents X-24A flight data at three upper flap settings, along with small scale and full scale wind tunnel data in terms of maximum L/D versus Mach number in the subsonic to transonic region. The data compare very well except for low speed data in the δU_B = -21 degrees upper flap configuration. Wind tunnel performance results were slightly optimistic with respect to Mach number or angle of attack in predicting L/D in the transition region between separated and unseparated flow. This trend was also found with the HL-10 lifting body (reference 9).

Due to the significant effects of this type of separation, it is important that wind tunnel studies accomplished prior to the test flight program be analyzed for these trends. Wind tunnel stability measurements were much more significant and gave a much clearer indication of tip fin flow separation than did wind tunnel performance measurements (appendix V).

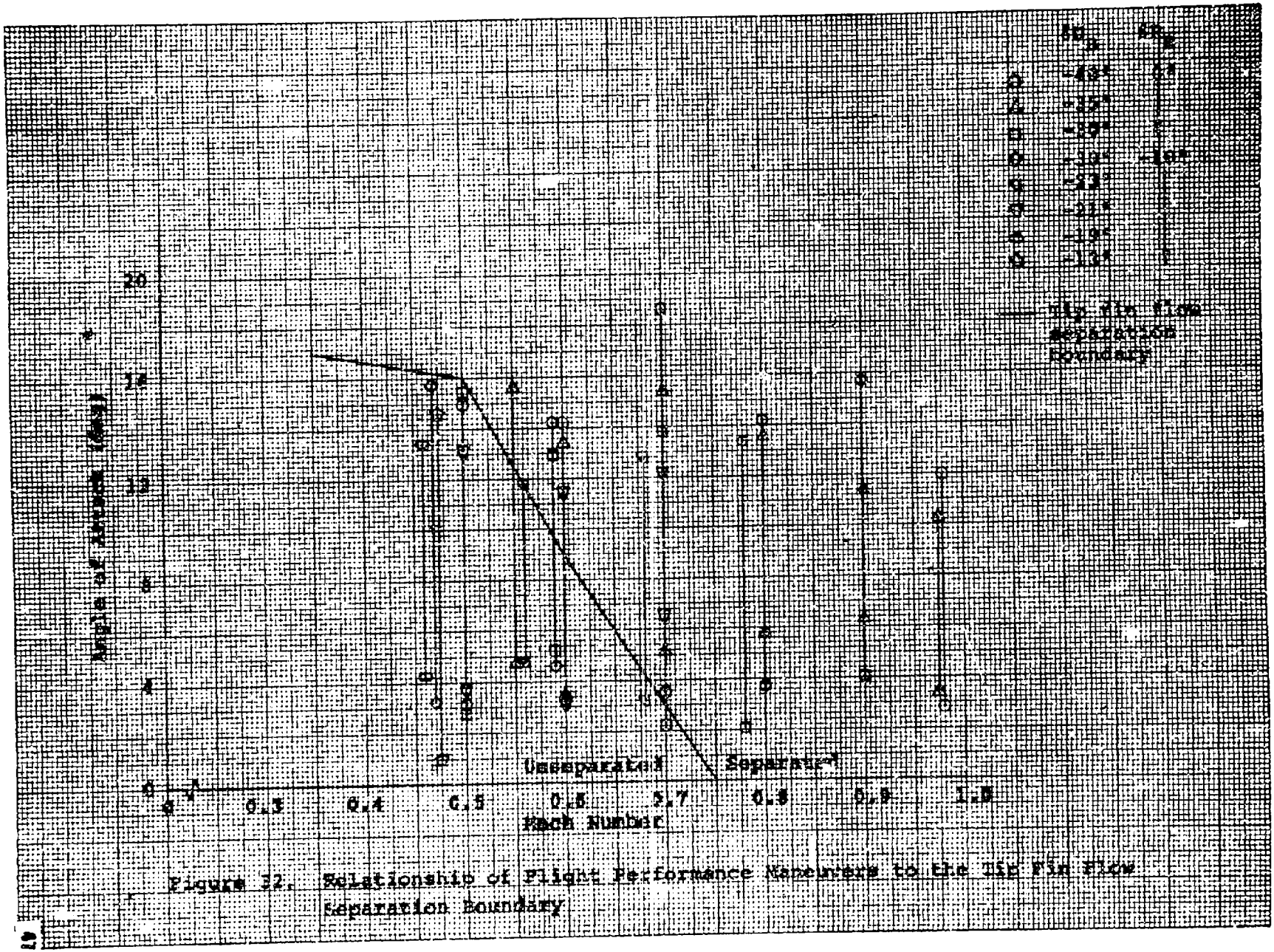

Figure 32. Relationship of Flight Performance Maneuvers to the Tip Fin Flow Separation Boundary

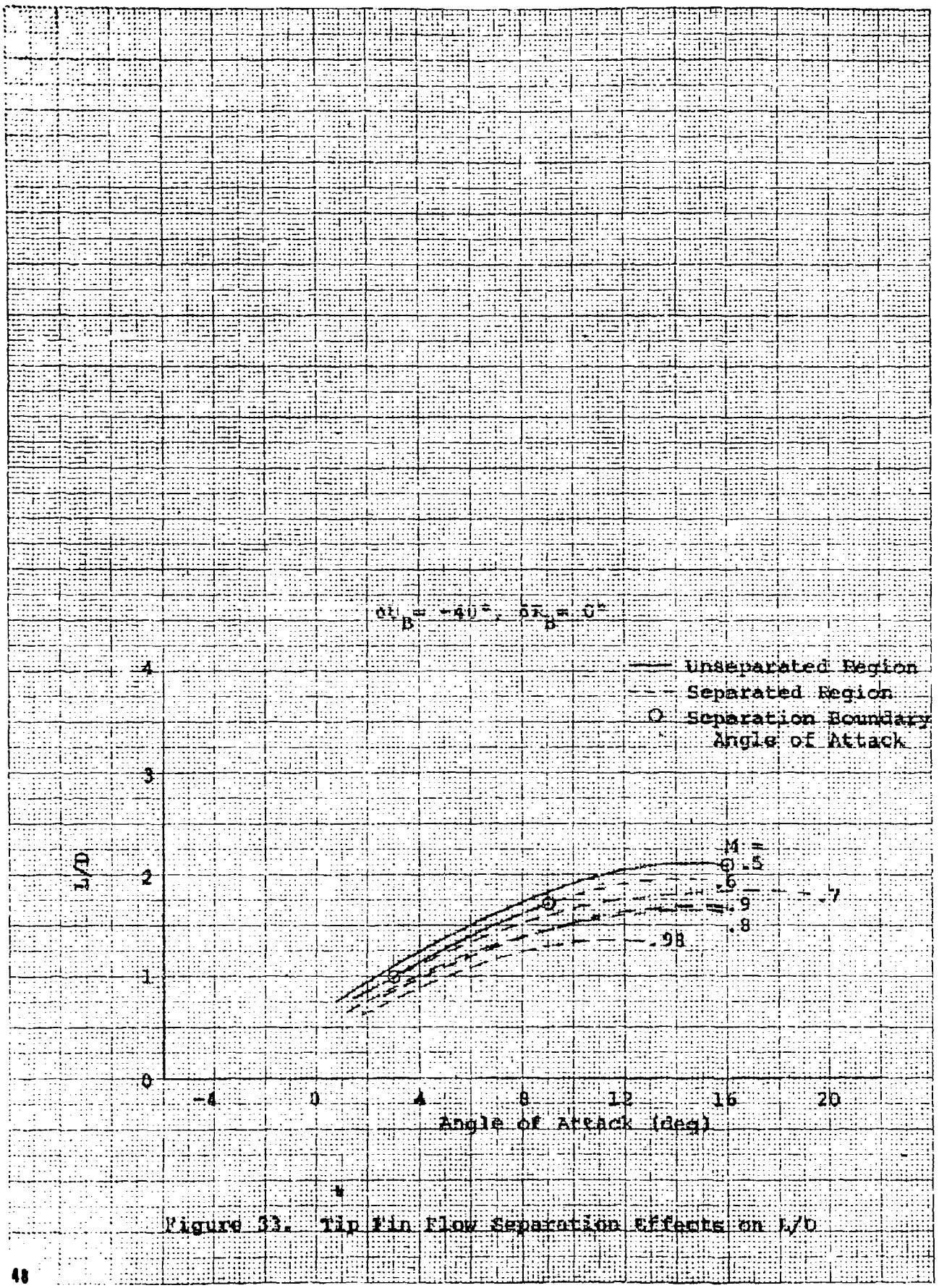

Figure 33. Tip Fin Flow Separation Effects on L/D

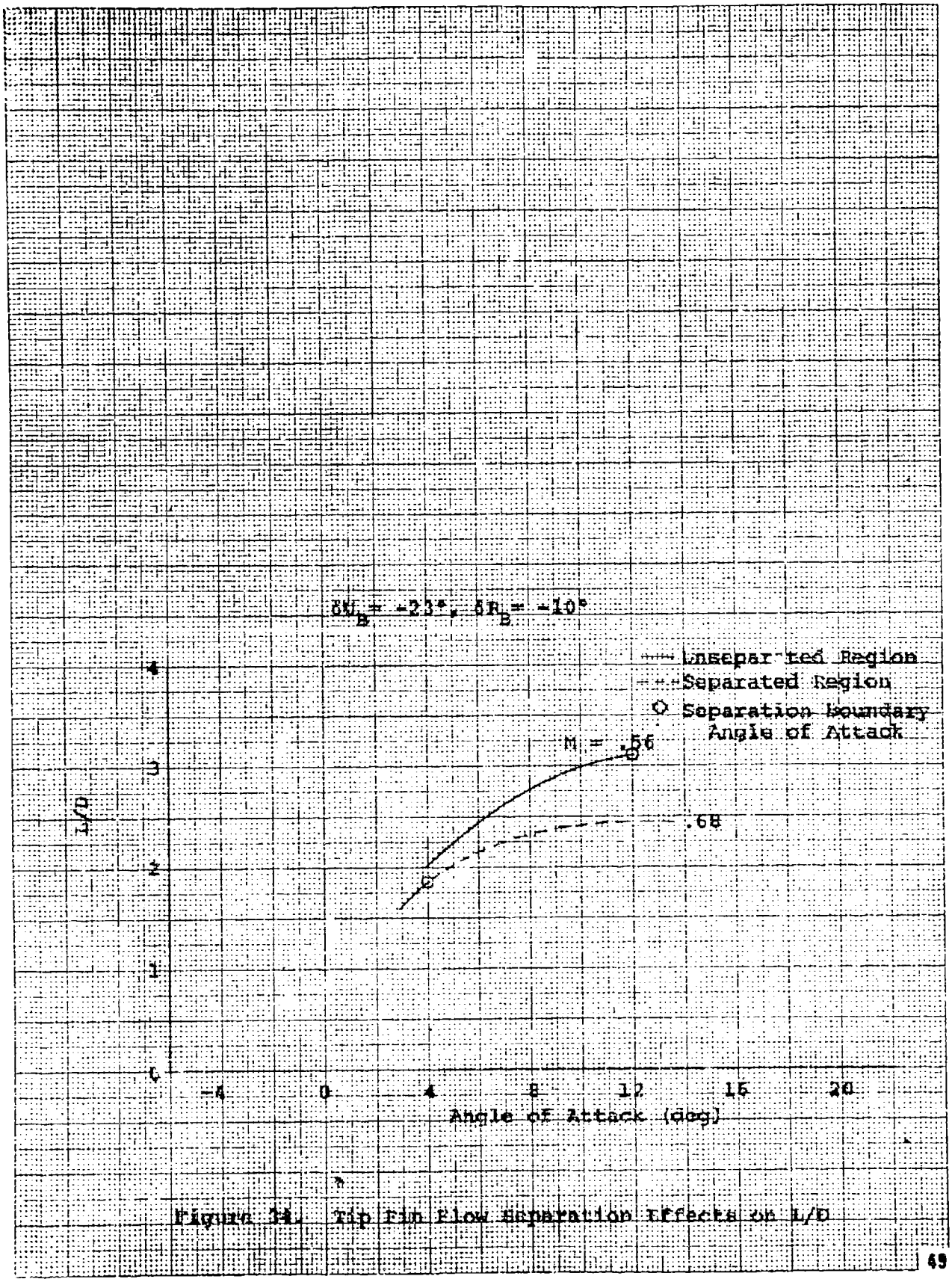

Figure 14. Tip Fin Flow Separation Effects on L/D

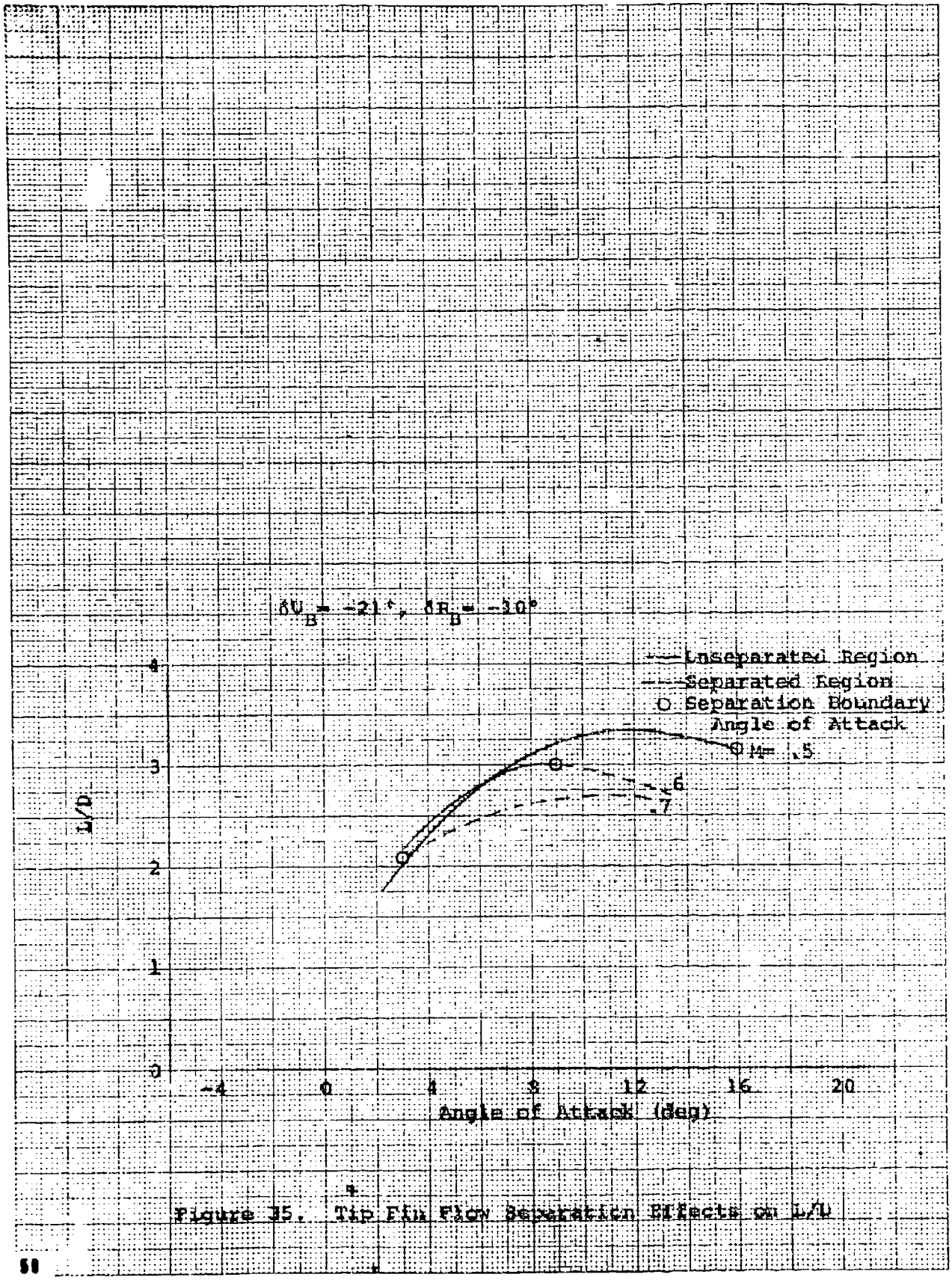

Figure 35. Tip Fin Flow Separation Effects on L/D

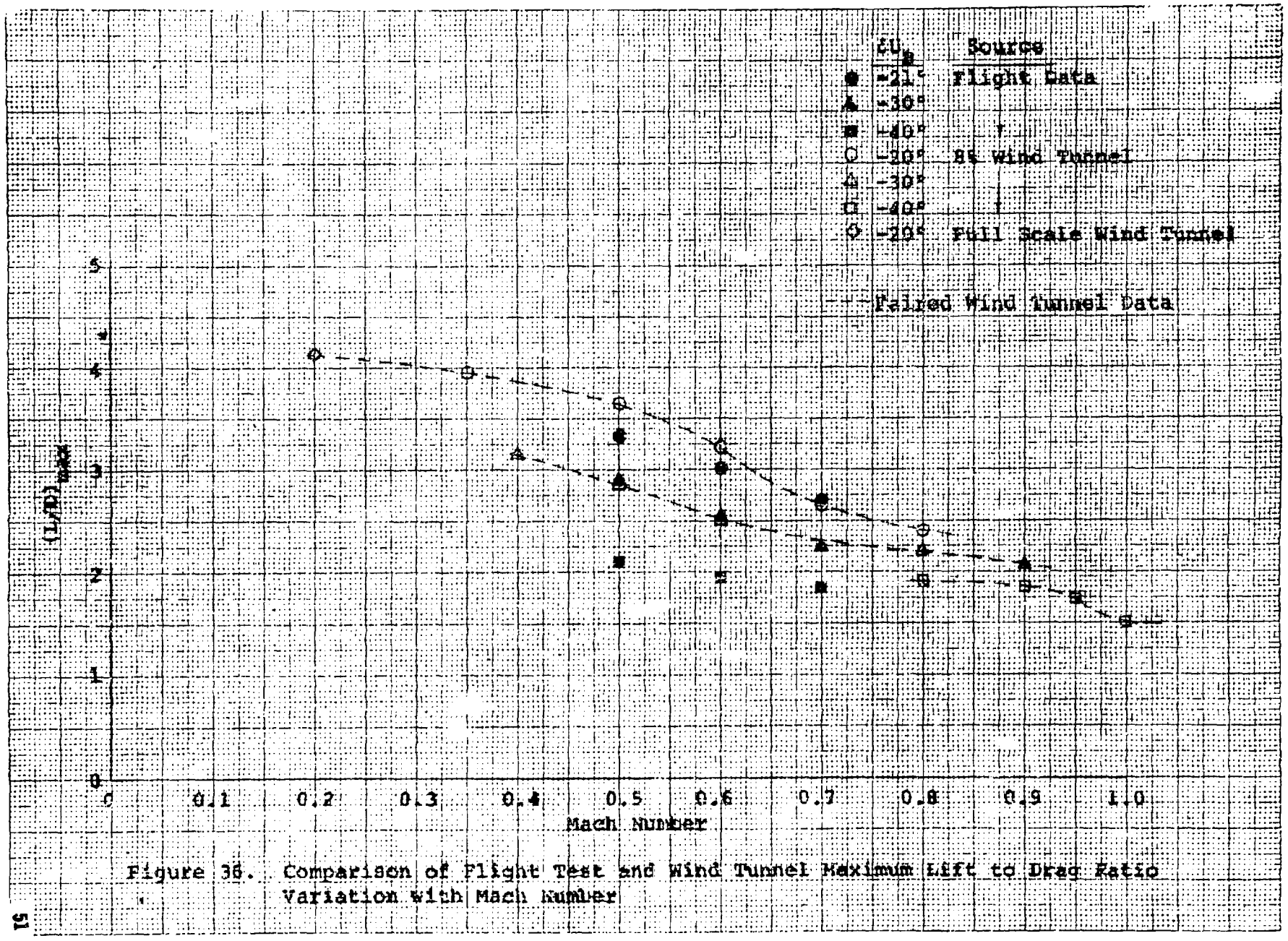

Figure 38. Comparison of Flight Test and Wind Tunnel Maximum Lift to Drag Ratio Variation with Mach Number

CONCLUSIONS

A large amount of performance data was obtained during the X-24A flight test program which confirmed the design goals of a subsonic L/D_{max} of over 4.0 and a supersonic L/D_{max} of approximately 1.25. The performance characteristics of the vehicle were defined for a variety of vehicle control surface configurations over a Mach number range of M = 0.26 to 1.50 and at angles of attack from 1.5 degrees to 19.6 degrees.

Different wind tunnel tests showed discrepancies with each other in their predictions. Generally, however, flight test data exhibited lower lift at the same angle of attack, and lift curve slopes that were less than most wind tunnel predictions. Flight test drag coefficient data were also generally slightly less than wind tunnel data with the result that flight L/D's were similar to wind tunnel predictions.

Some Mach number effects were apparent in the flight data. Flight lift curve slopes did not change appreciably with changing Mach number. However, lift coefficients at the same angle of attack showed significant decreases with increased Mach number above M=0.9. Zero lift drag coefficient data were derived and showed the expected transonic drag rise. The reduction in L/D with increasing Mach number which occurred in the low subsonic Mach range ($0.5 \leq M \leq 0.7$) was attributed to tip fin flow separation. Flight performance data substantiated the tip fin flow separation boundary which was developed from hinge moment data and tuft photos early in the flight test program.

The effects on performance of control flap configuration were found to be a total wedge angle effect. This was manifested by a change in base area which contributed a corresponding change in base drag. Flight chord force coefficient data at low subsonic Mach numbers were found to be a parabolic function of wedge angle which confirmed wind tunnel predictions.

The drag coefficient increment due to the landing gear alone ranged from 0.030 to 0.035. The total effect of landing gear deployment (landing gear plus an increase in wedge angle due to trim change) produced a reduction in L/D_{max} of 37 percent in the final gear down landing configuration (δL_E = 0 degrees).

The speed brake feature of the X-24A control system, which was developed during the test program, provided the capability for a variation of L/D_{max} from 4.25 to 2.10 at Mach numbers below 0.8.

APPENDIX I

FLIGHT TEST AND WIND TUNNEL TRIM PERFORMANCE DATA

Table I

LOG OF FLIGHT TEST PERFORMANCE MANEUVERS

Upper Flap Bias (deg)	Rudder Bias (deg)	Mach Number Range	Lower Flap Range (deg)	Angle of Attack Range (deg)	Flight Number	$R_c \times 10^{-6}$	Gross Weight (lb)	$\bar{X}$ (in.)	$\bar{Y}$ (in.)	$\bar{Z}$ (in.)	$\bar{X}$ (pct)
Transonic Configurations											
-40	0	.466 to .501	24.9 to 33.5	3.0 to 14.9	23	38.1	6,558	155.60	-.612	27.18	56.31
	+2.20	.509 to .534	24.6 to 30.4	3.8 to 11.5	27	34.5	6,157	156.16	.141	27.09	56.57
	0	.572 to .605	26.1 to 33.1	3.3 to 14.2	23	33.2	6,558	155.40	-.612	27.18	56.31
		.661 to .754	24.5 to 33.5	1.5 to 15.1	16	34.6	7,404	150.90	-.326	27.71	54.69
		.704 to .746	23.6 to 27.9	8.5 to 18.8	20	38.5	7,301	152.60	-.277	27.74	55.26
	+2.20	.695 to .733	24.8 to 30.2	3.8 to 13.5	27	26.8	6,157	156.16	.141	27.68	56.57
	0	.763 to .851	27.8 to 31.1	3.8 to 14.2	20	35.3	7,301	152.80	-.277	27.74	55.36
		.847 to .877	24.6 to 30.4	4.1 to 13.6	18	25.6	7,228	151.40	-.583	27.30	54.79
		.866 to .941	24.6 to 29.8	4.2 to 13.4	20	30.5	7,301	152.60	-.277	27.74	55.36
		.941 to 1.008	25.9 to 32.2	2.8 to 10.6	19	19.3	7,289	152.40	-.511	27.55	55.00
		.955 to 1.010	23.4 to 30.4	3.6 to 12.0	20	20.1	7,301	152.80	-.277	27.74	55.36
		1.240 to 1.334	26.8 to 31.0	7.8 to 12.4	20	15.6	7,301	152.80	-.277	27.74	55.36
		1.056 to 1.201	19.9 to 29.3	4.4 to 11.2	24	14.9	6,558	155.40	-.612	27.18	56.31
		1.414 to .486	17.1 to 20.4	8.4 to 10.8	23	17.6	6,558	155.40	.612	27.18	56.31
	+1.25	1.341 to 1.452	19.4 to 25.0	4.9 to 10.3	25	16.6	6,446	156.10	.184	27.0	56.55
	+2.00	1.071 to 1.337	19.9 to 23.6	6.5 to 13.4	26	12.5	6,324	157.80	-.122	27.03	57.16
-35	0	.518 to .597	20.2 to 25.4	6.5 to 12.5	11	39.6	6,394	156.20	-.959	26.76	56.58
		.523 to .539	18.5 to 27.2	4.7 to 15.6	14	29.9	6,430	156.00	.023	26.83	56.54
		.545 to .572	23.7 to 26.2	5.2 to 13.0	22	36.9	6,336	159.20	-.365	26.92	57.28
		.571 to .644	20.2 to 27.5	3.5 to 13.4	9	31.9	6,462	158.30	-.438	27.01	57.09
		.689 to .757	20.0 to 22.5	11.3 to 15.1	9	38.1	6,462	156.40	-.438	27.01	56.68
		.707 to .754	21.1 to 25.7	5.2 to 15.4	11	32.6	6,394	156.20	-.959	26.76	56.58
		.719 to .741	22.2 to 26.4	5.1 to 12.6	11	23.6	6,394	156.20	-.959	26.76	56.58
		.734 to .756	21.8 to 26.2	5.5 to 11.2	22	18.3	6,559	156.40	-.799	26.99	56.93
		.764 to .864	23.0 to 26.9	6.3 to 11.3	12	26.9	6,463	155.50	.493	26.87	56.42
		.755 to .855	21.7 to 24.9	7.0 to 13.7	14	27.0	6,430	156.00	.023	26.83	56.54
		.859 to .955	23.7 to 26.0	6.3 to 11.5	14	23.2	6,430	156.00	.023	26.83	56.54
		.662 to .987	21.5 to 26.8	3.8 to 10.2	14	12.3	6,220	154.90	-.574	27.22	56.33
-30		.496 to .534	22.1 to 21.5	2.7 to 15.4	20	36.6	6,335	158.20	.221	26.93	57.34
		.587 to .591	24.1 to 26.2	5.2 to 12.9	7	32.6	6,[illegible]80	159.59	-.151	26.56	57.45
		.666 to .684	26.4 to 27.3	4.0 to 12.9	8	34.1	6,266	158.9	-.251	26.68	57.47
		.664 to .724	15.3 to 22.0	2.3 to 13.9	19	42.1	6,289	157.40	-.514	26.95	57.20
		.750 to .805	16.6 to 22.1	4.1 to 13.6	29	38.7	6,289	157.40	-.514	26.95	57.20
Subsonic Configurations											
-30	-10	.421 to .527	21.3 to 31.3	3.2 to 15.8	19	42.6	6,[illegible]24	158.00	-.346	26.[illegible]2	57.[illegible]4
		.571 to .583	22.4 to 24.6	4.7 to 12.7	6	30.5	6,277	158.60	-.[illegible]01	27.[illegible]8	57.45
		.587 to .594	22.3 to 24.3	6.5 to 14.1	7	33.2	6,[illegible]80	158.59	-.[illegible]1	27.[illegible]6	57.45
-23		.556 to .569	11.7 to 21.2	4.8 to 11.8	5	23.6	6,294	156.68	-.[illegible]37	27.[illegible]1	57.55
-23.5		.671 to .693	14.7 to 22.1	3.2 to 12.4	2	32.3	6,[illegible]55	160.[illegible]	-.[illegible]56	27.[illegible]62	58.05
-21		.483 to .542	9.9 to 19.9	2.6 to 13.1	2	31.9,45.6	6,[illegible]08	160.[illegible]8	-.[illegible]65	27.[illegible]02	58.22
		.574 to .614	11.8 to 19.9	7.1 to 13.4	2	35.3	6,[illegible]09	160.[illegible]8	-.[illegible]65	27.[illegible]02	58.22
		.660 to .718	13.5 to 24.6	6.5 to 14.2	3	39.1	6,[illegible]36	161.[illegible]8	-.[illegible]65	27.[illegible]62	58.20
-2		.443 to .474	6.6 to 25.7	4.2 to 14.5	5	38.4	6,294	156.68	-.[illegible]37	27.71	57.55
Subsonic Approach Configurations											
-13	-10	.472 to .491	3.6 to 9.4	3.7 to 14.6	3	36.[illegible]	6,[illegible]24	158.[illegible]2	-.[illegible]46	27.[illegible]2	57.[illegible]4
		.[illegible]90 to .478	1.6 to 8.4	1.9 to [illegible].5	11	36.[illegible]		9.[illegible]2	-.[illegible]38	26.[illegible]7	57.[illegible]3
		.494 to .521	2.5 to 8.0	0.9 to [illegible].5	25	31.2,[illegible].8	[illegible]	158.[illegible]2	-.[illegible]46	27.[illegible]2	57.[illegible]4
-9.5 to -12.5		.477 to .496	$\delta_{LE} = 0°$	2.8 to 7.8	19	44.1,[illegible]4.8	6,[illegible]61	158.[illegible]1	-.[illegible]46	27.[illegible]2	57.[illegible]4
-8.8 to -12.7		.450 to .517	$\delta_{LE} = 0°$	3.0 to 16.[illegible]	23	41.[illegible]	6,[illegible]35	158.[illegible]2	-.[illegible]31	27.[illegible]2	57.[illegible]4
Subsonic Landing Gear Down Configuration											
-21	-10	.301 to .317	5.4 to 7.1	8.6 to 12.7	1	47.5	6,359	159.58	-.[illegible]8	27.[illegible]2	58.[illegible]0
-23		.256 to .323	0.4 to 5.8	10.7 to 1[illegible].4	4	44.4	6,434	161.[illegible]0	-.[illegible]49	27.[illegible]4	58.[illegible]2
-15.6 to -21.7		.250 to .351	$\delta_{LE} = 0$	9.4 to 15.[illegible]	6	47.[illegible]	6,280	159.[illegible]9	-.[illegible]57	27.[illegible]8	57.[illegible]6
-15.[illegible] to -16.[illegible]		.270 to .399	$\delta_{LE} = 0$	5.3 to 12.[illegible]	9	48.4	6,4[illegible]2	160.[illegible]4	-.[illegible]38	[illegible].[illegible]	57.[illegible]9
-[illegible] to -19.4		.[illegible]0 to .415	$\delta_{LE} = 0$	4.[illegible] to 10.7	13	54.2	6,395	159.[illegible]7	-.[illegible]23	26.[illegible]7	57.[illegible]4

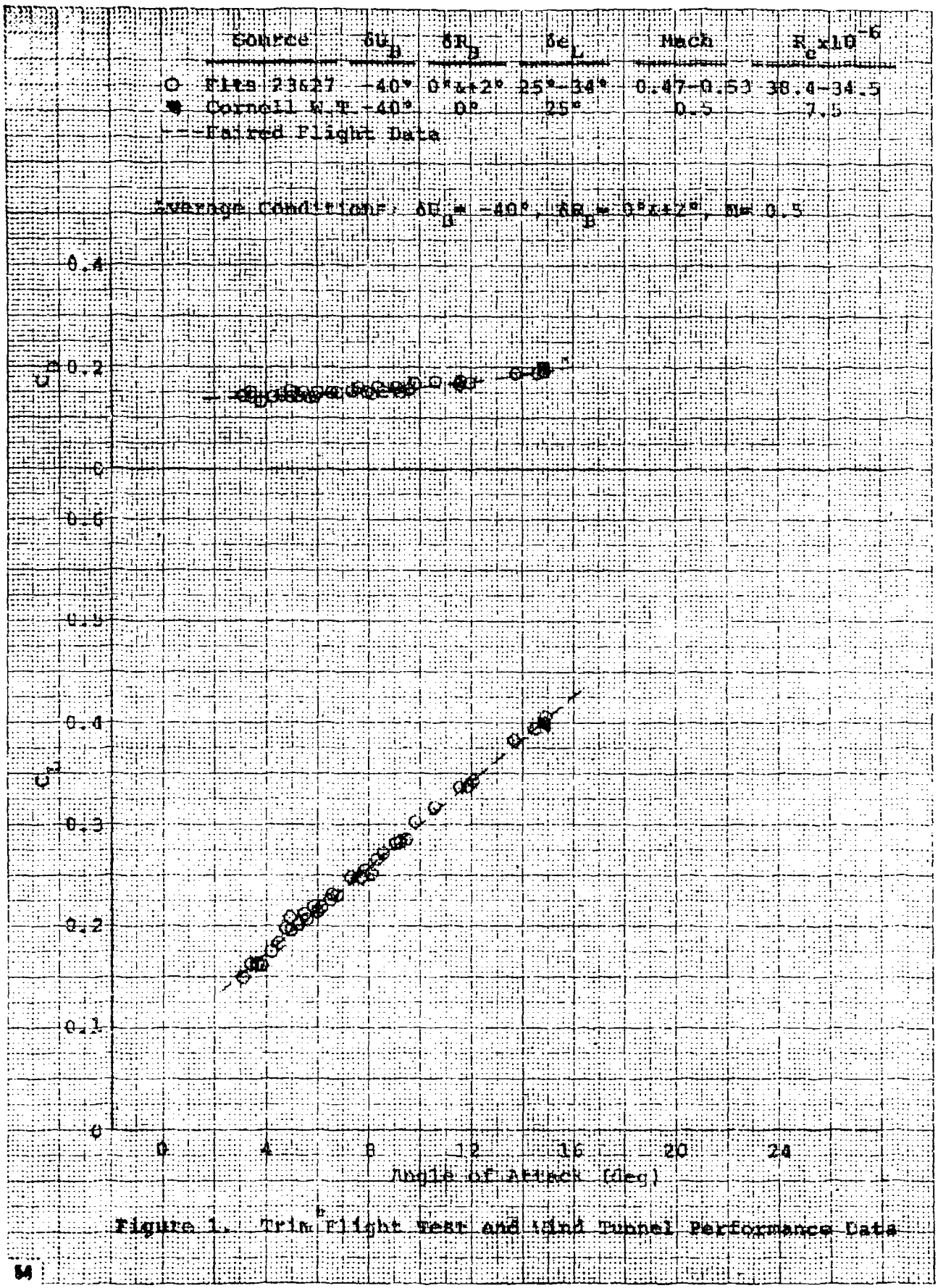

Figure 1. Trim Flight Test and Wind Tunnel Performance Data

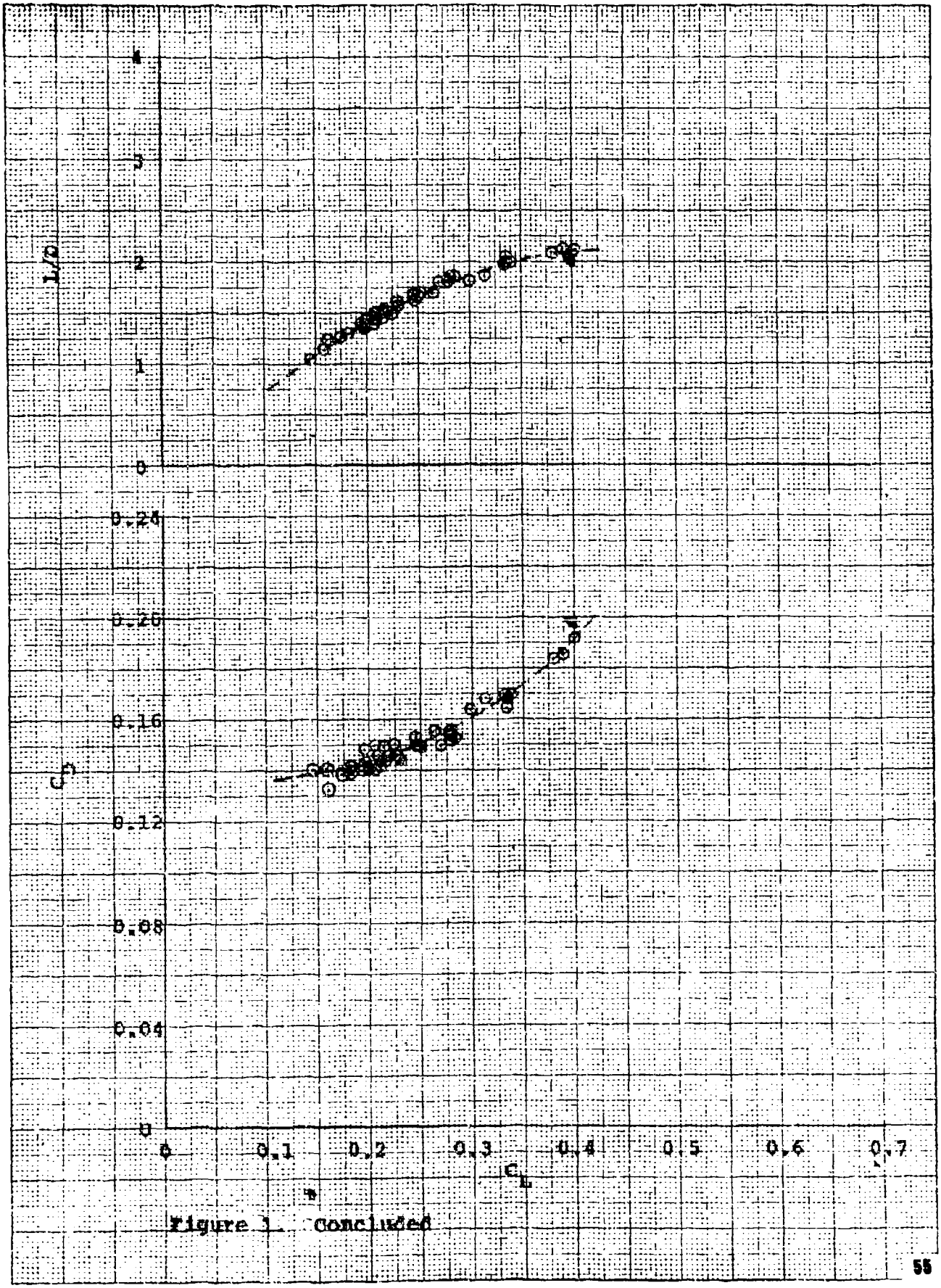

Figure 1. Concluded

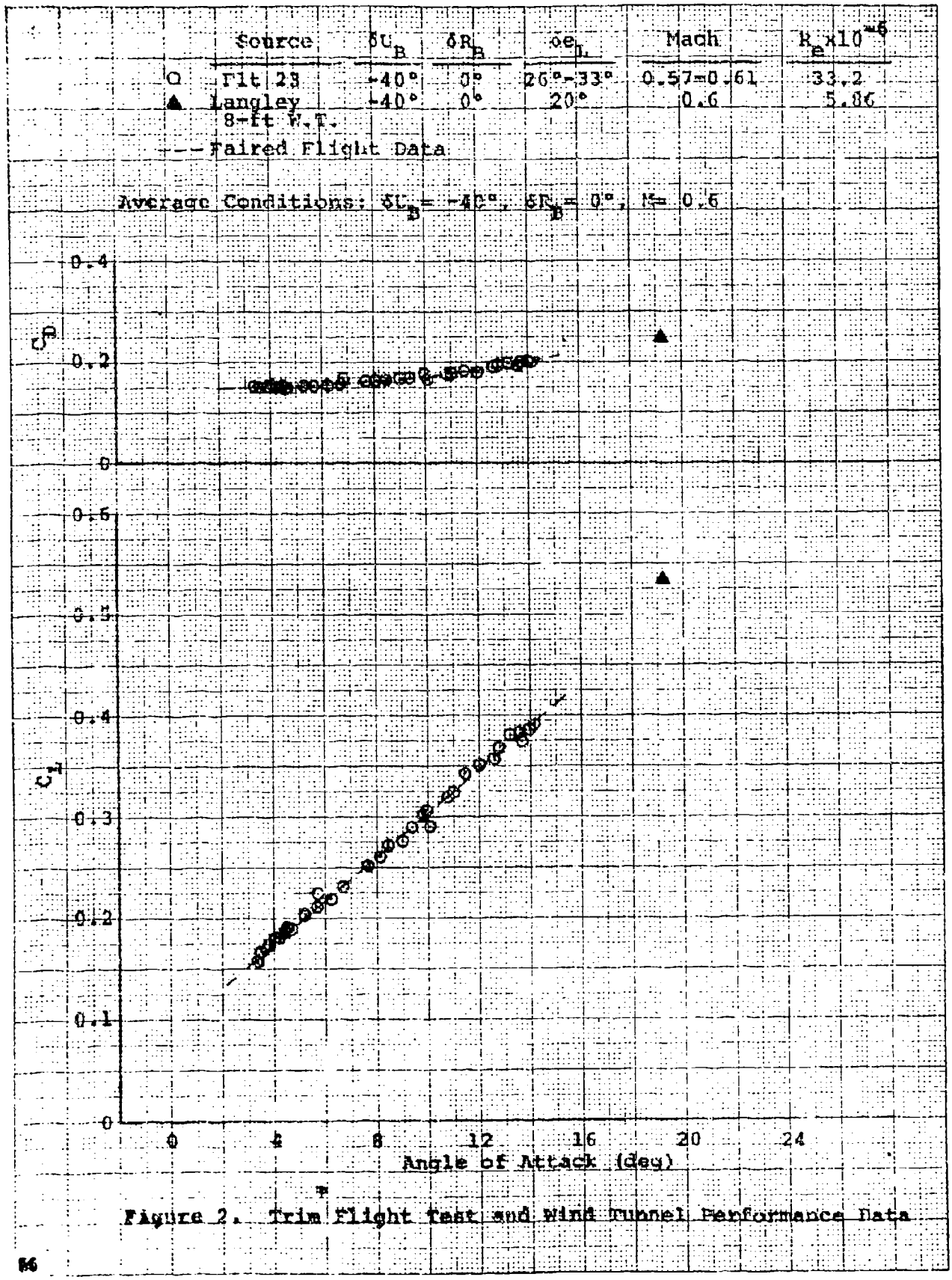

Figure 2. Trim Flight Test and Wind Tunnel Performance Data

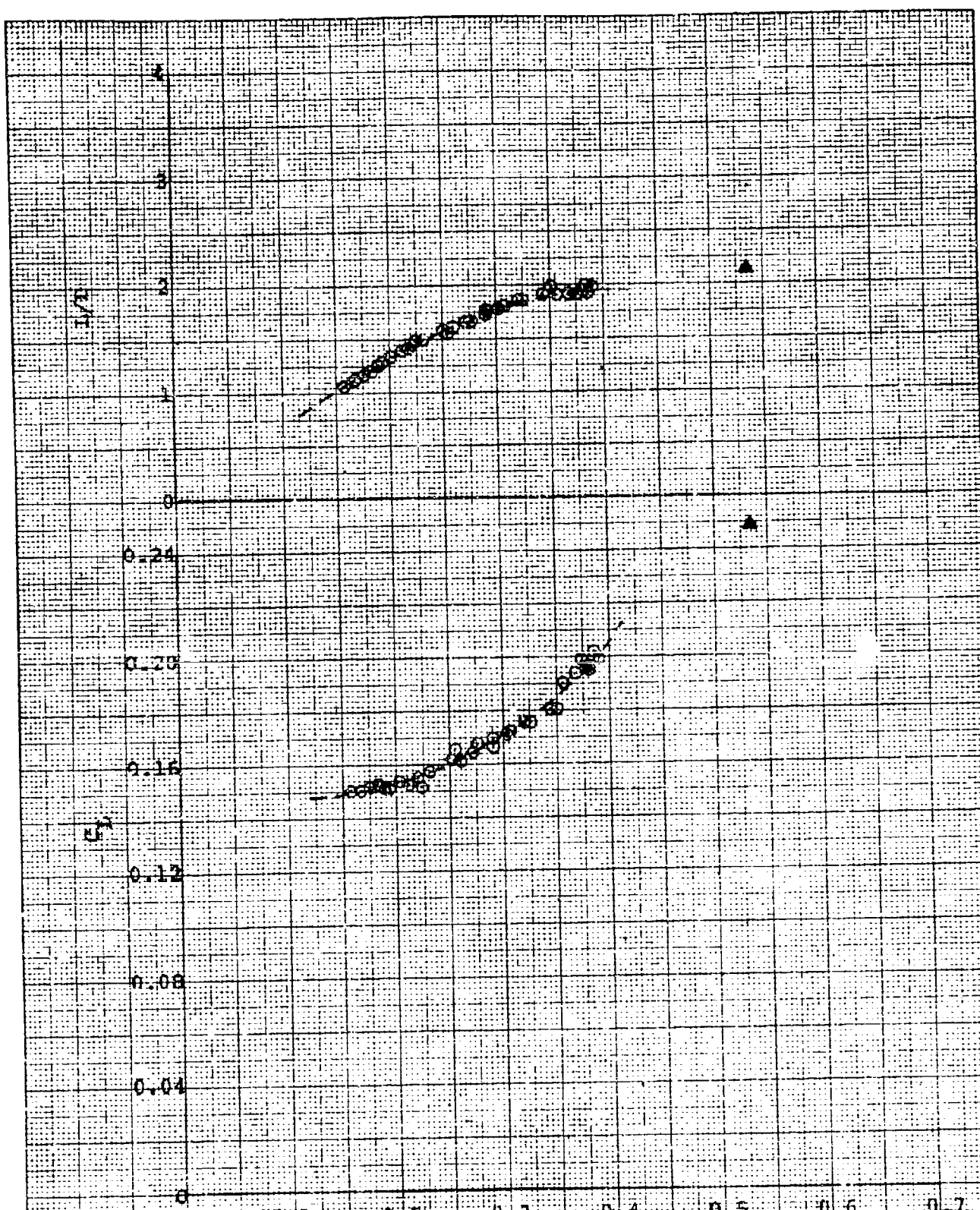

Figure 2. Concluded

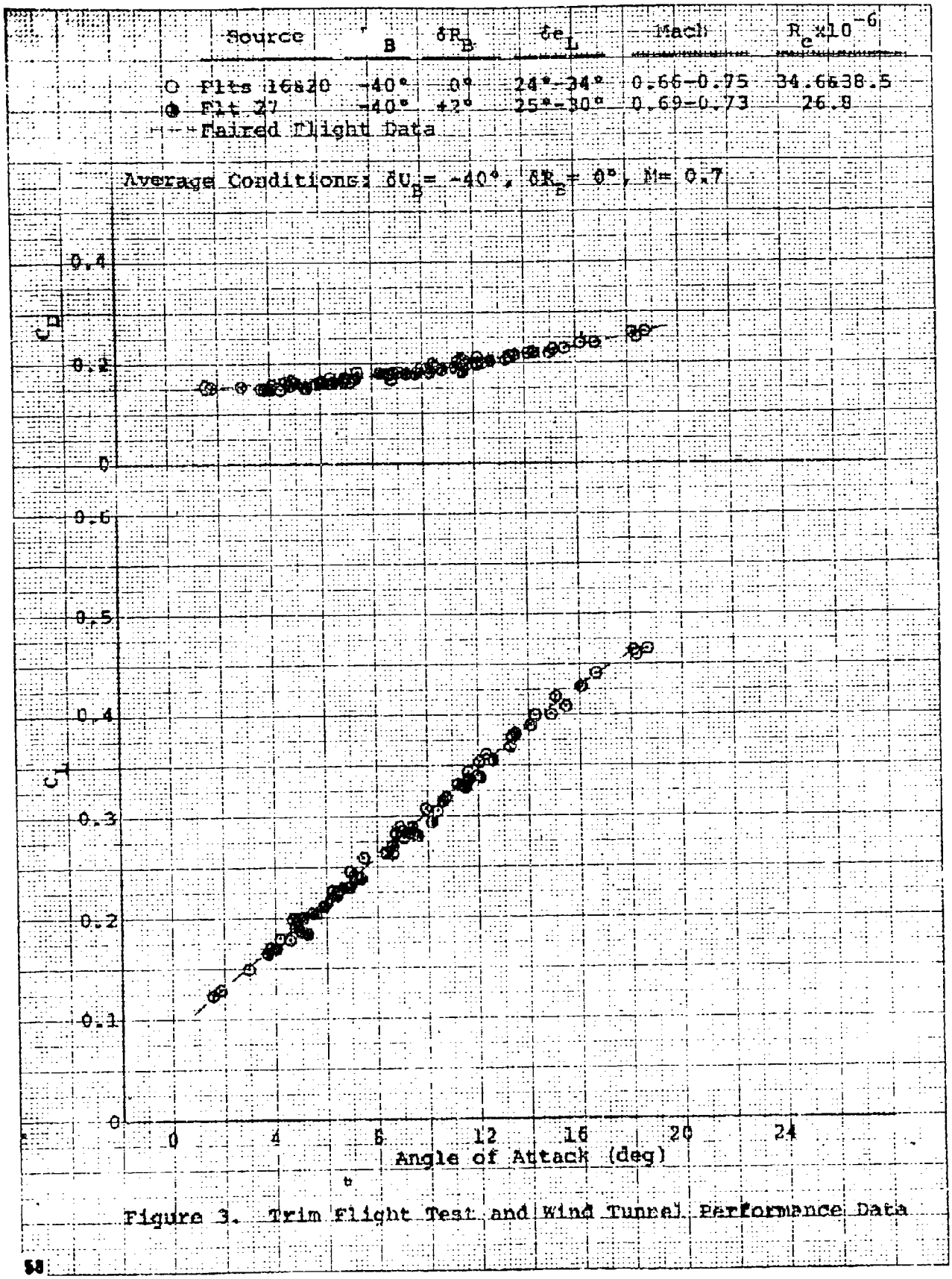

Figure 3. Trim Flight Test and Wind Tunnel Performance Data

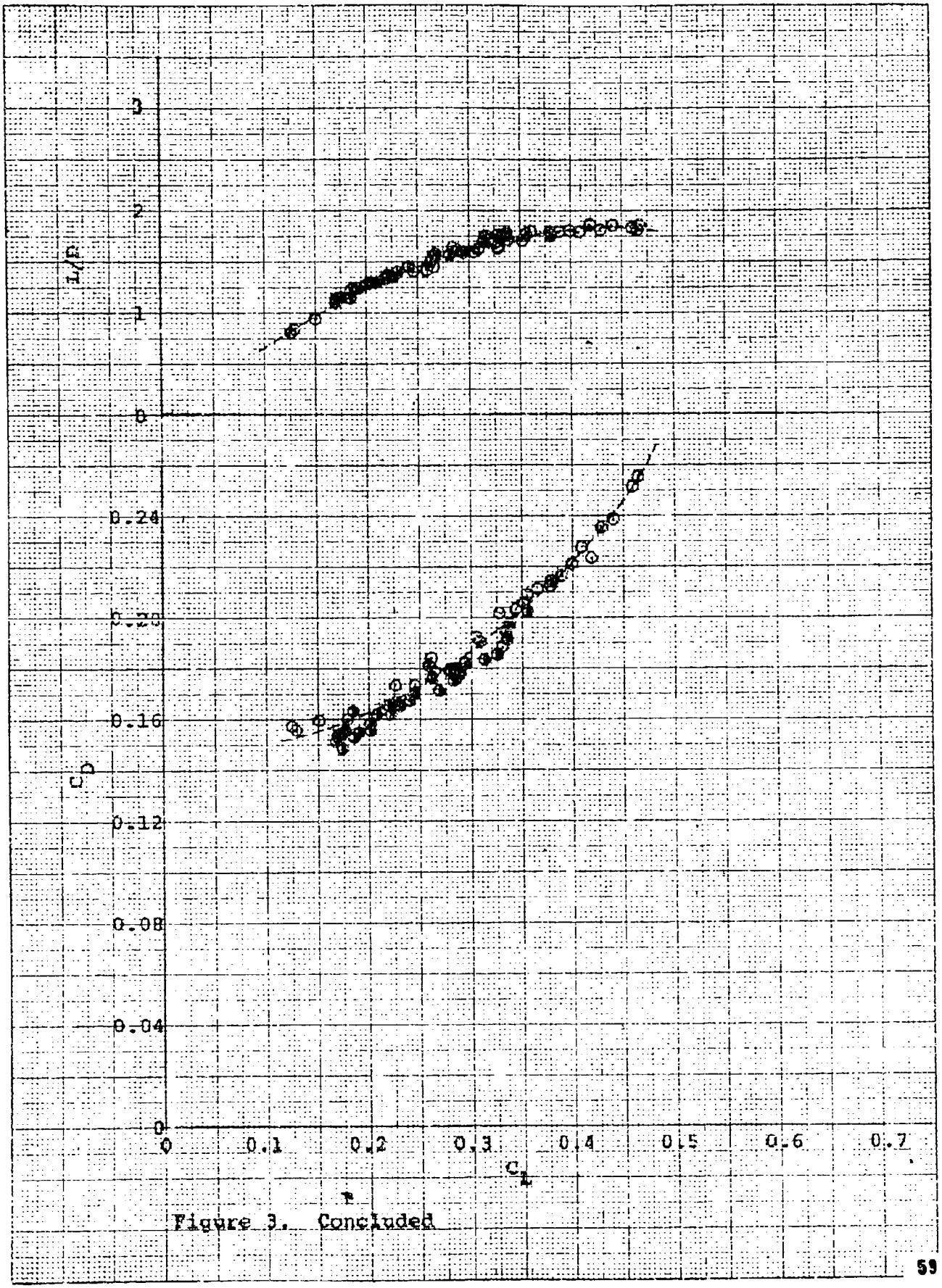

Figure 3. Concluded

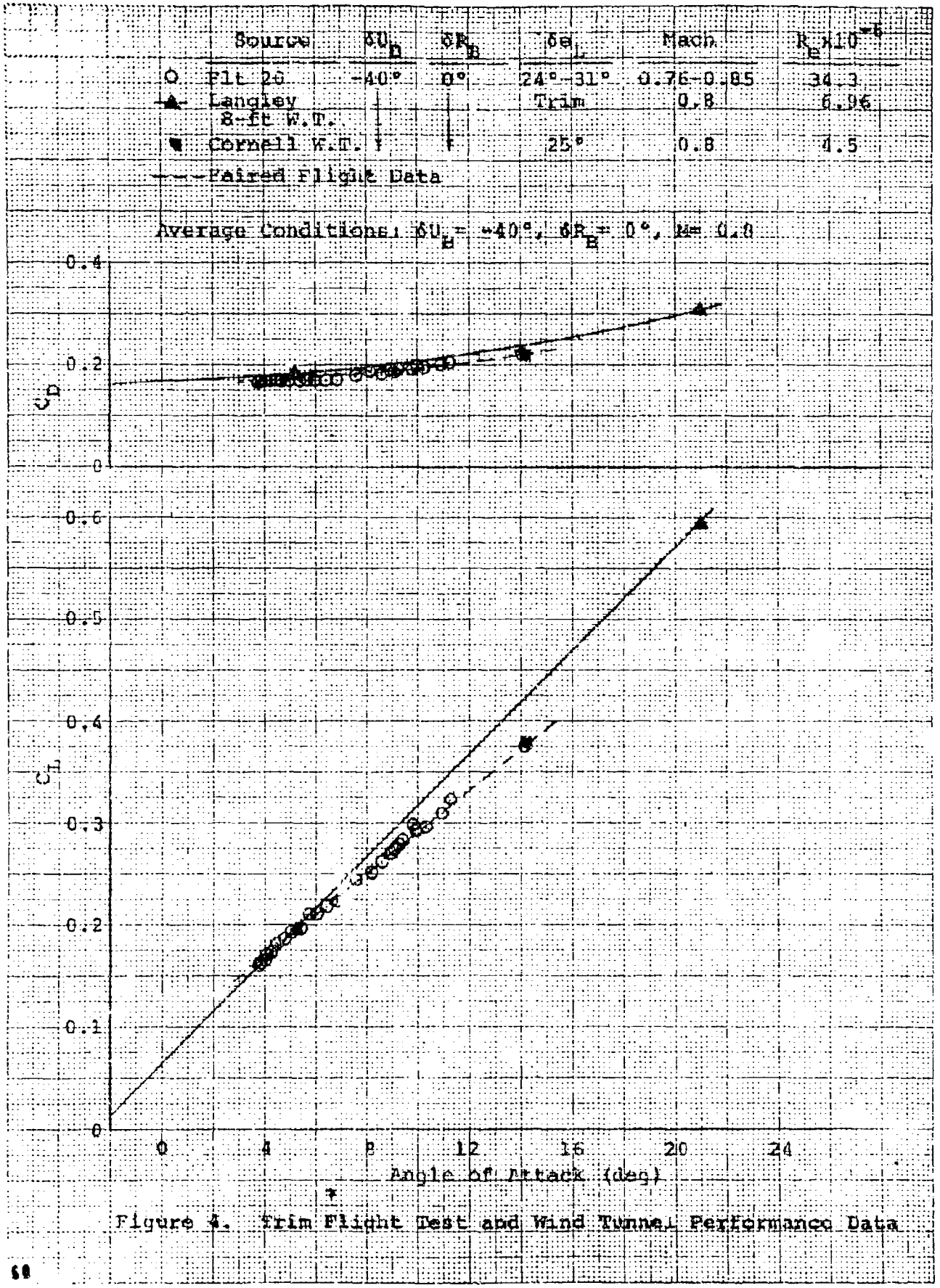

Figure 4. Trim Flight Test and Wind Tunnel Performance Data

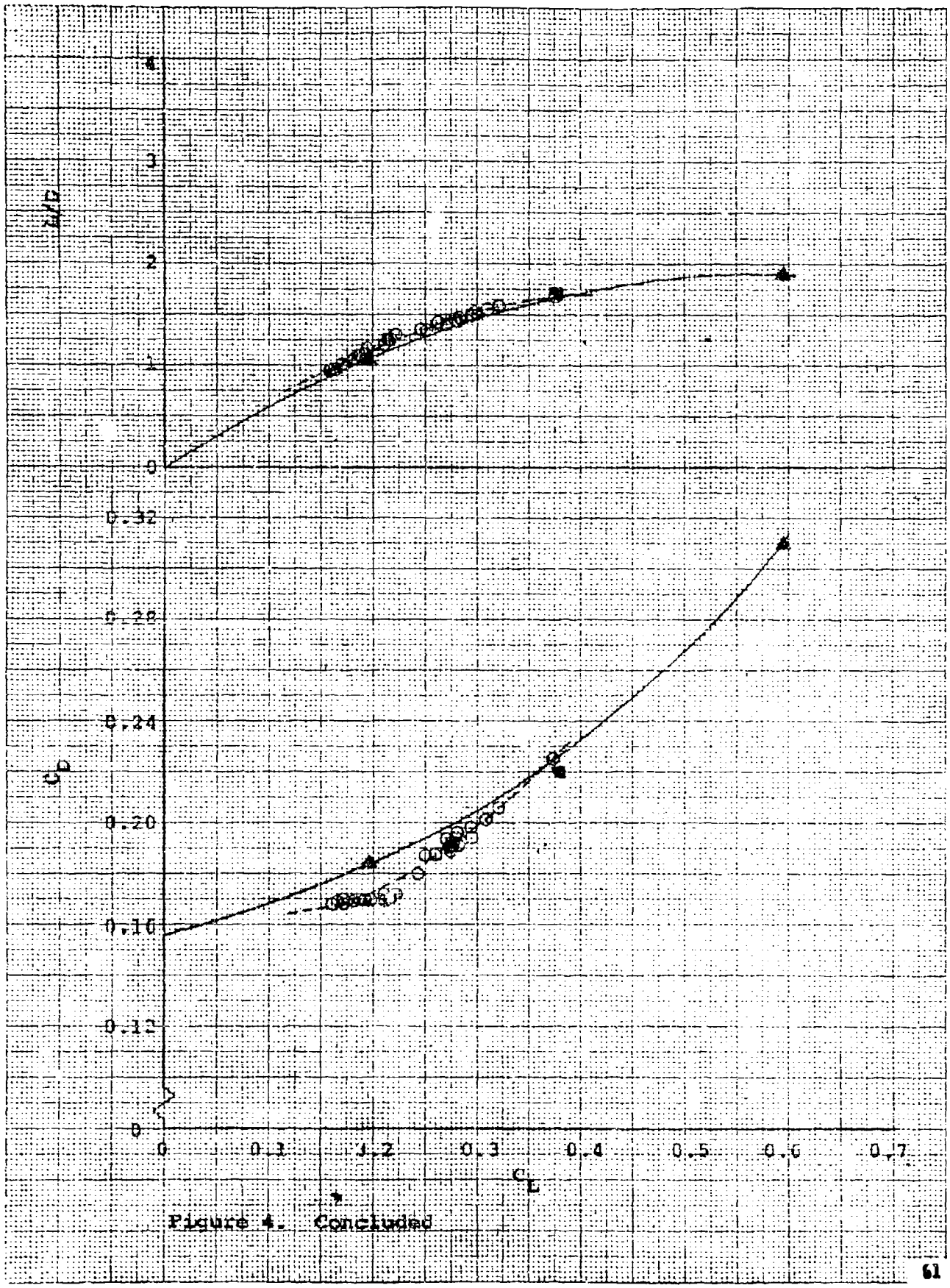

Figure 4. Concluded

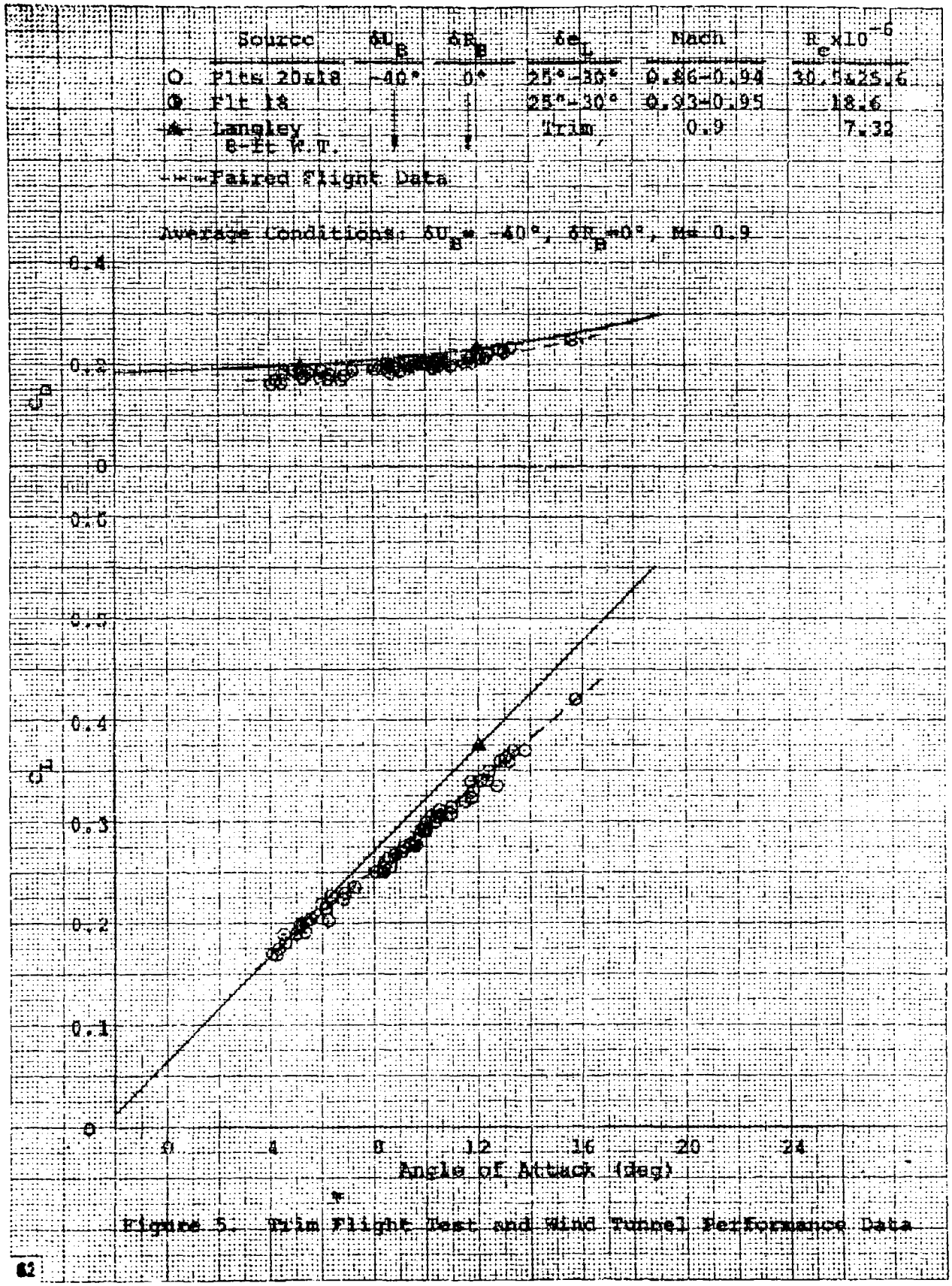

Figure 5. Trim Flight Test and Wind Tunnel Performance Data

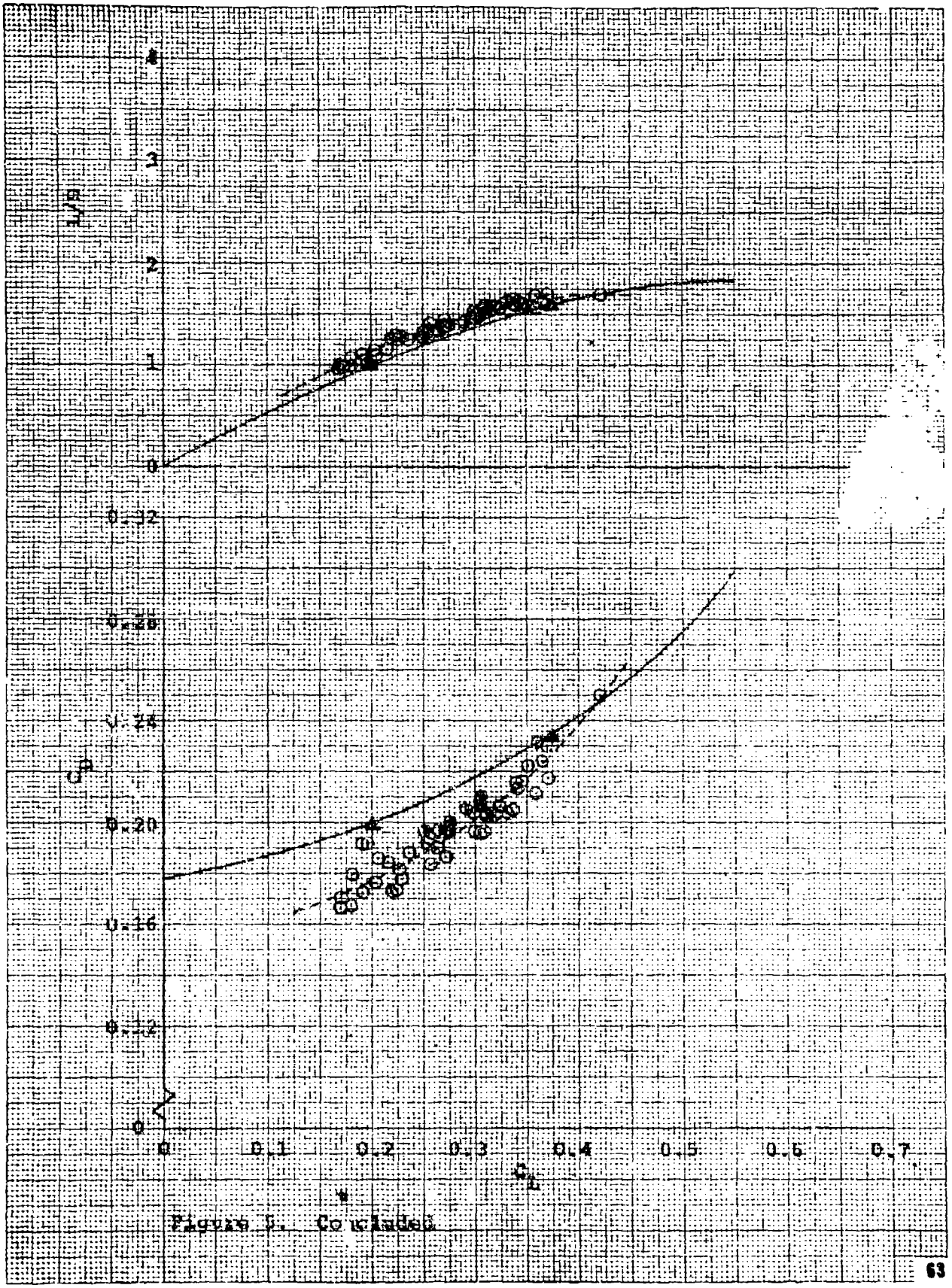

Figura 5. Co ciadel

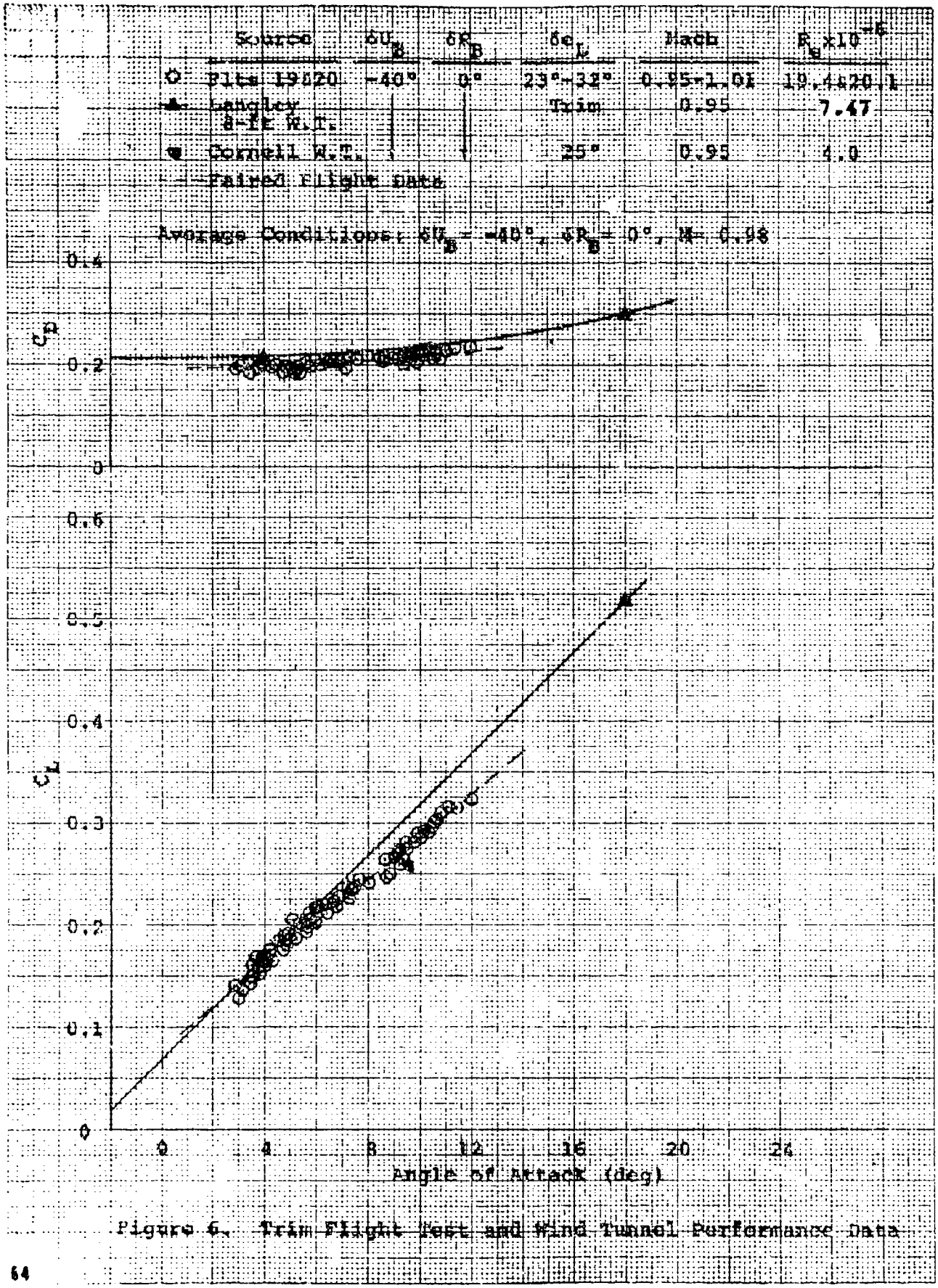

Figure 6. Trim Flight Test and Wind Tunnel Performance Data

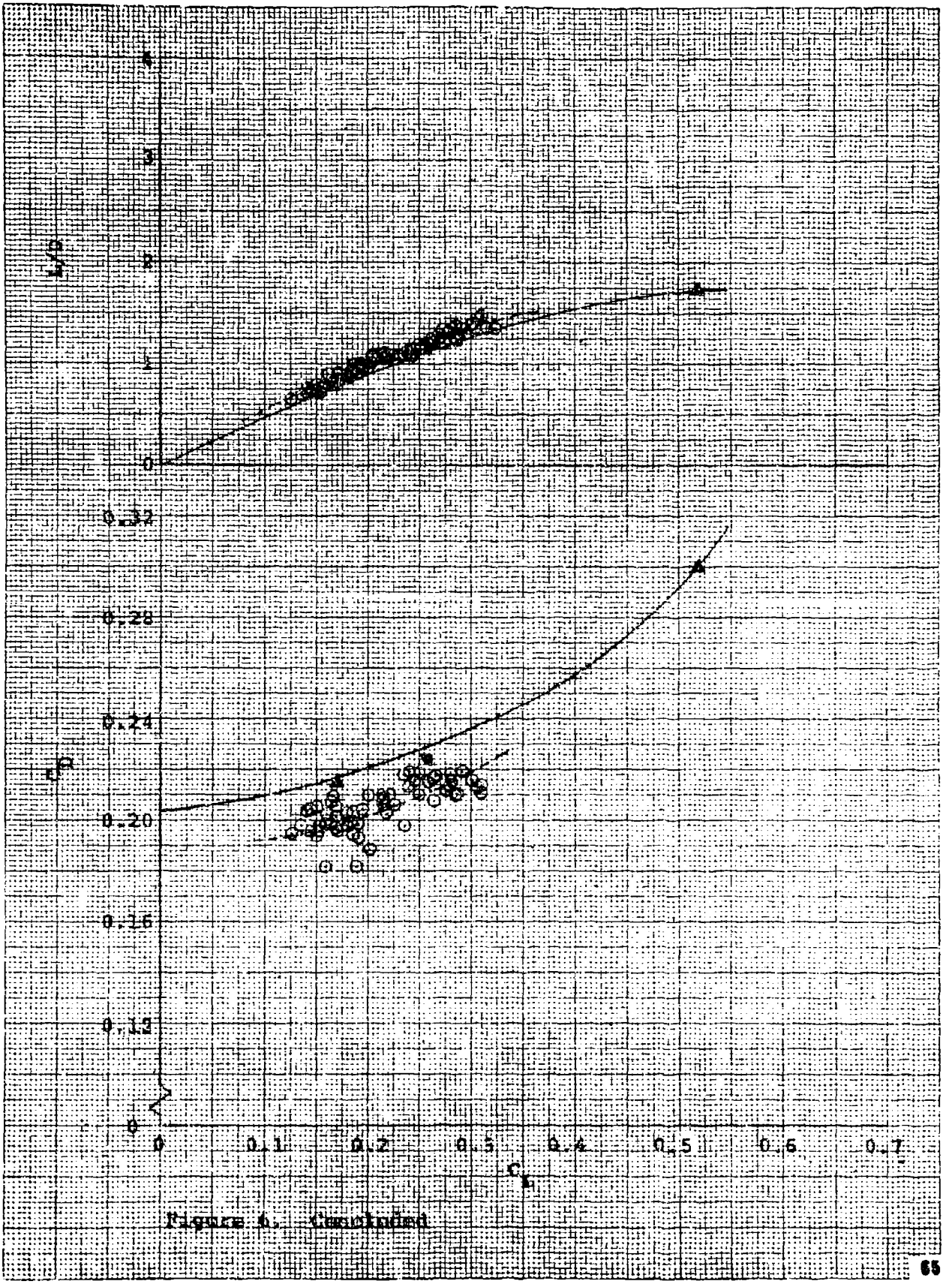

Figure 6. Concluded.

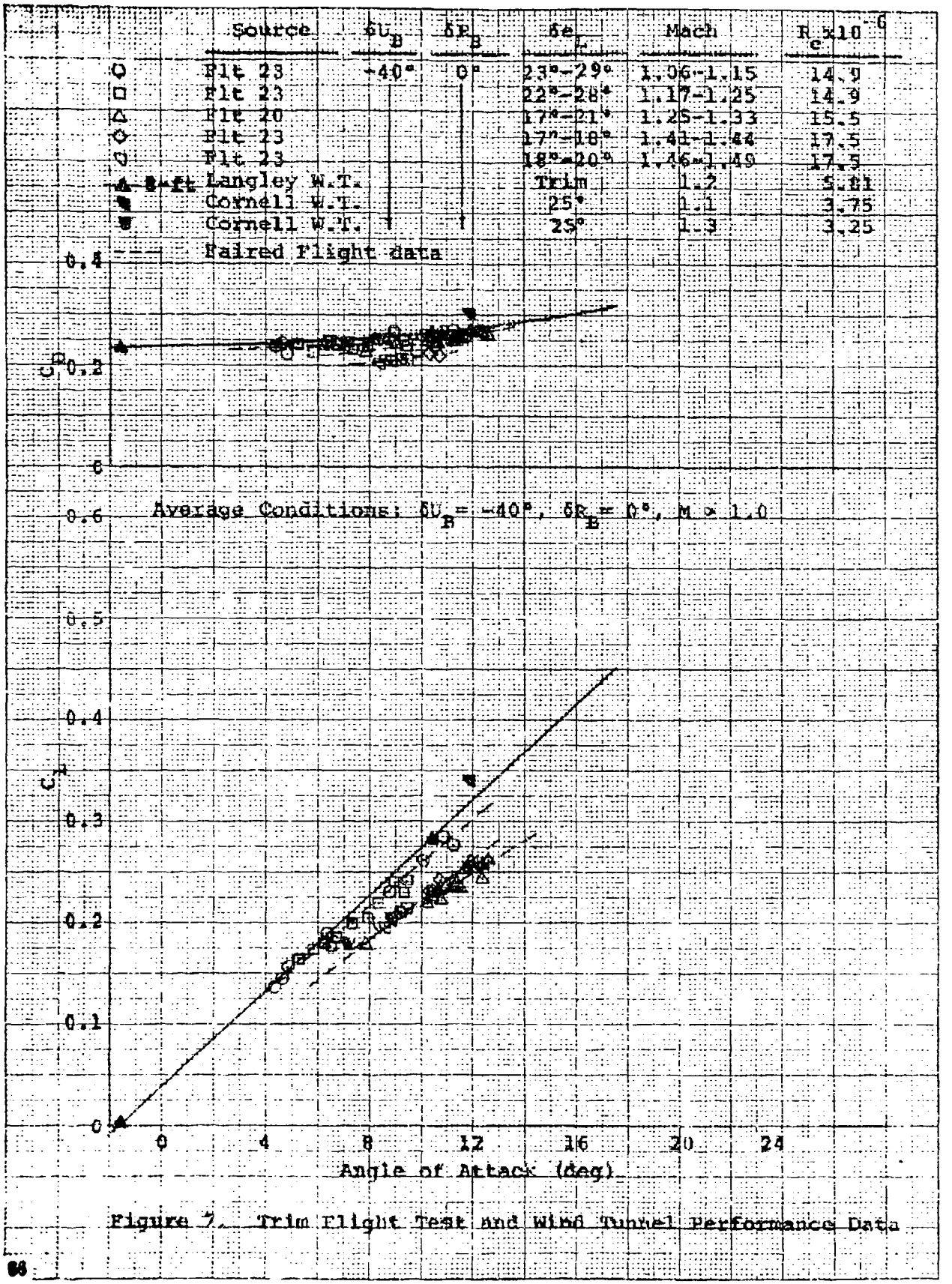

Figure 7. Trim Flight Test and Wind Tunnel Performance Data

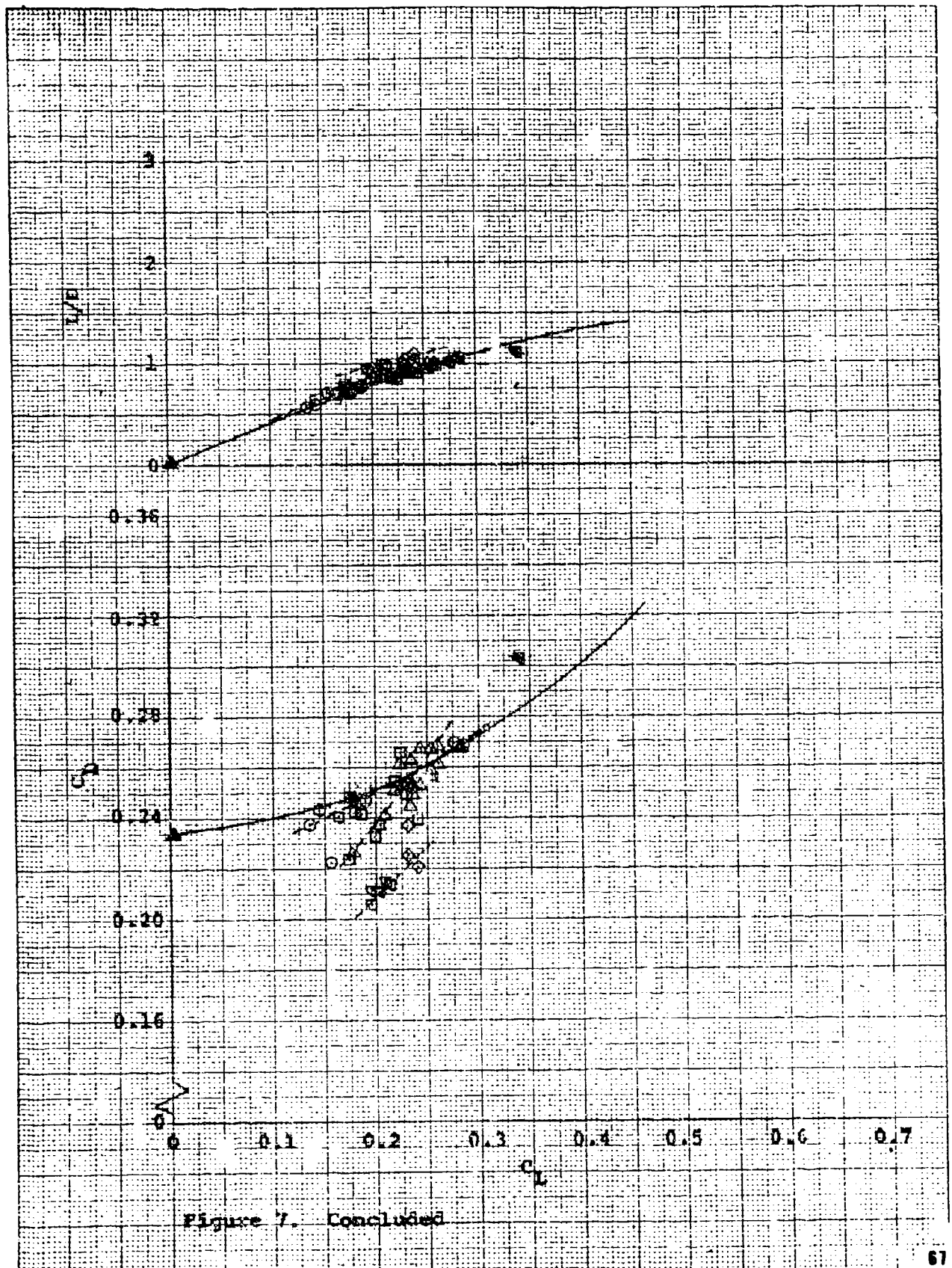

Figure 7. Concluded

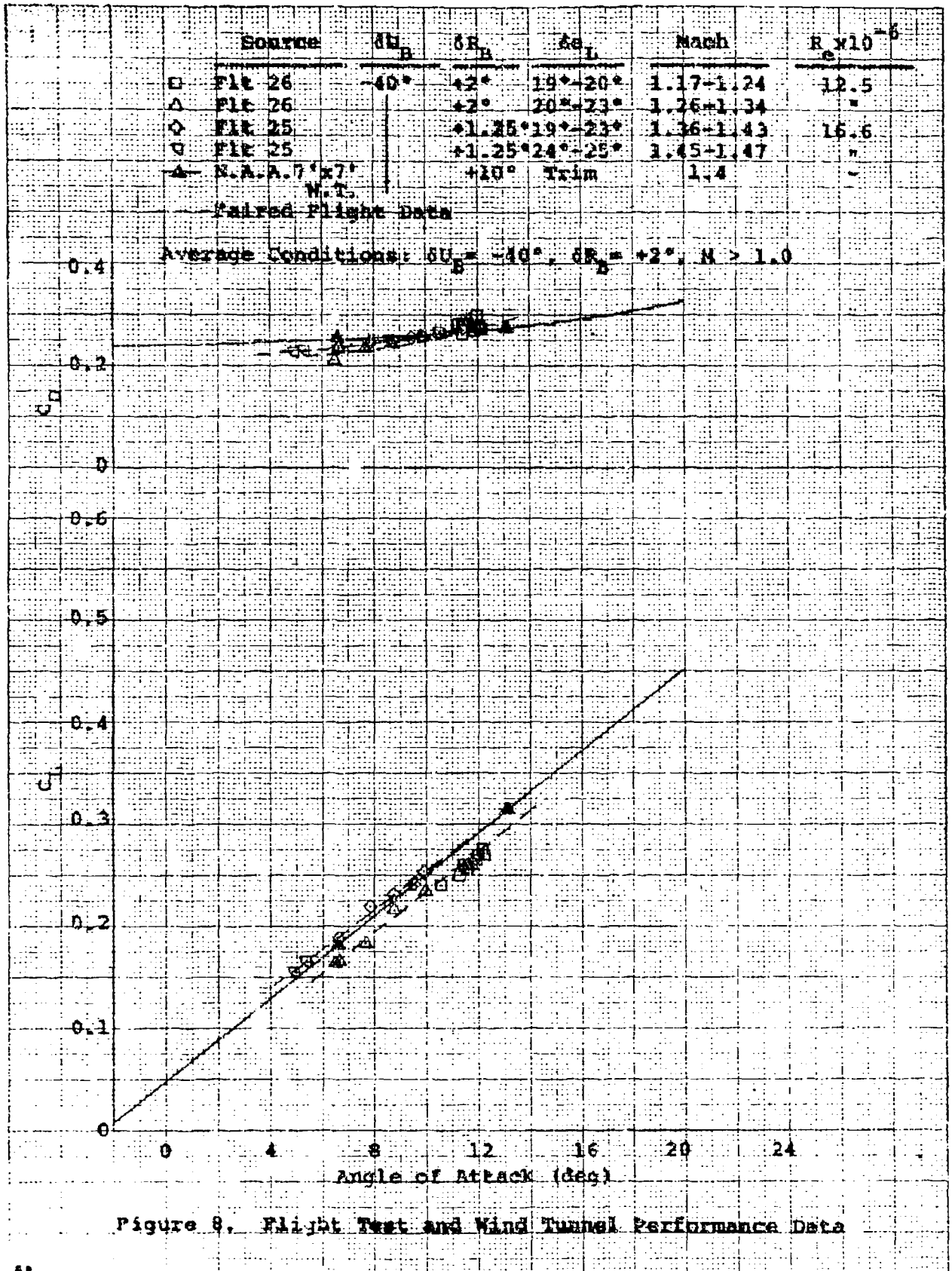

Figure 8. Flight Test and Wind Tunnel Performance Data

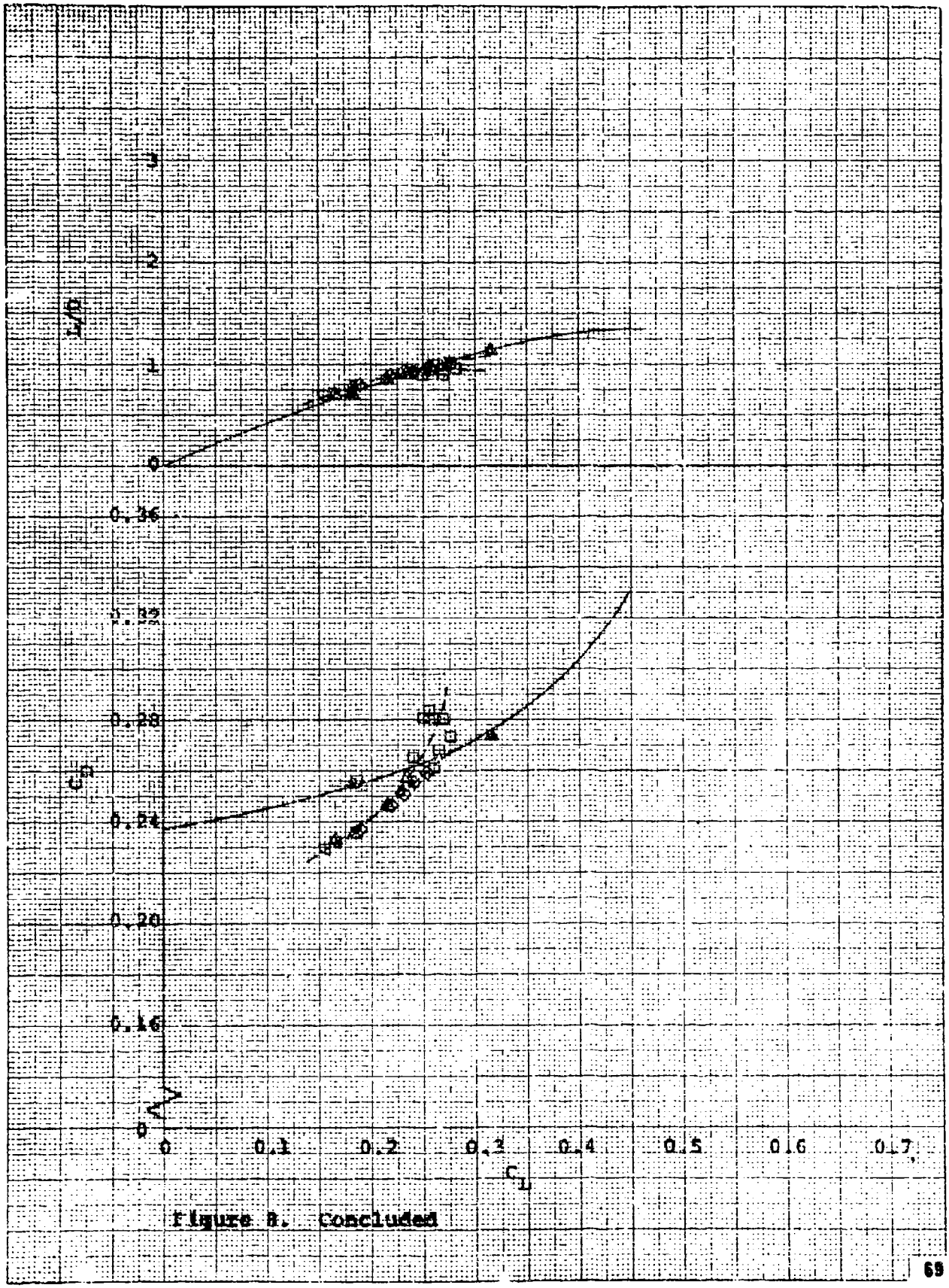

Figure 8. Concluded

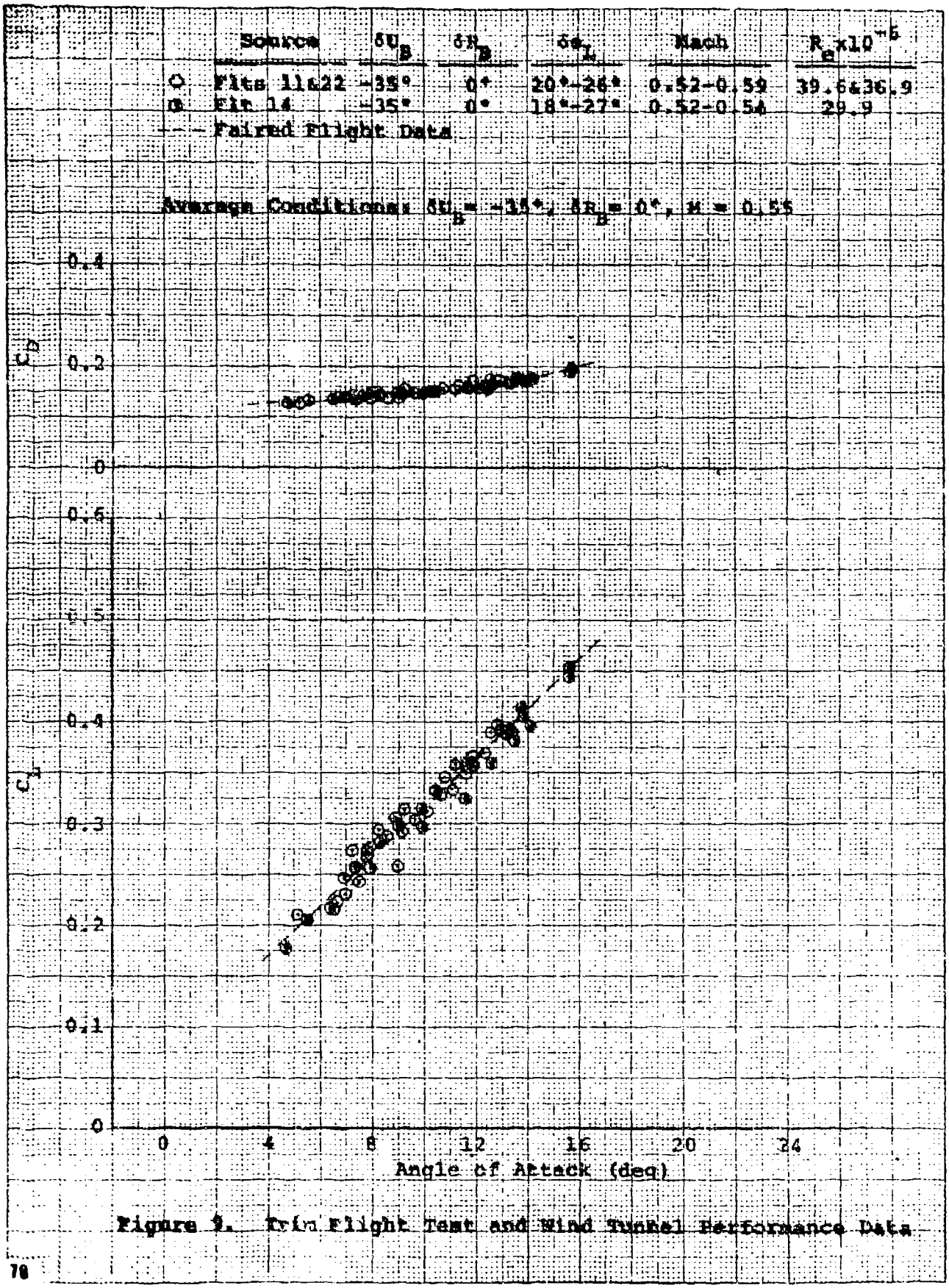

Figure 9. Trim Flight Test and Wind Tunnel Performance Data

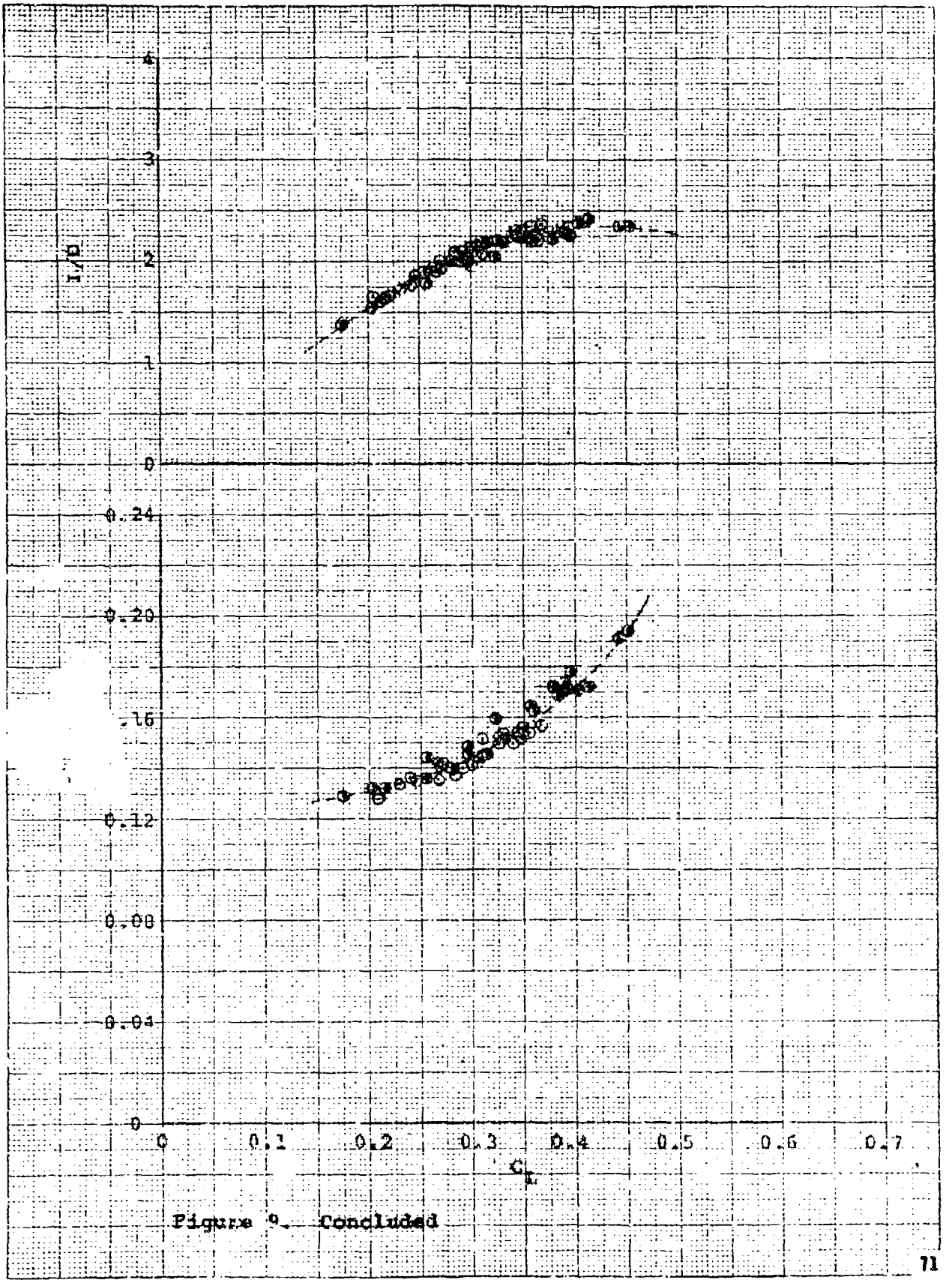

Figure 9. Concluded

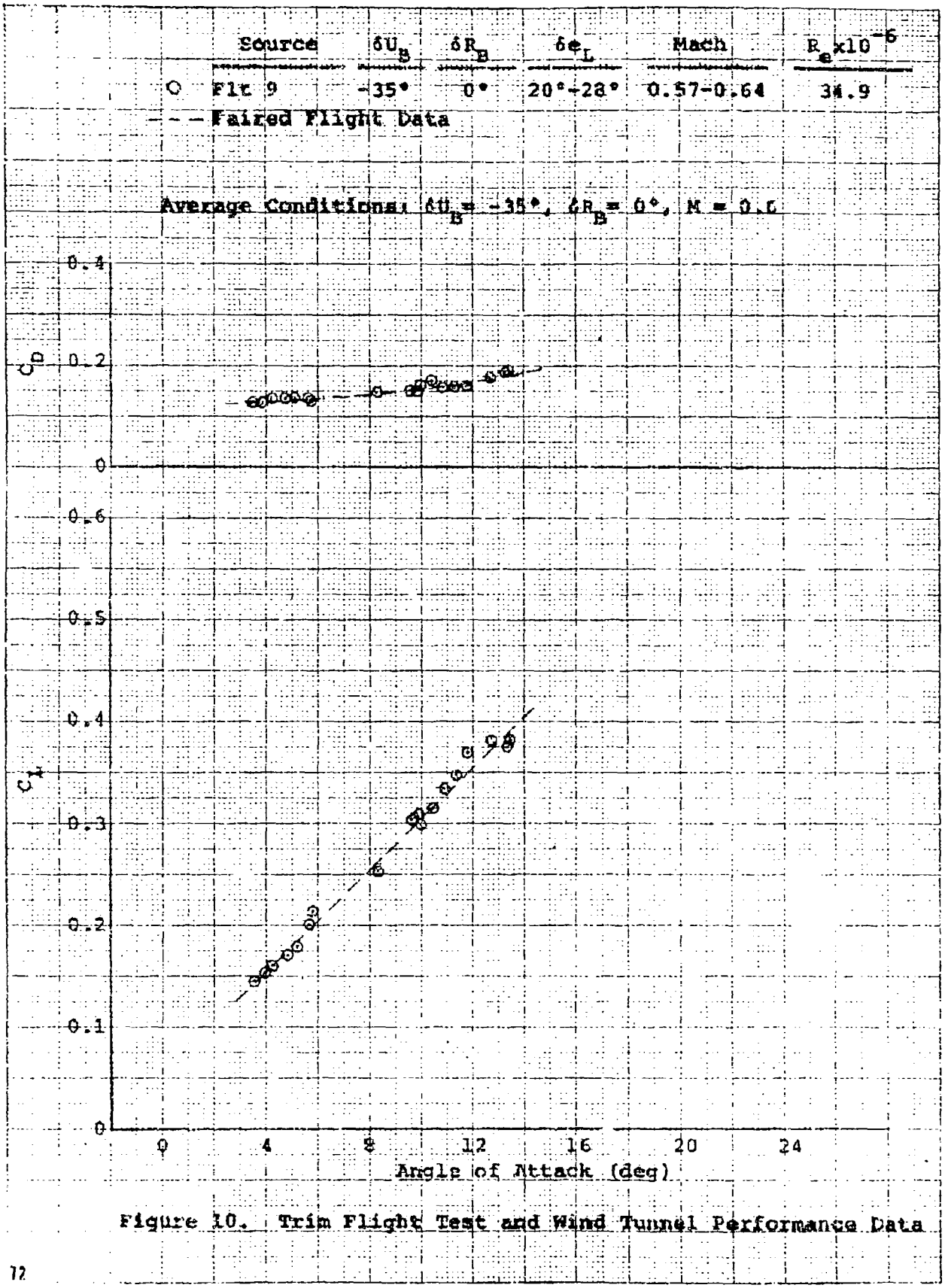

Figure 10. Trim Flight Test and Wind Tunnel Performance Data

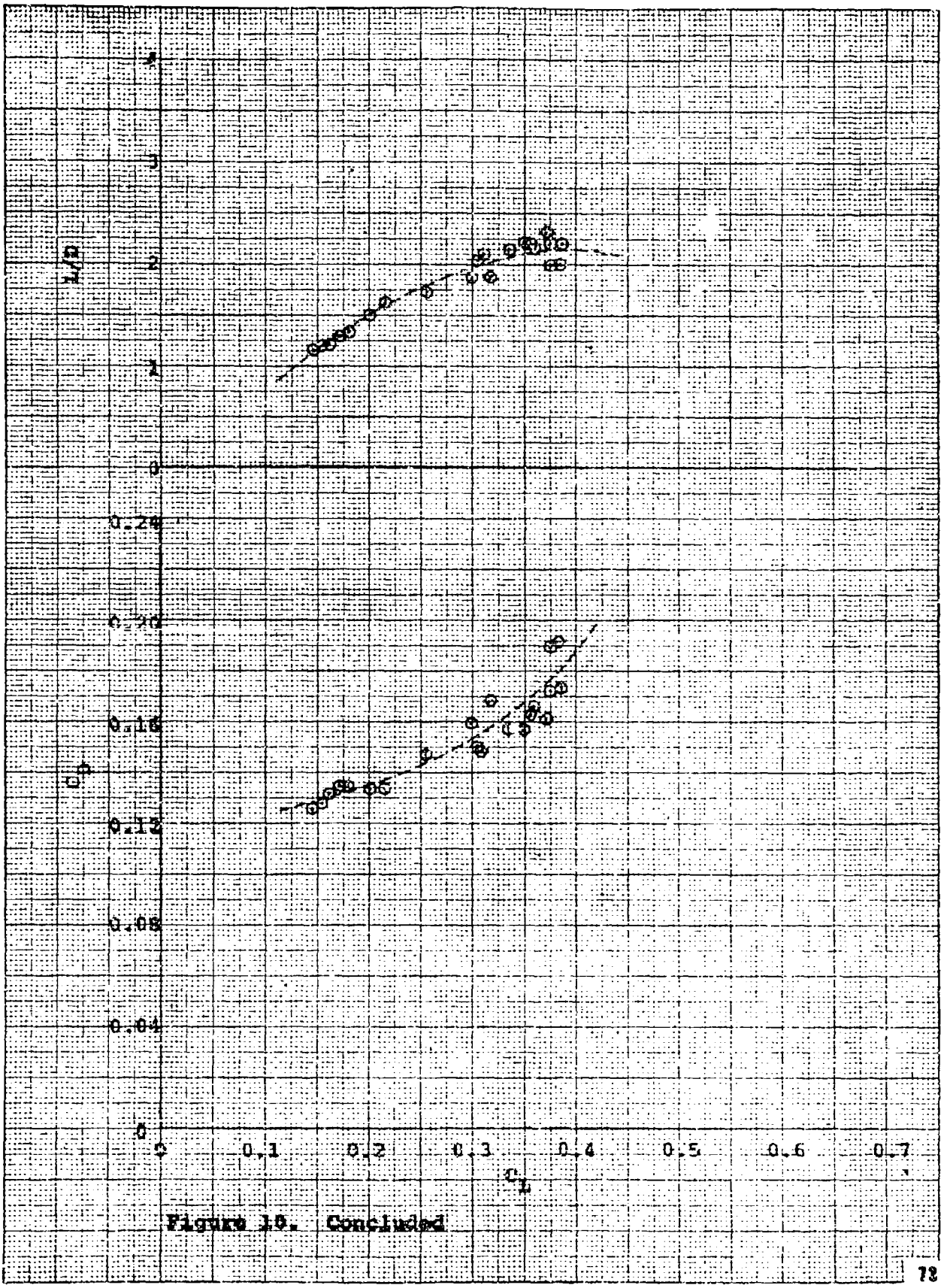

Figure 19. Concluded

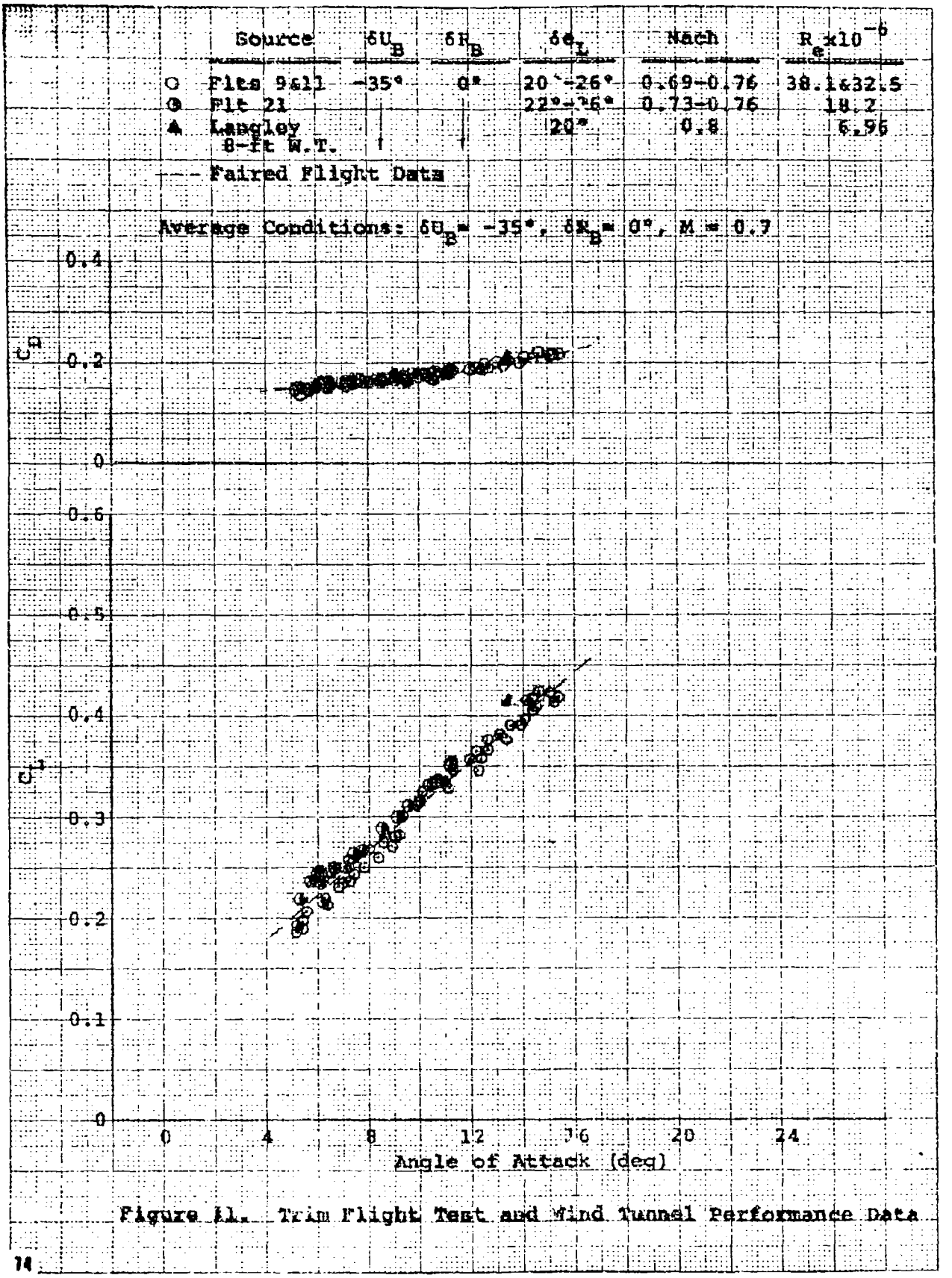

Figure 11. Trim Flight Test and Wind Tunnel Performance Data

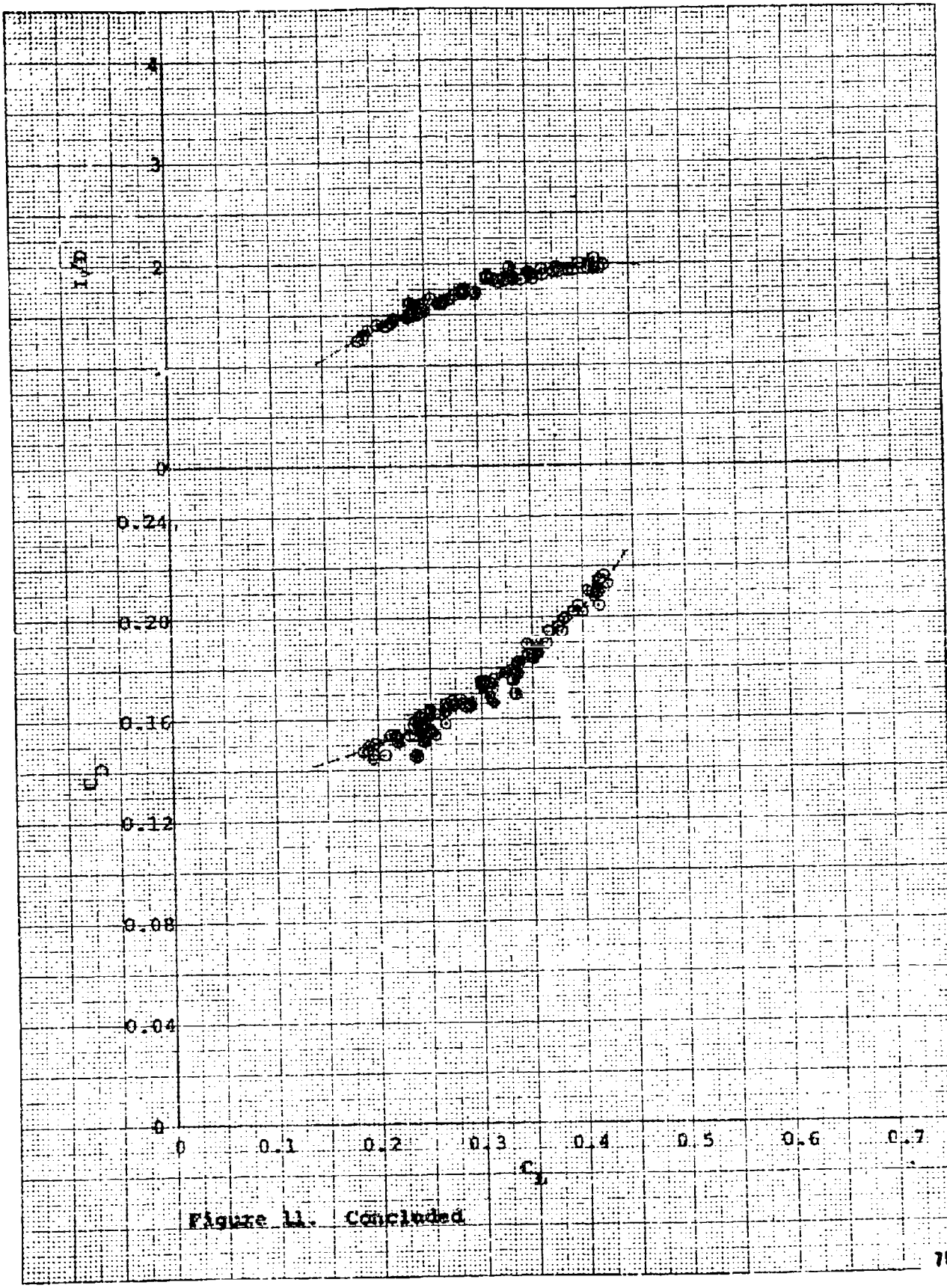

Figure 11. Concluded

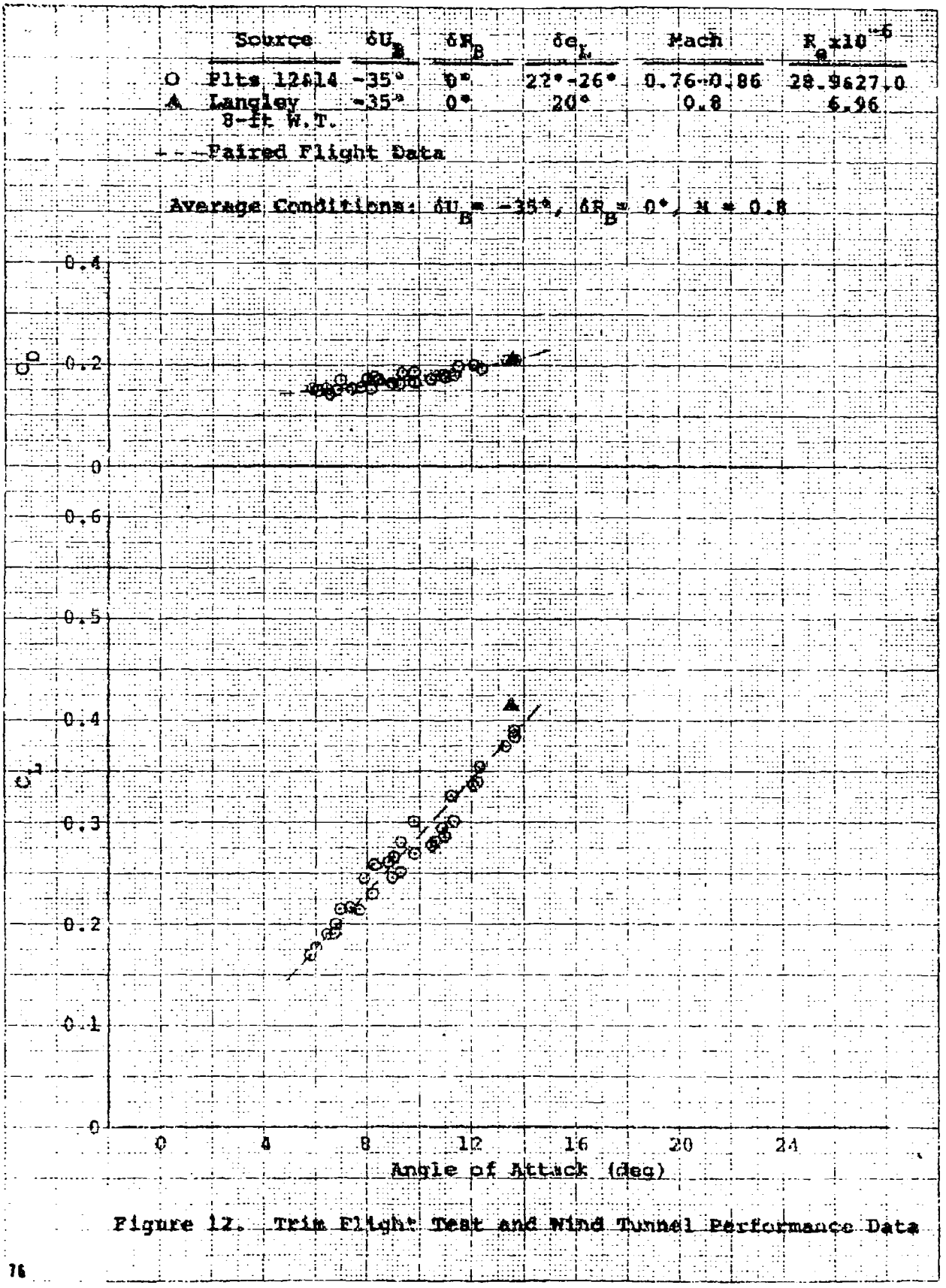

Figure 12. Trim Flight Test and Wind Tunnel Performance Data

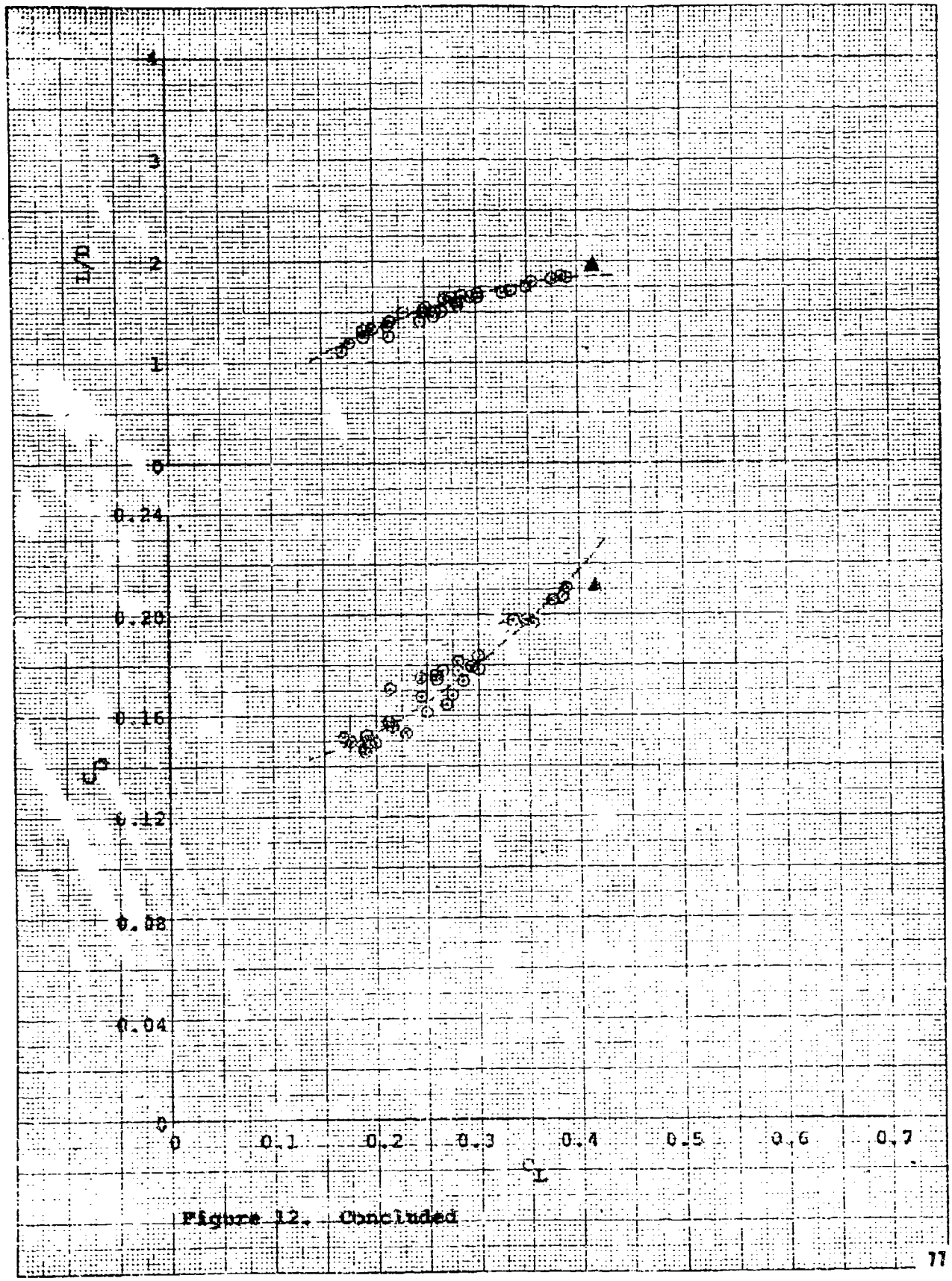

Figure 12. Concluded

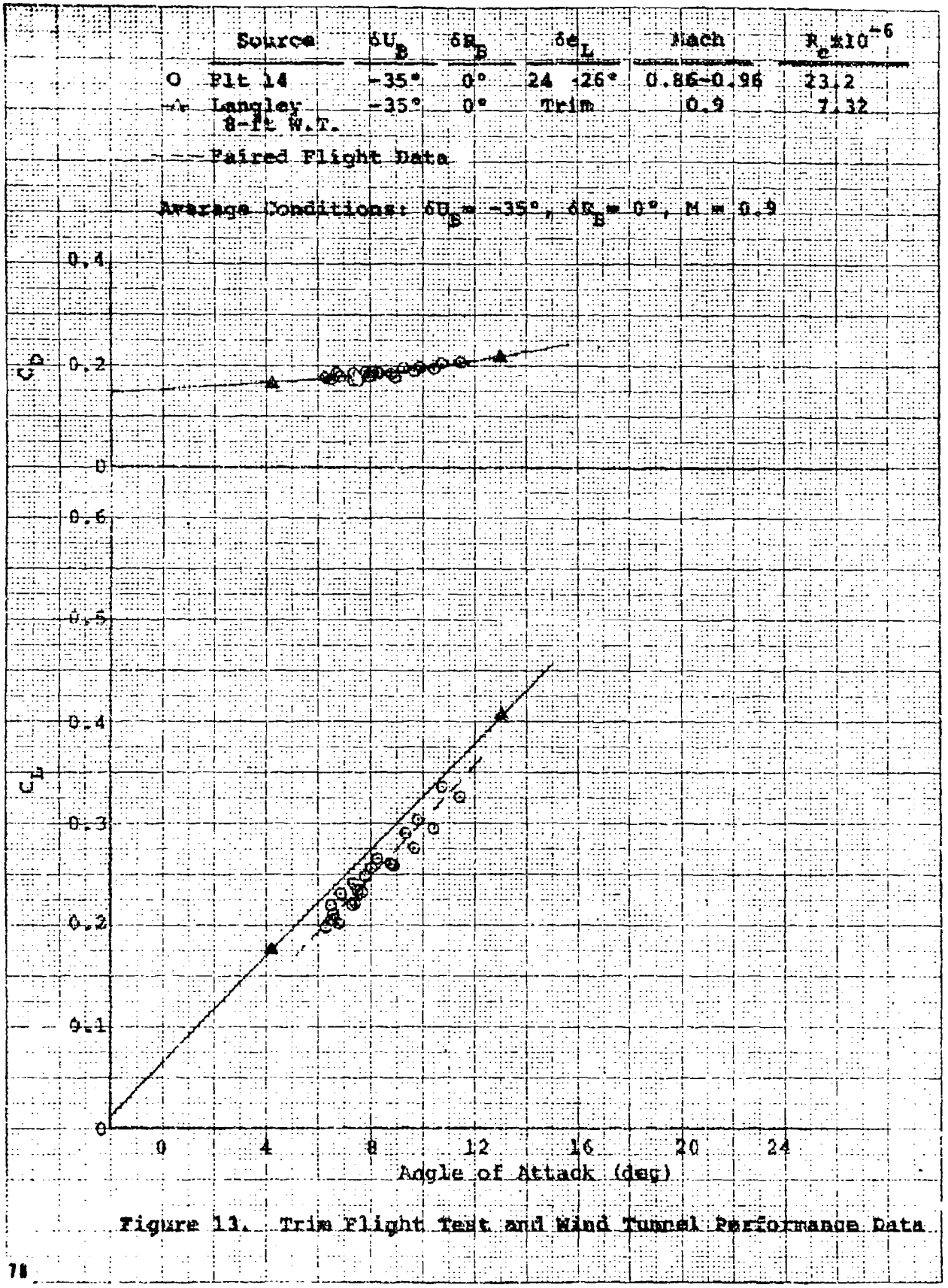

Figure 11. Trim Flight Test and Wind Tunnel Performance Data

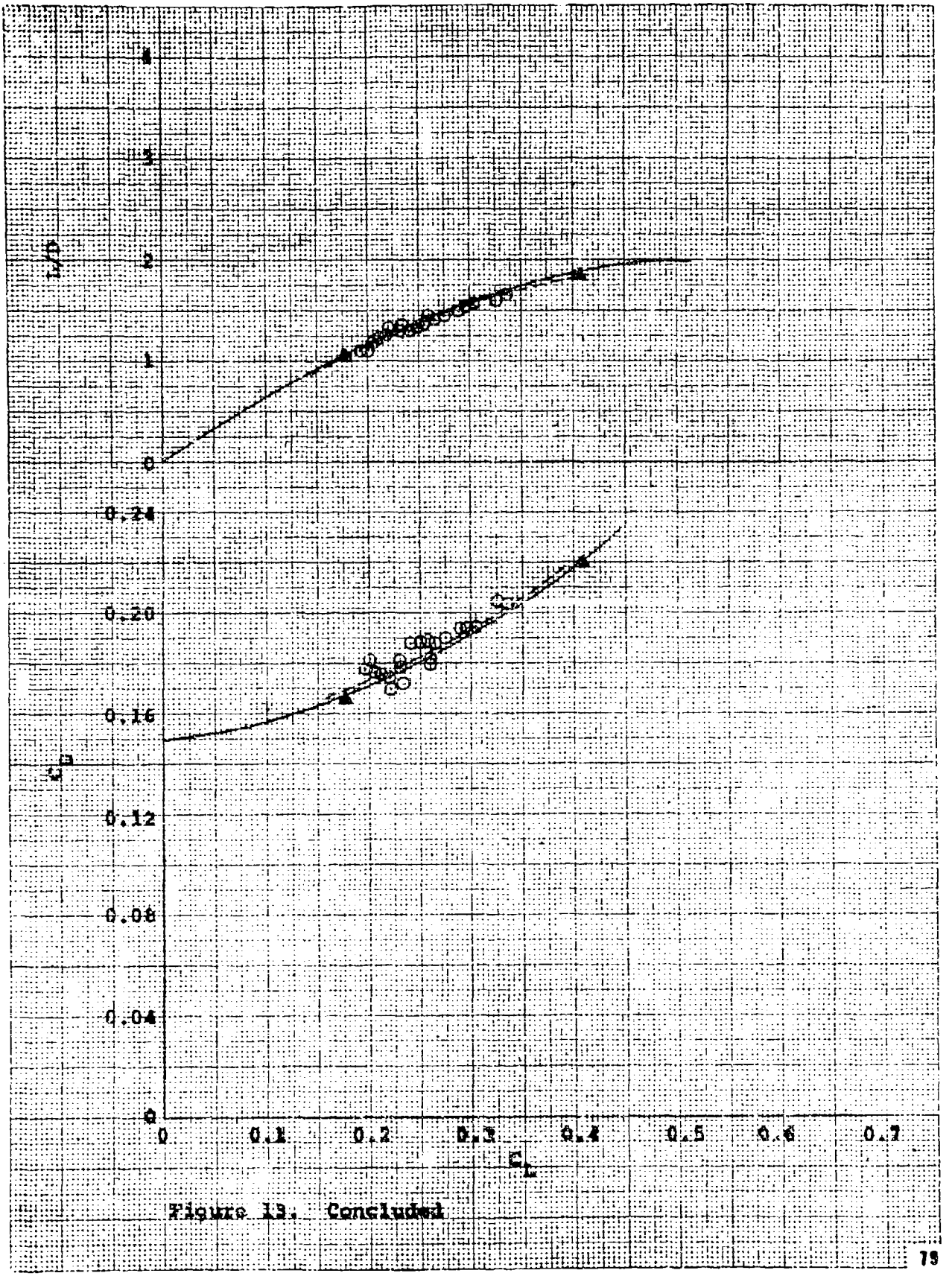

Figure 13. Concluded

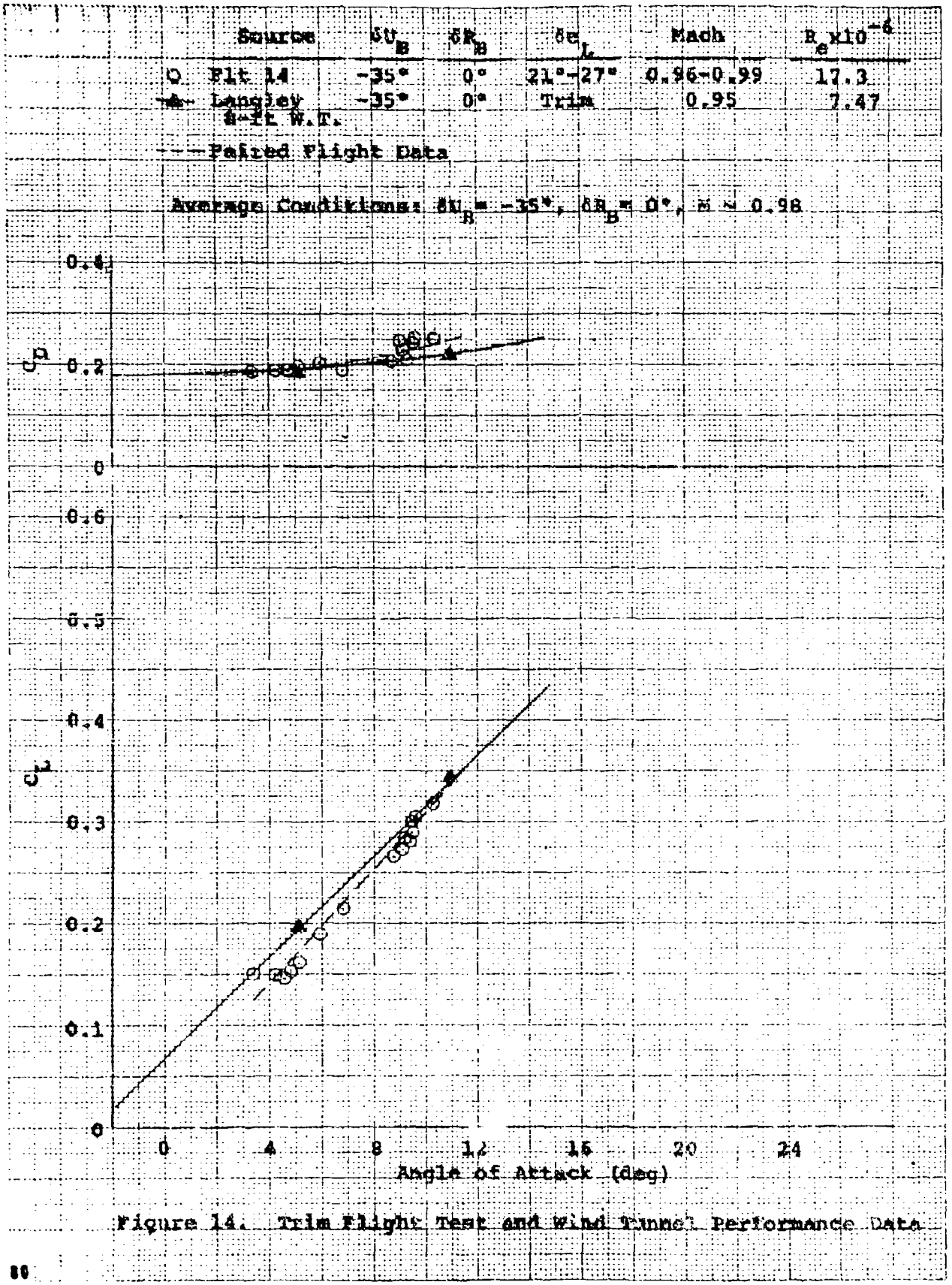

Figure 14. Trim Flight Test and Wind Tunnel Performance Data

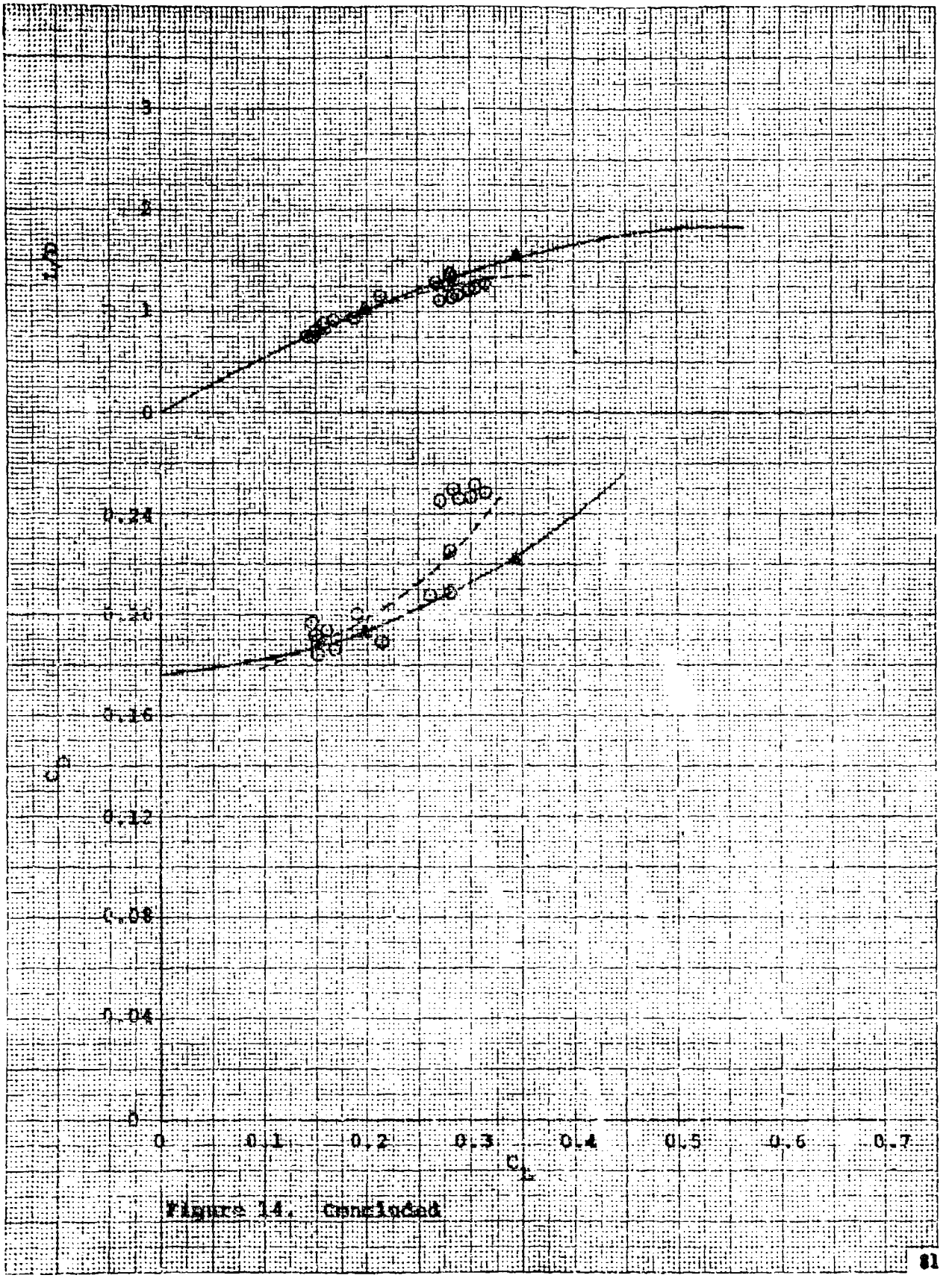

Figure 14. Concluded

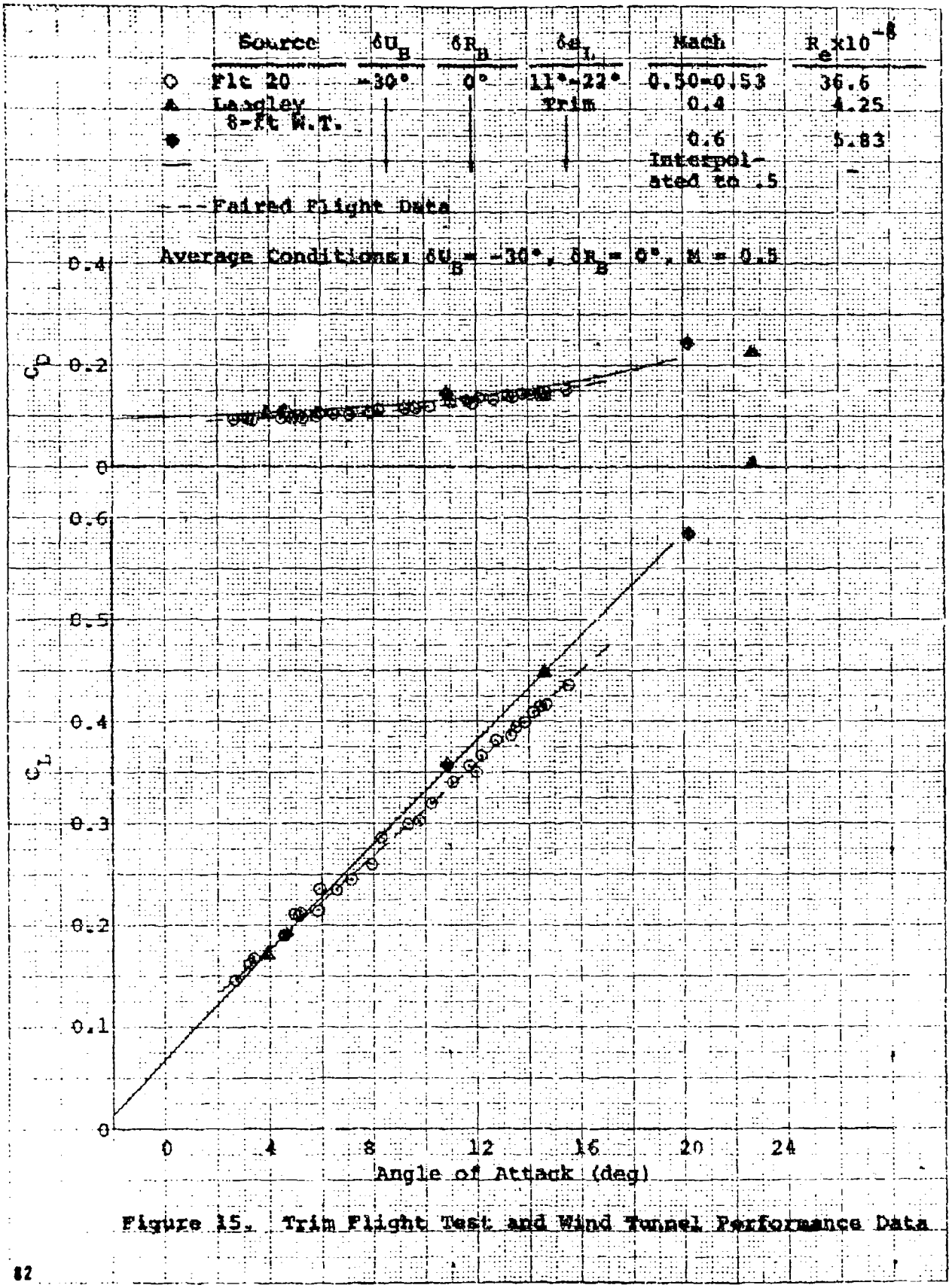

Figure 15. Trim Flight Test and Wind Tunnel Performance Data

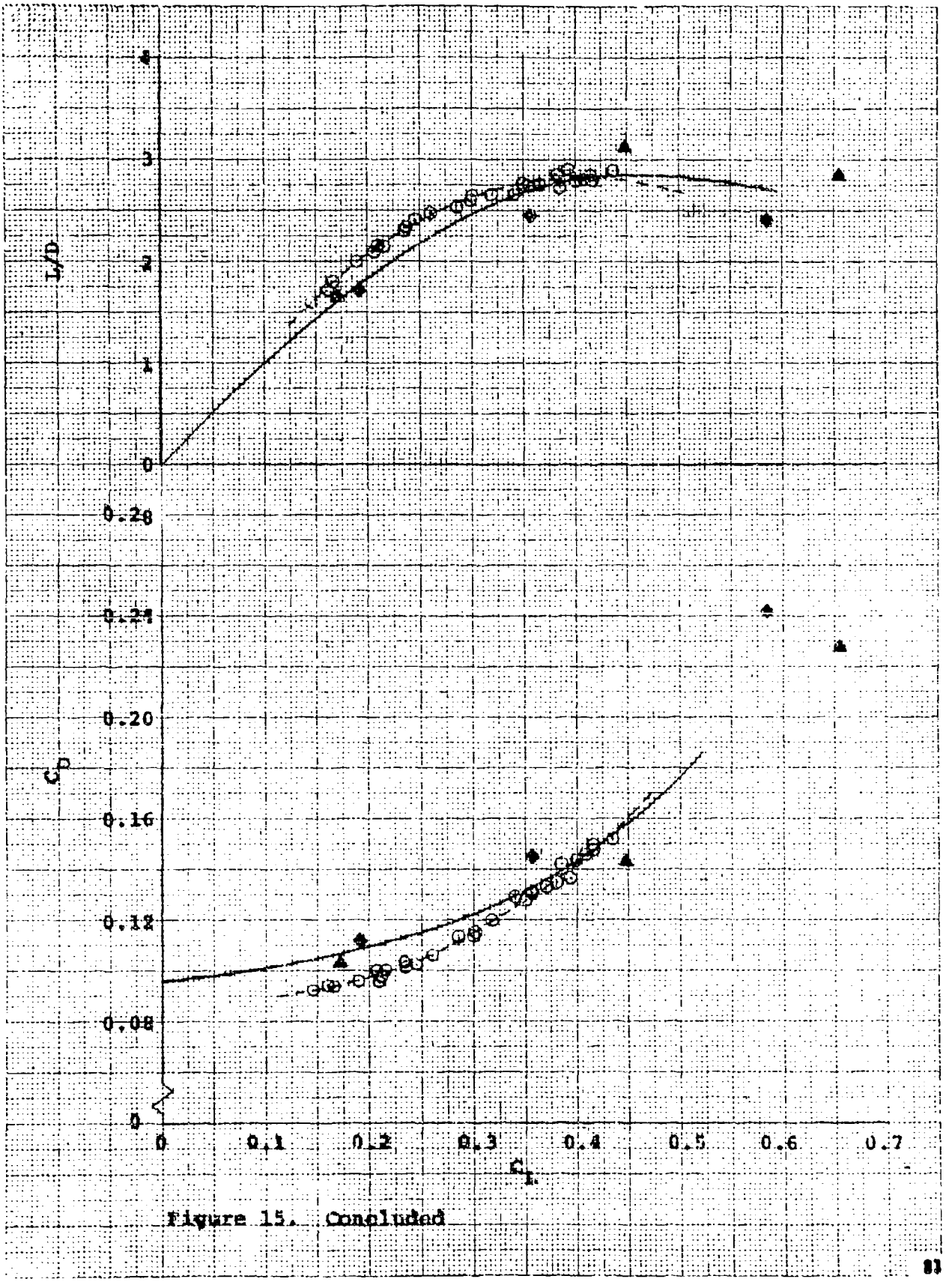

Figure 15. Concluded

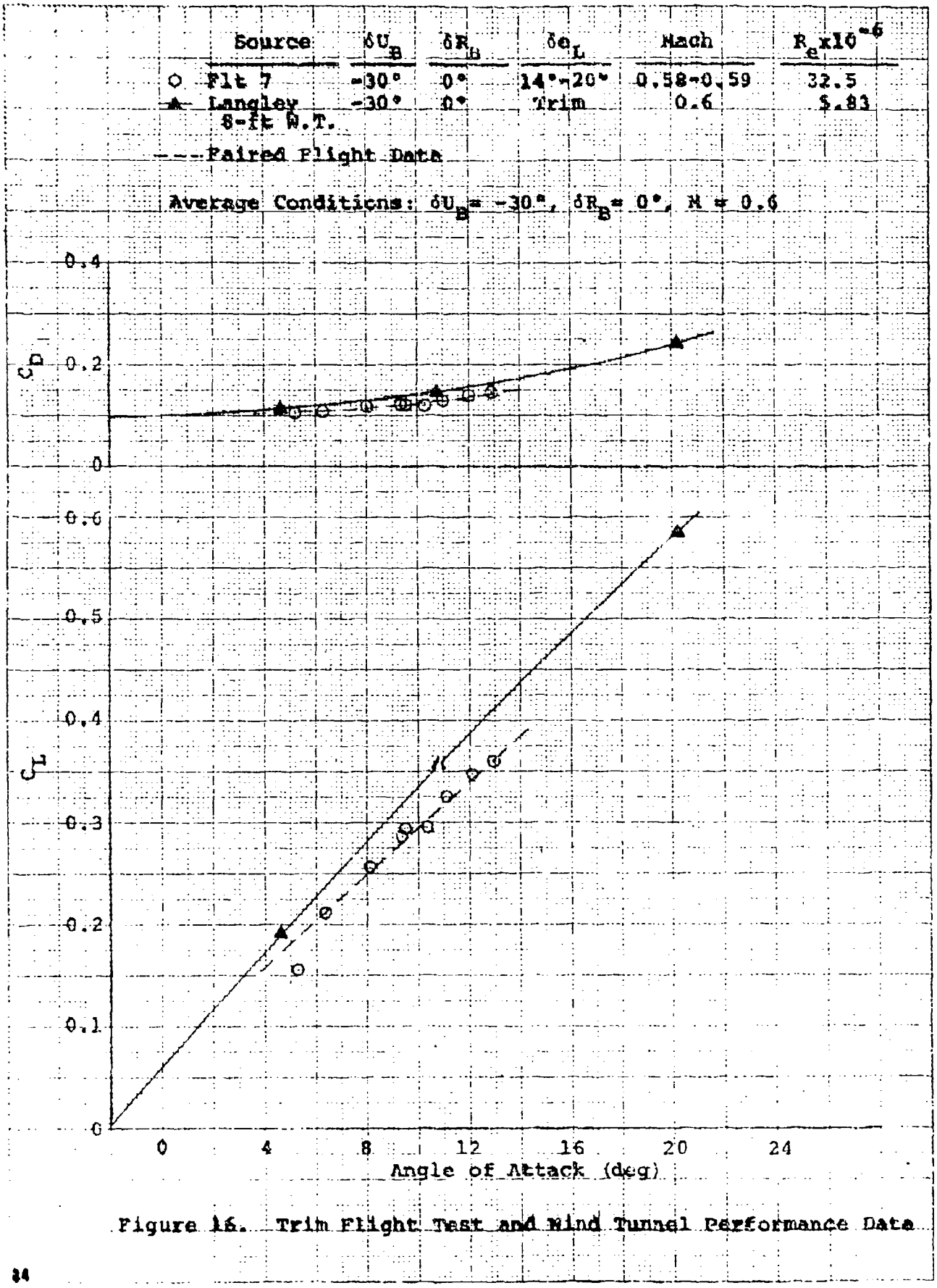

Figure 16. Trim Flight Test and Wind Tunnel Performance Data

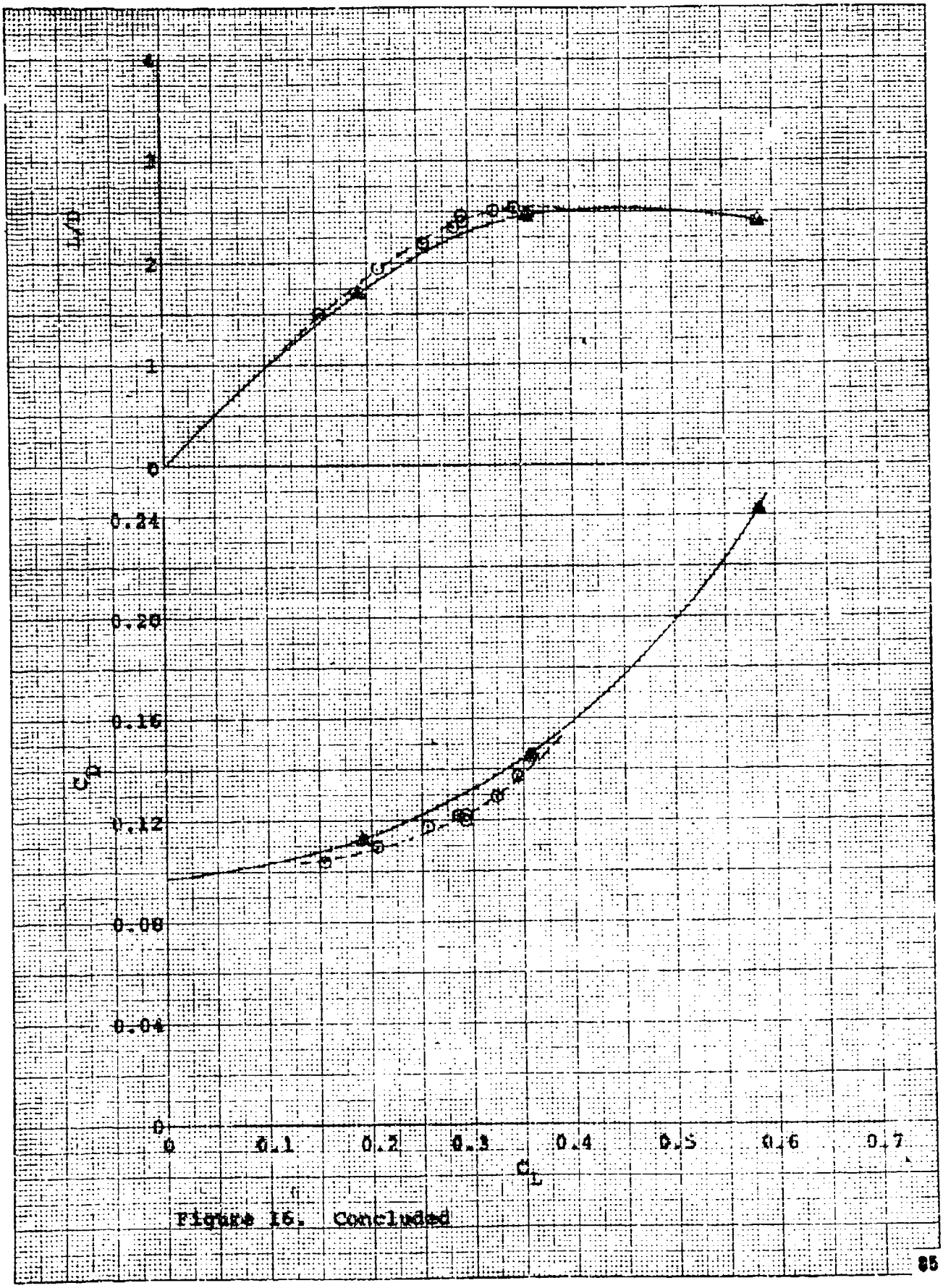

Figure 16. Concluded

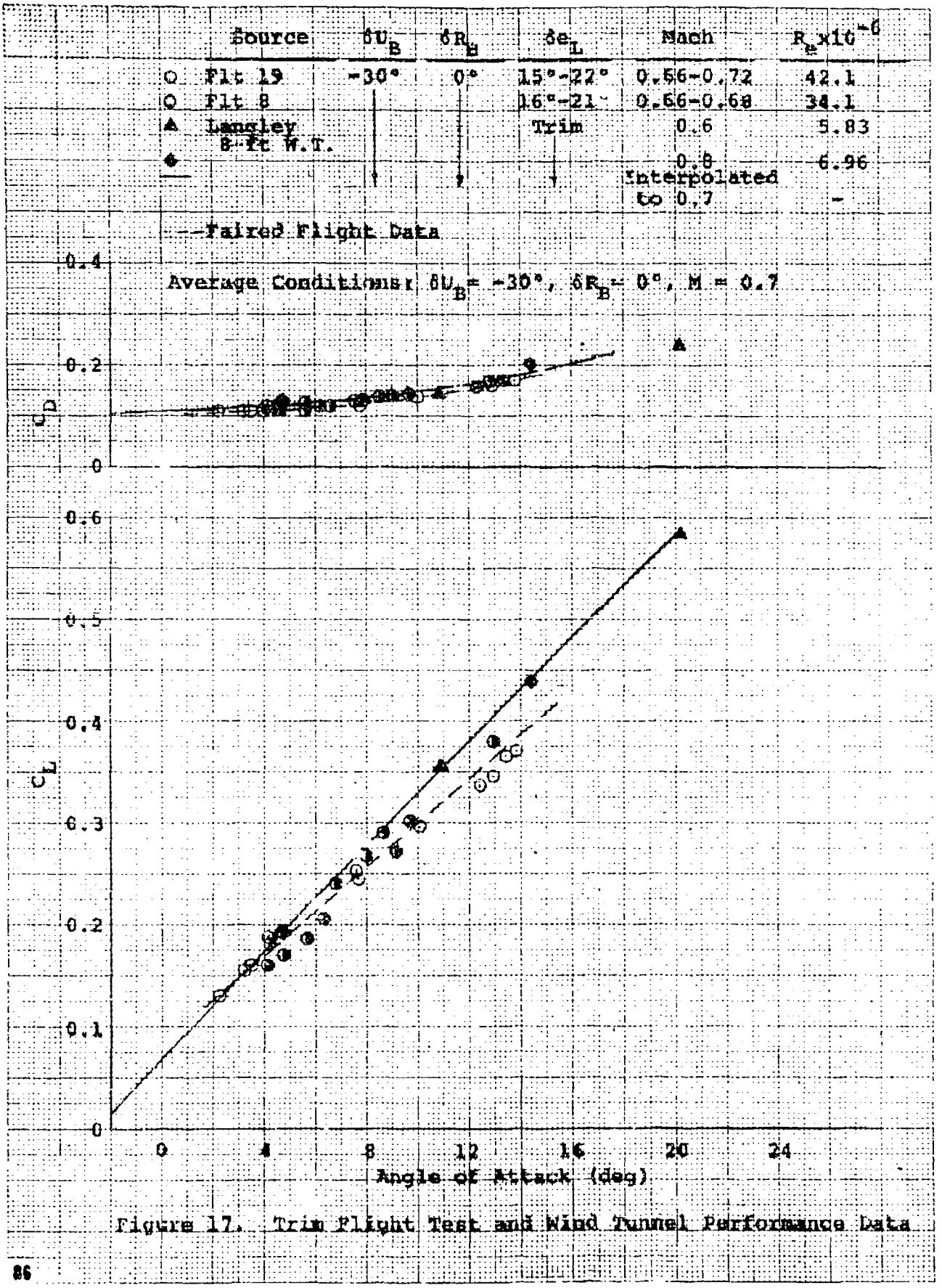

Figure 17. Trim Flight Test and Wind Tunnel Performance Data

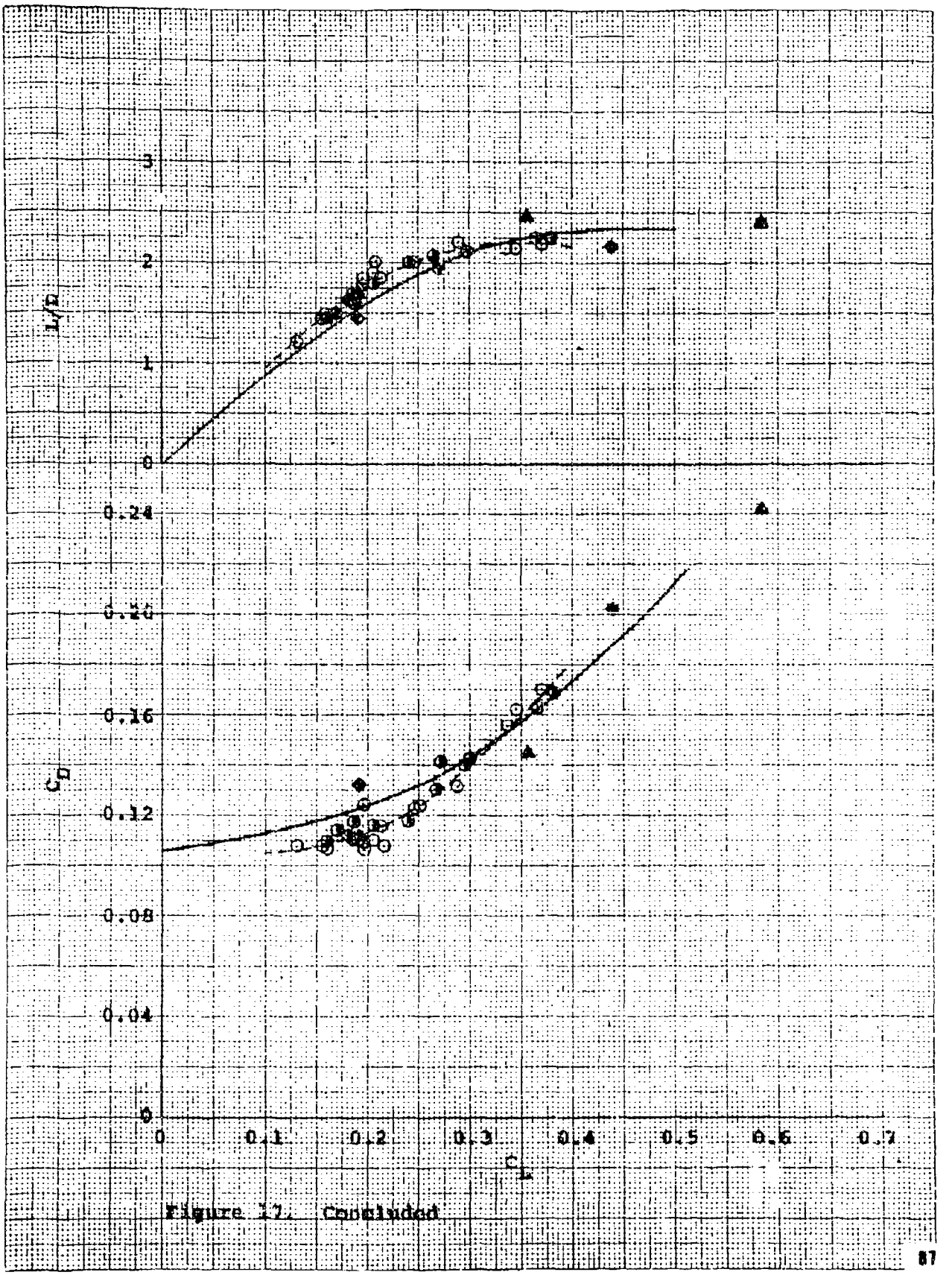

Figure 17. Concluded

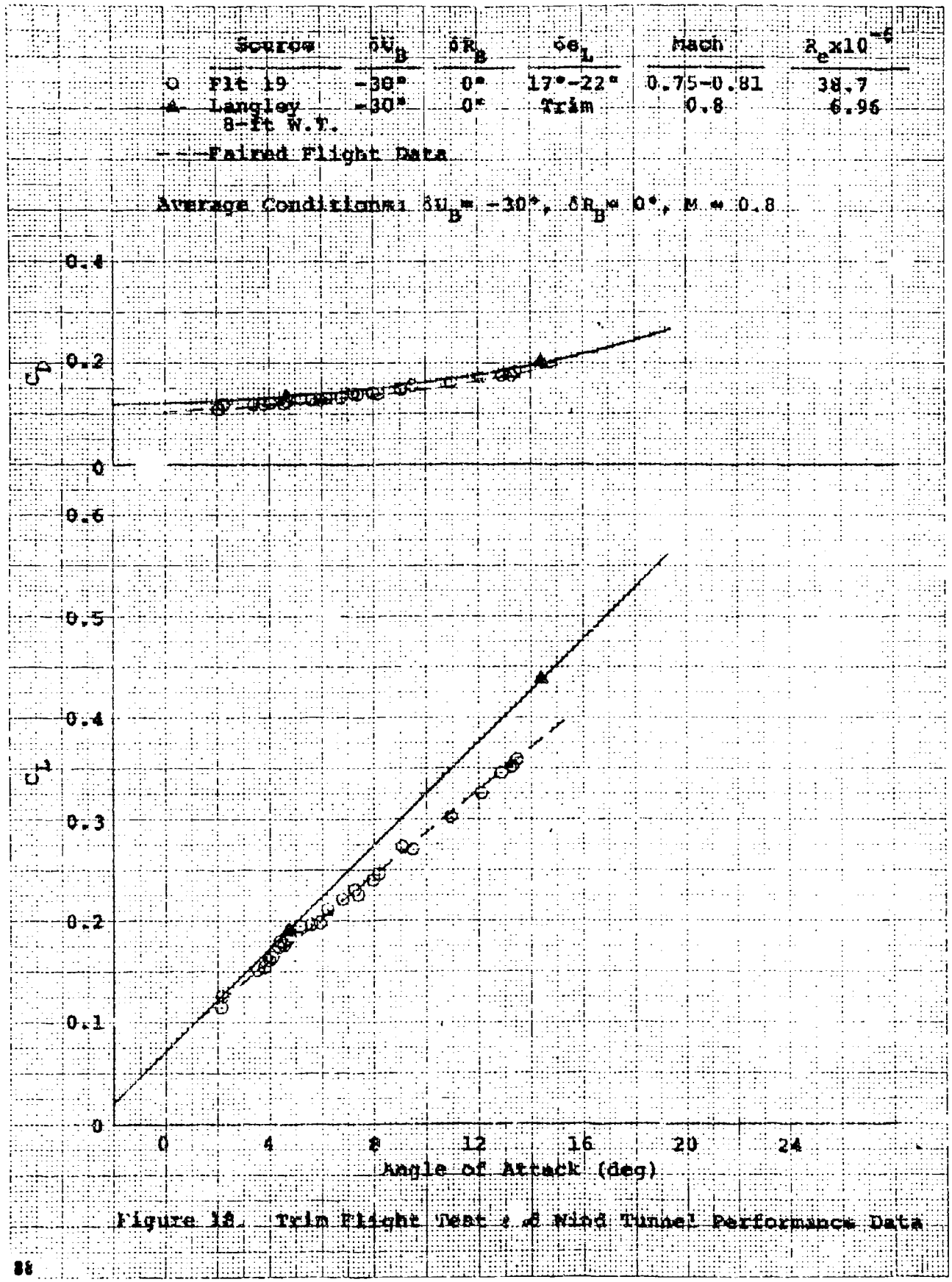

Figure 18. Trim Flight Test and Wind Tunnel Performance Data

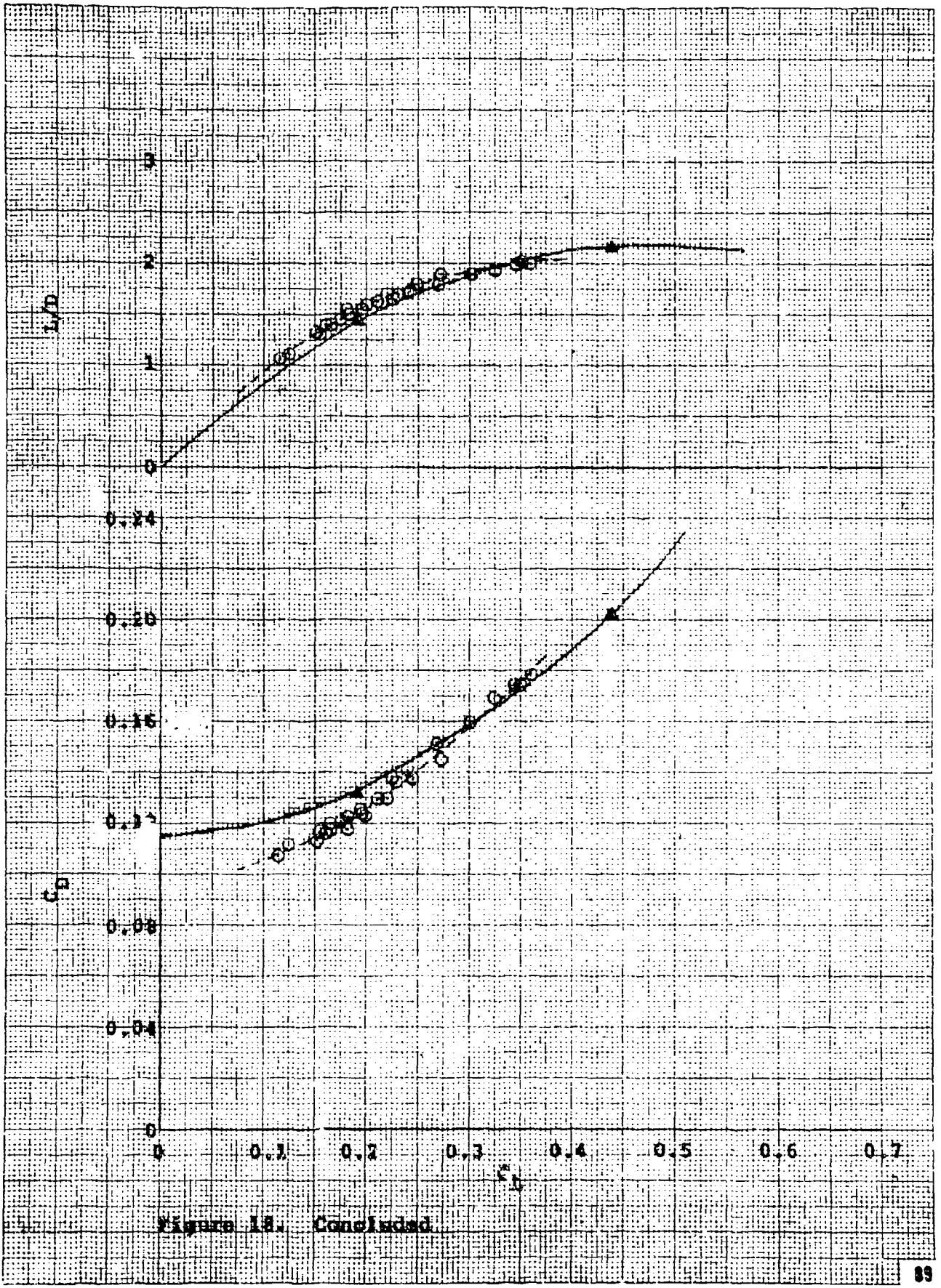

Figure 18. Concluded.

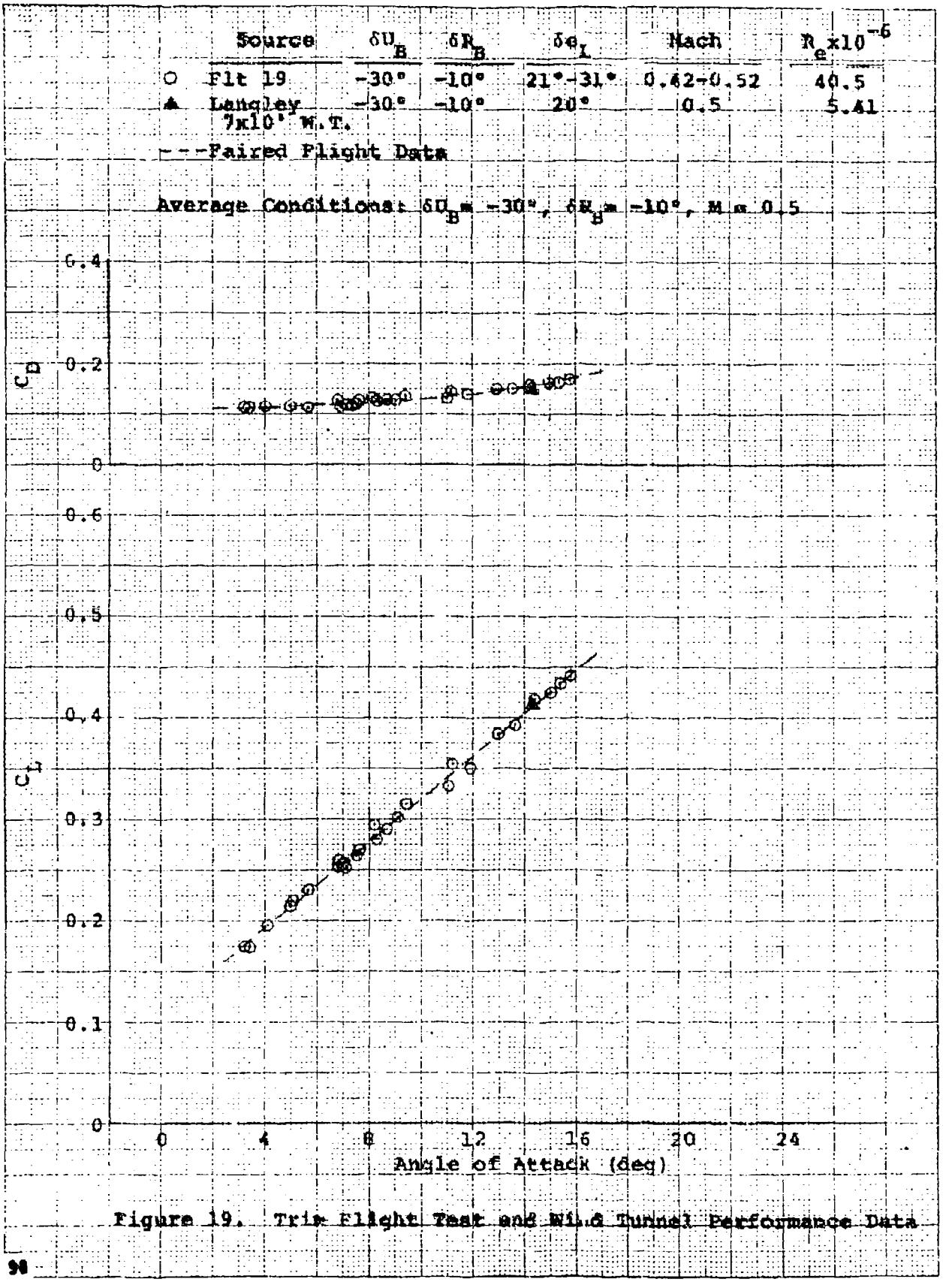

Figure 19. Trim Flight Test and Wind Tunnel Performance Data

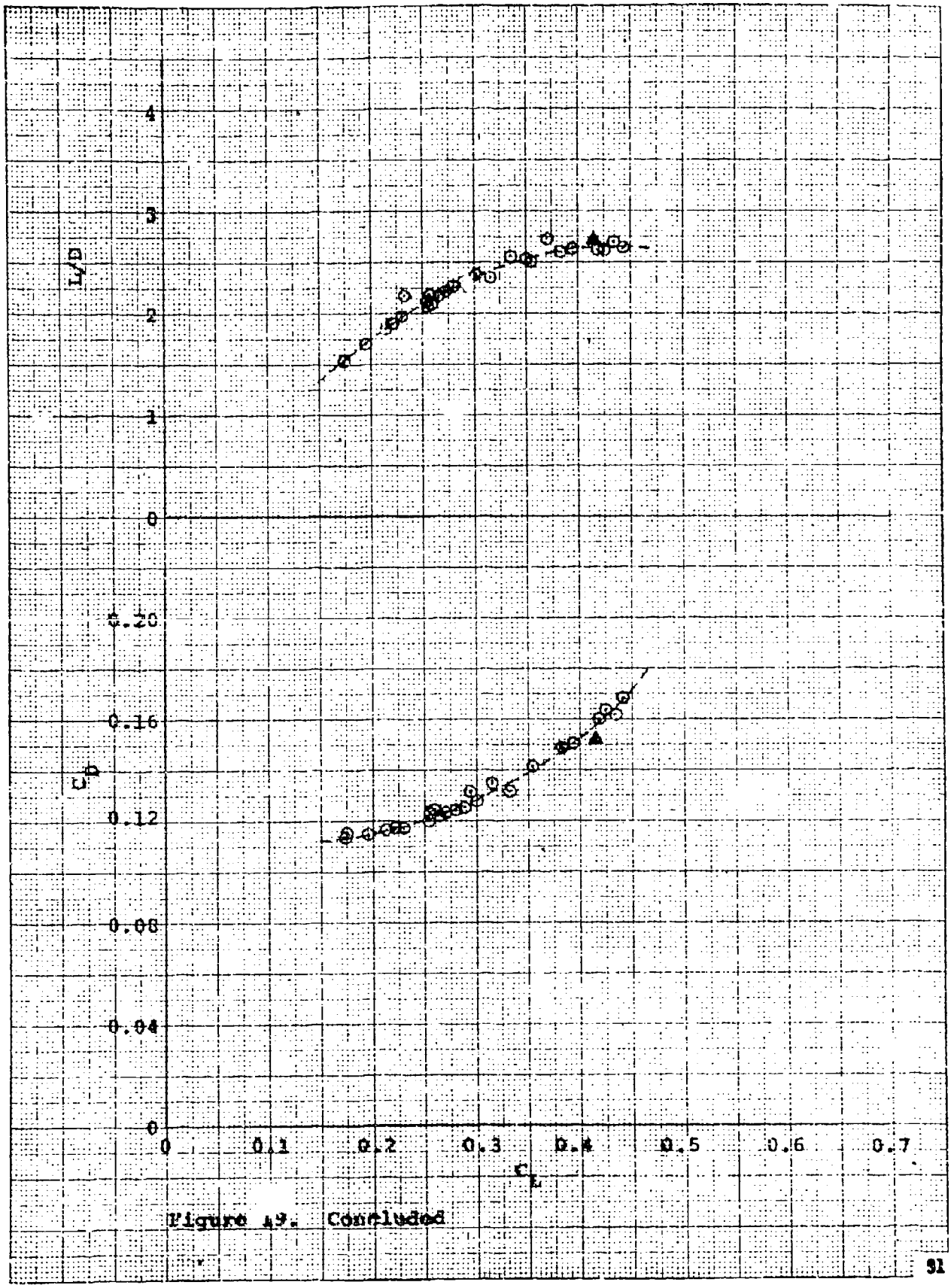

Figure 49. Concluded

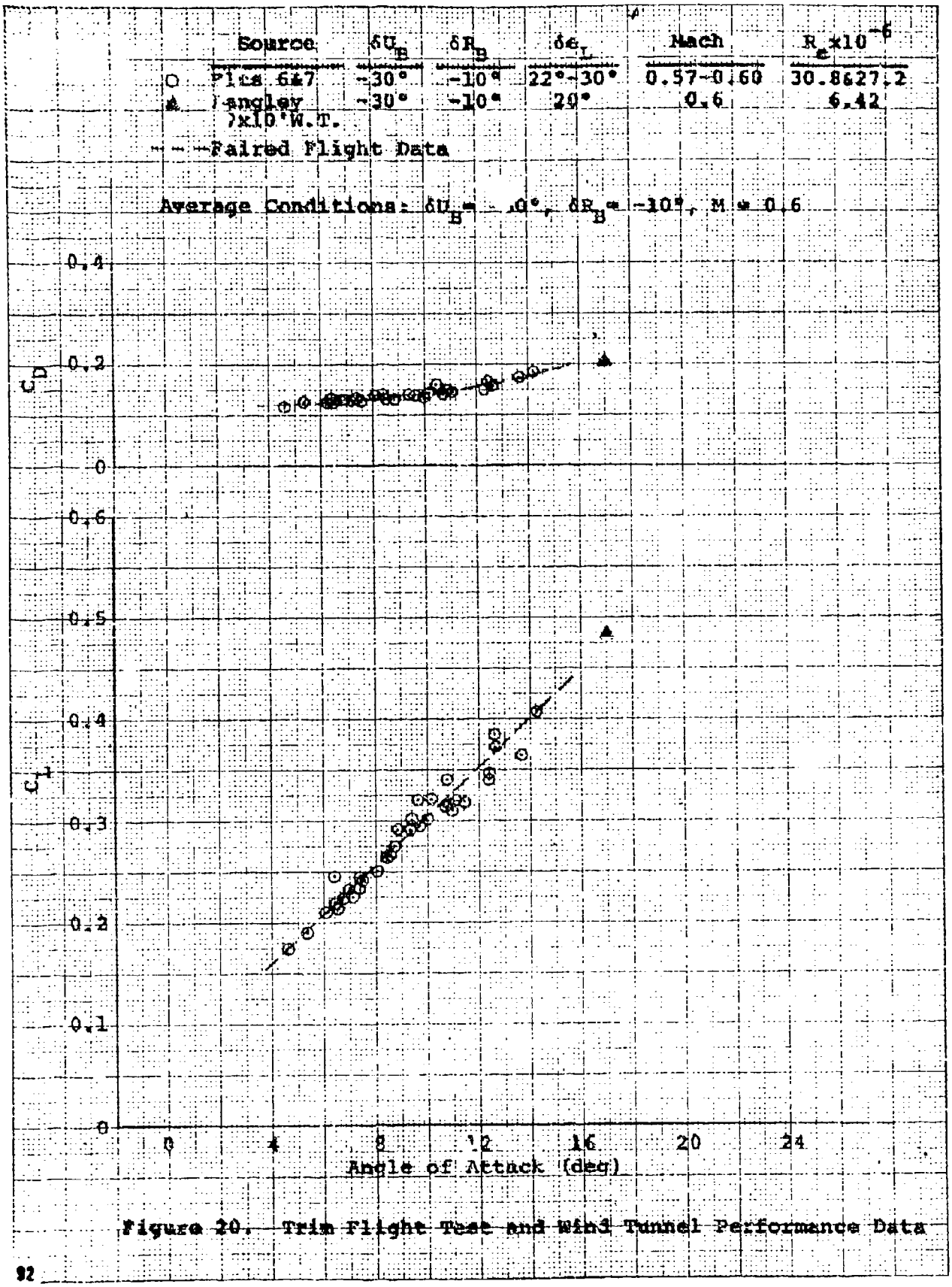

Figure 20. Trim Flight Test and Wind Tunnel Performance Data

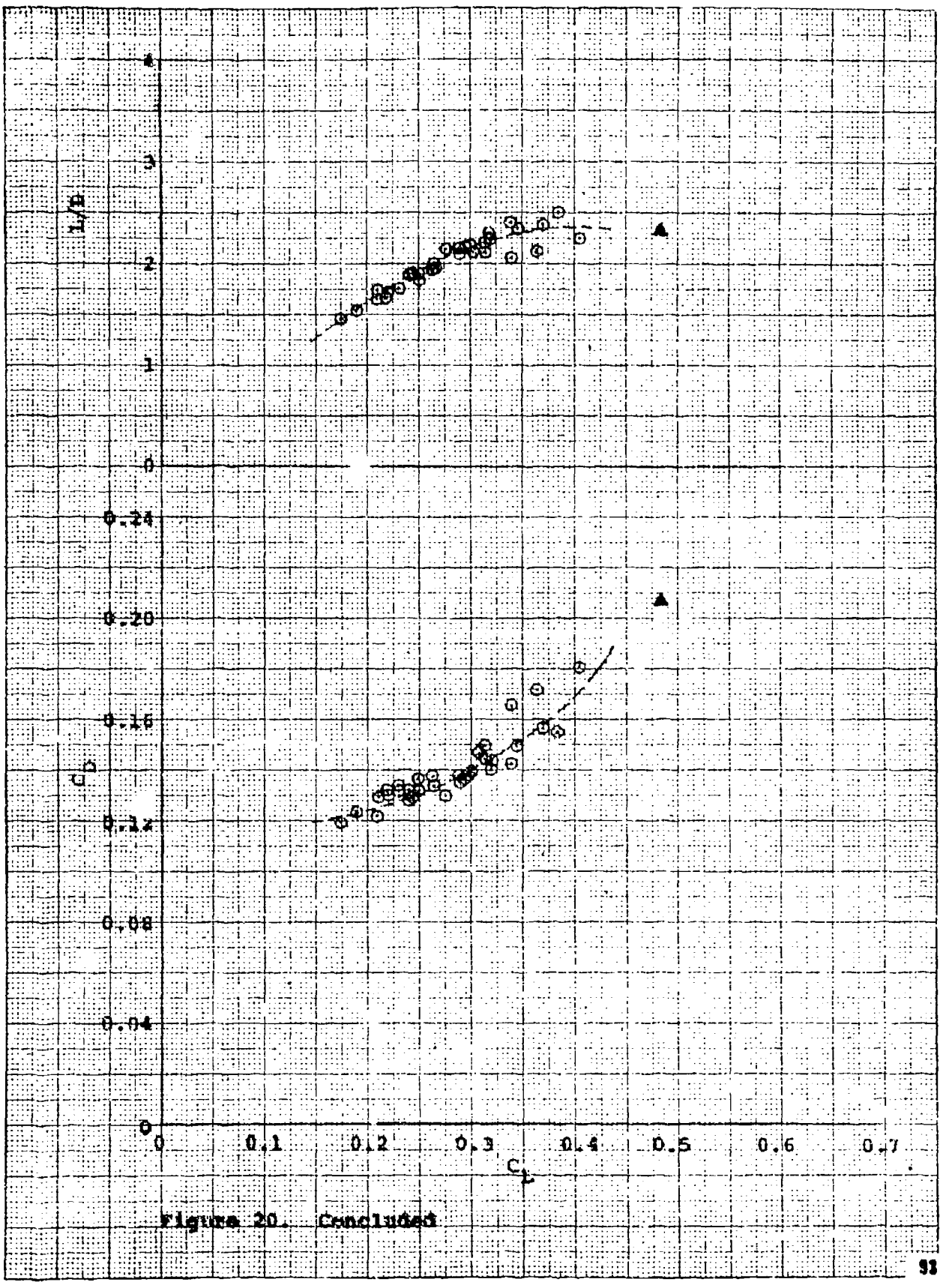

Figure 20. Concluded

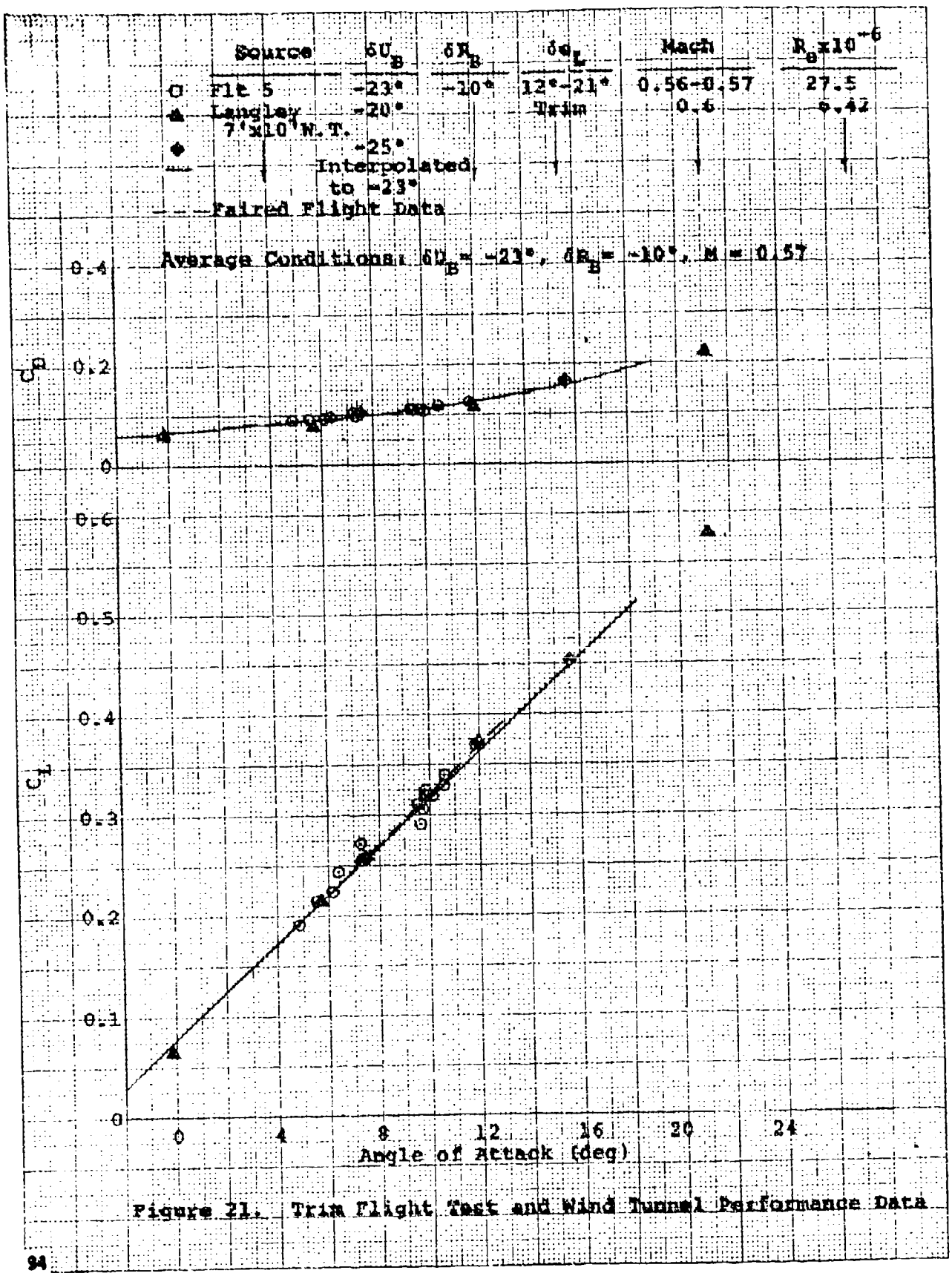

Figure 21. Trim Flight Test and Wind Tunnel Performance Data

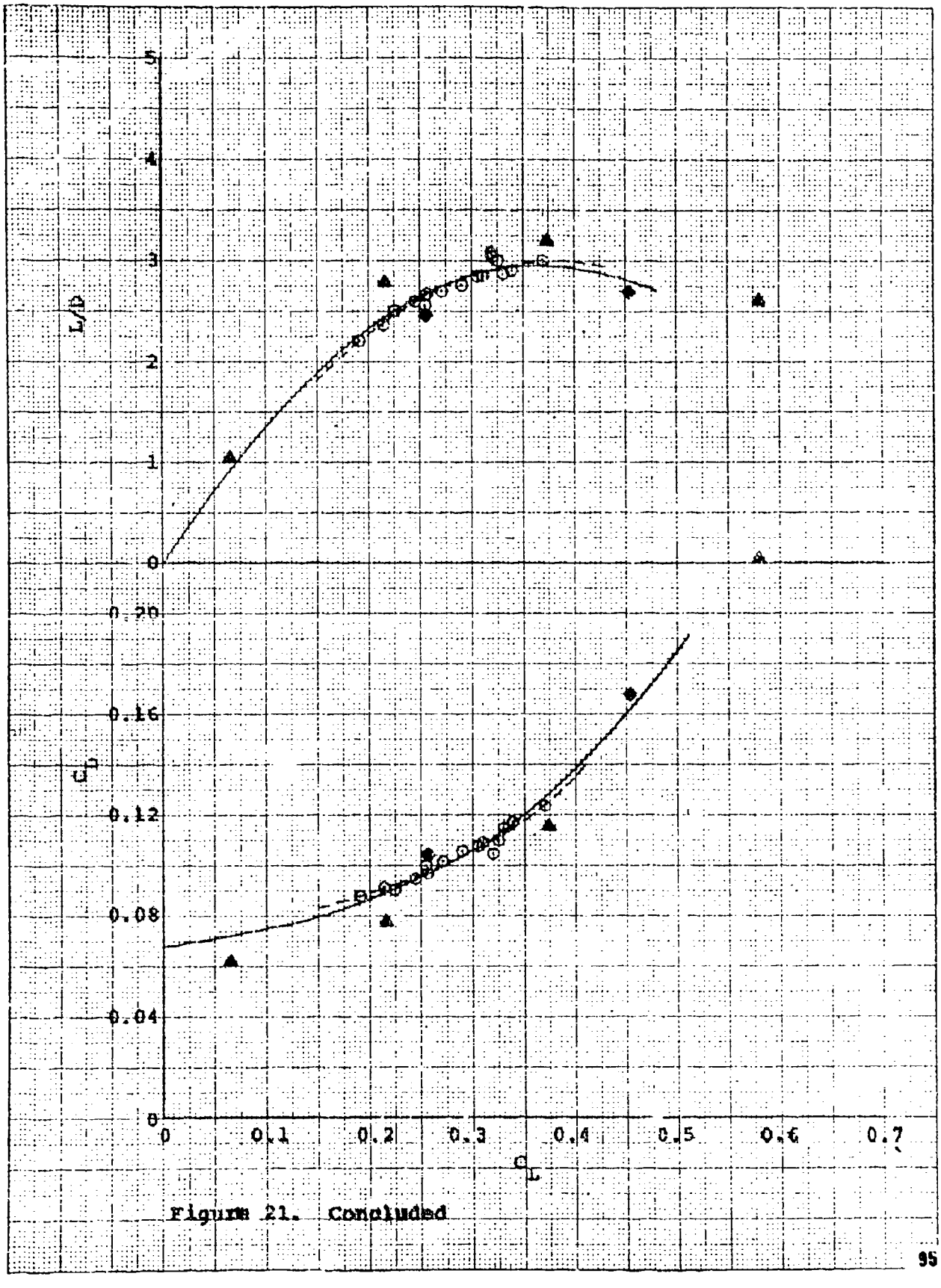

Figure 21. Concluded

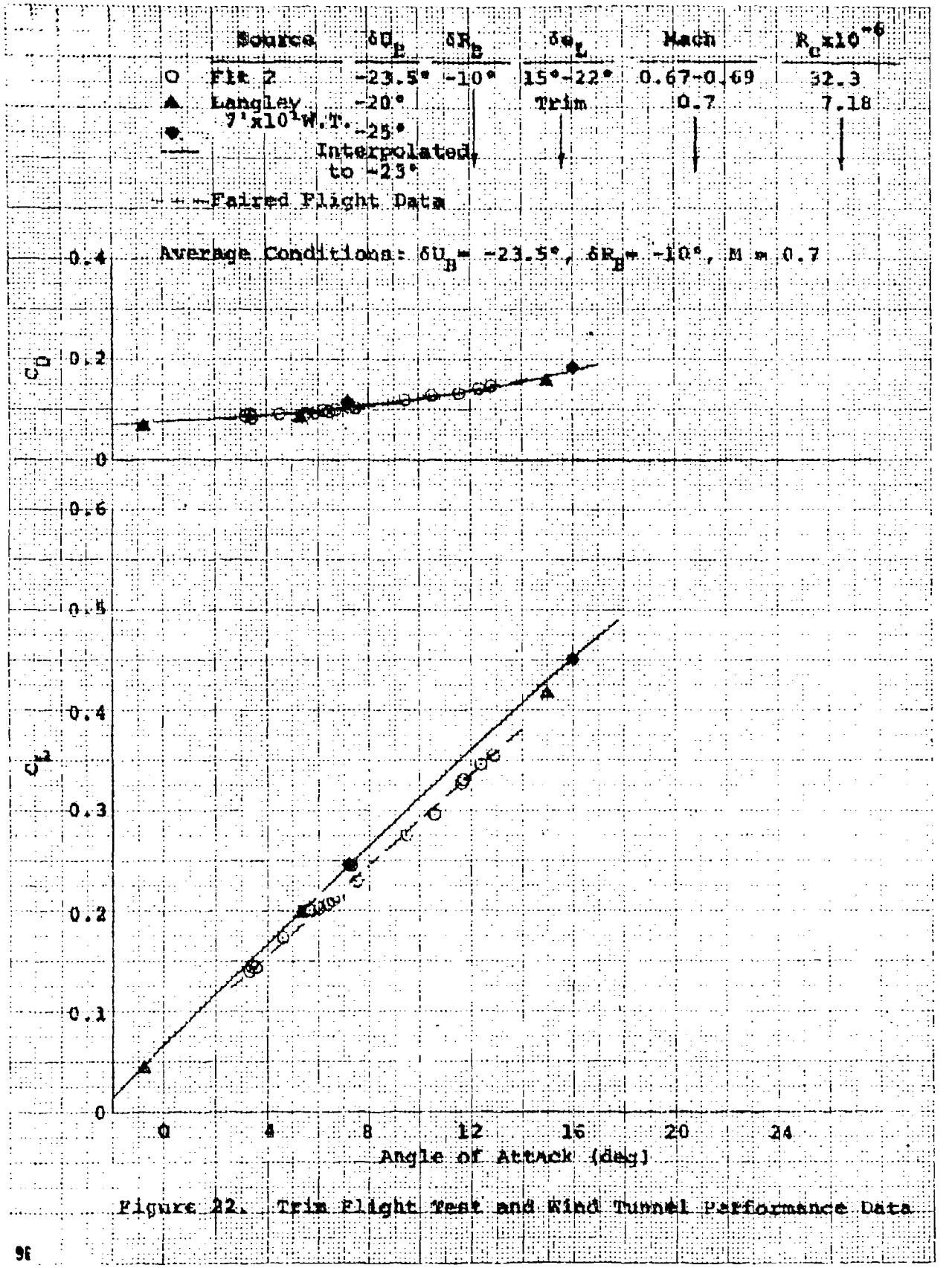

Figure 22. Trim Flight Test and Wind Tunnel Performance Data

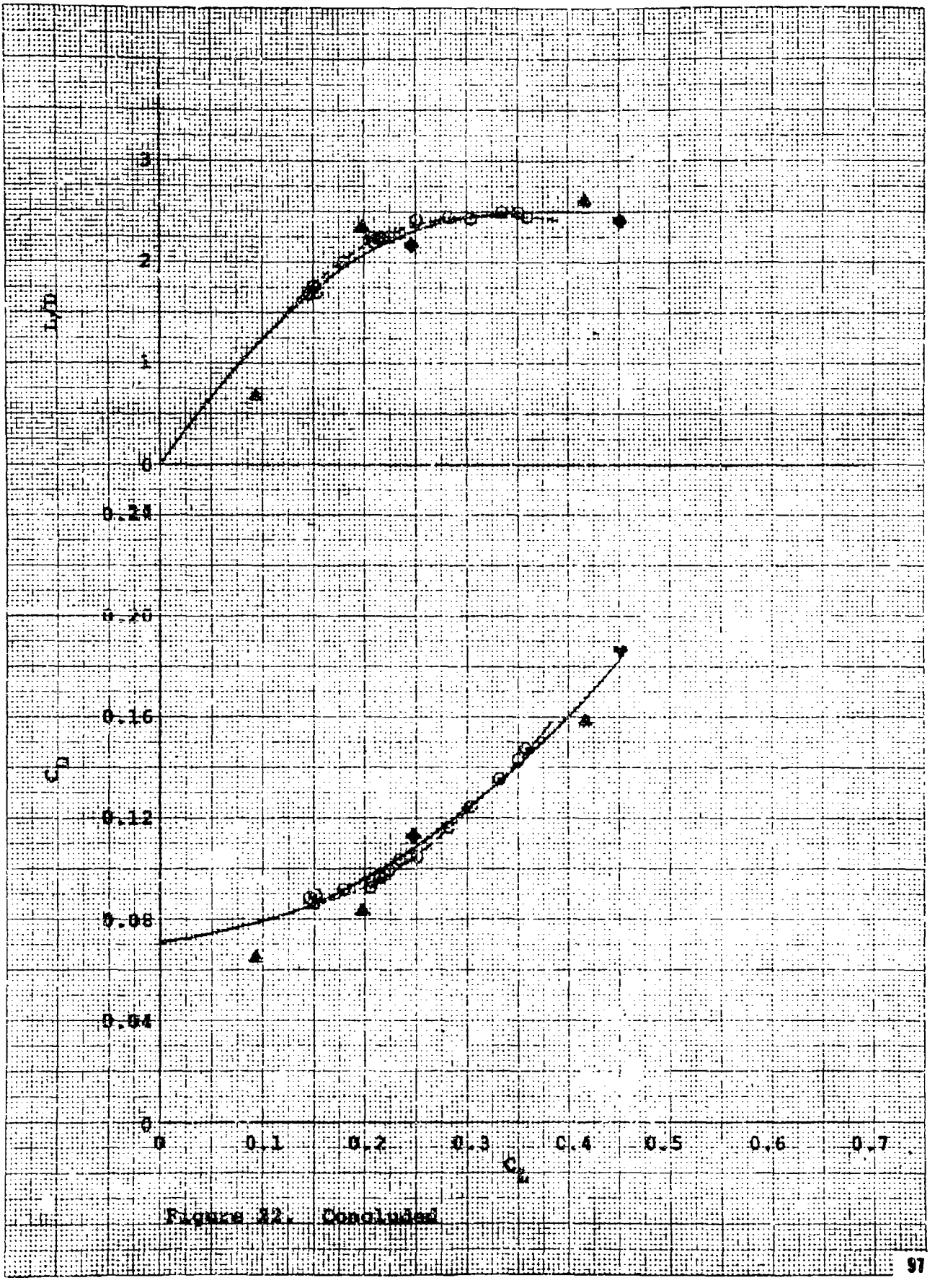

Figure 22. Concluded

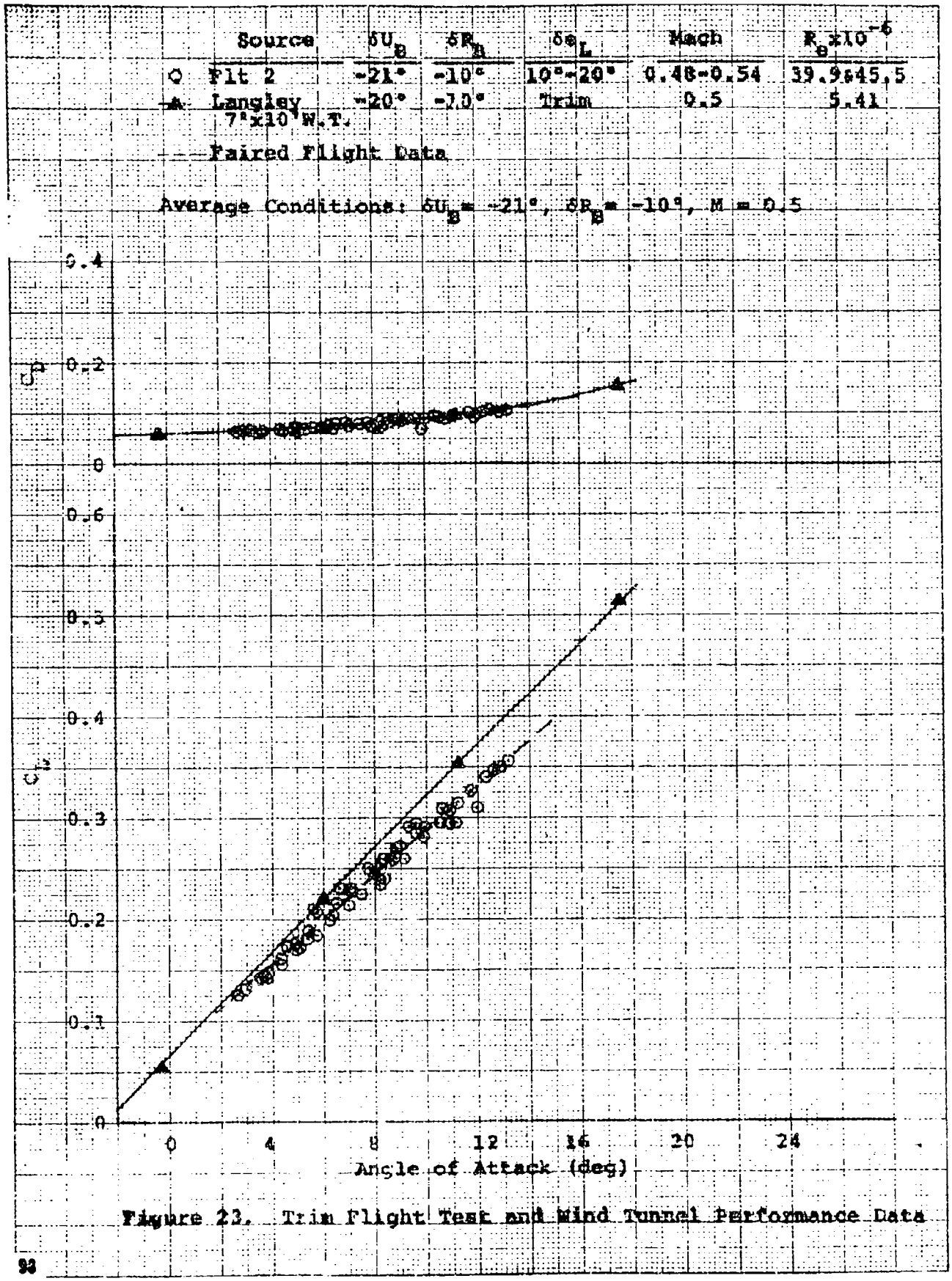

Figure 23. Trim Flight Test and Wind Tunnel Performance Data

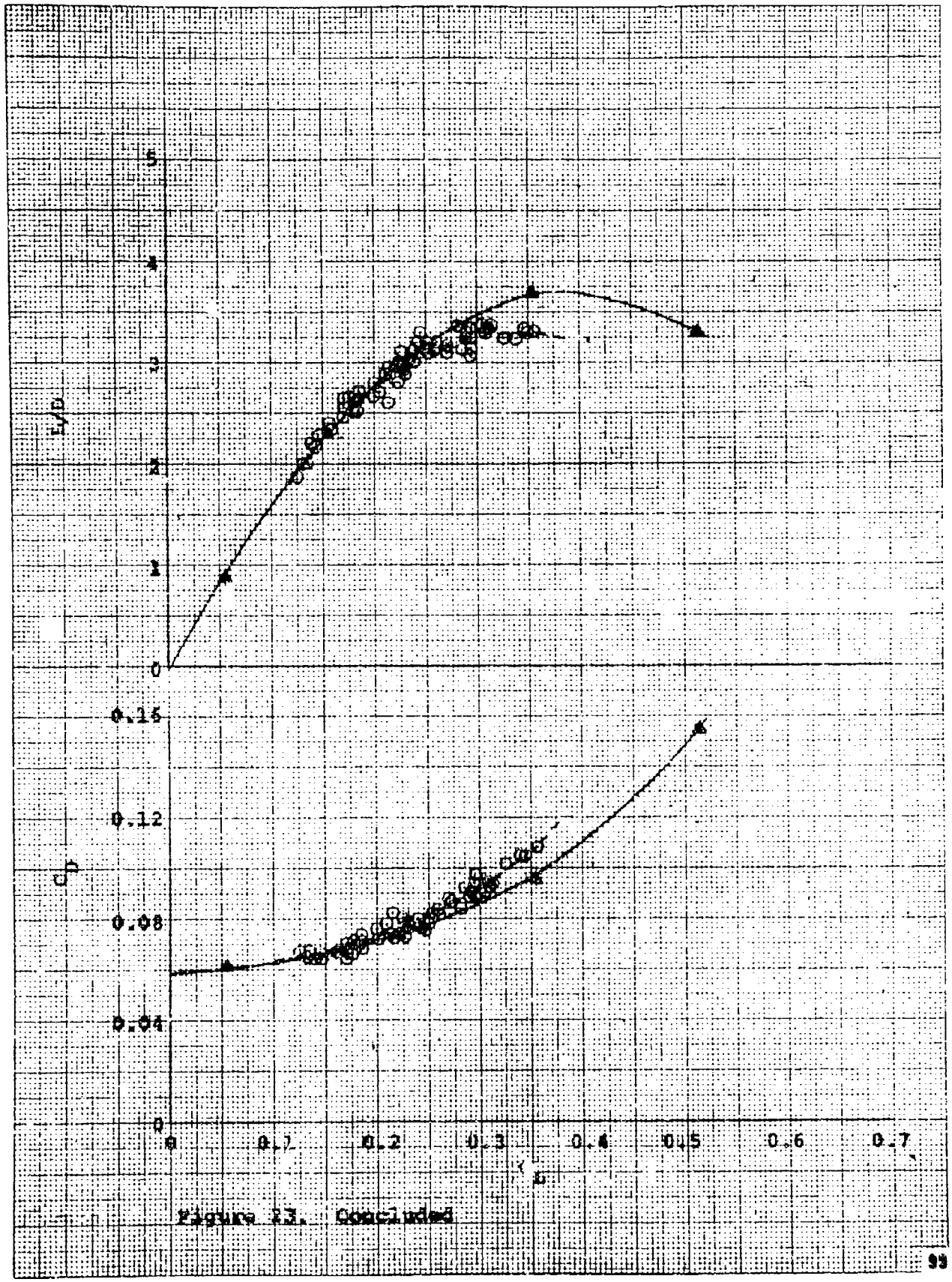

Figure 23. Concluded

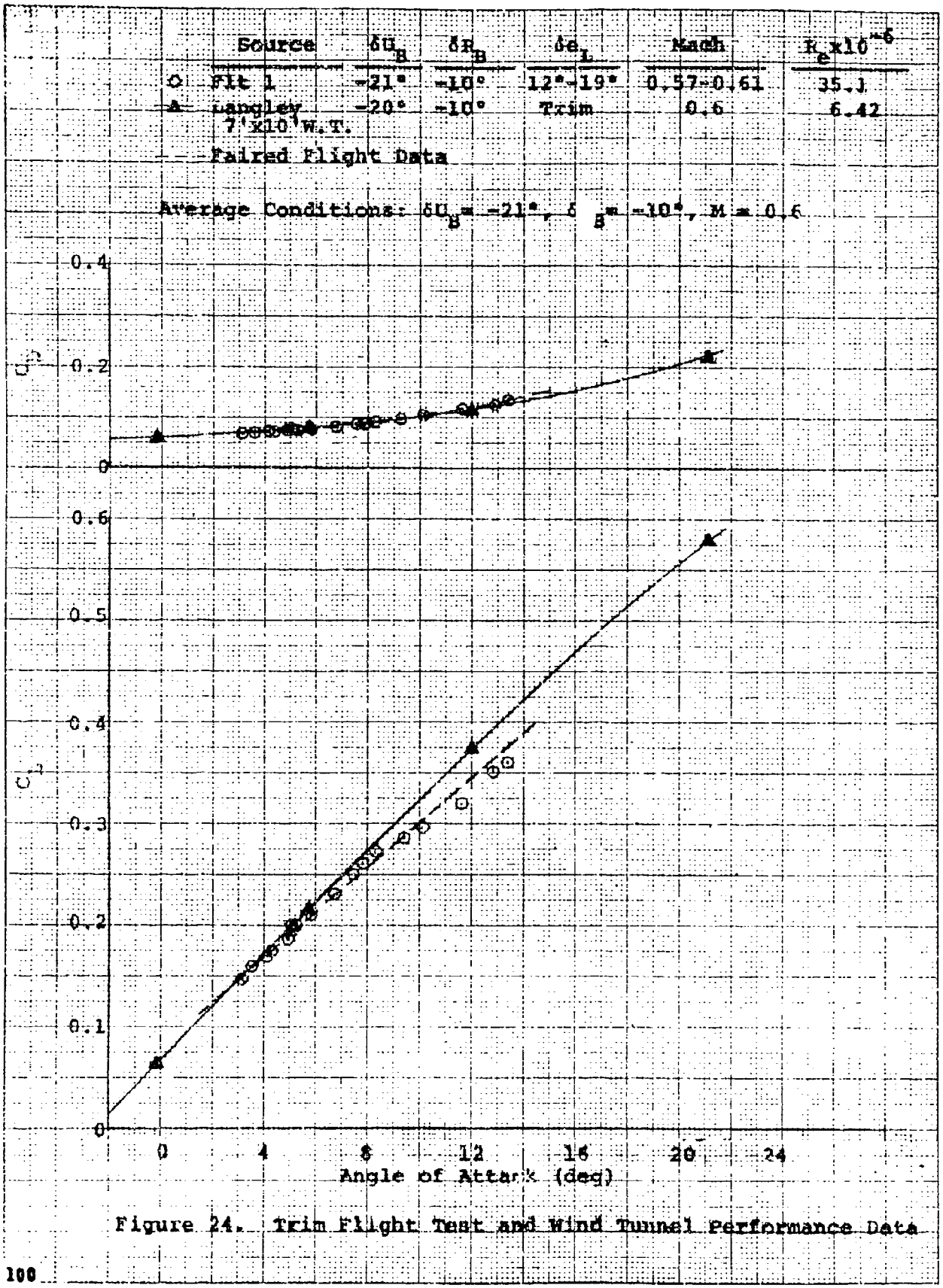

Figure 24. Trim Flight Test and Wind Tunnel Performance Data

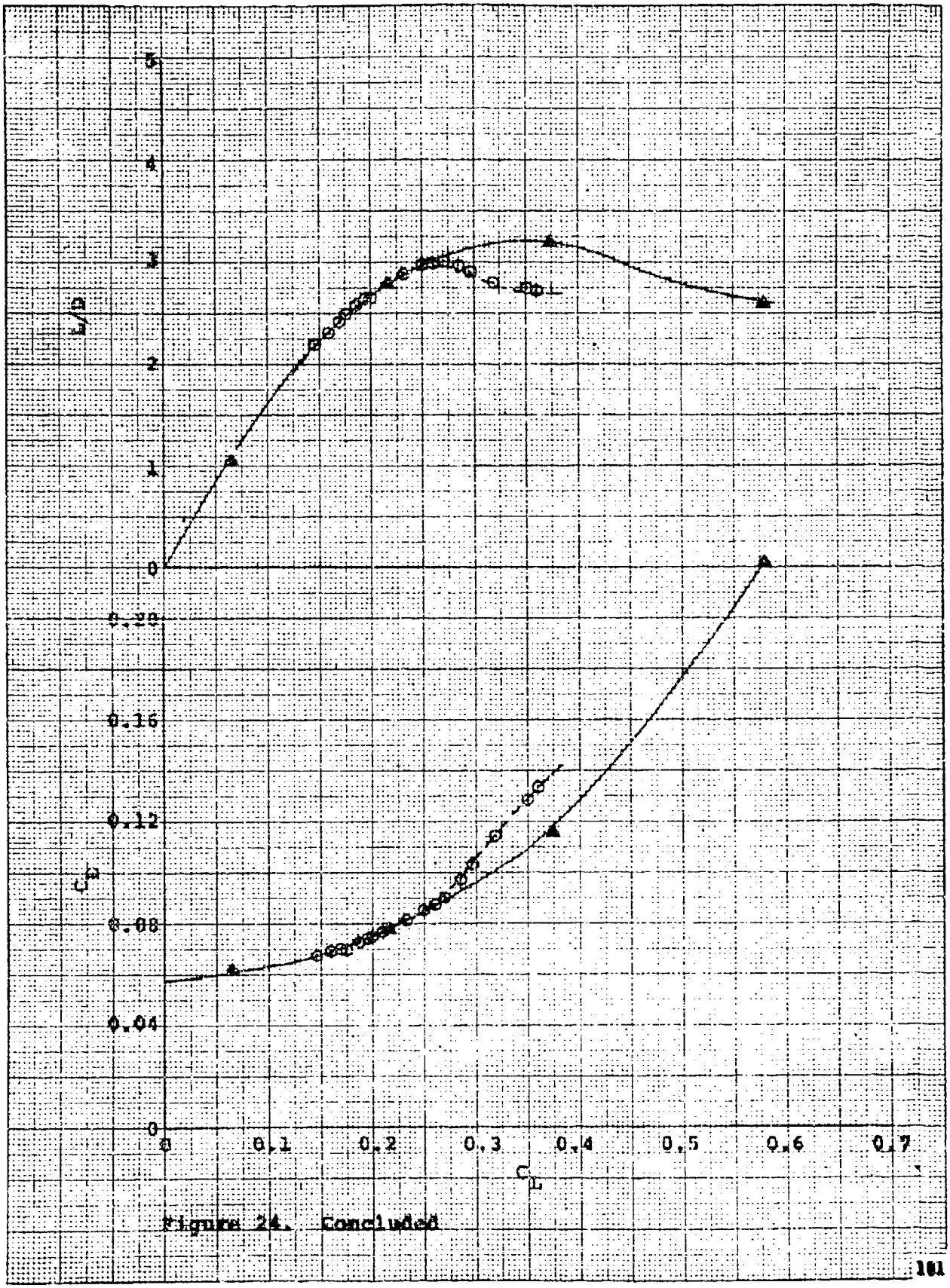

Figure 24. Concluded

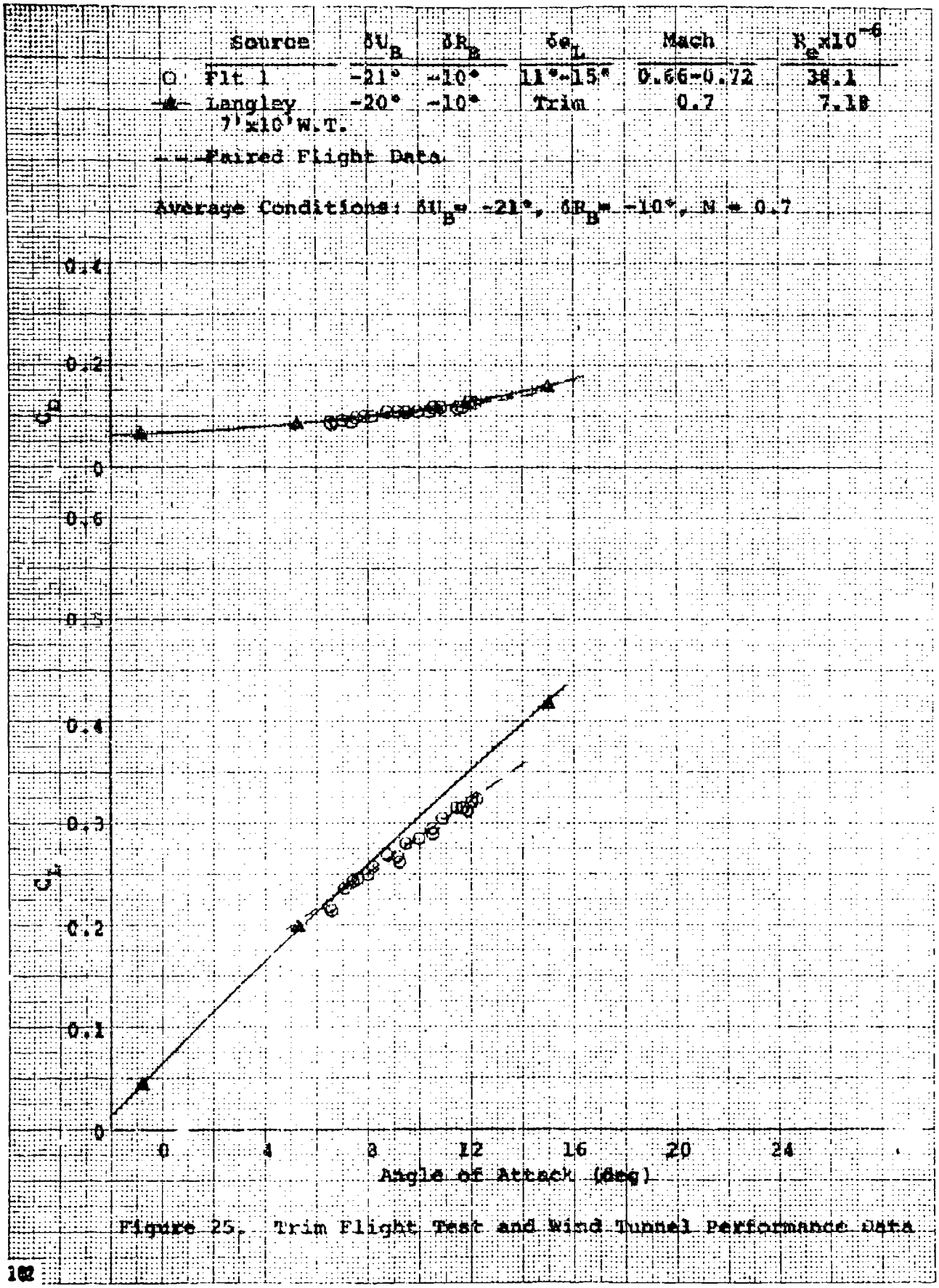

Figure 25. Trim Flight Test and Wind Tunnel Performance Data

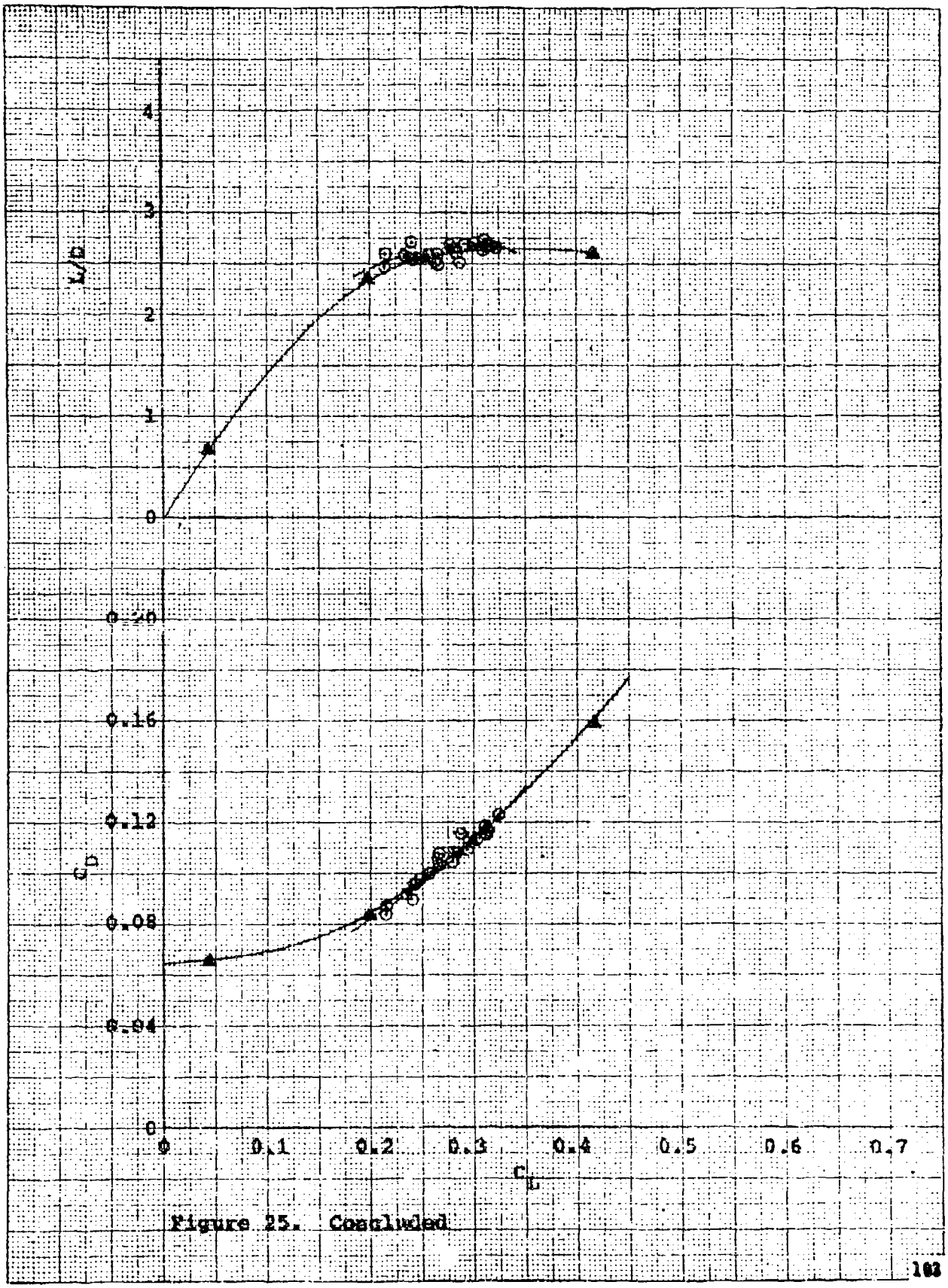

Figure 25. Concluded

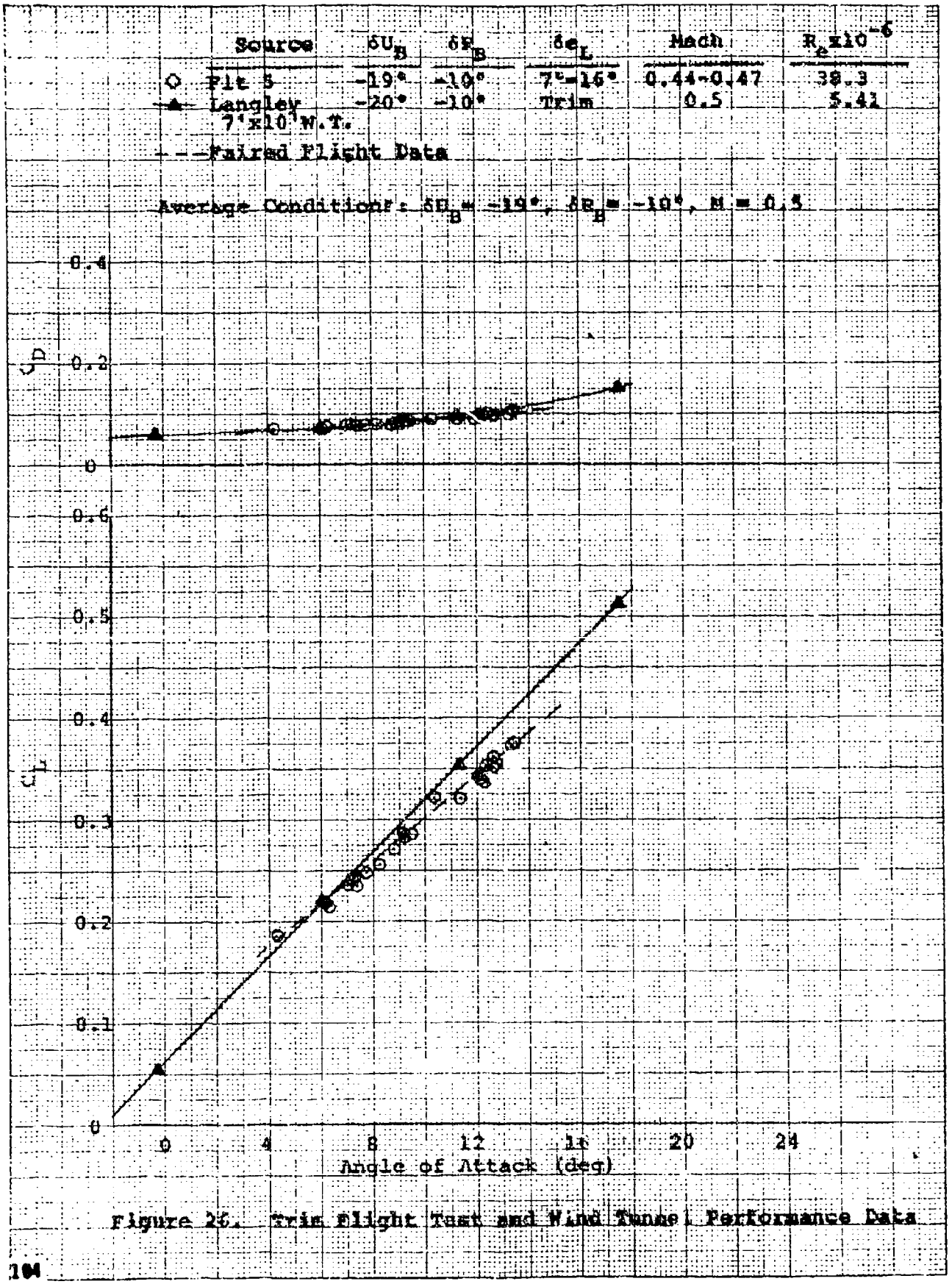

Figure 26. Trim Flight Test and Wind Tunnel Performance Data

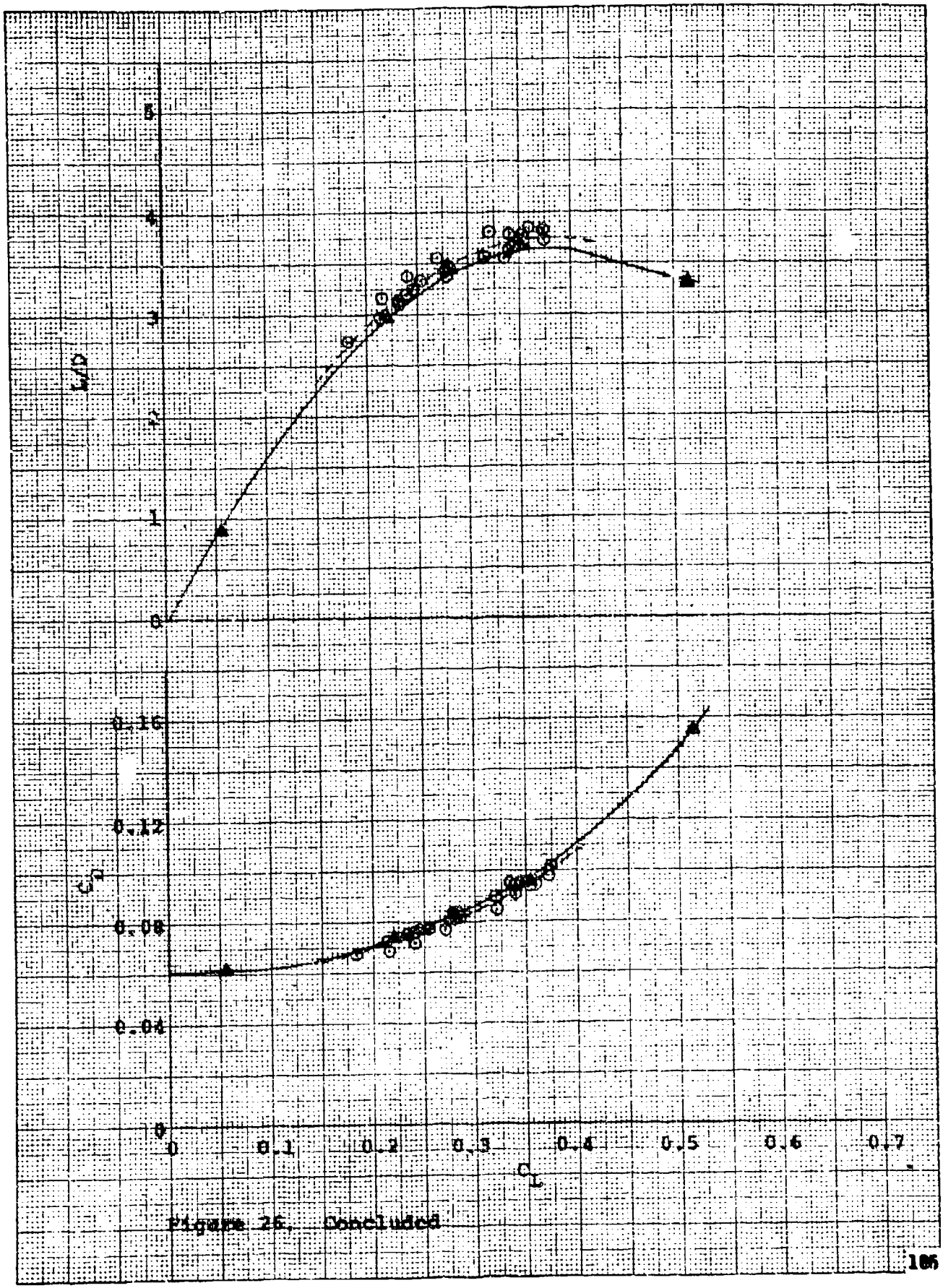

Figure 26. Concluded

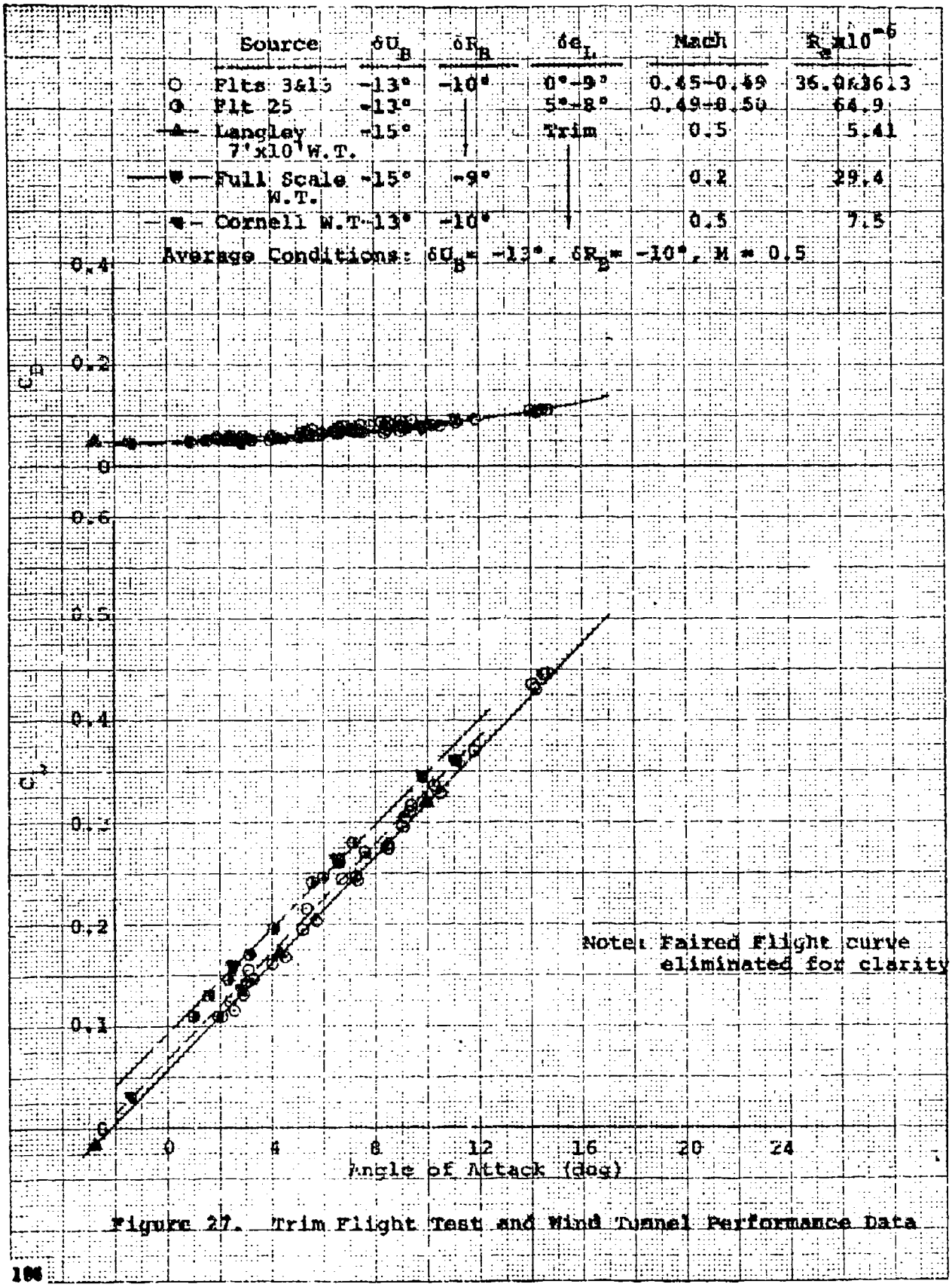

Figure 27. Trim Flight Test and Wind Tunnel Performance Data

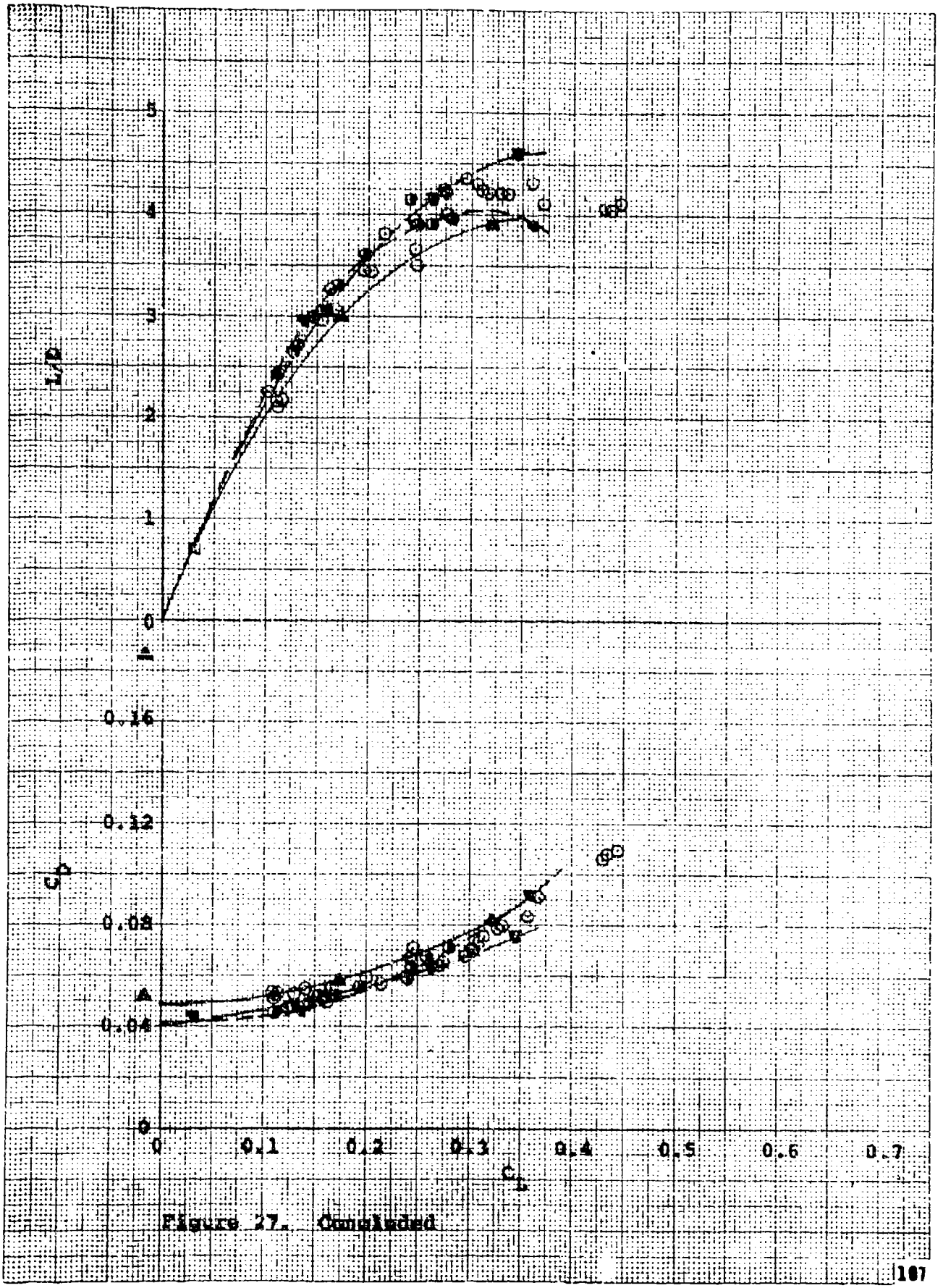

Figure 27. Concluded

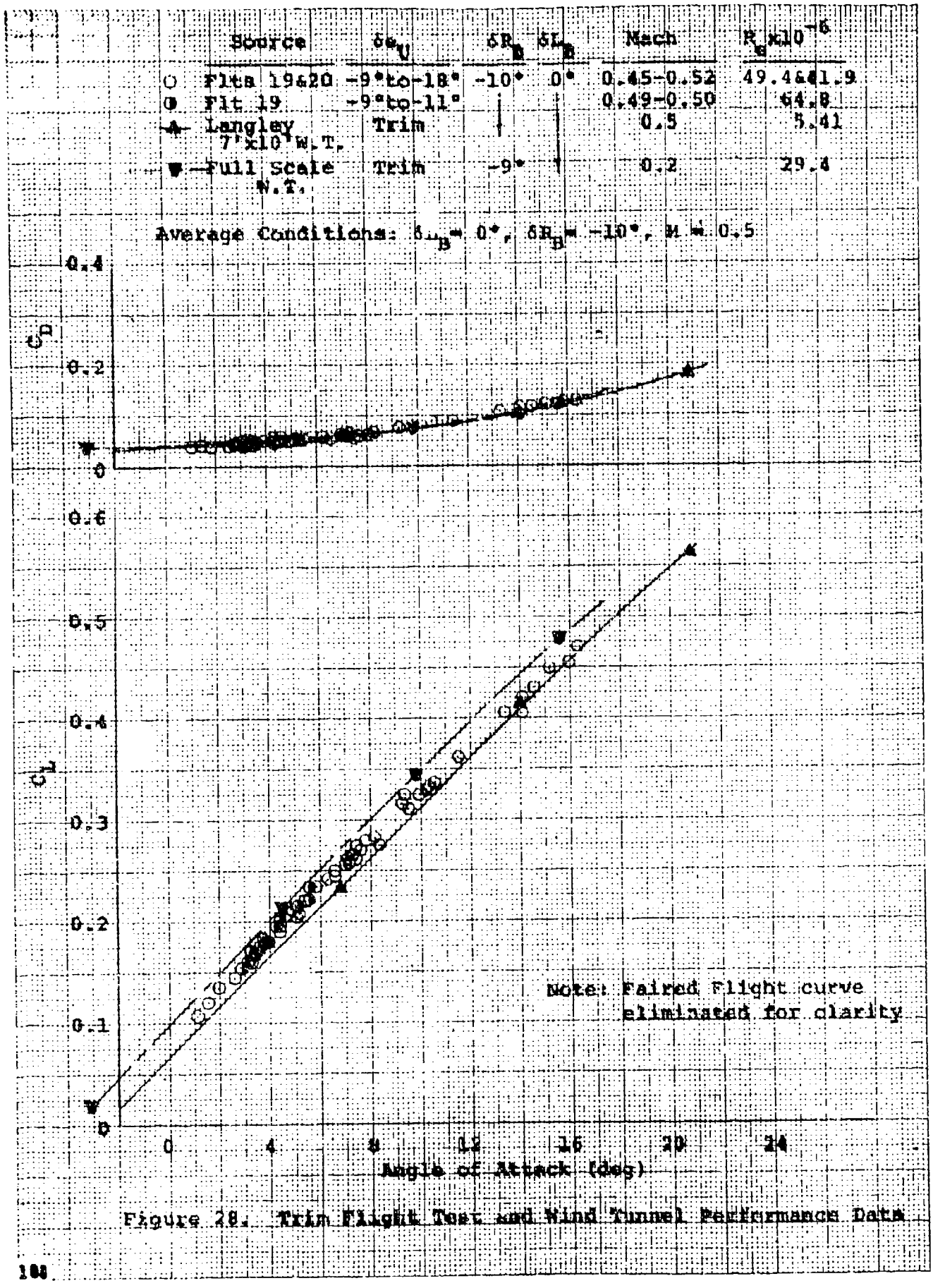

Figure 28. Trim Flight Test and Wind Tunnel Performance Data

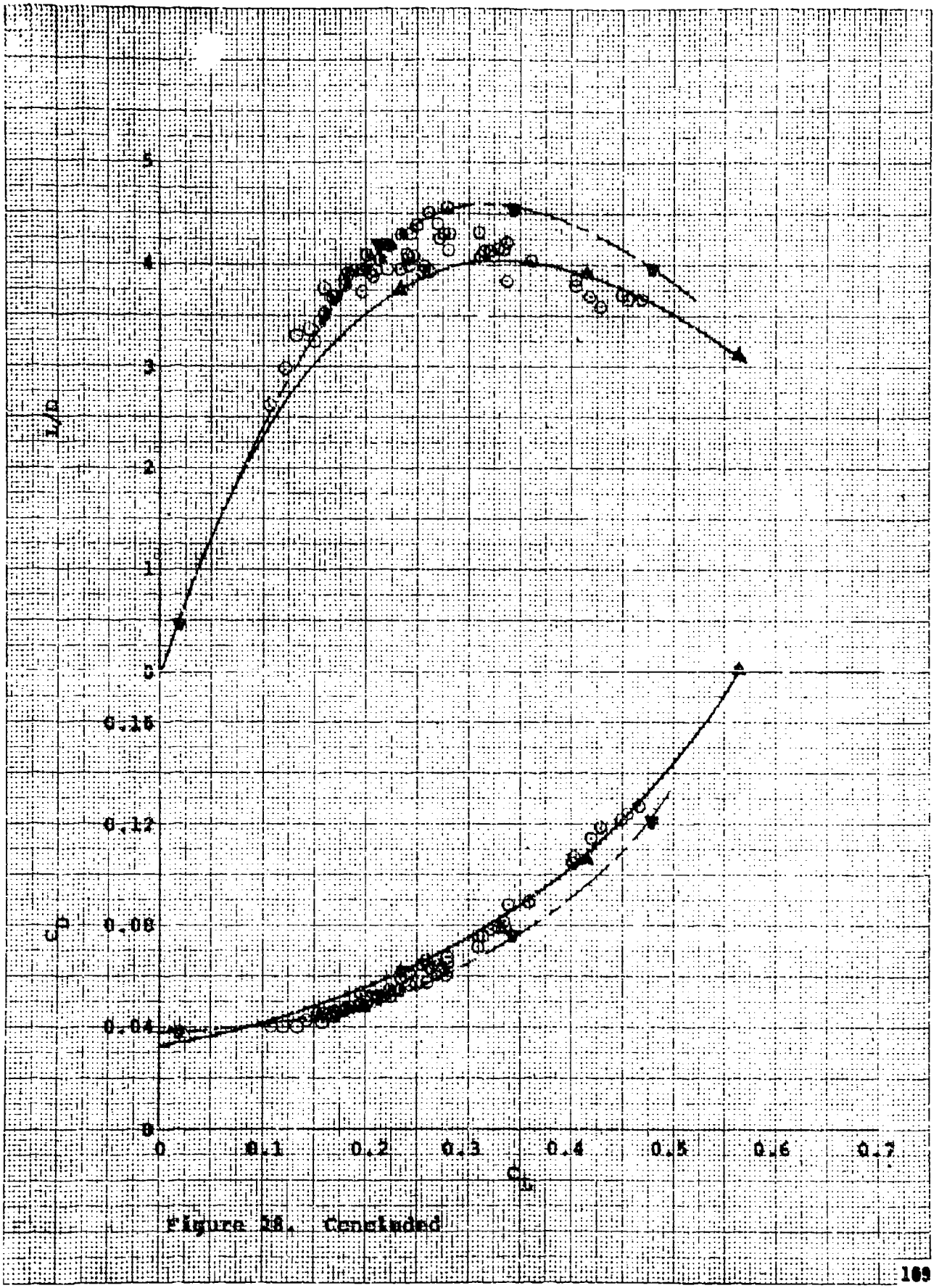

Figure 18. Concluded

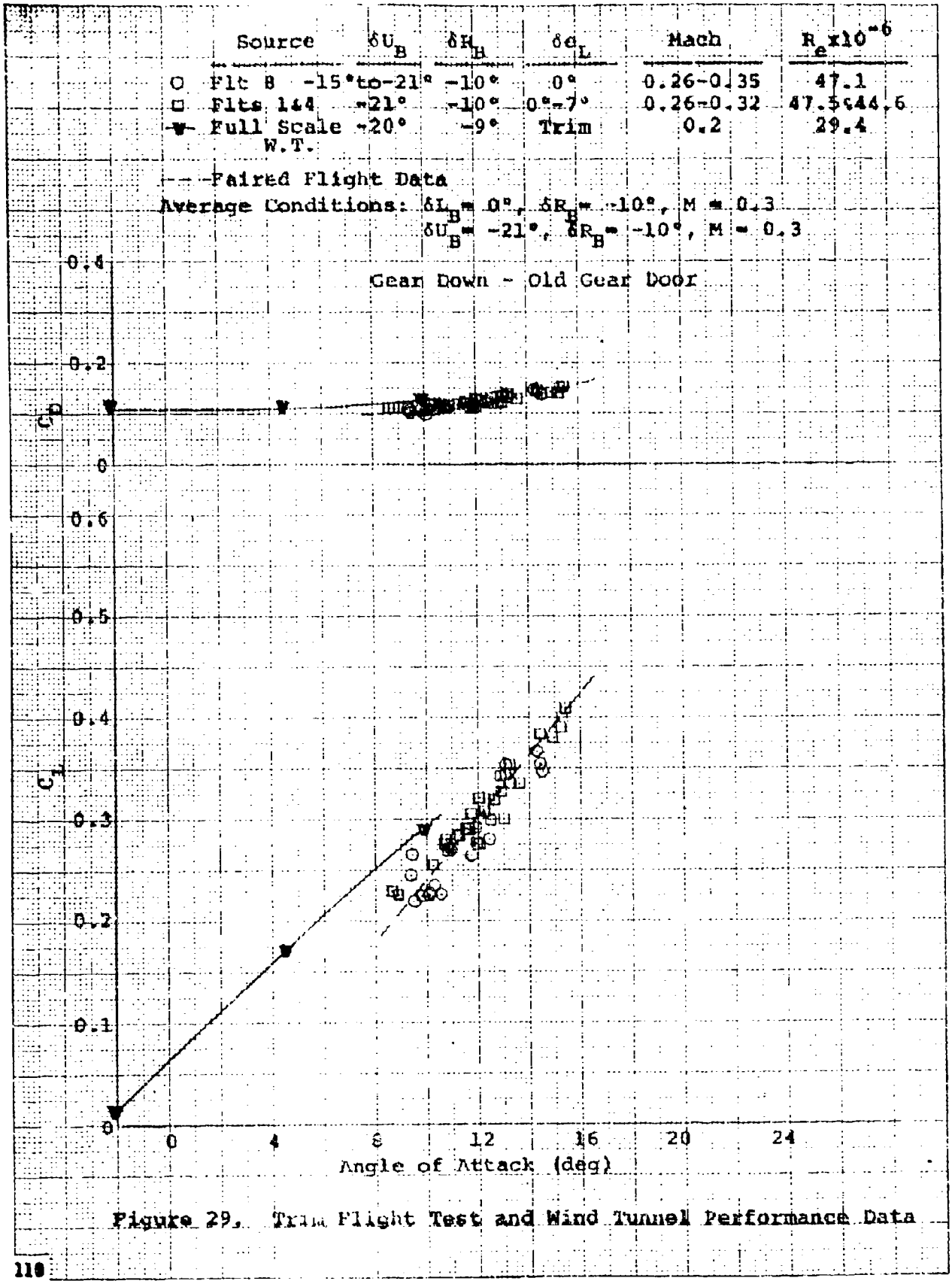

Figure 29. Trim Flight Test and Wind Tunnel Performance Data

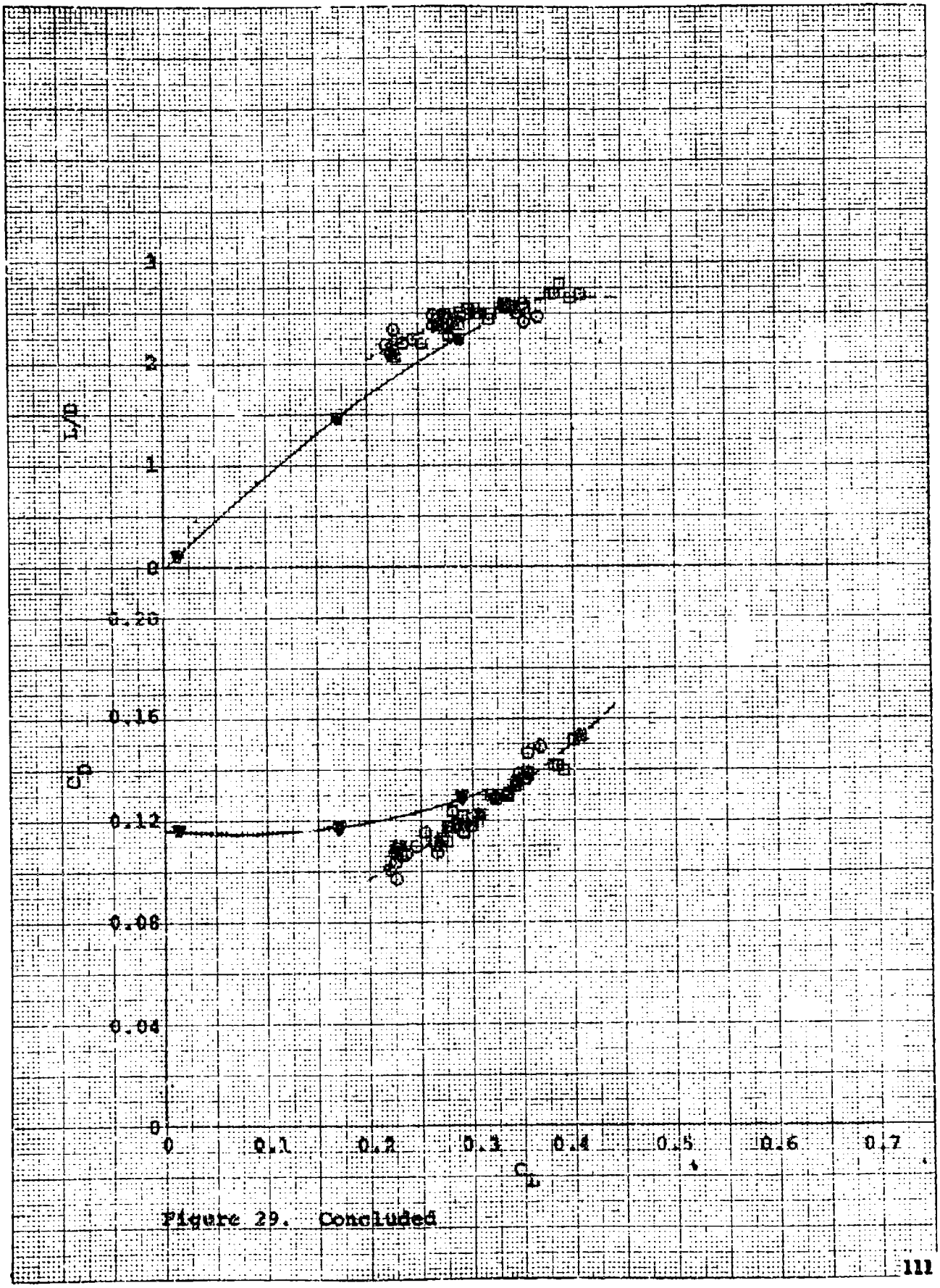

Figure 29. Concluded

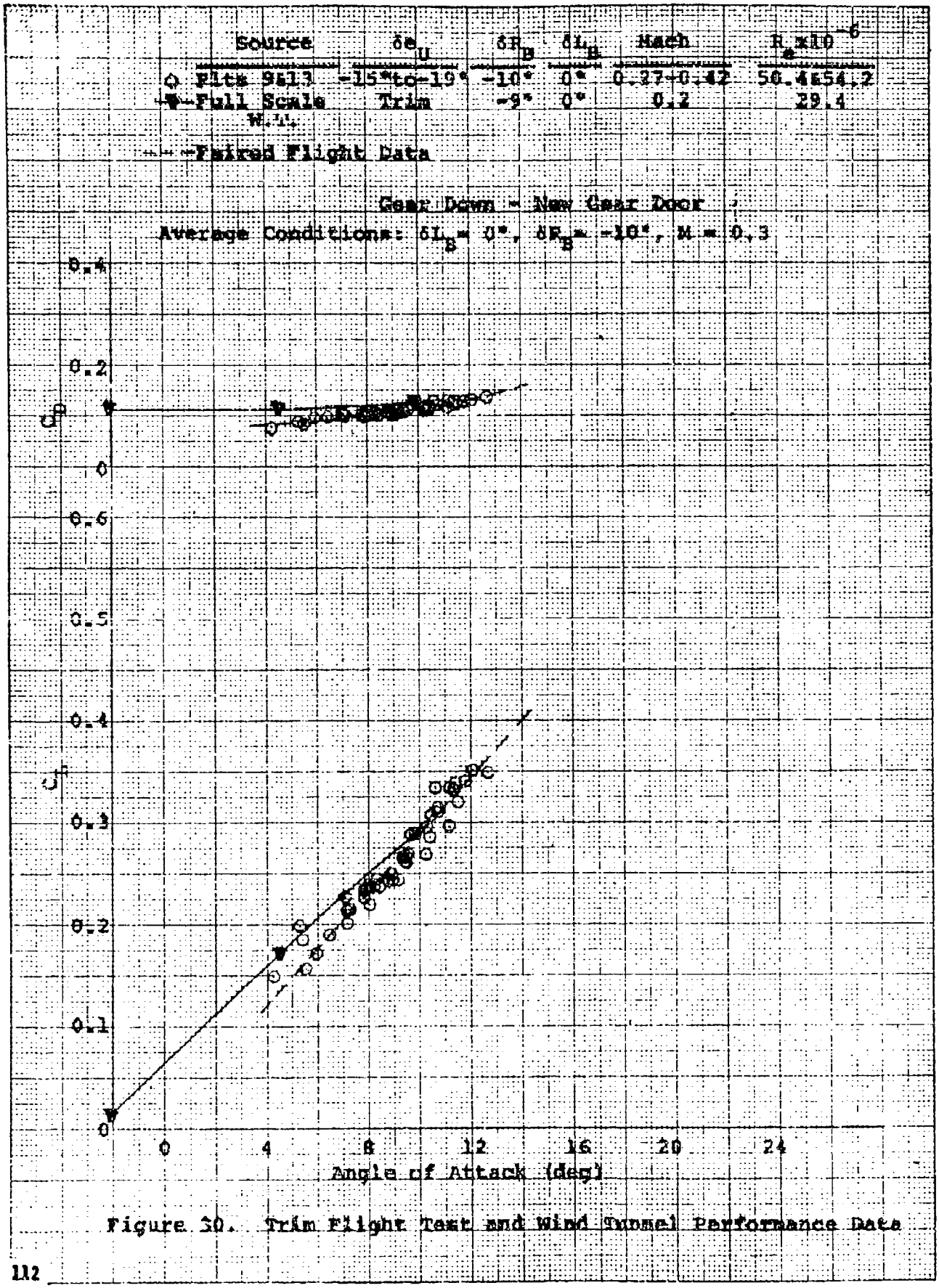

Figure 30. Trim Flight Test and Wind Tunnel Performance Data

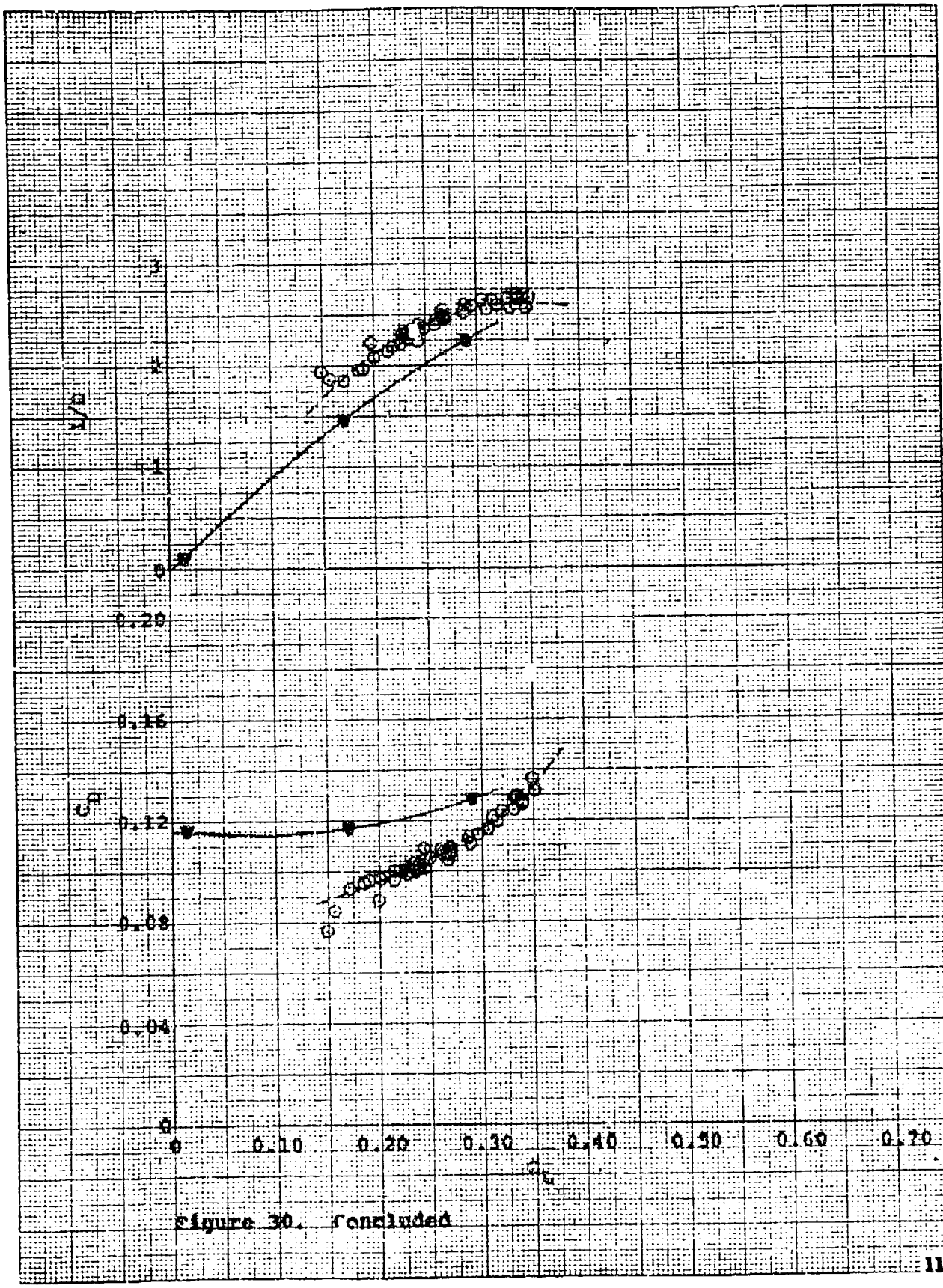

Figure 30. Concluded

APPENDIX II
ANGLE OF ATTACK CORRECTIONS

Figure 1 shows the results of a calibration performed on the angle of attack vane attached to the nose boom in the full scale wind tunnel at a Mach number of 0.2. In an attempt to verify the wind tunnel results, data from the second flight are also presented. Flight data were obtained by computing flight path angle from radar data and subtracting it from the measured pitch angle to obtain a true angle of attack while the vehicle was at zero bank angle. This is not a very accurate technique due to wind effects and inherent inaccuracies in the radar data. The data, though scattered, substantiated the wind tunnel calibration of the X-24A angle of attack vane and established higher confidence in the wind tunnel results.

The nose boom was mounted at a 6-degree nosedown angle with respect to the longitudinal axis of the vehicle to minimize errors in the airspeed system pressure measurements. The true angle of attack as established by the wind tunnel (α_T) was defined by the relationship

$$\alpha_T = 0.87\ (\alpha_i) = \frac{\alpha_i}{1.15} = \frac{\alpha_{boom} + 6\ \text{deg}}{1.15}$$

where $\alpha_i = \alpha_{boom} + 6$ deg

From this equation

$$\Delta\alpha_\varepsilon = \alpha_i - \alpha_T = \alpha_i - (0.87\ \alpha_i) = 0.13\ \alpha_i$$

at 0.2 Mach number.

To obtain the total upwash correction throughout the subsonic Mach number region, an attempt was made to compute the body and noseboom upwash effects using the methods of reference 10. The asymmetric shape of the X-24A made it very difficult to calculate the body upwash effects. Calculations were made using equivalent bodies of revolution generated individually by the top, bottom and side contours. Another calculation used the cross sectional area distribution of the X-24A to compute the radius of an equivalent body of revolution at a series of stations along the body. Both these methods yielded values for $\Delta\alpha_\varepsilon/\alpha_i$ at 0.2

Mach number that were less than half the wind tunnel value, and so were discarded.

Finally the equation from the original wind tunnel curve,

$$\alpha_T = \frac{(\alpha_{boom} + 6 \text{ deg})}{1.15}$$

was modified to incorporate compressibility effects by applying a Mach function to the correction factor as follows:

$$\alpha_T = \frac{(\alpha_{boom} + 6 \text{ deg})}{1 + .15\sqrt{1 - M^2}}$$

This expression is plotted in terms of $\Delta\alpha_\varepsilon/\alpha_i$ versus M in figure 2 along with the full scale wind tunnel point.

A correction was also made to angle of attack for the effects of boom bending due to normal accelerations ($\Delta\alpha_{bb}$). A final correction was made to α for pitch rate on the α vane which was 17.1 feet forward of the vehicle's center of gravity ($\Delta\alpha_q$).

Therefore, true angle of attack was obtained from the following summation:

$$\alpha = \frac{\alpha_{boom} + 6 \text{ deg}}{1 + .15\sqrt{1 - M^2}} + \Delta\alpha_{bb} + \Delta\alpha_q$$

where

$$\Delta\alpha_{bb} = (.0666)\ (a_{z_b} - 1)$$

$$\Delta\alpha_q = (17.1)(q/V_t)$$

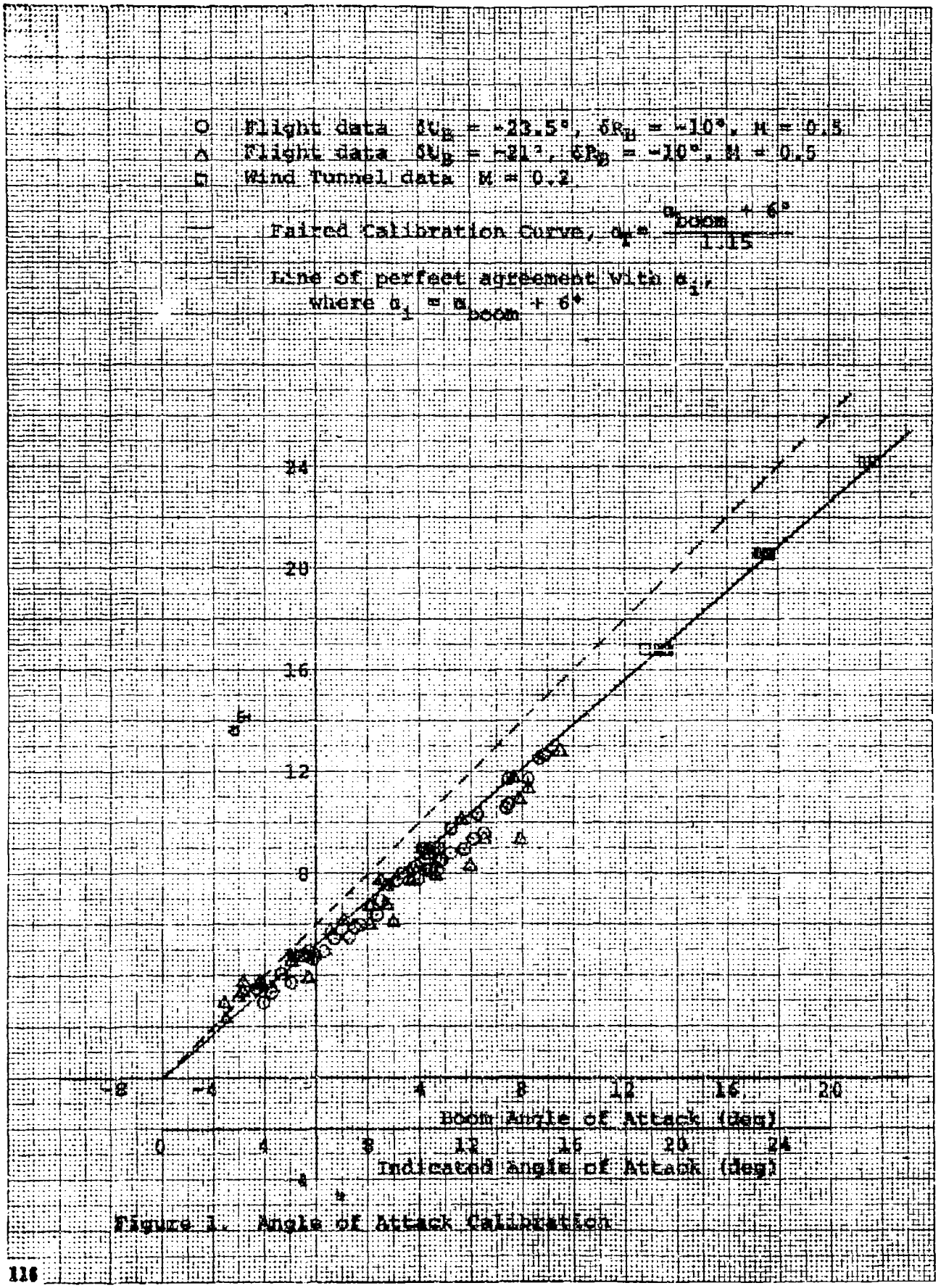

Figure 1. Angle of Attack Calibration

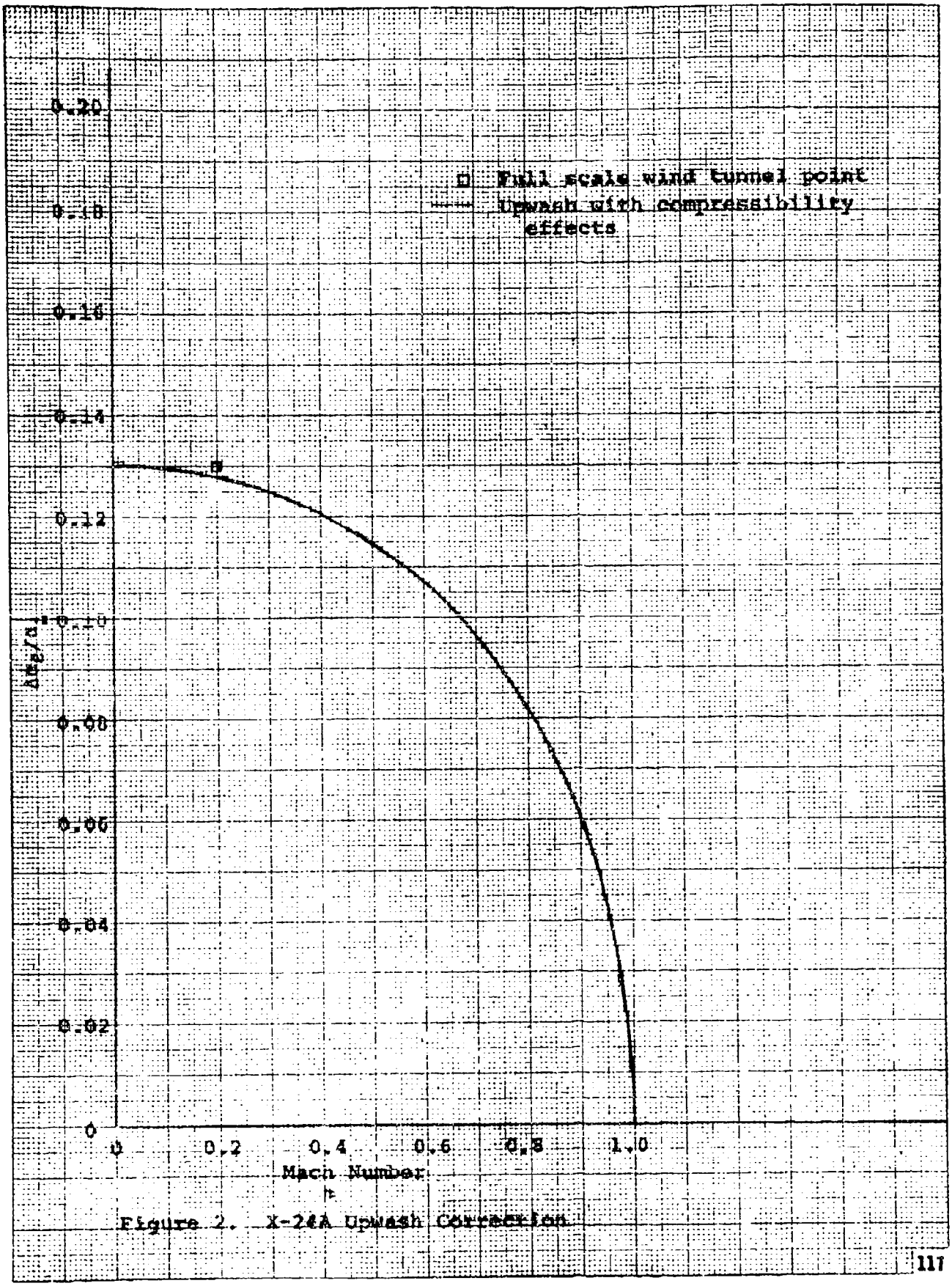

Figure 2. X-24A Upwash Correction

APPENDIX III
X-24A POSITION ERROR DETERMINATION

This appendix was adapted from an AFFTC Flight Test Technology Branch memo written by Christopher J. Nagy in January 1971.

INTRODUCTION

The position error measurement on the X-24A lifting body presented problems that are not encountered on most other types of aircraft. The common methods of position error measurements such as the tower fly-by, the ground speed course and the pacer would not work with the X-24A because there was little time spent in stabilized flight. The X-24's only power source was a rocket engine, which made it a boost-glide type vehicle. Thus, the aircraft was either gaining or losing energy very fast. This means that the altitude and/or airspeed was increasing or decreasing rapidly. These changes in altitude and airspeed introduced problems of lag in the static and dynamic pressure and transients in the position error. In addition, problems in the instrumentation were encountered. These problems and their solutions will be discussed in this appendix.

TECHNIQUE

The method of obtaining the position error is basically a comparison between the aircraft-measured static pressure and the actual static pressure at a given altitude. The data was prepared in a $\frac{\Delta P_p}{\bar{q}_{c_{ic}}}$ form and a ΔM form where:

$$\Delta P_p = P_s - P_a$$

$$\Delta M_{pc} = M - M_{ic} = f\left(M_{ic}, \frac{\Delta P_p}{\bar{q}_{c_{ic}}}\right)$$

from equation 5.65, page 74 of reference 6.

From equation 5.5, page 53, reference 6,

$$\frac{\Delta P_p}{\bar{q}_{c_{ic}}} = f\left(M_{ic}, C_{L_{ic}}\right)$$

$C_{L_{ic}}$ effects were neglected so that $\frac{\Delta P_p}{\bar{q}_{c_{ic}}}$ is a function of instrument corrected Mach number only. The aircraft measured a static pressure and a dynamic pressure using a standard NASA nose boom. The dimensions of this boom are given in figure 6. The actual static pressure was calculated from a Rawinsonde balloon temperature versus altitude curve using the hydrostatic equation (equation 1.17, page 87).

Once the necessary parameters were obtained, the first step was to limit the usable portions of a flight to those where the climb or sink rate was less than 150 feet per second. This helped to eliminate the lag problem. The second step was to select times that gave M_{ic} values at approximately 0.005 increments between the minimum and the maximum M_{ic} values available within the usable portions of the flight. More spacing than 0.005 gave uncertain data; less than this gave unnecessary scatter. Once the times and M_{ic} values were obtained, the P_a values

were derived. First the altitudes at the specific times were recorded from an altitude versus time radar track. Then P_a values were obtained for each altitude from weather balloon data. The Pic counts from the vehicle were then recorded at the same times and two slightly different calibrations were used depending on whether the pressure was increasing or decreasing. (The pressure transducer transmitted digital counts to the ground and calibrations were used to obtain pressure.) This was done to account for hysteresis. Next, $\frac{\Delta P_p}{q_{c_{ic}}}$ was calculated for each M_{ic} value and plotted versus M_{ic}. Once the $\frac{\Delta P_p}{q_{c_{ic}}}$ values were known, ΔM_{pc} was found from the following equations (equations 5.63 and 5.65, page 67, reference 6) for $\Delta M_{pc} < .04$:

$$\Delta M_{pc} = M - M_{ic} = \frac{(1.0 + 0.2\, M_{ic}^2)}{1.4\, M_{ic}} \left[(1.0 + 0.2\, M_{ic}^2)^{3.5} - 1.0\right] \frac{\Delta P_p}{q_{c_{ic}}}$$

for $\Delta M_{pc} > .04$:

$$\frac{\Delta P_p}{q_{c_{ic}}} = \frac{\dfrac{1.4\, M_{ic}\, \Delta M_{pc}}{(1.0 + 0.2 M_{ic}^2)} + \dfrac{0.7\,(1.0 - 1.6\, M_{ic}^2)\Delta M_{pc}^2}{(1.0 + 0.2\, M_{ic}^2)^2}}{(1.0 + 0.2\, M_{ic}^2)^{3.5} - 1.0}$$

This equation was solved to give a ΔM_{pc} versus M_{ic} curve.

RESULTS

The final data points of flights 10 to 13, 15 to 18, and 20, and the faired lines are shown in figure 1. Similar curves are given for comparison in figure 2 for the HL-10, another lifting body. Flights 1 through 9, the glide flights, were deleted for several reasons. First, they could not provide information on the higher portions of the Mach range, since, without power, the highest Mach number reached was about 0.7. Second, because the powered flights after burnout covered the same regime as the glide flights, the same data could be obtained from the powered flights. Third, the Rawinsonde balloon release time for flights 1 through 9 was not close enough to the launch time for the P_a values to be accurate. A late balloon release caused flight 14 to be deleted for the same reason. Flight 19 data was consistently high, and although a detailed study as to why was not made, a bad radar track was suspected.

Flight 21 data are not shown because it was consistently low. A closer look at the radar altitudes indicated that the radar may have lost track and may have been "hunting" during this time period. Flights 22 and 23, although not graphed, gave consistent data on or near the pre-

dicted curves. By flight 23, a fairly high level of confidence had been developed in the predicted curves. Succeeding flight data were not worked up since the Mach range was not extended beyond 1.35. A pressure system failure precluded use of data from flight 25 on which a maximum Mach of 1.6 was reached.

DISCUSSION OF RESULTS

The data indicate a leveling off of the ΔM_{pc} curve below 0.55 M_{ic}. It was decided to retain a straight line between 0.55 and 0.35 to accommodate the data between 0.40 and 0.55. Below 0.35, the position error was unimportant because the aircraft never flew below 0.35 Mach in the gear up configuration.

Transonic

The data indicated that the position error peaked around $M_{ic} = 0.920$. A detailed look at airspeed and altitude traces showed that the dynamic pressure peaked at $M_{ic} = 0.920$ and the static pressure at $M_{ic} = 0.940$. From this information one might expect a curve such as the solid line shown in figure 3. On flight 18 almost no second break was visible, the static pressure jump being masked by corresponding changes in dynamic pressure. Flight 20 showed a more pronounced break at $M_{ic} = 0.945$. To accommodate the flight data during the Mach jump, the ΔM_{pc} curve was drawn bent slightly outward as shown by the dashed line (figure 3). This seemed to fit all data points most accurately.

The data intercepted the ΔM_{pc} zero line at about $M_{ic} = 1.075$. A position error of zero was used above Mach 1.075. Although plotted data points are slightly negative supersonically the values are felt to be well within the measuring accuracy of the system.

Correlation with Predicted Data

In April 1966, a study was made by the Martin Company in an effort to predict the position error curve for the X-24A. Dimensions from the existing nose boom were used in theoretical calculations to obtain $\Delta P_p/q_{c_{ic}}$ as a function of Mach. This curve is shown in figure 4. Agreement between predicted and flight measured values was generally good, and the agreement between $M_{ic} = 0.550$ and 0.750 was exceptional. The Mach number at which the break point occurs (where the bow wave passes over the pressure ports) was the same in each case.

Particular Problems Studied

Lag

Lag was studied for both the static and dynamic pressure systems and estimates were made for each. The static pressure lag can be calculated from the equation (reference 6, equation 4.2, 4.9, page 29, 30).

$$\Delta P_{lag} = \lambda \frac{dp}{dt}$$

Where $\lambda = \frac{32\ mL^2}{D^2 \gamma P} \left(1 + \frac{Q}{LA}\right)$ = lag constant

and m = coefficient of viscosity $\approx 3.0 \times 10^{-7}$ for X-24 temp range.

L = length of tubing, ft ≈ 8.93

D = diameter of tubing, ft $\approx 1.43 \times 10^{-2}$

γ = ratio of specific heats ≈ 1.4

P = applied pressure, psf

Q = instrument volume, ft^3, $\approx 1.447 \times 10^{-2}$

A = cross sectional area of tubing, $ft^2 \approx 1.605 \times 10^{-4}$

This leads to

$$\Delta P_{lag} = \frac{29.7}{p} \frac{dp}{dt}$$

For a sink rate of 150 ft/sec at 40,000 ft

$$\Delta P_{lag} = \left(29.7\ \frac{lb\text{-}sec}{ft^2}\right)\left(3.9\ \frac{psf}{sec}\right)\left(\frac{1}{391.6\ psf}\right) = .3\ psf$$

This was not enough to affect the validity of the results.

A similar study was made for dynamic pressure lag. Taking landing as the most extreme case since the rate of change in dynamic pressure is highest here.

$$q_c \approx 300\ psf$$

$$\frac{dq_c}{dt} \approx 15\ \frac{psf}{sec}$$

λ can be calculated similarly for the dynamic pressure system giving

$$\Delta q_{c_{lag}} = (1.03 \times 10^2\ sec)\left(15\ \frac{psf}{sec}\right) = .155\ psf$$

Again this was not nearly enough to affect the results.

Zero Shifts in the Aircraft Pressure System

There was some concern that pressures taken at the balloon release time (within 30 minutes after landing) from both the balloon and the aircraft were different by as much as four psf after being corrected for altitude differences between the lakebed and the Rawinsonde station. The question was raised whether a zero shift correction should be applied to the X-24 pressure to make it conform with the ground pressure of the balloon. Starting with flight 14, checks were made on the two pressures and the results are shown in the following table:

Table I

DIFFERENCES IN X-24A AND WEATHER BALLOON STATIC PRESSURES

Flight No.	Rawinsonde Ground Pressure Minus X-24A Ground Pressure Corrected to Lakebed Altitude		Total Change Between Pre- and Post-flight Checks
	Pre-flight Correction	Post-flight Correction	
14	0.0	-2.9	2.9
15	+0.4	-2.0	2.4
16	+1.1	-1.6	2.7
17	+1.0	-1.5	2.5

It can be seen that the pre- and post-flight corrections were of opposite signs. The discrepancy was attributed to hysteresis in the X-24A static pressure transducer. Hysteresis, according to the manufacturer of the instrument is 7 psf. In actual calibration with pressure increasing and decreasing, the apparent hysteresis was more like 3 psf, which is in accordance with the change in pre- and post-flight checks. It was therefore concluded that the data should not be corrected for zero shifts but that hysteresis effects were of greater importance and should be accounted for when applying the calibrations.

Time Shifts

The most important factor in reducing the data was to insure that the balloon passed through the flight altitude at approximately the same time of day that the flight occurred. Best results were obtained when the balloon reached flight altitude within 30 minutes of flight time. Flight 14 is a good example of erroneous data because this rule was not observed. Due to transmitting difficulties, the balloon was not at altitude until four hours after the flight. Figure 5 shows the data according to the late balloon; in addition, data from a balloon seven hours prior to the flight and the expected results are shown. Data from late balloons may give good results depending on the stability of the atmosphere during that time period. However, any attempt at correcting for the time shift based on ground pressures is useless, since, while the pressure at ground level may have changed 1 psf, the pressure at 40,000 feet may have changed 3 or 4 psf.

Pacer

The first flight with the rockets called for a powered profile which would keep the X-24A at a somewhat constant altitude and speed for a reasonable amount of time. Therefore, this opportunity was taken to use a well calibrated T-38 pacer to establish some good points on the position error curve.

The pacer pilot turned on the event light three times during the flight indicating that he felt he was stabilized alongside the X-24A. One point was taken during the powered portion at 35,000 feet and at an X-24A M_{ic} of 0.660. The other two points were taken in the pattern at test indicated Mach numbers of 0.426 and 0.419.

Indicated altitude, velocity, and temperature data were taken from the pacer photopanel and instrument corrected. This data was put into a computer program along with corresponding X-24A data and the pacer position error curve. The program computed position errors using a ΔH_{pc} method and a ΔV_{pc} method.

The results show good agreement between the two methods for the point at 0.660 Mach number. Values for $\Delta P_p/q_{c_{ic}}$ were 0.058 and 0.062 which correspond to ΔM's of 0.023 and 0.025. These values were close to the other data which gave a ΔM_{pc} of 0.029 at 0.660 M_{ic}.

The two methods did not show good agreement for the two points in the pattern. Values for $\Delta P_p/q_{c_{ic}}$ ranged from 0.115 to 0.067 corresponding to ΔM_{pc}'s of 0.027 to 0.015. However, all points fall within the scatter of the other data.

The pacer points give good support to the data obtained through the other method explained in the report.

Figures 1 Through 6

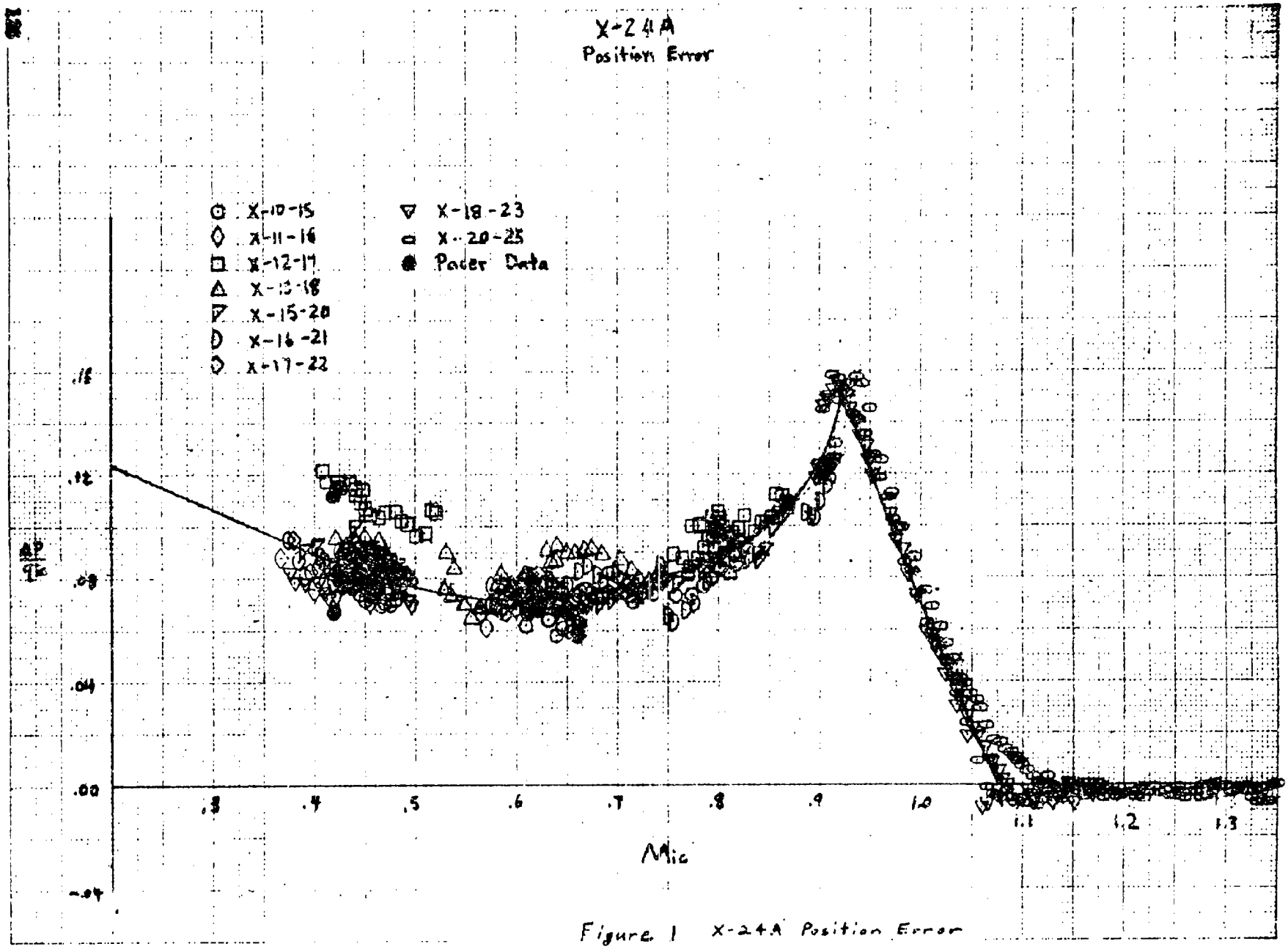

Figure 1 X-24A Position Error

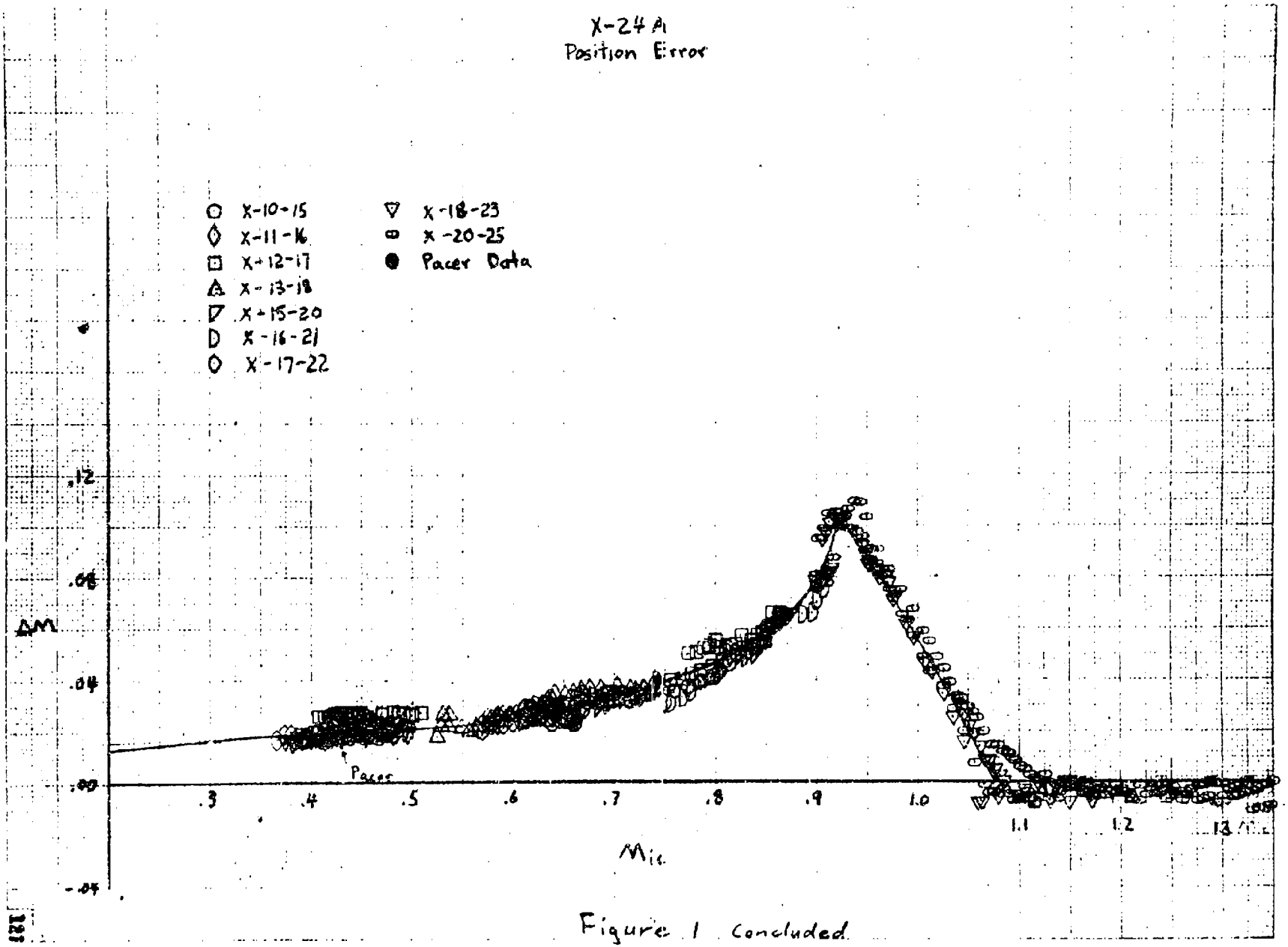

Figure 1 Concluded

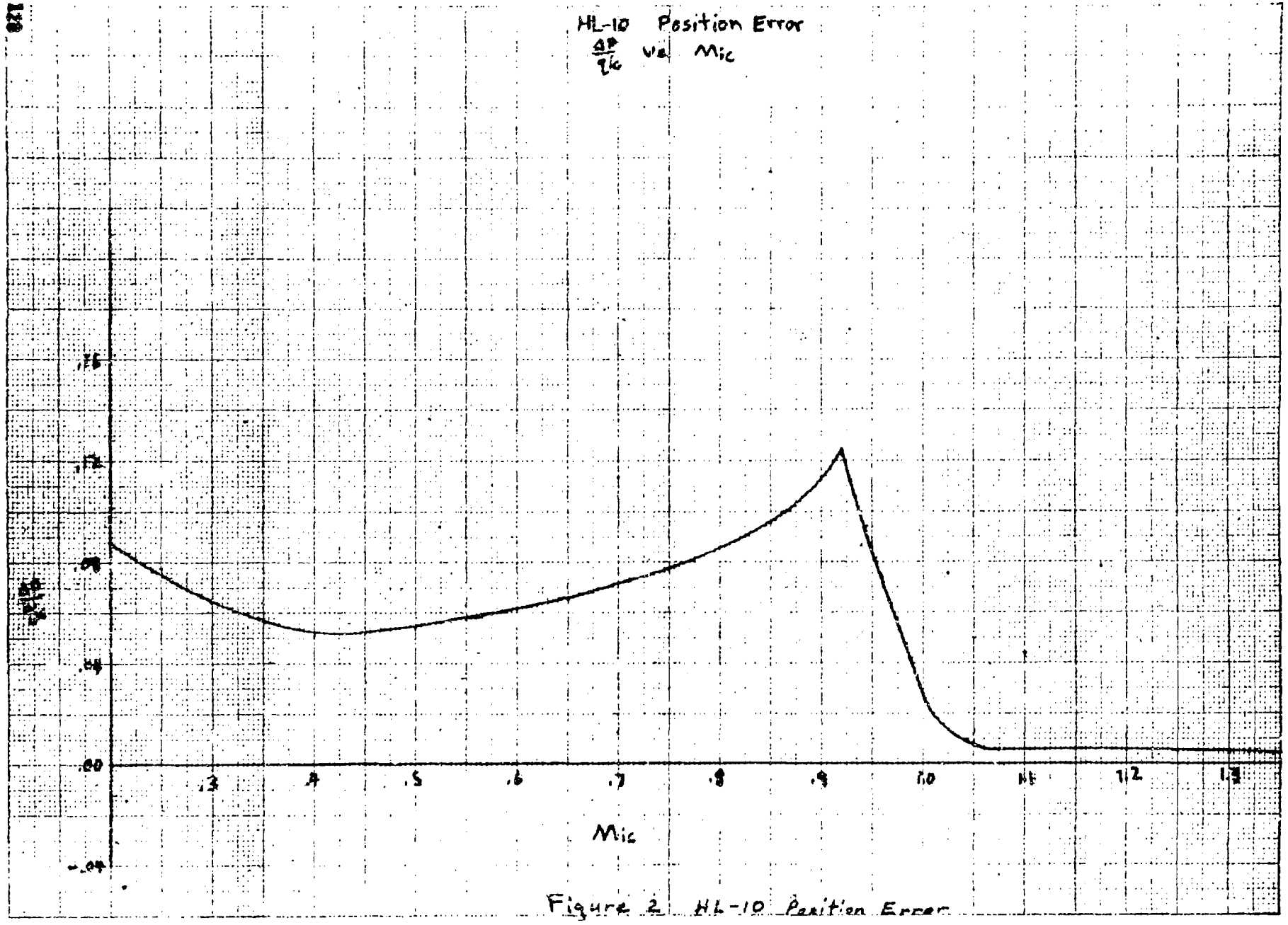

Figure 2 HL-10 Position Error

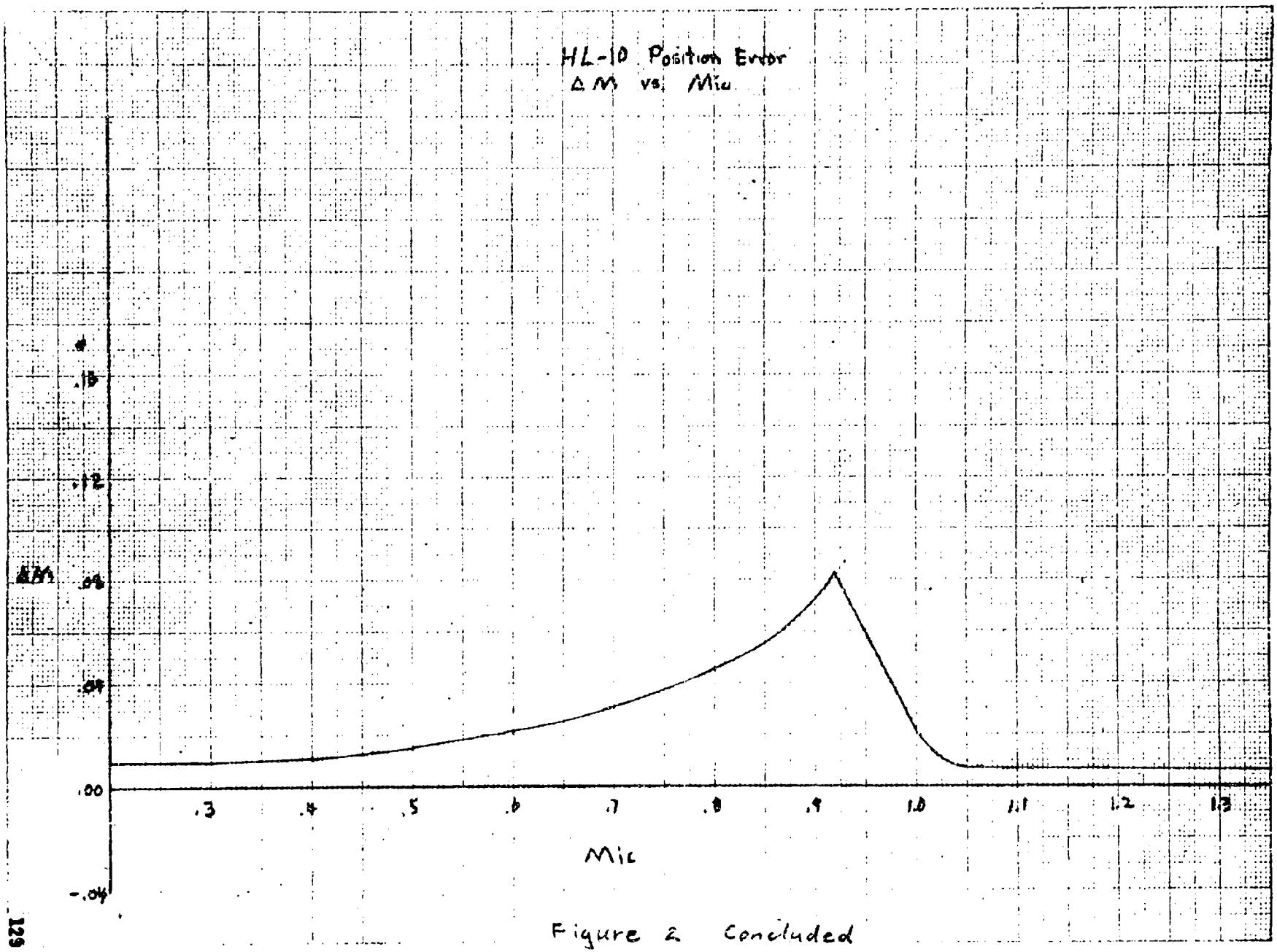

Figure 2 Concluded

Figure 3. X-24A Position Error, Transonic Mach Numbers

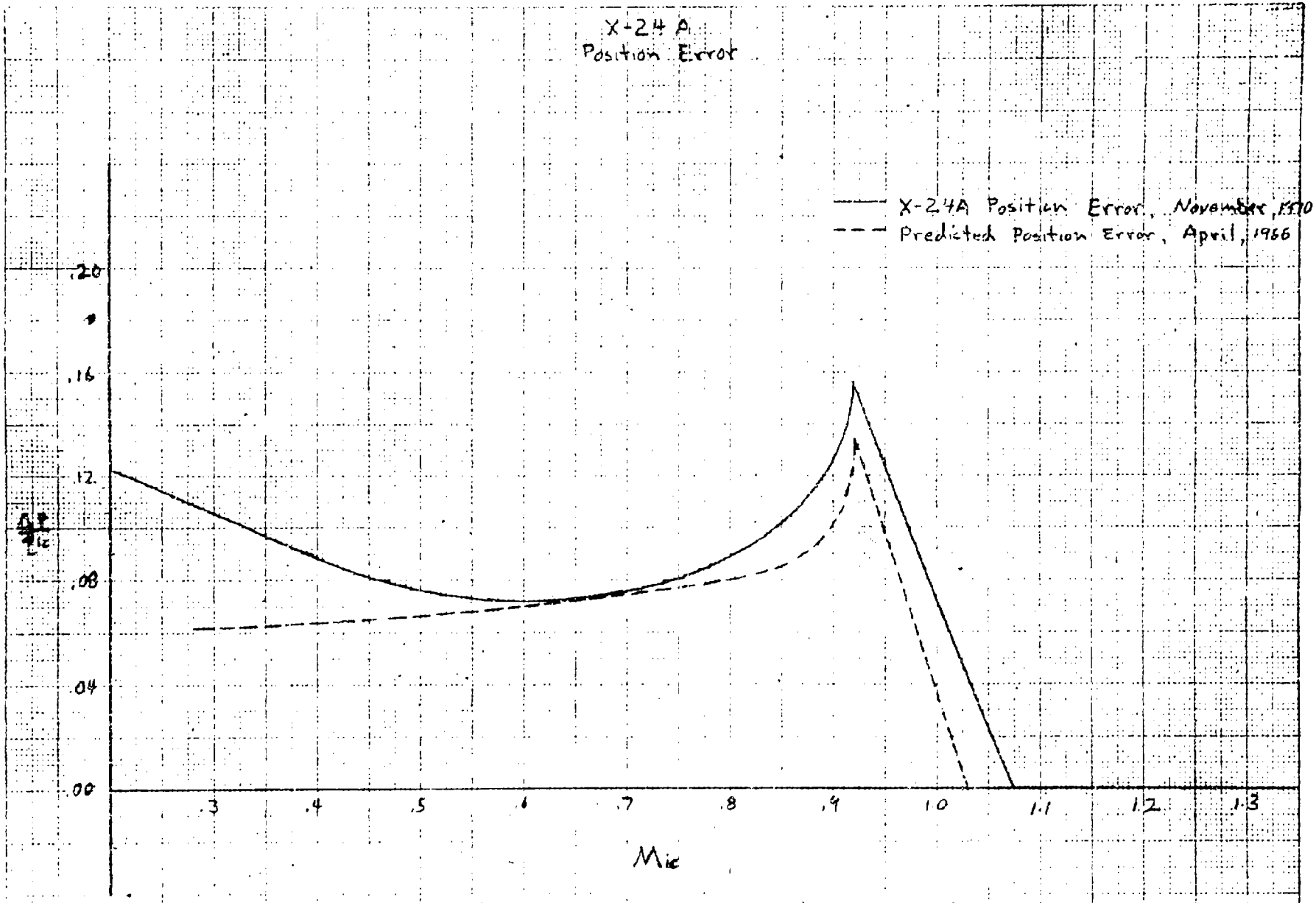

Figure 4 Comparison of Predicted and Calculated X-24A Position Error Curve

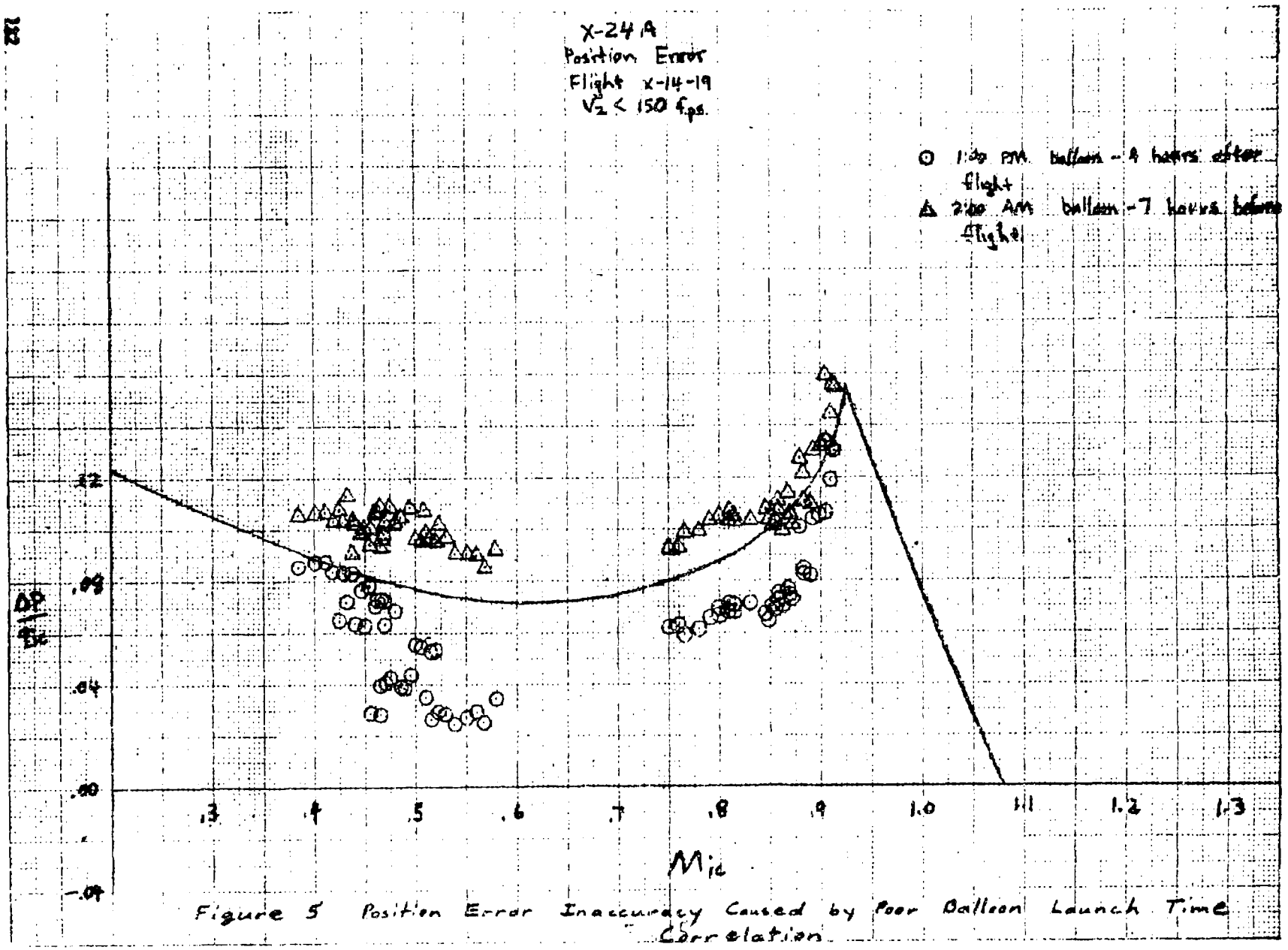

Figure 5 Position Error Inaccuracy Caused by Poor Balloon Launch Time Correlation

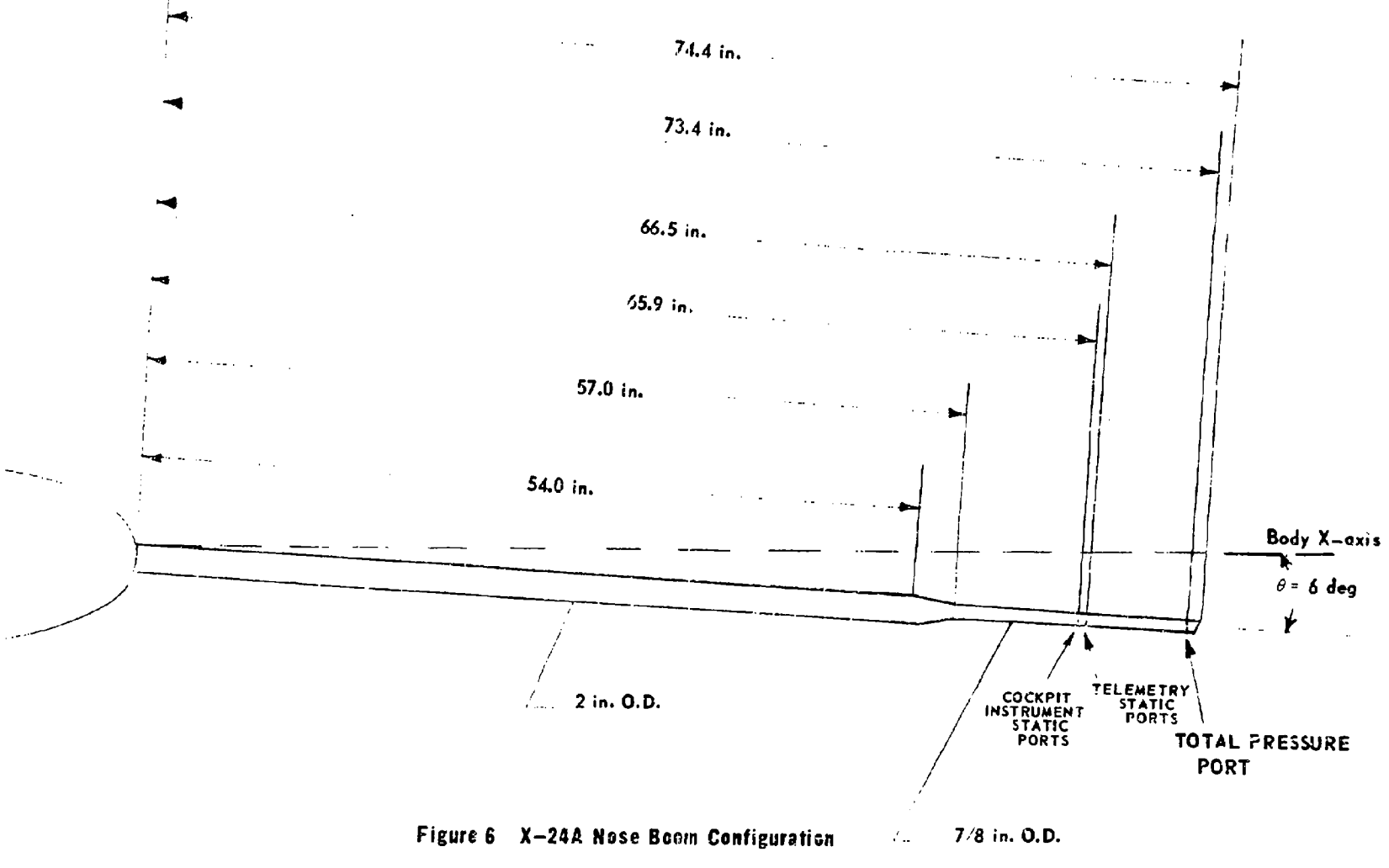

Figure 6 X-24A Nose Boom Configuration

APPENDIX IV

DIGITAL COMPUTER PROGRAM FOR DETERMINATION OF PERFORMANCE CHARACTERISTICS

This computer program was written by David F. Richardson of the Flight Test Technology Branch.

An IBM 1620 digital computer program was used to correct flight data and compute performance characteristics of the X-24A. A computer listout of the program is shown in figure 1. A list of equations used in the program is also presented. The following corrections were made to the flight data by the program:

1. A correction to the accelerometers for a pitch misalignment angle ϵ with the X- and Z-axes.

2. A correction for displacement of the accelerometers from the test center of gravity.

3. A correction to trim elevator position for pitch rate and for cg variation from a wind tunnel reference of 57 percent. This reference cg was used as the standard cg in the computer program. During the pushover/pullup the pitch rate was sustained by a δe input which contributed to lift and drag. Therefore, it was necessary to know the derivatives C_{m_q}, $C_{m_{\delta_e}}$, $C_{c_{\delta_e}}$, and $C_{N_{\delta_e}}$, in order to take out the normal and chord force increments due to the δe increment required to maintain the pitch rate. From pitch rate (q), C_{m_q}, and $C_{m_{\delta_e}}$, it was possible to determine the δe increment required to maintain the test pitch rate. The normal and chord force increments associated with this δe were subtracted from the test values of C_N and C_C to obtain the total test coefficients. The test values were then added to ΔC_N and ΔC_C due to variation from the standard cg to obtain the total standard coefficients for zero pitch rate at 57 percent cg.

Values of C_L and C_D at 57 percent standard cg were computed along with standard L/D by rotating the body axis coefficients using true angle of attack. The program printed out corrected trim elevator position, C_N and C_C test, and standard values for C_N, C_C, C_L, C_D, and L/D. The longitudinal stability and control derivatives, Mach number, and angle of attack, which were input data were also printed out for each data point. A sample printout is shown in figure 2. Table I gives a list of all symbols used in the program.

```
C       L/D DETERMINATION
        TYPE 1
     1  FORMAT    (//25X,18H L/D DETERMINATION/)
        READ 3
     3  FORMAT (20X 27H A/C TYPE  FLIGHT NO.  DATE,20X)
        TYPE 3
        TYPE 25
    25  FORMAT    (//48H TEST CN AND CA CORRECTED TO STANDARD CG AND Q=Ø)
        TYPE 26
    26  FORMAT(//2X7H MN/CNT,4X10H ALPHA/CAT,3X9H CNDE/CNS,3X9H CADE/CAS)
        TYPE 27
    27  FORMAT (40X,10X 9H CMDE/CLS,3X 8H CMQ/CDS,2X 11H DEC/(L/D)S//)
        READ 2,T,WT,TMAC,SAREA,E,X,Z
        READ 2,DXCG,DZCG,DXAX,DYAX,DZAX,DXAZ,DYAZ,DZAZ
        CK=1.7453292E-Ø2
        E=E*CK
    1Ø  READ 2,HT,P,R,DP,DR
        READ 2,CNDE,CADE,CMDE,CMQ,DE
        READ 2,MN,QB,VT,ALPHA,AX,AZ,Q,DQ
     2  FORMAT (8F1Ø.Ø)
        VT=VT*1.688
        AXC=AX*COS(E)-AZ*SIN(E)
        AZC=AZ*COS(E)+AX*SIN(E)
        AG=32.175-(3.Ø86E-Ø6)*HT
        AXCG=AXC+(CK*(DYAX*DR-DZAX*DQ)+CK**2*DXAX*(Q**2+R**2))/AG
        AZCG=AZC-(CK*(DXAZ*DQ-DYAZ*DP)+CK**2*DZAZ*(Q**2+P**2))/AG
        CNT=AZCG*WT/(QB*SAREA)
        CAT=(T-WT*AXCG)/(QB*SAREA)
        DDET= CMQ*Q*TMAC*CK/(CMDE*2.Ø*VT)
        CNTC=CNT+DDET*CNDE
        CATC=CAT+DDET*CADE
        DCMCG=(DXCG*CNTC-DZCG*CATC)/TMAC
        DDES=-DCMCG/CMDE
        CNS=CNTC+DDES*CNDE
        CAS=CATC+DDES*CADE
        ALPH1=ALPHA*CK
        CLS=CNS*COS(ALPH1)-CAS*SIN(ALPH1)
        CDS=CAS*COS(ALPH1)+CNS*SIN(ALPH1)
        SLDR=CLS/CDS
        IF(Z) 21,21,2Ø
    2Ø  DDET=DDET/CK
        DDES=DDES/CK
    21  DEC=DE+DDET+DDES
        TYPE 29,MN,ALPHA,CNDE,CADE,CMDE,CMQ,DEC
        TYPE 29,CNT,CAT,CNS,CAS,CLS,CDS,SLDR
    29  FORMAT (F9.6,F13.6,5F12.6)
        TYPE 3Ø
    3Ø  FORMAT (/)
        IF(X) 15,15,1Ø
        END
```

NOTE: *Indicates multiplication.
**Indicates an exponent.

Figure 1 Performance Digital Computer Program Listout

EQUATIONS USED IN PERFORMANCE DIGITAL COMPUTER PROGRAM

Correction to Accelerometers for Pitch Misalignment ε

$$a_{x_c} = a_x \cos \varepsilon - a_{z_b} \sin \varepsilon$$

$$a_{z_c} = a_{z_b} \cos \varepsilon + a_{x_b} \sin \varepsilon$$

Altitude Correction to Acceleration due to Gravity

$$a_g = 32.175 - (3.086 \times 10^{-6})\, h$$

Correction to Accelerometers to Test cg

$$a_{x_{cg}} = a_{x_c} + \frac{(\Delta y_{ax} \cdot \dot{r} - \Delta z_{ax} \cdot \dot{q}) + \Delta x_{ax} (q^2 + r^2)}{a_g}$$

$$a_{z_{cg}} = a_{z_c} - \frac{(\Delta x_{az} \cdot \dot{q} - \Delta y_{az} \cdot \dot{p}) - \Delta z_{az} (q^2 + p^2)}{a_g}$$

where

$+\Delta x$ = distance of accelerometer forward of test cg in ft

$+\Delta y$ = distance of accelerometer right of test cg in ft

$+\Delta z$ = distance of accelerometer down from test cg in ft

subscripts ax - longitudinal accelerometer

az - normal accelerometer

Calculation of C_N and C_c from Corrected Accelerations

$$C_{N_T} = (a_{z_{cg}} \cdot W)/(q_c \cdot S)$$

$$C_{c_T} = (T - W \cdot a_{x_{cg}})/(q_c \cdot S)$$

Correction to Elevator for Zero Pitch Rate

$$\Delta \delta e_t = C_{m_q} \cdot q \cdot \bar{c} \,/\, C_{m_{\delta e}} \cdot 2V_t$$

Correction to C_N and C_c for Elevator Trim Change

$$C_{N_{Tc}} = C_{N_T} + \Delta\delta e_t \cdot C_{N_{\delta e}}$$

$$C_{c_{Tc}} = C_{c_T} + \Delta\delta e_t \cdot C_{c_{\delta e}}$$

Change in Pitching Moment Induced by Translating Test cg to a 57 Percent Standard cg

$$\Delta C_{m_{cg}} = (\Delta x_{cg} \cdot C_{N_{Tc}} - \Delta z_{cg} \cdot C_{c_{Tc}}) / \bar{c}$$

where

$+\Delta x_{cg}$ = distance of test cg forward of 57% standard cg in ft

$+\Delta z_{cg}$ = distance of test cg down from 57% standard cg in ft

Correction to Elevator to Produce Zero Pitch Rate at Standard cg

$$\Delta\delta e_s = -\Delta C_{m_{cg}} / C_{m_{\delta e}}$$

Correction to C_N and C_c for Elevator Trim Change to Standard cg

$$C_N = C_{N_{Tc}} + \Delta\delta e_s \cdot C_{N_{\delta e}}$$

$$C_c = C_{c_{Tc}} + \Delta\delta e_s \cdot C_{c_{\delta e}}$$

Calculation of C_L, C_D and L/D at 57 Percent Standard cg

$$C_L = C_N \cos\alpha - C_c \sin\alpha$$

$$C_D = C_c \cos\alpha + C_N \sin\alpha$$

$$L/D = C_L / C_D$$

Calculation of Total Elevator Deflection Corrected to Zero Pitch Rate at 57 Percent Standard cg

$$\delta e_c = \delta e + \Delta\delta e_t + \Delta\delta e_s$$

L/D DETERMINATION

X-24A X-3-5 21 AUG 69

TEST CN AND CA CORRECTED TO STANDARD CG AND 0=0

MN/CNT	ALPHA/CAT	CNDE/CNS	CADE/CAS	CMDE/CLS	CMQ/CDS	DEC/(L/D)S
.487000	9.010000	.410000	.074000	-.110000	-.358000	3.518786
.314289	.023167	.301042	.020776	.294074	.067665	4.345976
.488000	9.300000	.415000	.072000	-.110000	-.359000	3.728989
.330789	.024566	.315933	.021989	.308227	.072756	4.236444
.489000	9.120000	.410000	.073000	-.110000	-.359000	3.265271
.324826	.024363	.310338	.021783	.302962	.070697	4.285311
.491000	9.150000	.410000	.073000	-.110000	-.360000	3.412839
.321896	.028972	.307890	.026478	.299762	.075102	3.991389
.491000	9.330000	.417000	.072000	-.110000	-.360000	2.204203
.319780	.025588	.305837	.023180	.298033	.072456	4.113252
.491000	10.070000	.425000	.071000	-.110000	-.360000	.981107
.350825	.019234	.337036	.016931	.328883	.075601	4.350223
.492000	12.060000	.450000	.066000	-.109000	-.360000	.393309
.419277	.011253	.401553	.008653	.390882	.092361	4.232091
.492000	13.740000	.467000	.062000	-.108000	-.360000	-.882719
.456329	.003263	.435197	.000457	.422634	.103811	4.071185
.491000	14.110000	.470000	.060000	-.107000	-.360000	-1.973856
.472640	.001601	.448656	-.001459	.435476	.107959	4.033700

Figure 2 Sample Output from Performance Digital Computer Program

Table I

PERFORMANCE DIGITAL COMPUTER PROGRAM SYMBOLS

Quantity	Program Symbol	Units
Thrust	T	lb
Vehicle weight	WT	lb
Mean aerodynamic chord	TMAC	ft
Wing area	SAREA	ft^2
Dynamic pressure	QB	lb/ft^2
Mach number	MN	--
Corrected altitude	HT	ft
True airspeed	VT	kt
True angle of attack	ALPHA	deg
Longitudinal acceleration	AX	g's
Normal acceleration	AZ	g's
X Distance to test cg	DXCG	ft
Z Distance to test cg	DZCG	ft
Distances of longitudinal accelerometer from test cg	DXAX DYAX DZAX	ft ft ft
Distances of normal accelerometer from test cg	DXAZ DYAZ DZAZ	ft ft ft
Roll rate	P	deg/sec
Pitch rate	Q	deg/sec
Yaw rate	R	deg/sec
Roll acceleration	DP	deg/sec^2
Pitch acceleration	DQ	deg/sec^2
Yaw acceleration	DR	deg/sec^2
$C_{N_{\delta e}}$	CNDE	deg^{-1} or rad^{-1}
$C_{A_{\delta e}}$	CADE	deg^{-1} or rad^{-1}
$C_{m_{\delta e}}$	CMDE	deg^{-1} or rad^{-1}
C_{m_q}	CMQ	rad^{-1}
Accelerometer alignment angle	E	deg
Conversion constant	CK	rad/deg
Accelerations corrected for alignment	AZC AXC	g's g's
Accelerations corrected to zero rotation rates	AXCG AZCG	rad/sec^2 rad/sec^2
Test normal force coefficient	CNT	--
Test axial force coefficient	CAT	--
Elevator correction for pitch rate	DDET	deg
Test normal and axial force coefficients corrected to zero pitch rate	CNTC CATC	-- --
cg Correction to pitching moment	DCMCG	--
cg Correction to elevator	DDES	deg
Standard normal and axial coefficients	CNS CAS	-- --
Standard lift and drag coefficients	CLS CDS	-- --
Standard lift to drag ratio	SLDR	--
Elevator position	DE	deg
Corrected elevator position	DEC	deg

APPENDIX V
TIP FIN FLOW SEPARATION STUDY

This appendix was adapted from an AFFTC Flight Test Technology Branch memo written by Robert G. Hoey in January 1970 after flight eight of the test program.

INTRODUCTION

Flow separation over the inner tip fin and rudder surfaces (tip fin stall) has occurred on each of the eight X-24A glide flights. The existence of separated flow is apparent in the rudder hinge moment and accelerometer data. It has been verified by tuft photos taken from the center fin camera and from chase plane photos. This has been manifested to the pilot as a mild, high frequency, Mach-type buffet.

TEST DATA

Tuft photos of the right tip fin from the center fin camera for 3 flight conditions are shown in figure 1. Three typical rudder hinge moment time histories are shown in figure 2 as the flight conditions crossed the tip fin stall boundary. These hinge moment traces are for the right rudder surfaces. The left rudder traces are generally similar, but the transition between attached and separated flow appears to be more gradual on the left side. Correlation between tuft photos and hinge moment traces for the onset of separation is good.

DISCUSSION

Analysis of wind tunnel data showed a large variation in the derivatives C_{n_α} and C_{l_β} for the Mach/angle of attack region in question (figure 3). The point of nonlinearity was probably related to the stalling of the tip fin. Notice in figure 3 that increasing the upper flap setting tended to increase the level of static stability in the region of separated flow but did not alter the angle of attack at which the flow separation occurred. Wind tunnel data at other Mach numbers showed similar trends and the apparent stall angle of attack has been plotted versus Mach number in figure 4. The flight conditions for the tuft pictures are shown by the three numbered circles. The three hinge moment time histories are represented by the arrowed lines. Reasonable correlation can be seen between the wind tunnel stall boundary and the flight test data points.

A summary plot of all observed separation or reattachment occurrences is shown in figure 5. These points represent a variety of upper flap and rudder bias configurations (δU_B = -21 degrees, -23.5 degrees, -30 degrees; δR_B = 0 degrees, -5 degrees, -10 degrees). Although there is a considerable amount of scatter in the plotted data, efforts to separate out the possible effects of rudder bias, upper flap bias, sideslip angle, rudder trim, or right versus left tip fin stall have been unsuccessful. It does appear that the intensity of the hinge moment vibrations was less in the stall region at the higher upper flap settings, a trend similar to that observed in the wind tunnel variations of C_{n_β} and C_{l_β} (figure 3).

The tip fin stall probably occurred when the local flow near the fin leading edge reached sonic velocity. This is indicated by the strong dependence of the stall boundary on Mach number and angle of attack.

A two-dimensional flow analysis for the tip fins conducted by R. Banner, NASA Flight Research Center, using wind tunnel pressure data confirms the possibility of local Mach numbers approaching 1.0 at freestream Mach numbers as low as 0.6.

EFFECT ON FUTURE FLIGHTS[1]

The tip fin stall observed during test flights to date has not produced any noticeable degradation in the inherent aerodynamic stability or controllability of the X-24A. The flow separation has, however, always occurred asymmetrically (or with asymmetric intensity) such that steady state pilot lateral control inputs of as much as 20 degrees have been required to maintain wings level flight. Since the lateral control power is quite low this could produce a dangerous situation if the asymmetry becomes worse at higher Mach numbers. Rudder trim has been used very effectively to compensate for a steady lateral mistrim; however, momentary angle of attack or configuration changes near the stall boundary produced transient lateral motions which were quite annoying to the pilot.

Analysis of the wind tunnel data before the first flight produced the boundary shown by the dotted lines in figure 5. This boundary was based upon analysis of the upper flap lateral control data which shows a sharp drop in effectiveness for flight conditions above this line. Note in tuft photo No. 2 that the flow over the upper flap is still attached even though the tip fins are stalled. This flight condition is above the predicted tip fin stall boundary, but below the predicted upper flap stall boundary. It is therefore anticipated that the predicted upper flap stall boundary is probably still valid with consequences which may be more severe than those associated with the tip fin stall. Since this boundary does appear to be a function of upper flap position larger upper flap settings should be used during exploratory flights to higher Mach numbers.

CONCLUSIONS

The tip fin stall observed on X-24A glide flights appears to correlate with nonlinearities in certain wind tunnel derivatives and is not in itself cause for concern. The flow separation boundary is most likely associated with the occurrence of sonic velocity near the tip fin leading edge and appears to be a primary function of only Mach number and angle of attack. Lateral-directional trim requirements associated with asymmetric tip fin stalling (or asymmetric intensity of the flow separation) was annoying to the pilot and could have become dangerous if the asymmetry became more severe at higher Mach numbers. Predicted boundaries for flow separation over the upper flaps are probably still valid and should be considered in the planning of high Mach number flights.

[1]Flights subsequent to this memo did not invalidate these statements.

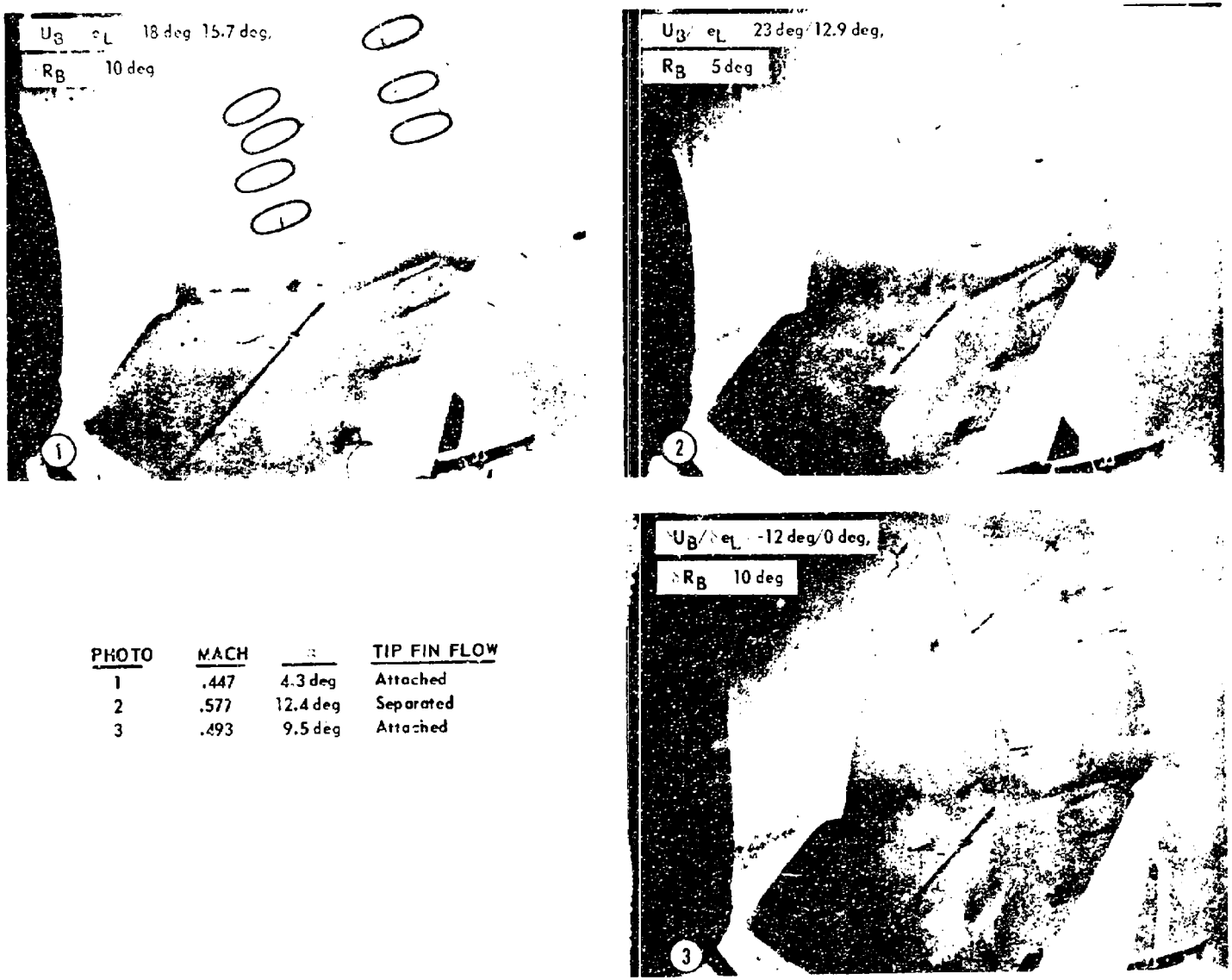

PHOTO	MACH		TIP FIN FLOW
1	.447	4.3 deg	Attached
2	.577	12.4 deg	Separated
3	.493	9.5 deg	Attached

Figure 1 X-24A Center Fin Camera Tuft Photos

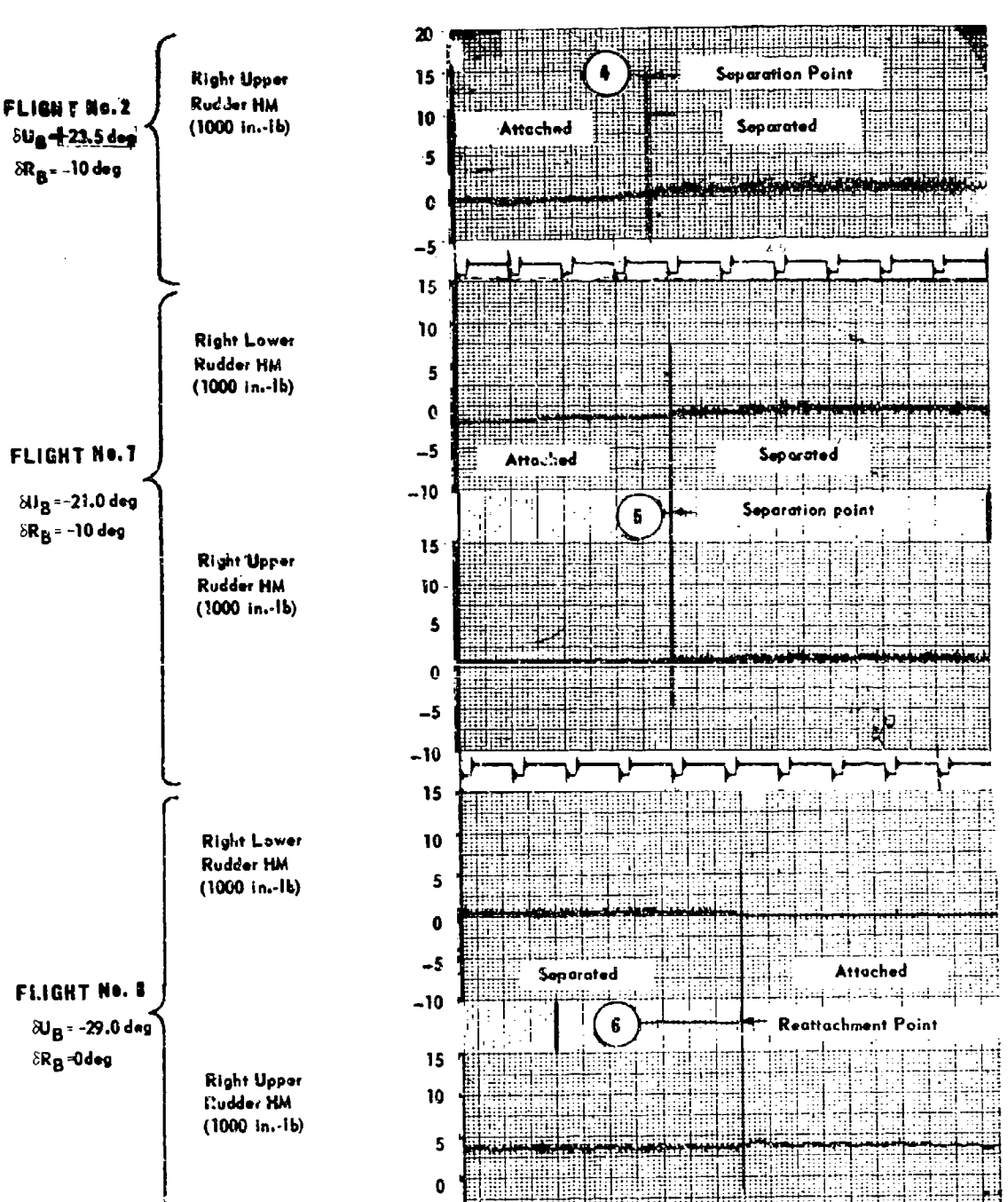

Figure 2 X-24A Rudder Hinge Moments

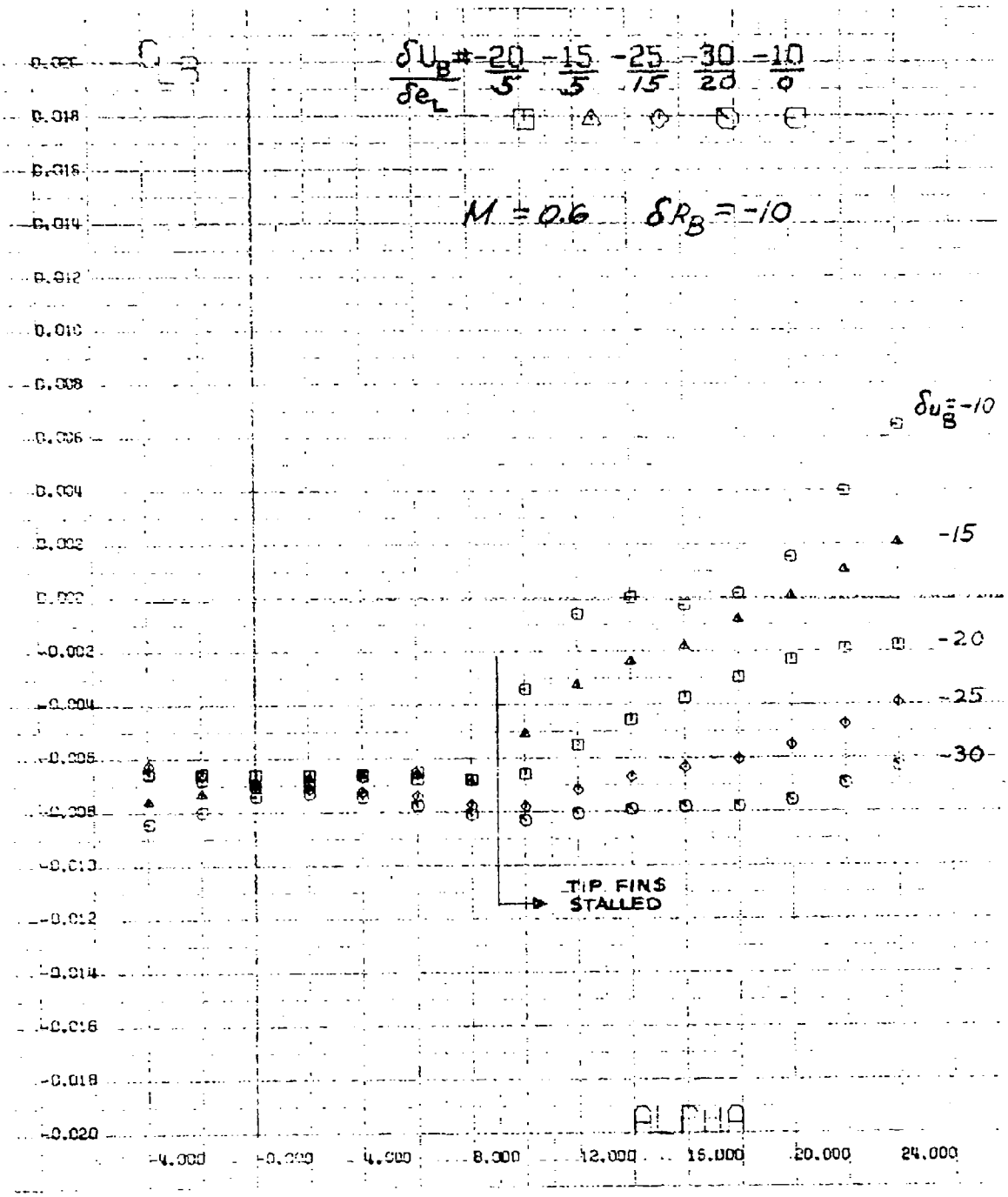

Figure 3 X-24A Wind Tunnel Data – C_{L_B}

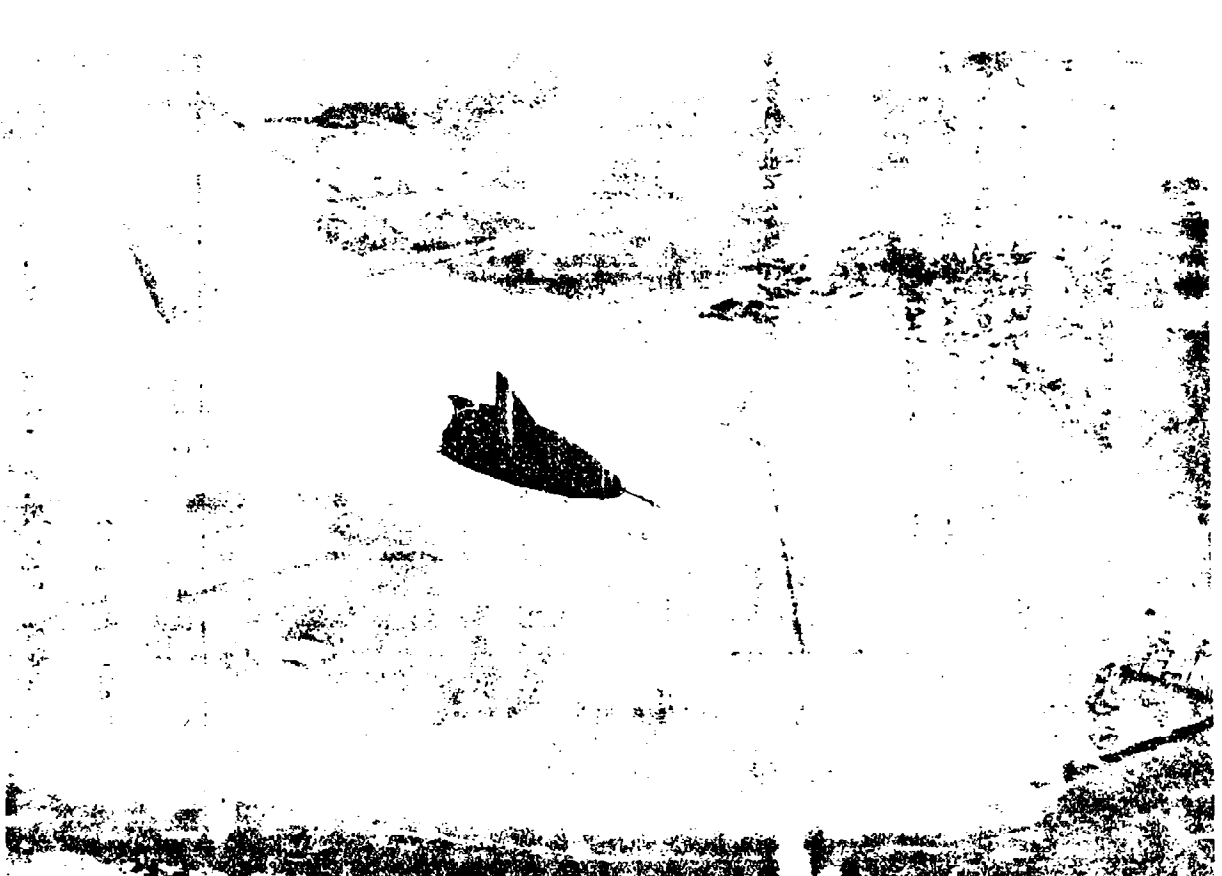

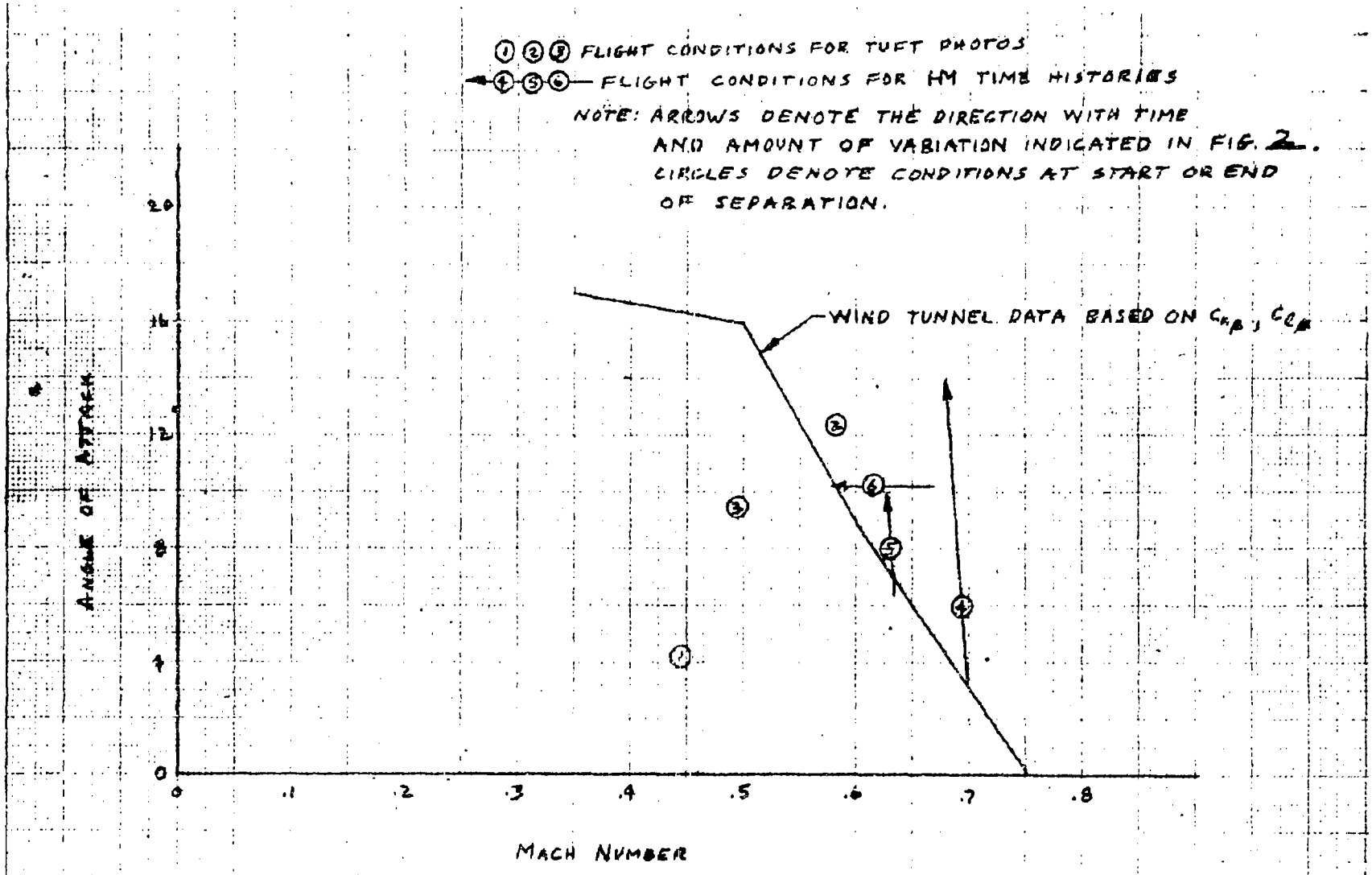

Figure 4. X-24A TIP FIN STALL BOUNDARY

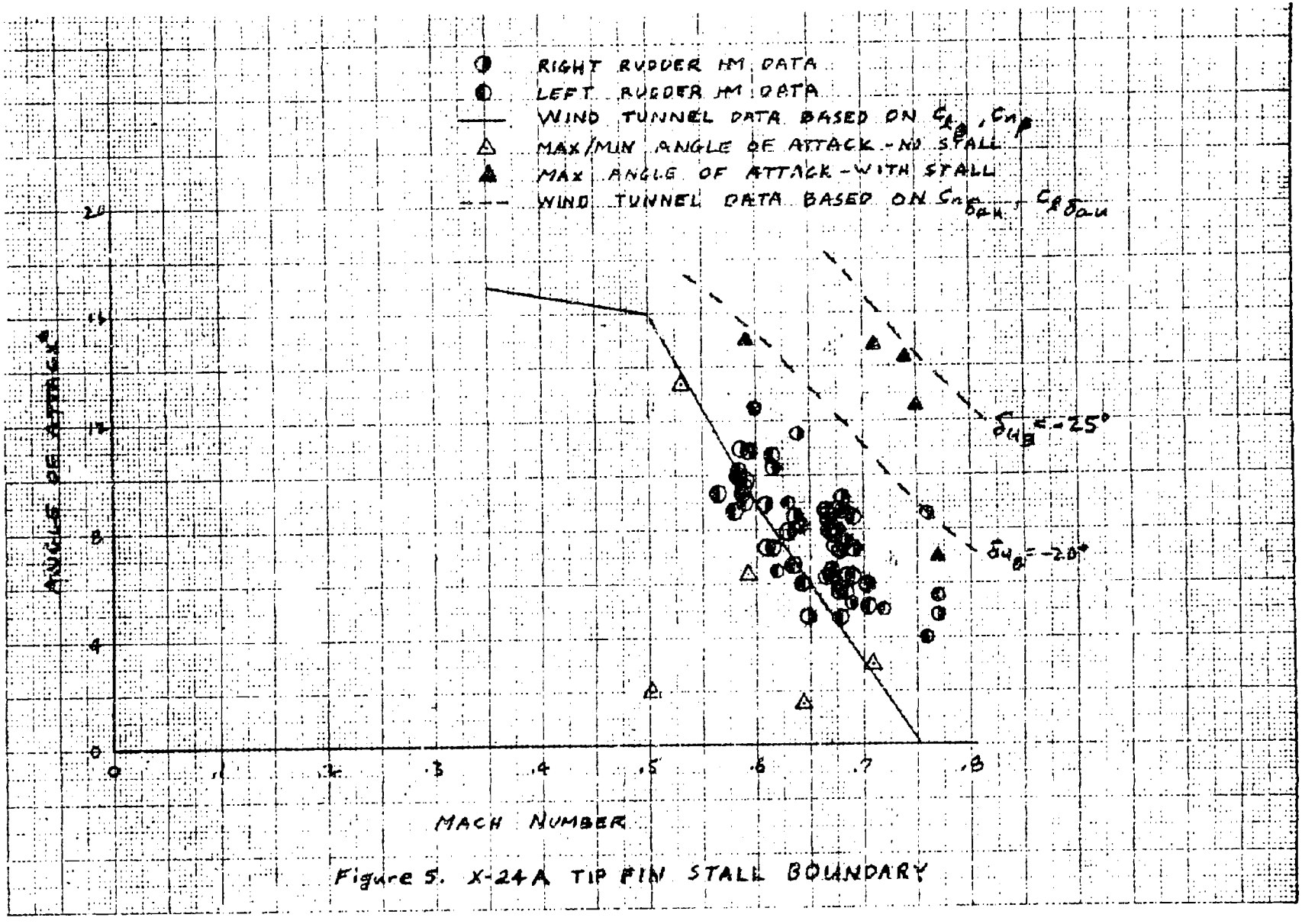

Figure 5. X-24A TIP FIN STALL BOUNDARY

REFERENCES

1. Measured Characteristics of the X-24A Lifting Body Flight Control System, FTC-TD-71-12, Air Force Flight Test Center, Edwards AFB, California, to be published.

2. Flight Planning and Conduct of the X-24A Lifting Body Flight Test Program, FTC-TD-71-10, Air Force Flight Test Center, Edwards AFB, California, to be published.

3. Retelle, John P., Jr., Captain USAF, Measured Weight, Balance, and Moments of Inertia of the X-24A Lifting Body, FTC-TD-71-6, Air Force Flight Test Center, Edwards AFB, California, November 1971.

4. Handling Qualities of the X-24A Lifting Body, FTC-TD-71-11, Air Force Flight Test Center, Edwards AFB, California, to be published.

5. Kirsten, Paul W., Wind Tunnel and Flight Test Stability and Control Derivatives for the X-24A Lifting Body, FTC-TD-71-7, Air Force Flight Test Center, Edwards AFB, California, February 1972.

6. Analysis of the Approach, Flare and Landing Characteristics of the X-24A Lifting Body, FTC-TD-71-9, Air Force Flight Test Center, Edwards AFB, California, to be published.

7. Flight Measured X-24A Lifting Body Control Surface Hinge Moments and Correlation with Wind Tunnel Predictions, NASA-TN-1234, NASA Flight Research Center, Edwards AFB, California, to be published.

8. X-24A Lifting Body Systems Operation and Performance, FTC-TD-71-13, Air Force Flight Test Center, Edwards AFB, California, to be published.

9. Pyle, Jon S., Lift and Drag Characteristics of the HL-10 Lifting Body During Subsonic Gliding Flight, NASA TND 6263, NASA Flight Research Center, Edwards AFB, California, March 1971.

10. Yaggy, Paul F., A Method for Predicting the Upwash Angles Induced at the Propeller Plane for a Combination of Bodies with an Upswept Wing, NACA TN 2528, 1951.

11. Herrington, Russel M., Major USAF, et al., Flight Test Engineering Handbook, AF-TR-6273, Air Force Flight Test Center, Edwards AFB, California, May 1951, revised January 1966.

UNCLASSIFIED
Security Classification

DOCUMENT CONTROL DATA - R & D

(Security classification of title, body of abstract and indexing annotation must be entered when the overall report is classified)

1. ORIGINATING ACTIVITY (Corporate author)	2a. REPORT SECURITY CLASSIFICATION
Air Force Flight Test Center Edwards AFB, California	Unclassified
	2b. GROUP N/A

3. REPORT TITLE

Flight Test and Wind Tunnel Performance Characteristics of the X-24A Lifting Body

4. DESCRIPTIVE NOTES (Type of report and inclusive dates)

Final

5. AUTHOR(S) (First name, middle initial, last name)

Lawrence G. Ash, Captain USAF

6. REPORT DATE	7a. TOTAL NO. OF PAGES	7b. NO. OF REFS
June 1972	150	11

8a. CONTRACT OR GRANT NO.	9a. ORIGINATOR'S REPORT NUMBER(S)
b. PROJECT NO.	FTC-TD-71-8
c. Project Directive 69-38 d. Program Structure 680A	9b. OTHER REPORT NO(S) (Any other numbers that may be assigned this report) N/A

10. DISTRIBUTION STATEMENT Distribution limited to U.S. Government agencies only (Test and Evaluation), April 1972. Other requests for this document must be referred to ASD (SDQR), Wright-Patterson AFB, Ohio 45433.

11. SUPPLEMENTARY NOTES	12. SPONSORING MILITARY ACTIVITY
This is Volume I of two volumes.	6510th Test Wing Edwards AFB, California

13. ABSTRACT The objectives of determining the performance characteristics of the X-24A lifting body from flight test data and correlating these results with wind tunnel predictions were successfully accomplished. Lift and drag characteristics were computed from onboard measured accelerations and flight conditions while the vehicle was in gliding flight. Performance data were obtained over Mach number and angle of attack ranges of 0.26 to 1.5 and 1.5 to 19.6 degrees, respectively. Discrepancies were apparent between different wind tunnel predictions. However, flight test data generally exhibited lower lift and slightly lower drag than wind tunnel predictions with the result that flight test and wind tunnel L/D values were in reasonably good agreement. Effects of Mach number, vehicle control surface configuration, and landing gear deployment on performance parameters were determined. Degradation of flight performance at low subsonic Mach numbers was attributed to tip fin flow separation. In Volume II of this report, supersonic performance comparisons are made between the PRIME and X-24A vehicles, both of which were the same aerodynamic configuration (SV-5). A significant degradation in subsonic performance due to simulated ablative surface roughness was obtained in full scale wind tunnel tests. Flight testing of simulated ablatives on the X-24A was not pursued; however, the estimated effects of the ablatives are discussed in Volume II.

DD FORM 1 NOV 65 1473

UNCLASSIFIED
Security Classification

KEY WORDS	LINK A		LINK B		LINK C	
	ROLE	WT	ROLE	WT	ROLE	WT
X-24A lifting body vehicle performance wind tunnel flight test lift drag glide flight powered flight ablatives						